



# **Growth and optical properties of isotopically enriched ZnO nanorods**

**Ciarán Gray, BSc (Hons)**

Thesis Submitted for the Award of

**Doctor of Philosophy**

School of Physical Sciences

Dublin City University

Research Supervisor

**Prof. Enda McGlynn**

January 2016

## **Declaration**

I hereby certify that this material, which I now submit for assessment on the programme of study leading to the award of Doctor of Philosophy, is entirely my own work, and that I have exercised reasonable care to ensure that the work is original, and does not to the best of my knowledge breach any law of copyright, and has not been taken from the work of others save and to the extent that such work has been cited and acknowledged within the text of my work.

Signed: \_\_\_\_\_

ID No.: 57435622

Date: \_\_\_\_\_

## Acknowledgements

This thesis is the culmination of the work of several years, and I wish to record my sincere thanks to those who helped me along the way, and contributed to its completion.

First and foremost, thanks to my research supervisor, Prof. Enda McGlynn, to whom I am indebted for taking me on as a PhD student and giving me the opportunity to carry out this research. His expertise and insight into the world of ZnO has been invaluable, as well as his constant encouragement and enthusiasm for my research.

Thanks to all members of the DCU School of Physical Sciences and the NCPST who have helped me during this work. In particular I wish to thank Prof. Martin Henry for his input and sharing of his knowledge of ZnO and Prof. Greg Hughes for his input on the SIMS. Thank you to Mr. Conor Byrne and Dr. Rajani Vijayaraghavan for their help with SIMS and Raman Measurements. I would also like to thank Dr. Daragh Byrne for always answering my questions and passing on his ZnO expertise.

I am also very grateful for the assistance of all our external collaborators, in particular Mr. Lukas Trefflich and Prof. Carsten Ronning (Jena, Germany), and Dr. Joseph Cullen (Linköping, Sweden).

Thanks also to all the technical and administrative staff in the School, particularly Pat Wogan, Alan Hughes, Des Lavelle and Lisa Peyton.

Thanks to everyone in my lab and office for their advice, help and friendship over the last few years. They are too many to name all, but I will mention Ruth, Séamus, Joe, Jack, Damien and Cathal. In addition, I would like to thank Mr. Saikumar Inguva, for many conversations on ZnO, and for his assistance and encouragement.

I am eternally grateful to my parents John and Marina, my sister Cróna, brother Eóin and my fiancée Emer for their constant love and support throughout my

journey. It would not have been possible without them. My thanks are also due to all my friends, in particular Adam and Jen, for their support and friendship.

Finally, my appreciation is also due to the Irish Research Council for funding this work through an EMBARK Postgraduate Scholarship. Needless to say, this work would not have happened without this financial support.

# Table of Contents

Declaration .....	ii
Acknowledgements .....	iii
Table of Contents .....	v
List of Acronyms and Symbols .....	ix
List of Figures .....	xi
List of Tables .....	xv
Publications .....	xvii
Conferences .....	xviii
Other Presentations and Awards .....	xix
Abstract .....	xxi
Chapter 1: Introduction to ZnO.....	1
1.1 Introduction and Applications .....	1
1.2 Structural Properties .....	3
1.3 Electronic Properties .....	5
1.4 Growth Techniques .....	8
1.5 Defects in ZnO and the Isotope Effect .....	12
1.6 Motivation and Objectives .....	13
1.7 Outline of Remainder of Thesis .....	16
1.8 References .....	17
Chapter 2: Growth and Characterisation Techniques .....	24
2.1 Introduction .....	24
2.2 Growth of Zn Isotope-enriched Nanorods.....	25
2.2.1 Substrate Preparation .....	25
2.2.2 Seed Layer Preparation .....	26
2.2.3 Chemical Bath Deposition .....	26
2.2.4 Vapour Phase Transport.....	30
2.3 Growth of O Isotope-enriched ZnO Nanorods .....	32
2.3.1 Method 1: Modified VS CTR-VPT method in DCU .....	33
2.3.2 Method 2: VLS VPT method in Jena.....	34
2.4 Characterisation Techniques .....	36
2.4.1 Scanning Electron Microscopy .....	36

2.4.2	X-ray Diffraction.....	40
2.4.3	Secondary Ion Mass Spectroscopy .....	42
2.4.4	Raman Spectroscopy.....	45
2.4.5	Photoluminescence.....	47
2.4.6	Reflectance Spectroscopy .....	56
2.5	References .....	57
Chapter 3: Background Theory of Elements of Optical Properties of ZnO .....		60
3.1	Introduction .....	60
3.2	Low Temperature Photoluminescence .....	61
3.3	Defects in Semiconductors .....	64
3.4	Structure of the ZnO PL emission spectrum .....	67
3.5	The Cu-related Defect at 2.86 eV.....	69
3.6	The Isotope Effect .....	74
3.7	Phonon modes .....	76
3.8	Conclusions .....	78
3.9	References .....	78
Chapter 4: Zn Isotope-enriched ZnO Nanorods.....		82
4.1	Introduction .....	82
4.2	Morphology - SEM .....	85
4.3	Alignment and Crystal Quality - XRD.....	90
4.4	Isotopic Enrichment - SIMS.....	94
4.5	Phonon Frequencies - Raman.....	98
4.6	Optical Quality and Enrichment - Low temperature PL .....	101
4.7	FX Energies - Reflectance Spectroscopy .....	106
4.8	Conclusions .....	107
4.9	References .....	108
Chapter 5: O Isotope-enriched ZnO Nanorods .....		111
5.1	Introduction .....	111
5.1.1	Initial Experiments regarding O-enriched Material .....	112
5.1.2	Method 1: Modified VS CTR-VPT method .....	114
5.1.3	Method 2: VLS VPT method.....	115
5.2	Morphology – SEM.....	116
5.3	Alignment and Crystal Quality – XRD .....	119

5.3.1	Note on Strain .....	122
5.4	Isotopic Enrichment – miniSIMS .....	126
5.5	Phonon Frequencies and Enrichment – Raman.....	128
5.6	Optical Quality and Enrichment - Low temperature PL .....	131
5.7	Conclusions .....	134
5.8	References .....	135
Chapter 6:	Optical Properties and the Cu-related Defect in Isotopically Enriched ZnO	137
6.1	Introduction .....	137
6.2	Zn-enriched Nanorods .....	138
6.2.1	PL Spectra .....	138
6.2.2	Discussion on Energy Shifts and Involvement of $Zn_i$ or $V_O$ in the Cu-related Emission at 2.86 eV .....	140
6.3	O-enriched Nanorods .....	145
6.3.1	PL Spectra .....	145
6.3.2	Energy Shifts.....	147
6.3.3	Discussion on Energy Shifts, Line Widths and Involvement of $O_i$ or $V_{Zn}$ in the Cu-related Emission at 2.86 eV.....	151
6.3.4	Estimate of Level of Enrichment in O-enriched ZnO.....	153
6.4	Discussion on Possible Causes of Reduced Oxygen Enrichment .....	155
6.5	Conclusions .....	158
6.6	References .....	159
Chapter 7:	Conclusions and Future Work.....	161
7.1	Conclusions .....	161
7.2	Future Work .....	164
7.3	References .....	166
Appendix A:	Some Applications of these Growth Methods and Materials in other Experiments.....	A1
A.1	Introduction .....	A1
A.2	TRPL of Zn-enriched ZnO nanorods .....	A2
A.3	Third harmonic UV generation with ZnO nanorods .....	A4
A.4	Particle and X-ray generation using ZnO nanorods .....	A6
A.5	References .....	A7

Appendix B: Efficiency of the SPEX grating and PMT .....	B1
B.1 References.....	B1
Appendix C: XRD Strain measurements for the Zn-enriched and VLS O-enriched samples.....	C1

## List of Acronyms and Symbols

$A^0X$	Acceptor bound exciton
Al	Aluminium
$Al_2O_3$	Sapphire
Ar	Argon
Au	Gold
BX	Bound exciton
C	Carbon
CCD	Charge-coupled device
CO	Carbon monoxide
$CO_2$	Carbon dioxide
CBD	Chemical bath deposition
CCD	Charge-coupled device
CTR-VPT	Carbothermal reduction vapour phase transport
Cu	Copper
CVD	Chemical vapour deposition
$D^0X$	Donor bound exciton
$D^+X$	Ionised donor bound exciton
DAP	Donor acceptor pair
DCU	Dublin City University
(DI)- $H_2O$	(Deionised) water
EDX	Energy-dispersive x-ray spectroscopy
FT	Fourier transform
FWHM	Full width half maximum
FX	Free exciton
Ga	Gallium
GaN	Gallium nitride
$H_2SO_4$	Sulphuric acid
H	Hydrogen
He	Helium
HeCd	Helium cadmium
Hg	Mercury

HMT	Hexamethylenetetramine
In	Indium
LA	Longitudinal acoustic
LED	Light emitting diode
LO	Longitudinal optical
MBE	Molecular beam epitaxy
MFC	Mass flow controller
MOCVD	Metal oxide chemical vapour deposition
N	Nitrogen
NaOH	Sodium hydroxide
O	Oxygen
O <sub>i</sub>	Oxygen interstitial
PL	Photoluminescence
PLD	Pulsed laser deposition
PMT	Photomultiplier tube
PTFE	Polytetrafluoroethylene
sccm	Standard cubic centimetres per minute
SEM	Scanning electron microscopy
Si	Silicon
SIMS	Secondary ion mass spectroscopy
SiO <sub>2</sub>	Silicon dioxide
SGB	Structured green band
SX	Surface exciton
TA	Transverse acoustic
TCO	Transparent conducting oxide
TES	Two electron satellite
Ti	Titanium
TO	Transverse optical
TRPL	Time resolved photoluminescence
UV	Ultraviolet
V <sub>Zn</sub>	Zinc vacancy
V <sub>O</sub>	Oxygen vacancy
VLS	Vapour-liquid-solid
VS	Vapour-solid

VPT	Vapour phase transport
XRD	X-ray diffraction
Zn <sub>i</sub>	Zinc interstitial
Zn	Zinc
ZnO	Zinc oxide
ZPL	Zero phonon line

## List of Figures

Figure 1.1: (a) Hexagonal wurtzite crystal structure of ZnO and (b) the wurtzite unit cell (yellow circles represent oxygen).....	3
Figure 1.2: The main crystal planes in wurtzite ZnO.....	4
Figure 1.3: Schematic of the ZnO electronic band structure. ....	6
Figure 1.4: Examples of ZnO nanostructure morphologies from the literature: (a,b) nanorods <sup>60,61</sup> , (c) nanowalls <sup>62</sup> , (d) nanodisks <sup>63</sup> , (e) nanobelts/nanohelices <sup>64</sup> and (f) nanobowls. <sup>65</sup> .....	9
Figure 2.1: (a) Schematic diagram, and (b) photograph, of the experimental setup used for the CBD growth step. ....	27
Figure 2.2: (a) Schematic diagram of the furnace setup used for the VPT growth of ZnO nanorods, and (b) photograph of the VPT furnace. ....	31
Figure 2.3: Schematic diagram of the experimental setup for the growth of O-enriched ZnO nanorods using a modified VS technique. ....	33
Figure 2.4: Schematic diagram showing the general experimental setup for the growth of O-enriched ZnO nanorods using the VLS technique in Jena. ....	35
Figure 2.5: (a) Schematic diagram showing the main components of a typical SEM system and (b) a more detailed diagram showing the secondary electron (SE) and backscattered electron (BSE) detectors and the associated electronics. (c) Diagram of the process of generation of EDX signal, (d) Photograph of the Carl-Zeiss SEM system in DCU. ....	39
Figure 2.6: (a) Schematic diagram of the layout of an XRD system with zoom showing diffraction from adjacent crystal planes and the geometry of the Bragg	

equation, and (b) photograph of the Bruker AXS D8 Advance Texture Diffractometer.....	41
Figure 2.7: (a) Schematic diagram showing the sputtering process used in SIMS, (b) photograph of the SIMS system and (c) photograph of the Millbrook miniSIMS alpha system.....	44
Figure 2.8: Energy level diagram showing Rayleigh scattering, and Raman Stokes and anti-Stokes scattering processes.....	46
Figure 2.9: (a) Schematic, and (b) photograph, of the optical setup used for PL with the SPEX monochromator.....	48
Figure 2.10: (a) Schematic, and (b) photograph, of the optical setup used for PL with the FT spectrometer.....	51
Figure 2.11: (a) Schematic, and (b) photograph, of the optical setup used during reflectance spectroscopy experiments with the FT spectrometer. ....	56
Figure 3.1: Diagram showing the excitation and recombination processes in (a) direct, and (b) indirect, band gap semiconductors. ....	62
Figure 3.2: (a) Schematic of a FX and D <sup>0</sup> X; (b) Representation of the main transitions with PL: i) FX, ii) BX, iii) electron to acceptor, iv) donor to acceptor, v) hole to donor. ....	66
Figure 3.3: Diagram showing the main types of bound exciton in the band edge region of ZnO.....	67
Figure 3.4: Configurational coordinate diagram describing the ground and excited states of an impurity and the absorption and emission spectra due electron-phonon coupling.....	72
Figure 3.5: Illustration of how the phonon sideband shape evolves with increasing S parameter.....	73
Figure 3.6: E <sub>2</sub> <sup>low</sup> , E <sub>2</sub> <sup>high</sup> , E <sub>1</sub> and A <sub>1</sub> phonon modes in wurtzite ZnO.....	78
Figure 4.1: Graphical representation of the Zn isotopic content of the eight Zn-enriched samples. ....	82
Figure 4.2: Typical buffer layer of CBD deposited nanorods.....	83
Figure 4.3: VPT-grown ZnO nanorods with (a) 60 mg and (b) 10 mg of each source powder at 900°C.....	85
Figure 4.4: SEM images showing typical morphology of the ZnO nanorods: (a) plan view, (b) 30° to the vertical and (c) 90° to the vertical. Images are from the <sup>64</sup> ZnO sample. ....	86

Figure 4.5: (a) 90° angle of <sup>66/68</sup> ZnO nanorods with CBD buffer layer visible; (b) <sup>64/66</sup> ZnO nanorods with CBD buffer layer visible at 90°; (c) CBD buffer layer at 90° in <sup>64/66</sup> ZnO; and (d) 30° view of longer nanorods on part of <sup>66</sup> ZnO which have lost their alignment and become entangled;.....	87
Figure 4.6: <sup>64/66/68</sup> ZnO samples at 30° (a and c), 90° (b and d). The first sample (a and b) shows poor nanorod morphology. The second sample (c and d) has improved nanorod morphology. ....	88
Figure 4.7: 2θ-ω spectra of several Zn-enriched ZnO samples dominated by the Si substrate peak at 69.1° and the ZnO peak at 34.4°. ....	90
Figure 4.8: XRD rocking curves of the 34.4° (0002) ZnO peak from the <sup>nat</sup> ZnO, <sup>64</sup> ZnO, <sup>66</sup> ZnO and <sup>68</sup> ZnO samples. ....	93
Figure 4.9: 2θ-ω diffractograms of CBD buffer layer nanorods and ZnO seed layer only. (Inset shows rocking curve of ZnO (0002) peak in CBD nanorods.) ....	94
Figure 4.10: SIMS spectra from each sample in the Zn-enriched set. ....	96
Figure 4.11: miniSIMS spectra from each sample in the Zn-enriched set. ....	97
Figure 4.12: Raman spectra of isotopically enriched <sup>64</sup> ZnO, <sup>66</sup> ZnO and <sup>68</sup> ZnO nanorods. Inset shows the signal from the Si substrate. ....	100
Figure 4.13: PL spectra of the <sup>66</sup> ZnO sample showing (a) a broad range spectrum displaying the typical PL emission from ZnO nanorods, (b) the intense UV band edge emission in detail, and (c) the Cu-related 2.86 eV ZPL and associated SGB (from annealed portion). ....	101
Figure 4.14: Comparison of PL intensities of VPT and CBD nanorods. ....	103
Figure 4.15: Typical PL spectra of selected enriched ZnO nanorod samples showing the band edge region including the I <sub>9</sub> line. ....	104
Figure 4.16: Reflectance spectrum of a (a) single crystal ZnO sample showing the A-exciton and B-exciton clearly, and (b) reflectance spectrum of the <sup>64</sup> ZnO, <sup>66</sup> ZnO and <sup>68</sup> ZnO samples. A and B label the A- and B-excitons. ....	106
Figure 5.1: Image of CBD buffer following VPT step in oxygen-depleted atmosphere. No nanorod growth is observed. ....	115
Figure 5.2: SEM images of sample Zn <sup>16</sup> O-VS at (a) ~40° and (b) ~90°, and the middle of sample Zn <sup>16/18</sup> O-VS at (c) ~40° and (d) ~90°. ....	116
Figure 5.3: SEM images of the morphology of the VLS samples with 30° tilt; (a) Zn <sup>16</sup> O-VLS, (b) Zn <sup>16</sup> O-VLS showing hexagonal structure, (c) Zn <sup>18</sup> O-VLS and (d) Zn <sup>16/18</sup> O-VLS. ....	118

Figure 5.4: $2\theta$ - $\omega$ diffractograms of the VS O-enriched samples dominated by the Si substrate peak at $69.1^\circ$ and the ZnO peak at $34.4^\circ$ . Inset shows rocking curves of the ZnO (0002) peak. ....	119
Figure 5.5: $2\theta$ - $\omega$ diffractograms of the VLS O-enriched samples dominated by the Si substrate peak at $69.1^\circ$ and containing multiple ZnO peaks. Inset shows rocking curves of the ZnO (0002) peak.....	122
Figure 5.6: (a) Symmetric and (b) asymmetric XRD reflections, which enables (c) the mapping along a line in reciprocal space which is not normal to the substrate. ....	123
Figure 5.7: s-plane and r-plane $2\theta$ peaks (with in-plane component) in the tilted VS O-enriched samples.....	124
Figure 5.8: Typical miniSIMS spectra of the Zn <sup>16</sup> O and Zn <sup>18</sup> O samples in the VS set (a and b) and the VLS set (b and d). ....	126
Figure 5.9: Raman spectra of the VS method O-enriched ZnO nanorods. Inset shows the signal from the Si substrate. ....	128
Figure 5.10: Raman spectra of the VLS method O-enriched ZnO nanorods. Inset shows the signal from the Si substrate. ....	128
Figure 5.11: Effect of the $900^\circ\text{C}$ 10 minute anneal on the green band region.....	131
Figure 5.12: Band edge region of the PL spectrum in the (a) VS and (b) VLS O-enriched samples. ....	133
Figure 6.1: Band edge (a and b) and Cu-related 2.86 eV ZPL (c and d) spectra from the Zn-enriched samples from the SPEX system (a and c) and the FT system (b and d) .....	139
Figure 6.2: Energies of the I <sub>9</sub> lines (black) and Cu-related ZPL lines (blue) in the Zn-enriched ZnO samples, from the (a) SPEX and (b) FT systems. ....	144
Figure 6.3: Band edge (a and b) and Cu-related 2.86 eV ZPL (c and d) spectra from the VS and VLS O-enriched samples from the FT system (a, b and d) and the SPEX system (c). ....	146
Figure 6.4: Energies of the I <sub>9</sub> lines (black) and Cu-related ZPL lines (blue) in the (a) VS, and (b) VLS, O-enriched ZnO samples, from the SPEX system.....	149
Figure 6.5: Energies of the I <sub>9</sub> lines (black) and Cu-related ZPL lines (blue) in the (a) VS, and (b) VLS, O-enriched ZnO samples, from the FT system. ....	150
Figure A.1: TRPL decay curves of (a) the I <sub>9</sub> recombination, (b) the I <sub>9</sub> -1LO line, and (c) the I <sub>9</sub> and SX features, in Zn-enriched ZnO nanorods.....	A3
Figure A.2: CBD grown ZnO nanorods on a fused silica substrate.....	A5

Figure A.3: ZnO nanorods on Ti foil grown by the (a) NaOH and (b) HMT chemical baths. ....	A6
Figure B.1: SPEX grating and PMT efficiency curves. ....	B1

## List of Tables

Table 2.1: Natural abundances of Zn isotopes in ZnO and the enrichment levels of the source powders used to produce Zn-isotopically enriched nanorods.....	32
Table 4.1: Set of Zn-enriched ZnO nanorods.....	83
Table 4.2: ZnO (0002) peaks, FWHM and crystallite size and ZnO c lattice constants, and Si (004) peaks and lattice constants in Zn-enriched nanorods. ....	91
Table 4.3: Peaks and FWHM of the rocking curves of the 34.4° ZnO (0002) peak in all samples.....	93
Table 4.4: Frequencies and FWHM of the $E_2^{\text{low}}$ and $E_2^{\text{high}}$ phonons for $^{64}\text{ZnO}$ , $^{66}\text{ZnO}$ and $^{68}\text{ZnO}$ samples. ....	100
Table 4.5: Energies and FWHM of the $I_9$ exciton recombination in samples with different Zn isotopic enrichments. ....	104
Table 5.1: Sets of O-enriched ZnO nanorods successfully produced using both methods. ....	112
Table 5.2: ZnO (0002) $2\theta$ peak and FWHM, and calculated crystallite size and c lattice constant for the VS and VLS O-enriched samples.....	120
Table 5.3: Peaks and FWHM of the rocking curves of the 34.4° ZnO (0002) reflection the VS O-enriched samples. ....	120
Table 5.4: s-plane and r-plane $2\theta$ peaks in the VS (with in-plane component) and VLS O-enriched samples (from standard out-of-plane diffractograms for comparison).....	125
Table 5.5: Frequencies and FWHM of the $E_2^{\text{low}}$ and $E_2^{\text{high}}$ phonons for the VS and VLS O-enriched samples. ....	130
Table 5.6: Peak positions and FWHM of the $I_9$ exciton recombination in the VS and VLS O-enriched samples. ....	133
Table 6.1: Energies and widths of the $I_9$ and ZPL lines in Zn-enriched ZnO, from the SPEX system.....	142

Table 6.2: Energies and widths of the I <sub>9</sub> and ZPL lines in Zn-enriched ZnO, from the FT system. ....	142
Table 6.3: Energies and widths of the I <sub>9</sub> and ZPL lines in O-enriched ZnO, from the SPEX system. ....	147
Table 6.4: Energies and widths of the I <sub>9</sub> and ZPL lines in O-enriched ZnO, from the FT system. ....	148
Table 6.5: Summary of the band edge and ZPL energy shifts in the O-enriched samples. ....	150
Table 6.6: <sup>18</sup> O enrichment as % of literature PL and Raman references for Zn <sup>18</sup> O and Zn <sup>16/18</sup> O nanorods. ....	154
Table A.1: Fast (τ <sub>f</sub> ) and slow (τ <sub>s</sub> ) component time constants of the I <sub>9</sub> decay lifetime and their relative amplitudes in Zn-enriched ZnO nanorods. ....	A4
Table C.1: s-plane and r-plane 2θ peaks (with in-plane component) in the Zn-enriched and VLS O-enriched samples. ....	C2

## Publications

Ciarán Gray, Lukas Trefflich, Carsten Ronning, Enda McGlynn. Growth of oxygen-enriched ZnO nanorods by two novel VPT methods. [In preparation]

Ciarán Gray, Enda McGlynn, *et al.* Optical properties of isotopically enriched ZnO nanorods and study of the Cu-related defect at 2.86 eV. [In preparation]

Saikumar Inguva, Ciarán Gray, Enda McGlynn, Jean-Paul Mosnier. Origin of the 3.331 eV emission in ZnO nanorods: comparison of vapour phase transport and pulsed laser deposition grown nanorods. [Submitted to the Journal of Luminescence]

A. Andreev, K. Platonov, J. Braenzel, A. Lübcke, S. Das, H. Messaoudi, R. Grunwald, C. Gray, E. McGlynn, M. Schnürer. Relativistic laser nano-plasmonics for effective fast particle production. *Plasma Physics and Controlled Fusion*. 58, 014038 (2016).

Ciarán Gray, Joseph Cullen, Conor Byrne, Greg Hughes, Irina Buyanova, Weimin Chen, Martin O. Henry, Enda McGlynn. Growth of isotopically enriched ZnO nanorods of excellent optical quality. *Journal of Crystal Growth* 429 (2015) 6–12.

S.K. Das, F. Güell, C. Gray, D. Byrne, P.K. Das, R. Grunwald, G. Steinmeyer, E. McGlynn. Comparison of linear and nonlinear optical properties of ZnO nanorods. Chapter 11 (pages 193-206) of *Progress in Nonlinear Nano-Optics* (Editors: S. Sakabe, C. Lienau and R. Grunwald). Springer Verlag, 2015.

S.K. Das, F. Guell, C. Gray, P.K. Das, R. Grunwald, E. McGlynn. ZnO nanorods for efficient third harmonic UV generation: erratum. *Optical Materials Express*, 4 (2014) 1243.

S.K. Das, F. Guell, C. Gray, P.K. Das, R. Grunwald, E. McGlynn. ZnO nanorods for efficient third harmonic UV generation. *Optical Materials Express*, 4 (2014) 701–709.

## **Conferences**

A. Andreev, K. Platonov, J. Braenzel, A. Lübcke, S. Das, H. Messaoudi, R. Grunwald, C. Gray, E. McGlynn, M. Schnürer. Relativistic laser nano-plasmonics. Oral presentation (by A. Andreev) at the 42nd European Physical Society, EPS, Conference on Plasma Physics, 22-26 June 2015, Lisbon, Portugal.

Enda McGlynn, Frank Güell, Susanta Kumar Das, Ciarán Gray, Daragh Byrne, Prasanta Kumar Das, Günter Steinmeyer, and Ruediger Grunwald. THG of ZnO nanorods for efficient third order interferometric FROG. Oral presentation (by Enda McGlynn) at the Laserlab Europe Users Meeting, 29-30 September 2014, Prague, Czech Republic.

Julia Braenzel, Matthias Schnürer, Alexander Andreev, Susanta Kumar Das, Hamza Messaoudi, Ruediger Grunwald, Ciarán Gray, Enda McGlynn. Laser ion acceleration with optimized foil target morphology and atomic composition. Oral presentation (by Julia Braenzel) at the European Conference on Laser Interaction with Matter, ECLIM 2014, 31 August – 5 September 2014, Paris, France.

Susanta Kumar Das, Frank Güell, Ciarán Gray, Daragh Byrne, Prasanta Kumar Das, Ruediger Grunwald, Enda McGlynn, Günter Steinmeyer. THG of ZnO nanorods for efficient third order interferometric FROG. Oral presentation (by Günter Steinmeyer) at the Conference on Lasers and Electro-Optics: Science & Innovations (CLEO/SI) 2014, 8-13 June 2014, San Jose CA, USA.

C. Gray, M.O. Henry, E. McGlynn. Effects of Zn isotopic enrichment on the Cu-related 2.86 eV emission in ZnO nanorods. Poster presentation at Photonics Ireland 2013, 4-6 September 2013, Belfast, UK.

Ciarán Gray, Martin O. Henry, Daragh Byrne, Enda McGlynn. Effects of Zn isotopic enrichment on the Cu-related 2.86 eV emission in ZnO nanorods. Poster presentation at the International Conference on Defects in Semiconductors, ICDS27, 21-26 July 2013, Bologna, Italy.

C. Gray, D. Byrne, M. Henry, E. McGlynn. Isotope enrichment and substitution in the study of impurities and defects in ZnO semiconductors. Oral presentation at Condensed Matter Division of the European Physical Society, CMD-24, 3-7 September 2012, Edinburgh, Scotland, UK.

## **Other Presentations and Awards**

C. Gray, L. Trefflich, J. Cullen, C. Byrne, G. Hughes, I. Buyanova, W. Chen, C. Ronning, M.O. Henry, E. McGlynn. Growth and Optical Properties of Isotopically Enriched ZnO Nanorods. Poster presentation at NCPST Postgraduate Poster Competition, Dublin City University, 10 December 2015.

Ciarán Gray, Martin O. Henry, Daragh Byrne, Enda McGlynn. Effects of Zn isotopic enrichment on the Cu-related 2.86 eV emission in ZnO nanorods. Poster presentation at NCPST Postgraduate Poster Competition, Dublin City University, 17 December 2013. **Runner-up.**

C. Gray, D. Byrne, M. Henry, E. McGlynn. Isotope enrichment and substitution in the study of impurities and defects in ZnO semiconductors. Poster presentation at BOC School of Physical Sciences Poster Competition, Dublin City University, 31 May 2013.

C. Gray, D. Byrne, M. Henry, E. McGlynn. Isotope enrichment and substitution in the study of impurities and defects in ZnO semiconductors. Poster presentation at NCPST Postgraduate Poster Competition, Dublin City University, 18 December 2012. **Winner, Best Early Stage Researcher.**

C. Gray, D. Byrne, E. McGlynn, M.O. Henry. Isotope enrichment and substitution in the study of impurities and defects in ZnO semiconductors. Poster presentation at BOC School of Physical Sciences Poster Competition, Dublin City University, 13 April 2012.

## Abstract

### Growth and optical properties of isotopically enriched ZnO nanorods

Ciarán Gray, BSc (Hons)

The growth and analysis of the optical properties of isotopically enriched ZnO nanorods is presented. ZnO nanorods were grown on silicon substrates by chemical bath deposition on a drop-coated ZnO seed layer followed by carbothermal-reduction vapour phase transport (VPT). Zn-isotopically enriched samples were grown using very small amounts of Zn-enriched ZnO source powders in the VPT phase. Oxygen-enriched ZnO nanorods were grown by two modified novel vapour-solid (VS) and vapour-liquid-solid (VLS) methods. Characterisation by scanning electron microscopy and x-ray diffraction confirm the growth of high quality, dense, c-axis aligned nanorods over a large surface area in Zn-enriched and VS O-enriched nanorods, and non-aligned nanorods for VLS O-enriched samples. Zn isotopic enrichment was confirmed by secondary ion mass spectroscopy and Raman. Optical studies by low temperature photoluminescence (PL) show shifts in the band edge exciton recombination energy with changing isotopic masses, again confirming enrichment. The optical quality of the nanorods was excellent. The well-known Cu-related emission at 2.86 eV was studied by PL in order to investigate possible involvement of intrinsic, native defects such as interstitials and vacancies in this deep centre. Shifts in this zero phonon line (ZPL) energy were measured and compared to changes in the band edge energies. No relative shift was observed in these Zn-enriched samples, indicating only O atoms in the vicinity of the Cu atom, and no involvement of Zn interstitials or O vacancies in this Cu defect. PL and Raman shifts in the O-enriched samples were less than those previously reported for the same nominal enrichment levels, indicating possible lower enrichment than anticipated. Band edge and ZPL emissions in samples with O-enrichment displayed a relative shift and the ZPL line widths showed a substantial increase, which could indicate O interstitials or Zn vacancies complexing with Cu, however we attribute these effects instead to the multiple local configurations possible for O atoms in these mixed isotope environments in such lesser enriched samples.

# **Chapter 1: Introduction to ZnO**

## **1.1 Introduction and Applications**

This chapter presents an introduction to zinc oxide (ZnO). It begins with a brief overview of semiconductors in general as well as ZnO, in addition to presenting a description of the uses and applications of ZnO more recently. Basic material properties of ZnO, including its structural and electronic properties are discussed. The main growth techniques used to produce ZnO crystals and nanostructures are described. Finally, the motivation for the present work and a brief outline of this thesis is presented.

Since the first semiconductor transistors were developed in the mid-twentieth century, the industries built on these devices have permeated modern life and been at the centre of a technological revolution. Almost every modern electronic device that we use today contains semiconductor transistors. Silicon (Si) has become the dominant semiconductor material used in the computing and electronics industries. However Si is not suitable for some other applications, in particular for devices involving optical emission, because of its indirect band gap. Subsequently, many other semiconducting materials have received much research attention as their properties may be more suited to a particular application. ZnO is a semiconductor which has received very considerable attention from many researchers. This has

been driven by the large array of potential applications of the material, both in single crystal and nanostructure forms, particularly in recent decades.

ZnO is a widely known II-VI wide band gap compound semiconductor material which has been used and studied for many years. For example, it has recorded as being used in metallurgy processes over 3000 years ago.<sup>1</sup> More recently, there was much research done on ZnO over the last century with a first peak around the 1960s, encouraged by improved growth techniques for high quality single crystal material. The semiconducting properties of ZnO were recognised around the 1920s<sup>2</sup> and by mid-century its UV and green emission spectrum were known, as well as many of its structural and electronic properties.<sup>3</sup> ZnO continued to be a popular material with researchers before experiencing a second peak in output in the literature in the last twenty years including a large amount related to nanostructure research as ZnO forms nanostructures with a wide variety of morphologies. This is unsurprising given the huge interest in nanotechnology for device applications at the present time. However there are much fewer reports in general on ZnO-based devices than on nanostructure growth methods and optical properties.

ZnO is a direct band gap material which has received much attention due to its favourable optical properties for potential use in photonic and optoelectronic devices. It can also be synthesised using many different methods. It tends to deposit in nanostructured form and in a wide range of morphologies which can be controlled using various growth parameters. ZnO has a band gap of 3.3 eV at room temperature and an exciton binding energy of 60 meV.<sup>4</sup> ZnO is therefore a very efficient emitter in the ultraviolet (UV) region of the spectrum and this exciton binding energy compares favourably to other materials known for their blue or UV emissions, for example the figure for gallium nitride (GaN) is 25 meV.<sup>5</sup> These optical properties, which are of special interest in this work, make it attractive for use in devices such as UV emitters, photodetectors (including photodiodes and photovoltaics) and UV emitters such as LEDs<sup>6</sup> and laser diodes.<sup>7-10</sup> ZnO has also been used in transparent conducting oxides (TCO) in solar cells and as a transistor material.<sup>11-13</sup> Nanorods in particular allow increased surface area in solar cells which in turn increases the amount of photons captured and the current produced. ZnO nanostructures have attracted attention for use in solid state gas sensors due to their large surface to volume ratio and surface reactivity.<sup>14,15</sup> Metal doped ZnO may

be ferromagnetic giving rise to potential spintronics applications.<sup>16,17</sup> Applications making use of its piezoelectric properties for energy scavenging and surface acoustic wave applications have also been reported.<sup>18,19</sup> ZnO has been used in cold cathode applications like field emission in flat panel displays.<sup>8,20,21</sup> Ordered ZnO nanorods arrays in particular have shown much potential in this area.<sup>22</sup> ZnO has shown potential uses in biomedical applications, such as pharmaceuticals, because it is a biocompatible material.<sup>23,24</sup> Additionally, ZnO has been used in cosmetics, sun cream, food, paints, pigments and rubber materials. Over 100,000 tonnes of ZnO is produced annually, mostly for use in these lower “tech” applications.<sup>3</sup>

## 1.2 Structural Properties

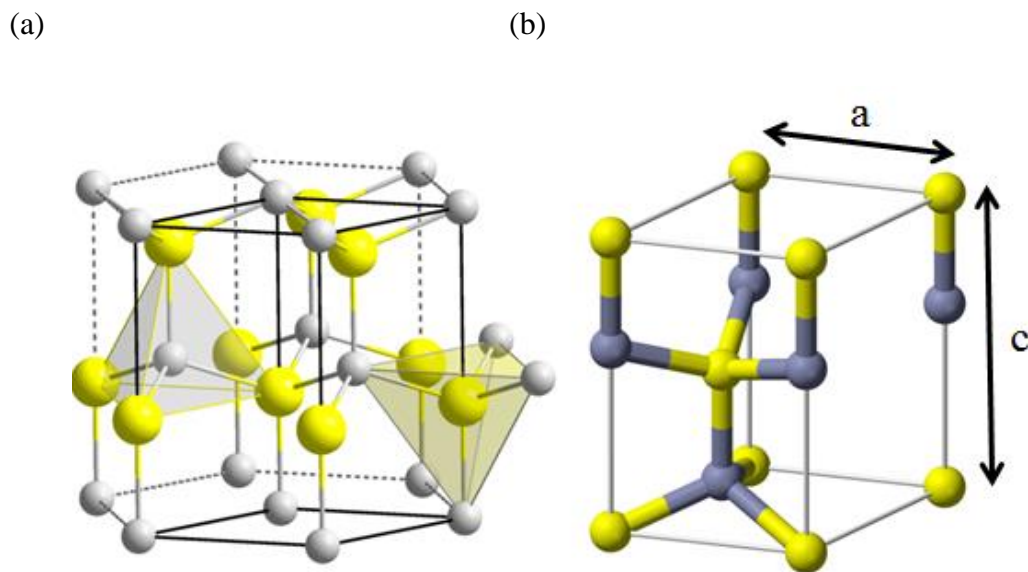


Figure 1.1: (a) Hexagonal wurtzite crystal structure of ZnO and (b) the wurtzite unit cell (yellow circles represent oxygen). Reproduced from reference 25.

ZnO is usually found in the hexagonal wurtzite form as this is its most stable phase at standard temperature and pressure and over a wide range of temperatures and pressures. However ZnO can also crystallize in the cubic zinc-blende or rocksalt allotropes in some circumstances.<sup>26</sup> Grown on cubic substrates, the zinc-blende form is stable in ambient conditions.<sup>27</sup> ZnO can also crystallize in the rocksalt phase at

higher pressures around ~9-10 GPa, which is a metastable phase at lower pressures.<sup>28</sup> The zinc-blende and rocksalt forms are more common in other II-VI compounds and oxides. As this work involving ZnO was carried out at or below atmospheric pressure, wurtzite is the relevant phase here and only this allotrope is discussed in detail.

The wurtzite form has a hexagonal structure where each zinc (Zn) atom is surrounded by four oxygen (O) atoms in the shape close to a tetrahedron. Likewise, each O atom is surrounded by four Zn atoms. This structure is shown in figure 1.1(a). The wurtzite unit cell is described by two lattice parameters, denoted  $a$  and  $c$ , as shown in figure 1.1(b). Ideally, i.e. in the case where the coordination is perfectly tetrahedral, they have an axial ratio of  $c/a = \sqrt{8/3} = 1.6330$ .<sup>3</sup> Experimental measurements of these lattice parameters in ZnO have been reported as  $a = 0.32498$  nm and  $c = 0.52066$  nm, giving with  $c/a = 1.6021$ . However there are reports of this ratio varying over a small range. For example, the figure has been given as 1.6021<sup>29</sup> and 1.590<sup>30</sup>, and also varying over a similar range with pressure.<sup>31</sup> The observed variations from the ideal structure may be due to the partially ionic nature of the ZnO bond which could lead to a distortion in the bonding angle.<sup>7</sup> The volume of the wurtzite ZnO unit cell is  $23.8 \times 10^{-3} \text{ nm}^3$ .<sup>32</sup>

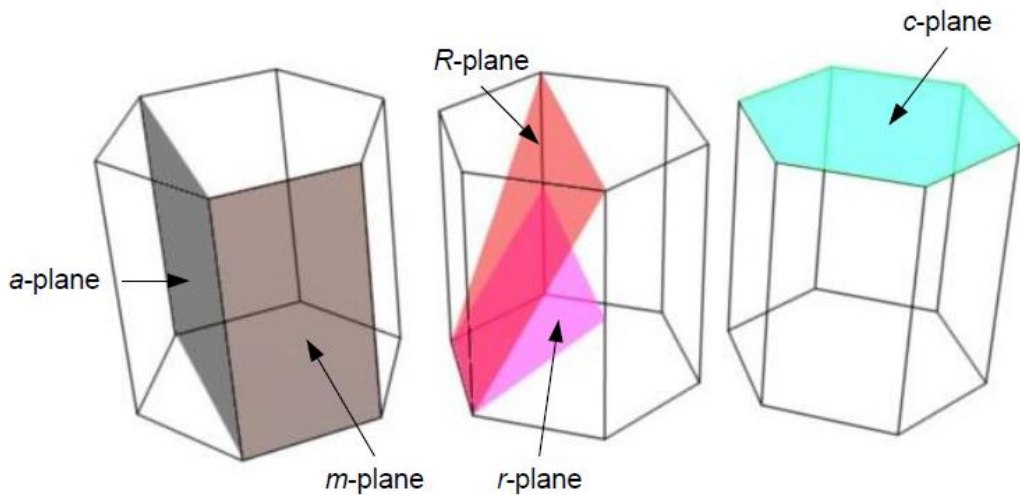


Figure 1.2: The main crystal planes in wurtzite ZnO. Reproduced from reference 33.

The main crystal planes of wurtzite ZnO are shown in figure 1.2.<sup>33</sup> The structure along the  $c$ -axis consists of alternating close packed planes containing Zn or O atoms, with each atom coordinated with four atoms of the other type in the close packed tetrahedron structure described above. This pattern leads to polar symmetry along the  $c$ -axis as the  $c$ -plane is terminated with either Zn or O atoms. The  $c$ -plane is denoted (0001) for the positive planes (Zn-terminated) and (000-1) for the negative planes (O-terminated) using the usual Miller-Bravais notation. The  $a$ -plane (1-120) and  $m$ -plane (10-10) contain the  $c$ -axis and are not polar, as they contain equal amounts of Zn and O atoms. The semi-polar  $r$ -plane (10-11) and  $R$ -plane (10-12) are also shown, although there is less published information in terms of studies involving these planes and it has proven difficult to achieve epitaxial growth in these directions.<sup>34</sup> The  $c$ -plane has the lowest surface energy which gives rise to preferential nanostructure growth along this direction as new material deposits more favourable on the polar faces than the non-polar ones.<sup>35</sup> This property is inherent to the growth of ZnO nanorods in this work. This type of crystal structure, without a centre of inversion, also gives rise to piezoelectric and pyroelectric properties.

### 1.3 Electronic Properties

The electronic properties of ZnO are one reason why there has been much interest in the material. As mentioned above, ZnO is a wide band gap semiconductor whose band gap at room temperature is 3.3 eV. This band gap energy corresponds to photon emission in the UV region. The material exciton binding energy of 60 meV<sup>4</sup> is larger than the thermal energy  $kT$  at room temperature. This is an important parameter as it means that many correlated electron-hole pairs, called excitons, can exist up to, and even above, room temperature, and the correlation of the electron and hole motion leads to closer proximity and a larger optical matrix element. ZnO is therefore an efficient emitter in the near UV region at room temperature via exciton recombination, leading to much interest in research in possible optoelectronic devices based on ZnO.<sup>9,36</sup>

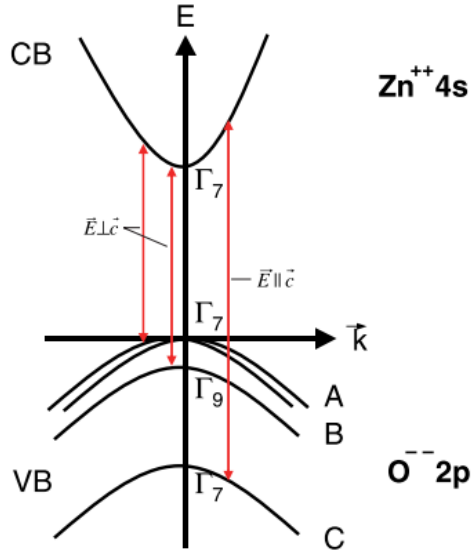


Figure 1.3: Schematic of the ZnO electronic band structure. Reproduced from reference 37.

Figure 1.3 shows a schematic diagram of the electronic band structure in ZnO.<sup>37</sup> The outer electron configuration in Zn is  $3d^{10} 4s^2$ , and the outer configuration in O is  $2s^2 2p^4$ . ZnO displays hybridised  $sp^3$  bonding. The outer  $4s^2$  electrons in Zn atom enter into partially ionic bonds with the O atom to stabilise the O outer shell, due to the greater electronegativity of the O atom, and we can view aspects of the band structure in terms of an ionic bonding perspective. The ZnO 3.3 eV band gap is between the  $O^{2-} 2p$  valence band and the  $Zn^{2+} 4s$  conduction band states. The band gap is direct meaning that the conduction band minimum and valence band maximum are at the same position in reciprocal space (their  $k$ -vectors are the same). The conduction band mainly consists of empty  $Zn^{2+} 4s$  orbitals with  $\Gamma_7$  symmetry while the valence band is made up of the occupied  $O^{2-} 2p$  orbitals. These O  $p$ -type orbitals are split by both spin-orbit coupling and crystal field effects (i.e. a departure from cubic symmetry) into three twofold degenerate (Kramers degeneracy) bands labelled A, B and C, with symmetries of  $\Gamma_7$ ,  $\Gamma_9$  and  $\Gamma_7$  respectively, from the highest energy to the lowest, by the tetrahedral crystal field and spin-orbit coupling.<sup>3,37</sup> The ordering of the  $\Gamma_7$ ,  $\Gamma_9$  and  $\Gamma_7$  bands has been the subject of great controversy and discussion over the years, but the  $\Gamma_7$ ,  $\Gamma_9$  and  $\Gamma_7$  ordering (different to other II-VI materials such as cadmium sulfide) seems well

established now, and the specific ordering is of little importance for the present work, so we do not dwell on it. Further detail is given in reference 37, and the influence of Zn 3d levels are suspected to be the origin of the difference between ZnO and other II-VI materials. This topic is also related to other discrepancies in terms of the band structure in ZnO, specifically that some experiments are not totally explained by theoretical calculations.<sup>7</sup> The Zn 3d electrons are treated as core shell electrons in theoretical models, however experimental results suggest that they may have an influence on the position of the Zn 4s and O 2p valence band electrons.<sup>7,38-41</sup> However, the primary influence on the valence band position is the hybrid orbitals of the Zn 4s and O 2p electrons as discussed above.

ZnO, in its natural and nominally undoped state, actually in almost all cases, has a significant abundance of *n*-type carriers i.e. electrons. A number of explanations for this property have been proposed in the literature. Deviations in the material stoichiometry can lead to an excess of Zn interstitials ( $Zn_i$ , an additional Zn atom where there should be none) or O vacancies ( $V_O$ , a defect of a missing O atom surrounded by Zn atoms) in the ZnO lattice. It has been suggested that these native defects are responsible for this *n*-type conductivity, but uncertainty remains as to whether this is due to the interstitials or vacancies.<sup>7,42,43</sup> It has also been suggested that hydrogen (H) is responsible for this conductivity due to the generally ubiquitous presence of H during the growth of ZnO material, as well as its high diffusivity.<sup>7,42,44,45</sup> Although H is amphoteric in most semiconductors which means it is in the  $H^+$  state in *p*-type material and in the  $H^-$  state in *n*-type material, it is always found in the  $H^+$  state in ZnO and acts as a donor as would be expected in *n*-type ZnO.<sup>7,45</sup> The *n*-type behaviour can also be increased with further intentional doping with aluminium (Al), gallium (Ga) and indium (In), all of which are present in trace amounts in the material grown in this work. Further discussion of such defects in ZnO is contained in chapter 3.

In contrast, *p*-type doping of ZnO material has proven difficult, due, at least in part, to its intrinsic *n*-type state. This type of electronic behaviour is known as unipolarity. Other potential contributing factors include a low solid solubility of *p*-type dopants<sup>46</sup> and a large ionisation energies of possible acceptors.<sup>2</sup> Indeed many elements which would be expected to act as acceptors in ZnO do not actually contribute to *p*-type conductivity.<sup>7</sup> There are some reports in the literature of *p*-type

doping in ZnO using a number of techniques and dopants<sup>7,47-53</sup>, but there are no reports of reliable and stable *p*-type ZnO being synthesised in a reproducible manner. This has obvious detrimental consequences for ZnO photonic or optoelectronic devices which generally rely on a *p-n* junction to operate, and where stable *p*-type material is thus a prerequisite. Indeed attempts to produce *p-n* junction based devices of ZnO have proven unsuccessful thus far, at least in terms of reproducible production at scales beyond once-off laboratory realisations. However, progress has been made in producing heterojunction devices using *n*-type ZnO and other *p*-type materials, e.g. GaN or organic thin films, among others.<sup>6,54-56</sup>

## 1.4 Growth Techniques

ZnO has been produced in a wide variety of morphologies, including single crystals and a variety of nanostructures, by a multitude of techniques. The most common ones are discussed briefly in this section. The growth method used will depend on the specific properties required for a particular application.

Bulk single crystals of ZnO have been synthesised in a number of ways including vapour phase transport (VPT)<sup>43,57</sup> and hydrothermal techniques.<sup>58</sup> The VPT method typically involves the reduction of high quality ZnO to Zn and O<sub>2</sub> at high temperatures in a furnace. The Zn vapour is then transported to a cooler part of the furnace where it oxidises on the substrate. The temperature is usually in the 850-1150 °C range, depending on the reducing agent. Although significant sublimation and decomposition of ZnO requires temperatures greater than 1900 °C, the reducing agent allows for growth at lower temperatures. The growth time can be several weeks for larger crystals.<sup>59</sup> In hydrothermal growth methods, the transport of Zn from the source to the substrate is by convection through a solvent solution. Instead of the reducing agent as in VPT, the method makes use of a mineralisation agent which dissolves the ZnO into solution. The ZnO is then transported to the cooler region and precipitates out of the solution forming the crystals.

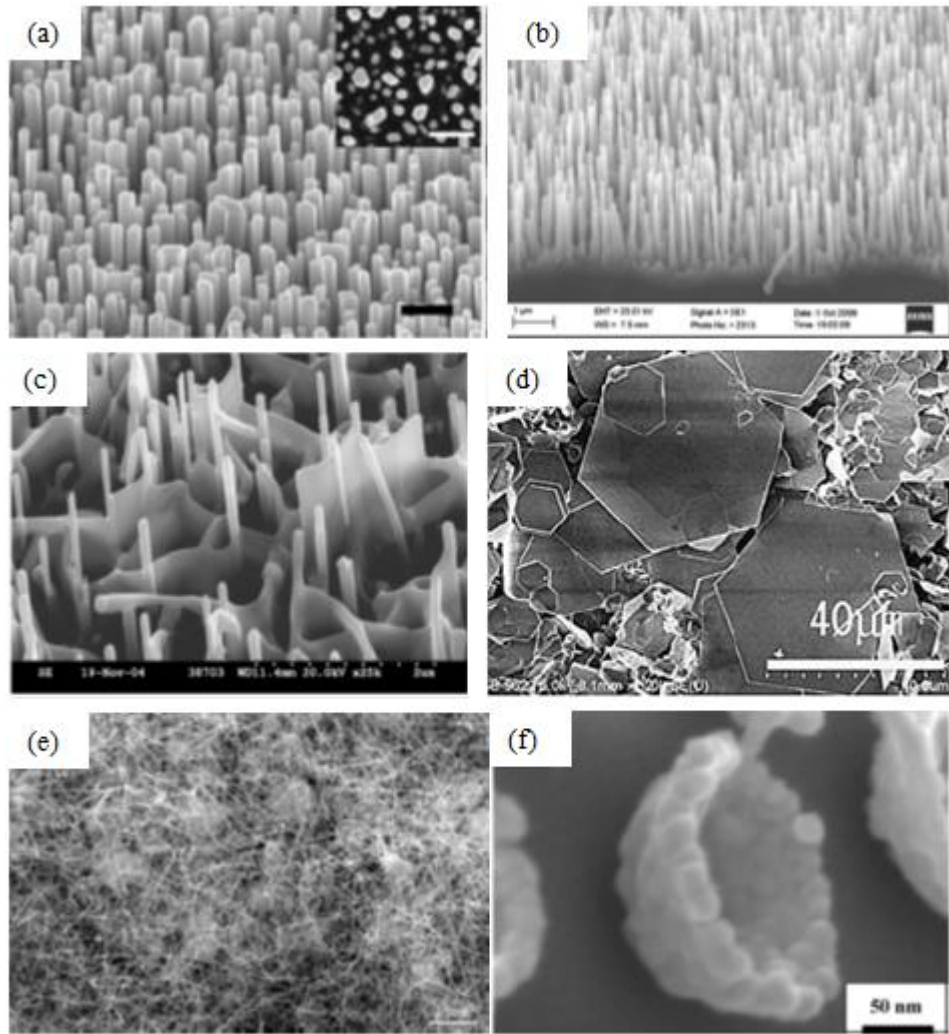


Figure 1.4: Examples of ZnO nanostructure morphologies from the literature: (a,b) nanorods<sup>60,61</sup>, (c) nanowalls<sup>62</sup>, (d) nanodisks<sup>63</sup>, (e) nanobelts/nanohelices<sup>64</sup> and (f) nanobowls.<sup>65</sup>

Nanostructures of ZnO have been of much interest in the literature. ZnO nanostructures have been produced in the form of nanorods and nanowires<sup>12,20,60,61,66</sup>, nanowalls<sup>62</sup>, nanodisks<sup>63</sup>, nanohelices, nanosprings, nanorings, nanobelts<sup>64</sup>, nanobowls<sup>65</sup>, nanosheets<sup>67</sup> and thin films<sup>68</sup>, to name a few. Some examples of these morphologies are shown in figure 1.4. One popular method often used to deposit ZnO nanostructures and thin films is chemical bath deposition (CBD).<sup>26,60,69</sup> This is a relatively inexpensive technique that takes place at relatively low temperatures, usually below 100 °C. This allows for the use a wide variety of substrates which

might not be capable of withstanding higher temperatures. Generally a Zn salt such as Zn acetate, nitrate, chloride or sulphate is used as a precursor and reacted with a base chemical to form a partially soluble Zn hydroxide.<sup>60,70-72</sup> A number of chemicals have been used as a base including hexamethylenetetramine (HMT), sodium hydroxide (NaOH), ammonia, ethanolamine and urea.<sup>26,69,72,73</sup> The Zn hydroxide then decomposes into ZnO or Zn<sup>2+</sup> which is then oxidised to form ZnO.<sup>74</sup> The exact reaction pathway will depend on the particular bath and conditions used. Solvents used in chemical baths have included water, ethanol, methanol and propanol.<sup>75</sup> The morphology of the final nanostructures or thin films can be controlled by altering the chemicals used, the solvent, the pH, the temperature, growth time, substrate and the addition of surfactant. As such, CBD is a flexible and popular, low temperature method used to deposit ZnO. CBD is used extensively throughout this work and is described further in chapters 2 and 4.

In addition to bulk single crystals, VPT is also commonly used to deposit nanostructures.<sup>76,77</sup> The source powder can be Zn metal or a ZnO powder mixed with a reducing agent. As in the bulk crystal case, the Zn vapour produced is carried by a carrier gas to the substrate where it is oxidised and deposits. The substrate is usually downstream of the source in the furnace, but can also be beside or above it. The reducing agent allows for the reduction of ZnO at temperatures of ~900 °C while direct sublimation of ZnO requires much higher temperatures of greater than 1900°C. Having said this, sufficient evaporation of ZnO occurs at temperatures of around 1350°C to allow growth.<sup>78,79</sup> VPT is used extensively in this work to grow ZnO nanorods on buffer layers grown by CBD. The reducing agent used here is graphite. With the addition of carbon (C) the method is known as carbothermal reduction vapour phase transport (CTR-VPT). There are two main growth pathways which may be used with VPT. The first is the vapour-solid (VS) method, where Zn is adsorbed onto the surface and oxidised to form ZnO. In this case the CBD buffer layers provide energetically favourable nucleation sites on the substrate for deposition.<sup>80</sup> The second method is the vapour-liquid-solid (VLS) method. In this case a thin layer of a metal catalyst like gold (Au) is deposited on the substrate in advance of VPT growth.<sup>76</sup> The Au is molten at the growth temperature and the Zn vapour is adsorbed into the Au droplets forming a saturated alloy. The Zn then precipitates out of the Au droplet and oxidised to form ZnO nanorods. The Au

droplets end up at the top of the nanorods after growth. VPT growth is discussed in more detail in chapters 2, 4 and 5.

There are many alternative ways which have been used to produce ZnO nanostructures and thin films, including chemical vapour deposition (CVD), molecular beam epitaxy (MBE) and pulsed laser deposition (PLD).<sup>81</sup> CVD involves exposing the heated substrate to a volatile precursor which is transported to the substrate by a carrier gas. The precursor decomposes on the substrate and forms the deposit. When the precursor used is metal organic (MO), this is known as MOCVD. MOCVD is routinely used for growth of thin films, as well as aligned nanostructures.<sup>82</sup> MBE is widely used in the growth of thin films.<sup>2,83</sup> It involves a number of thermally generated molecular beams interacting on a substrate in a high vacuum. It has also been used to produce ZnO nanorods.<sup>84</sup> PLD has been used to deposit ZnO films and nanostructures using a pulsed laser beam to vapourise the surface of a ZnO or Zn metal target in a vacuum.<sup>85-87</sup> The resulting plasma expands in the chamber and is incident on a substrate a small distance away from the target and the material deposits on the substrate. The properties of the resulting nanostructure can be controlled by altering parameters like temperature, laser intensity and chamber gas ambient chemistry and pressure.

ZnO nanorods are the primary structures of interest in this work. The reason for this is because nanostructures, which have a small “footprint”, can be grown on a variety of substrates with minimal strain in the main body of the nanorod, regardless of lattice match at the interface, due to the free surfaces of the nanorod sidewalls, which can relieve the effects of mismatch. Nanorods grown at high temperatures can display excellent crystalline and optical properties, and can be grown with relatively small amounts of source material and in short periods, enabling a range of systematic experiments to be undertaken. The main growth method used here is a three step process involving the deposition of a buffer layer of ZnO nanorods using drop coating and CBD, followed by the primary growth of nanorods using CTR-VPT. The growth method used here was developed in our group based upon other work in the literature.<sup>60,61</sup> Chapter 2 details this process. It is expanded and developed further in this work to take account of the use of isotopically enriched growth materials.

## 1.5 Defects in ZnO and the Isotope Effect

Low temperature photoluminescence (PL) is a powerful and useful technique in the study of ZnO and other semiconductor materials. It can reveal information about the electronic, vibrational and optical characteristics of the material under investigation. It is therefore extremely useful in the study of defects and impurities in sample because these phenomena induce changes in the electronic, vibrational structure of the material, and therefore the optical characteristics also. Low temperature PL is used extensively in this work to investigate defects and impurities in ZnO. PL investigations are commonly carried out low temperature as this allows much greater detail to be observed in the emission spectrum at high resolutions. Typical temperatures for low temperature PL are  $< 20$  K. PL relies on the recombination of correlated electron-hole pairs called excitons following excitation by photons with energy greater than the band gap. The excitation is typically carried out using a laser beam with an above band gap photon energy. When the excitons recombine, they emit a photon at an energy which is lower than that of the material's band gap. When these excitons are bound at the site of a defect or impurity, their recombination gives rise to a photon at a particular energy (due to the specific exciton confinement energy at the defect) which is unique to that defect or impurity, and this allows PL to be used to study the defects in great detail. The growth method used to produce ZnO nanorods in this work yields material with excellent optical quality (in terms of both emission intensity and spectral line widths), which allows high resolution PL investigations subsequently.

ZnO low temperature PL emission spectra typically display an intense emission near the band gap energy in the UV which is called the band edge region. This is mostly due to excitons bound to donors such as Al, Ga or In.<sup>88,89</sup> ZnO also often emits a broad band structure with specific spectral features in the visible range called the structured green band (SGB), in addition to other broad defect-related features in the visible region.<sup>7,90,91</sup> This SGB emission has been assigned to a copper (Cu) impurity atom with a zero phonon line (ZPL) at 2.86 eV<sup>92</sup> and a broad band multi-phonon emission at lower energies peaking at about 2.4 eV. This emission was first posited to be related to Cu by Dingle in 1969.<sup>92</sup> However, several other sources, including native defects such as  $Zn_i$  and  $V_O$ , have also been suggested as

being responsible for this emission.<sup>7,42,91</sup> Cu was subsequently confirmed to be involved in this defect by Byrne et al.<sup>93</sup> One of the purposes of the present work is to study the involvement of native defects in the centre responsible for this emission. Very high optical quality is vital in such studies and nanostructured deposits can provide the very high quality material required, as explained above.

Isotopic enrichment is another very useful technique in the study of defects in semiconductor materials including ZnO, particularly in conjunction with optical methods like PL. Briefly, the technique involves enriching the crystal with either specific isotopes of an atom involved in, or suspected of involvement in, a defect or enriching the surrounding native crystal lattice with specific isotopes. The vibrational states in the crystal couple to electronic states, including those at defect sites, to produce so-called vibronic levels. This is known as electron-phonon coupling. Transitions between different vibronic levels, either at a defect or the surrounding lattice produce the ZPL and phonon side-bands involving multiple phonon replicas, as seen for the Cu-related green band in ZnO. Changes in the energies of exciton recombinations may arise due to changes in both the isotopes make up of a defect or a surrounding lattice, both of which affect the vibrational nature of the vibronic levels because of the difference in mass of different isotopes.<sup>94,95</sup>

PL, defects in semiconductors, the structure of the ZnO PL emission spectrum, the Cu-related defect at 2.86 eV, and the isotope effect are all discussed in more detail in chapter 3.

## 1.6 Motivation and Objectives

The first objective of this work was to adapt common previously used methods of producing ZnO nanostructures such as nanorods to grow ZnO nanorods which were enriched with particular isotopes of Zn. The natural Zn isotopic abundance in ZnO is 48.6% <sup>64</sup>Zn, 27.9% <sup>66</sup>Zn, 4.1% <sup>67</sup>Zn, 18.8% <sup>68</sup>Zn and 0.6% <sup>70</sup>Zn.<sup>96</sup> Natural ZnO therefore has an average atomic mass of <sup>65.4</sup>ZnO. We set out to synthesise ZnO nanorods enriched with <sup>64</sup>Zn, <sup>66</sup>Zn and <sup>68</sup>Zn. We have successfully

produced these Zn isotopically enriched ZnO nanorods by developing a novel synthesis technique using CBD and VPT, based on previous work carried out in our group. This new growth method is fast, relatively cheap and relatively easy to carry out. Studies using isotopically enriched samples in the past have included work on band gap energies, phonon positions and line widths and heat capacity, but in all cases using bulk single crystal samples.<sup>96-99</sup> The use of nanostructures, rather than bulk single crystals, means that rather small amounts of isotopically enriched material can be grown, which is advantageous given the cost of the isotopically enriched source materials. It is also relevant to the potential applications of these structures. The optical quality of these enriched samples, as observed using low temperature PL, is excellent which makes them ideal for use in detailed optical studies of defects and impurities.

The second objective was to grow ZnO material which was isotopically enriched with <sup>18</sup>O isotopes. Natural O in its normal isotopic abundance state is 99.76% <sup>16</sup>O. This work proved more challenging, and ultimately ZnO nanorod samples enriched with <sup>18</sup>O were successfully grown by two separate novel methods. The first method was a modified VS VPT technique in Dublin City University (DCU) based on the three step process developed by our group, and modified for the Zn-enriched samples, further modified to produce O-enriched samples. The second method was a VLS technique using the direct sublimation of ZnO powder at higher temperatures. These growths were carried out in the University of Jena in Germany with collaborators there. Details are given in chapter 2. The O-enriched samples produced by both methods were of similar excellent optical quality to the Zn-enriched samples, and therefore were also suitable for use in detailed optical studies of defects and impurities using low temperature PL.

The third objective of this work was to carry out an investigation, using the materials described above, into any possible involvement of native defects in the Cu-related ZPL 2.86 eV emission and associated broad band SGB in ZnO. Isotopically enriched material is very useful for this study since changing the isotopic content of the material, either in the case of the Zn or O atoms, may result in anomalous shifts (i.e. different to the overall shifts in band gap energy) in the energies of bound exciton recombinations, as well as systemic changes in emission line widths. The recombination energies of the band edge excitons, which occur near the band gap at

around 3.3 eV, and the 2.86 eV Cu-related emission, can be determined. If, in addition to the known Cu atom, native defects such as Zn<sub>i</sub> or O interstitials (O<sub>i</sub>), or Zn vacancies (V<sub>Zn</sub>) or V<sub>O</sub>, are involved in the 2.86 eV emission, then the change in band edge exciton recombination energies and line widths with isotope changes might be different to the change in same for the 2.86 eV ZPL, due to the additional presence of the native defects complexing with the Cu atom in this defect. The effect of changing isotopic abundance is therefore used in this work to investigate this defect. This study is carried out using low temperature PL and is made possible by the very high optical quality of the isotopically enriched nanorods produced using novel growth methods.

It is worth noting once again that this is the first time isotopically enriched ZnO has been produced in nanostructured form, specifically nanorods, as key previous studies of such material have used bulk single crystals.<sup>96–98,100</sup> The optical quality of these nanorods, in terms of their band edge emission intensities, and more specifically their line widths, is significantly better than that reported previously for ZnO bulk single crystals.<sup>96,97</sup> This indicates their excellent structural quality and their great potential for use in PL defect studies. These points constitute one of the main original and novel features of the present work. Understanding the nature of defects and impurities in semiconductor materials like ZnO is vital for the control and optimisation of the optical and electronic properties of the materials and thus for their potential use in many existing and proposed applications. As such this study aims to achieve definitive conclusions on the involvement of native defects in the Cu-related defect at 2.86 eV in ZnO. These experiments are described in chapters 4, 5 and 6.

Finally, a number of other experiments were carried out using ZnO samples prepared during this work. This includes work carried out by the author solely, or in collaboration with colleagues, both in DCU and elsewhere, using both natural and isotopically enriched ZnO nanorods. This work demonstrates that the growth methods and material produced here can be used in many different studies to provide useful new information in a number of fields. These experiments are described in appendix A.

## 1.7 Outline of Remainder of Thesis

This thesis describes the growth of isotopically enriched ZnO nanostructures using novel, fast and relatively easy growth techniques. The morphology, crystal structure and optical properties are studied. In particular, a comprehensive optical study of the near band edge and Cu-related defect at 2.86 eV is carried out using low temperature PL to determine any possible involvement of native defects in the 2.86 eV emission. A number of other applications and experiments using these methods and materials are then described. A brief outline of the remainder of the thesis is as follows:

Chapter 2 describes in detail the experimental techniques used throughout this work. This includes the growth of ZnO nanorods and Zn-isotopically enriched ZnO nanorods using a novel modified combined CBD and VPT technique and two growth techniques used to produce the O-isotopically enriched ZnO samples in DCU and in Jena. This chapter also describes the experimental setups of the investigative techniques used to study the structural and optical characteristics of samples throughout this work.

Chapter 3 presents background theory relevant to the PL optical studies on defects in this work in detail. This includes background theory on the PL technique itself, as well as general information on defects in semiconductors, a description of the typical structure of the PL emission spectrum in ZnO and specific background information on the Cu-related defect at 2.86 eV in ZnO. This chapter also discusses the effect of isotope substitution on the PL spectrum and its relevance to this work.

Chapter 4 describes the results of the growth of Zn isotopically enriched ZnO nanorods. This includes studies on the morphology, crystal quality, isotopic enrichment and optical quality using a number of characterisation techniques.

Chapter 5 presents the results of the growth of O isotopically enriched ZnO nanorods using the two separate methods used in DCU and in Jena. The results of studies on the morphology, crystal quality, isotope enrichment and optical quality are presented.

Chapter 6 looks at the optical properties of isotopically enriched ZnO. This includes studies on the shifts of the band edge exciton recombination energies as well as shifts in the 2.86 eV ZPL with changing isotope enrichments using low temperature PL spectroscopy. This chapter also discusses what these results mean in terms of involvement of native defects such as interstitials or vacancies in the Cu-related defect at 2.86 eV.

Chapter 7 outlines the final general conclusions of the thesis and includes some suggestions for further work on the topics in the thesis.

## 1.8 References

- <sup>1</sup> A.K. Biswas, *Indian J. Hist. Sci.* **28**, 309 (1993).
- <sup>2</sup> C. Jagadish and S. Pearton, editors, *Zinc Oxide Bulk, Thin Films and Nanostructures* (Elsevier, Oxford, 2006).
- <sup>3</sup> C.F. Klingshirn, B.K. Meyer, A. Waag, A. Hoffmann, and J. Geurts, *ZnO: From Fundamental Properties Towards Novel Applications* (Springer-Verlag, Berlin, Heidelberg, 2010).
- <sup>4</sup> D. Reynolds, D. Look, B. Jogai, C. Litton, T. Collins, W. Harsch, and G. Cantwell, *Phys. Rev. B* **57**, 12151 (1998).
- <sup>5</sup> S.J. Xu, W. Liu, and M.F. Li, *Appl. Phys. Lett.* **81**, 2959 (2002).
- <sup>6</sup> M. Willander, O. Nur, Q.X. Zhao, L.L. Yang, M. Lorenz, B.Q. Cao, J. Zúñiga Pérez, C. Czekalla, G. Zimmermann, M. Grundmann, A. Bakin, A. Behrends, M. Al-Suleiman, A. El-Shaer, A. Che Mofor, B. Postels, A. Waag, N. Boukos, A. Travlos, H.S. Kwack, J. Guinard, and D. Le Si Dang, *Nanotechnology* **20**, 332001 (2009).
- <sup>7</sup> U. Özgür, Y.I. Alivov, C. Liu, a. Teke, M. a. Reshchikov, S. Doğan, V. Avrutin, S.-J. Cho, and H. Morkoç, *J. Appl. Phys.* **98**, 041301 (2005).
- <sup>8</sup> C.J. Lee, T.J. Lee, S.C. Lyu, Y. Zhang, H. Ruh, and H.J. Lee, *Appl. Phys. Lett.* **81**, 3648 (2002).
- <sup>9</sup> M.H. Huang, S. Mao, H. Feick, H. Yan, Y. Wu, H. Kind, E. Weber, R. Russo, and P. Yang, *Science (80-. )*. **292**, 1897 (2001).

- <sup>10</sup> Y.-H. Chou, B.-T. Chou, C.-K. Chiang, Y.-Y. Lai, C.-T. Yang, H. Li, T.-R. Lin, C.-C. Lin, H.-C. Kuo, S.-C. Wang, and T.-C. Lu, *ACS Nano* **9**, 3978 (2015).
- <sup>11</sup> F.D. Nayeri, E.A. Soleimani, and F. Salehi, *Renew. Energy* **60**, 246 (2013).
- <sup>12</sup> M. Law, L.E. Greene, J.C. Johnson, R. Saykally, and P. Yang, *Nat. Mater.* **4**, 455 (2005).
- <sup>13</sup> C. Opoku, K.F. Hoettges, M.P. Hughes, V. Stolojan, S.R.P. Silva, and M. Shkunov, *Nanotechnology* **24**, 405203 (2013).
- <sup>14</sup> H. Nanto, T. Minami, and S. Takata, *J. Appl. Phys.* **16**, 482 (1986).
- <sup>15</sup> J.X. Wang, X.W. Sun, Y. Yang, H. Huang, Y.C. Lee, O.K. Tan, and L. Vayssieres, *Nanotechnology* **17**, 4995 (2006).
- <sup>16</sup> B. Ul Haq, R. Ahmed, A. Shaari, A. Afaq, B. a. Tahir, and R. Khenata, *Mater. Sci. Semicond. Process.* **29**, 256 (2015).
- <sup>17</sup> A. Mesquita, F.P. Rhodes, R.T. da Silva, P.P. Neves, A.O. de Zevallos, M.R.B. Andreetta, M.M. de Lima, A. Cantarero, I.S. da Silva, M. a. Boselli, X. Gratens, V.A. Chitta, A.C. Doriguetto, W.B. Ferraz, A.C.S. Sabioni, and H.B. de Carvalho, *J. Alloys Compd.* **637**, 407 (2015).
- <sup>18</sup> Y.Q. Fu, J.K. Luo, X.Y. Du, A.J. Flewitt, Y. Li, G.H. Markx, A.J. Walton, and W.I. Milne, *Sensors Actuators B Chem.* **143**, 606 (2010).
- <sup>19</sup> Z.L. Wang and J. Song, *Science (80-. )*. **312**, 242 (2006).
- <sup>20</sup> S.H. Jo, J.Y. Lao, Z.F. Ren, R.A. Farrer, T. Baldacchini, and J.T. Fourkas, *Appl. Phys. Lett.* **83**, 4821 (2003).
- <sup>21</sup> E. McCarthy, S. Garry, D. Byrne, E. McGlynn, and J.-P. Mosnier, *J. Appl. Phys.* **110**, 124324 (2011).
- <sup>22</sup> S. Garry, É. McCarthy, J.-P. Mosnier, and E. McGlynn, *Nanotechnology* **25**, 135604 (2014).
- <sup>23</sup> X. Huang, X. Wang, S. Wang, J. Yang, L. Zhong, and J. Pan, *Nanoscale* **5**, 5596 (2013).
- <sup>24</sup> K. Memarzadeh, A.S. Sharili, J. Huang, S.C.F. Rawlinson, and R.P. Allaker, *J. Biomed. Mater. Res. Part A* **103**, 981 (2015).

- <sup>25</sup> Wurtzite Crystal Structure - Wikipedia, the free Encyclopedia, [Online]. Accessed 13-02-2015. Available at: [http://en.wikipedia.org/wiki/Wurtzite\\_crystal\\_structure](http://en.wikipedia.org/wiki/Wurtzite_crystal_structure)
- <sup>26</sup> K. Govender, D.S. Boyle, P.B. Kenway, and P. O'Brien, *J. Mater. Chem.* **14**, 2575 (2004).
- <sup>27</sup> A. Ashrafi and C. Jagadish, *J. Appl. Phys.* **102**, 071101 (2007).
- <sup>28</sup> H. Liu, J.S. Tse, and H. Mao, *J. Appl. Phys.* **100**, 093509 (2006).
- <sup>29</sup> E.H. Kisi and M.M. Elcombe, *Acta Crystallogr. Sect. C Cryst. Struct. Commun.* **45**, 1867 (1989).
- <sup>30</sup> J.E. Jaffe and A.C. Hess, *Phys. Rev. B* **48**, 7903 (1993).
- <sup>31</sup> H. Sowa and H. Ahsbahs, *J. Appl. Crystallogr.* **39**, 169 (2006).
- <sup>32</sup> S. Desgreniers, *Phys. Rev. B* **58**, 14102 (1998).
- <sup>33</sup> D. Byrne, *The Growth and Characterisation of Ordered Arrays of Zinc Oxide Nanostructures and Optical Studies of Defects in Zinc Oxide*, Dublin City University, 2012.
- <sup>34</sup> R. Aggarwal, H. Zhou, C. Jin, J. Narayan, and R.J. Narayan, *J. Appl. Phys.* **107**, 113530 (2010).
- <sup>35</sup> N. Fujimura, T. Nishihara, S. Goto, J. Xu, and T. Ito, *J. Cryst. Growth* **130**, 269 (1993).
- <sup>36</sup> R. Yousefi and B. Kamaluddin, *J. Alloys Compd.* **479**, L11 (2009).
- <sup>37</sup> C. Klingshirn, *Phys. Status Solidi* **244**, 3027 (2007).
- <sup>38</sup> P. Schröer, P. Krüger, and J. Pollmann, *Phys. Rev. B* **47**, 6971 (1993).
- <sup>39</sup> R.T. Girard, O. Tjernberg, G. Chiaia, S. Söderholm, U.O. Karlsson, C. Wigren, H. Nylén, and I. Lindau, *Surf. Sci.* **373**, 409 (1997).
- <sup>40</sup> S.-H. Wei and A. Zunger, *Phys. Rev. B* **37**, 8958 (1988).
- <sup>41</sup> S.B. Zhang, S.-H. Wei, and A. Zunger, *Phys. Rev. B* **52**, 13975 (1995).
- <sup>42</sup> M.D. McCluskey and S.J. Jokela, *J. Appl. Phys.* **106**, 071101 (2009).
- <sup>43</sup> D.C. Look, D.C. Reynolds, J.R. Sizelove, R.L. Jones, C.W. Litton, G. Cantwell, and W.C. Harsch, *Solid State Commun.* **105**, 399 (1998).
- <sup>44</sup> A. Janotti and C.G. Van de Walle, *Phys. Rev. B* **76**, 165202 (2007).

- <sup>45</sup> C.G. Van de Walle, Phys. B Condens. Matter **308-310**, 899 (2001).
- <sup>46</sup> C.G. Van de Walle, D.B. Laks, G.F. Neumark, and S.T. Pantelides, Phys. Rev. B **47**, 9425 (1993).
- <sup>47</sup> L. Yu, Q. Zhu, D. Fan, and Z. Lan, J. Wuhan Univ. Technol. Mater. Sci. Ed. **27**, 1184 (2012).
- <sup>48</sup> Y. Marfaing and A. Lusson, Superlattices Microstruct. **38**, 385 (2005).
- <sup>49</sup> D.C. Look, D.C. Reynolds, C.W. Litton, R.L. Jones, D.B. Eason, and G. Cantwell, Appl. Phys. Lett. **81**, 1830 (2002).
- <sup>50</sup> M. Joseph, H. Tabata, and T. Kawai, Jpn. J. Appl. Phys. **38**, L1205 (1999).
- <sup>51</sup> K. Kim, D.-H. Lee, S. Lee, G.-E. Jang, and J.-S. Kim, Nanoscale Res. Lett. **7**, 273 (2012).
- <sup>52</sup> M. Kumar, T.-H. Kim, S.-S. Kim, and B.-T. Lee, Appl. Phys. Lett. **89**, 112103 (2006).
- <sup>53</sup> Y.. Ryu, S. Zhu, D.C. Look, J.M. Wrobel, H.M. Jeong, and H.W. White, J. Cryst. Growth **216**, 330 (2000).
- <sup>54</sup> Y.I. Alivov, E. V Kalinina, a E. Cherenkov, D.C. Look, B.M. Ataev, a K. Omaev, M. V. Chukichev, and D.M. Bagnall, Appl. Phys. Lett. **83**, 4719 (2003).
- <sup>55</sup> J.B. Kim, D. Byun, S.Y. Ie, D.H. Park, W.K. Choi, J.-W. Choi, and B. Angadi, Semicond. Sci. Technol. **23**, 095004 (2008).
- <sup>56</sup> S. Vempati, S. Chirakkara, J. Mitra, P. Dawson, K. Kar Nanda, and S.B. Krupanidhi, Appl. Phys. Lett. **100**, 162104 (2012).
- <sup>57</sup> X. Zhang, F. Herklotz, E. Hieckmann, J. Weber, and P. Schmidt, J. Vac. Sci. Technol. A Vacuum, Surfaces, Film. **29**, 03A107 (2011).
- <sup>58</sup> H. Xu, H. Wang, Y. Zhang, W. He, M. Zhu, B. Wang, and H. Yan, Ceram. Int. **30**, 93 (2004).
- <sup>59</sup> M. Mikami, T. Eto, J. Wang, Y. Masa, and M. Isshiki, J. Cryst. Growth **276**, 389 (2005).
- <sup>60</sup> L.E. Greene, M. Law, D.H. Tan, M. Montano, J. Goldberger, G. Somorjai, and P. Yang, Nano Lett. **5**, 1231 (2005).
- <sup>61</sup> D. Byrne, E. McGlynn, K. Kumar, M. Biswas, M.O. Henry, and G. Hughes, Cryst.

Growth Des. **10**, 2400 (2010).

<sup>62</sup> J. Grabowska, a. Meaney, K. Nanda, J.-P. Mosnier, M. Henry, J.-R. Duclère, and E. McGlynn, Phys. Rev. B **71**, 115439 (2005).

<sup>63</sup> T. Long, S. Yin, K. Takabatake, P. Zhnag, and T. Sato, Nanoscale Res. Lett. **4**, 247 (2009).

<sup>64</sup> X.Y. Kong and Z.L. Wang, Nano Lett. **3**, 1625 (2003).

<sup>65</sup> Y. Wang, X. Chen, J. Zhang, Z. Sun, Y. Li, K. Zhang, and B. Yang, Colloids Surfaces A Physicochem. Eng. Asp. **329**, 184 (2008).

<sup>66</sup> S. Vempati, A. Shetty, P. Dawson, K. Nanda, and S.B. Krupanidhi, J. Cryst. Growth **343**, 7 (2012).

<sup>67</sup> S. Vempati, J. Mitra, and P. Dawson, Nanoscale Res. Lett. **7**, 470 (2012).

<sup>68</sup> D. Bao, H. Gu, and A. Kuang, Thin Solid Films **312**, 37 (1997).

<sup>69</sup> R.B. Peterson, C.L. Fields, and B.A. Gregg, Langmuir **20**, 5114 (2004).

<sup>70</sup> M. Afzaal, M. a. Malik, and P. O'Brien, New J. Chem. **31**, 2029 (2007).

<sup>71</sup> S.-H. Yi, S.-K. Choi, J.-M. Jang, J.-A. Kim, and W.-G. Jung, J. Colloid Interface Sci. **313**, 705 (2007).

<sup>72</sup> K. Kakiuchi, E. Hosono, T. Kimura, H. Imai, and S. Fujihara, J. Sol-Gel Sci. Technol. **39**, 63 (2006).

<sup>73</sup> M. Kokotov and G. Hodes, J. Mater. Chem. **19**, 3847 (2009).

<sup>74</sup> M.N.R. Ashfold, R.P. Doherty, N.G. Ndifor-Angwafor, D.J. Riley, and Y. Sun, Thin Solid Films **515**, 8679 (2007).

<sup>75</sup> M. Wang, E.J. Kim, S.H. Hahn, C. Park, and K. Koo, Cryst. Growth Des. **8**, 501 (2008).

<sup>76</sup> J. Grabowska, K.K. Nanda, E. McGlynn, J.-P. Mosnier, and M.O. Henry, Surf. Coatings Technol. **200**, 1093 (2005).

<sup>77</sup> M. Biswas, E. McGlynn, M.O. Henry, M. McCann, and a. Rafferty, J. Appl. Phys. **105**, 094306 (2009).

<sup>78</sup> C. Borchers, S. Mu, D. Stichtenoth, D. Schwen, and C. Ronning, J. Phys. Chem. B **110**, 1656 (2006).

- <sup>79</sup> D. Hou, T. Voss, C. Ronning, A. Menzel, and M. Zacharias, *J. Appl. Phys.* **115**, 233516 (2014).
- <sup>80</sup> D. Byrne, R. Fath Allah, T. Ben, D. Gonzalez Robledo, B. Twamley, M.O. Henry, and E. McGlynn, *Cryst. Growth Des.* **11**, 5378 (2011).
- <sup>81</sup> R. Triboulet and J. Perrière, *Prog. Cryst. Growth Charact. Mater.* **47**, 65 (2003).
- <sup>82</sup> D.J. Park, D.C. Kim, J.Y. Lee, and H.K. Cho, *Nanotechnology* **17**, 5238 (2006).
- <sup>83</sup> J.R. Arthur, *Surf. Sci.* **500**, 189 (2002).
- <sup>84</sup> Y.W. Heo, M. Kaufman, K. Pruessner, D.P. Norton, F. Ren, M.F. Chisholm, and P.H. Fleming, *Solid. State. Electron.* **47**, 2269 (2003).
- <sup>85</sup> B. Doggett, S. Chakrabarti, R. O’Haire, a. Meaney, E. McGlynn, M.O. Henry, and J.P. Mosnier, *Superlattices Microstruct.* **42**, 74 (2007).
- <sup>86</sup> Y. Sun, G.M. Fuge, and M.N.R. Ashfold, *Superlattices Microstruct.* **39**, 33 (2006).
- <sup>87</sup> A. Fouchet, W. Prellier, B. Mercey, L. Méchin, V.N. Kulkarni, and T. Venkatesan, *J. Appl. Phys.* **96**, 3228 (2004).
- <sup>88</sup> M. Schilling, R. Helbig, and G. Pensl, *J. Lumin.* **33**, 201 (1985).
- <sup>89</sup> S. Müller, D. Stichtenoth, M. Uhrmacher, H. Hofsäss, C. Ronning, and J. Röder, *Appl. Phys. Lett.* **90**, 012107 (2007).
- <sup>90</sup> J. Čížek, J. Valenta, P. Hruška, O. Melikhova, I. Procházka, M. Novotný, and J. Bulíř, *Appl. Phys. Lett.* **106**, 251902 (2015).
- <sup>91</sup> H. Morkoç and U. Özgür, *Zinc Oxide Fundamentals, Materials and Device Technology* (Wiley-VCH, Weinheim, 2009).
- <sup>92</sup> R. Dingle, *Phys. Rev. Lett.* **23**, 579 (1969).
- <sup>93</sup> D. Byrne, F. Herklotz, M.O. Henry, and E. McGlynn, *J. Physics. Condens. Matter* **24**, 215802 (2012).
- <sup>94</sup> E. McGlynn, *A Photoluminescence Study of Cadmium and Aluminium-Related Defects in Silicon*, Dublin City University, 1996.
- <sup>95</sup> B. Henderson and G.F. Imbusch, *Optical Spectroscopy of Inorganic Solids* (Clarendon Press, Oxford, 1989).
- <sup>96</sup> F.J. Manjón, M. Mollar, M.A. Hernández-Fenollosa, B. Marí, R. Lauck, and M.

Cardona, Solid State Commun. **128**, 35 (2003).

<sup>97</sup> S. Tsoi, X. Lu, A.K. Ramdas, H. Alawadhi, M. Grimsditch, M. Cardona, and R. Lauck, Phys. Rev. B **74**, 165203 (2006).

<sup>98</sup> J. Serrano, F. Manjón, A. Romero, F. Widulle, R. Lauck, and M. Cardona, Phys. Rev. Lett. **90**, 055510 (2003).

<sup>99</sup> J. Serrano, R. Kremer, M. Cardona, G. Siegle, a. Romero, and R. Lauck, Phys. Rev. B **73**, 094303 (2006).

<sup>100</sup> J. Serrano, F. Widulle, A.H. Romero, A. Rubio, R. Lauck, and M. Cardona, Phys. Status Solidi **235**, 260 (2003).

# Chapter 2: Growth and Characterisation Techniques

## 2.1 Introduction

This chapter presents the experimental techniques used during this work. It describes both the growth techniques used to synthesise the ZnO nanorod samples, including isotopically enriched ZnO, and the characterisation techniques used to examine and study the material subsequently. Section 2.2 describes the basic growth procedure for ZnO nanorods, and how it was modified to produce Zn isotopically enriched samples. The growth procedure is based upon a three-step process previously developed previously in our group.<sup>1</sup> This involves (i) the deposition of a seed layer of ZnO, (ii) growth of a ZnO buffer layer by CBD, and finally (iii) the growth of *c*-axis aligned ZnO nanorods by VPT. Section 2.3 describes the growth of the O isotopically enriched ZnO samples by two separate methods, one in DCU and another in the University of Jena in Germany with collaborators there. The characterisation techniques are then described in section 2.4. The morphology and crystal quality of the samples were examined using scanning electron microscopy (SEM) and X-ray diffraction (XRD). The isotopic enrichment was examined using secondary ion mass spectroscopy (SIMS). Some energy dispersive x-ray spectroscopy (EDX) was also performed. The optical quality was examined using Raman spectroscopy, and the primary optical technique in this work, that of low

temperature PL spectroscopy. Optical reflectance studies were also carried out on some samples. This chapter describes the experimental details of these techniques as well as some brief background information on them. Some further information on the growth and optical techniques are described in subsequent chapters, alongside their respective results.

## **2.2 Growth of Zn Isotope-enriched Nanorods**

This section describes the basic procedures for the growth of ZnO nanorods as developed by our group. The procedure is then modified to produce Zn-enriched isotopically pure nanorods in this work.

### **2.2.1 Substrate Preparation**

The large majority of ZnO nanorods in this work were grown on Si substrates. Typically phosphorous-doped *n*-type Si with a (100) surface orientation was used. Some growths were also performed on other substrates such as fused quartz, *a*-plane sapphire (Al<sub>2</sub>O<sub>3</sub>) or *c*-plane sapphire and the growth methods used produced very similar deposits on such substrates. Si was chosen as the substrate as it is relatively cheap and easily available. It is also electrically conductive which is useful in characterisation techniques like SEM and SIMS. Typically, Si (100) wafers were cleaved into small pieces of approximately 1-4 cm<sup>2</sup> in size using a diamond scribe. The pieces of Si were then blown with a stream of nitrogen (N) to remove any dust or other particles from the surface. The substrate was then cleaned before use by sonication in acetone for approximately 10 minutes, rinsing with fresh acetone, sonication in ethanol for a further 10 minutes and then rinsing in fresh ethanol. They were then dried in a nitrogen stream. No attempt was made to remove the native silicon dioxide (SiO<sub>2</sub>) layer.

### 2.2.2 Seed Layer Preparation

The first step in the growth of the ZnO is the deposition of a thin seed layer of ZnO on the Si substrate. Si is not epitaxially lattice matched with ZnO therefore a seed layer of ZnO is required to provide nucleation sites for subsequent aligned nanorod growth. This seed layer was deposited on the bare Si substrate using the method reported by Greene and Law *et al.*<sup>2,3</sup> A 0.005 M solution of Zn acetate dihydrate (Riedel-de Haen) in absolute ethanol was prepared. This solution was sonicated for up to about an hour until the Zn acetate had completely dissolved in the ethanol and was then left to cool before use. The seed layer was deposited by drop coating. Approximately  $3.75 \mu\text{l}$  of solution per  $\text{cm}^2$  of sample area was applied to the substrate surface using a pipette. This droplet was allowed to spread so that it evenly coated the entire surface and was left for 20 seconds before being rinsed off the surface with copious amounts of fresh ethanol. The substrate was then dried in a gentle nitrogen stream. This process was repeated four more times for each sample. During this process,  $\text{H}_2\text{O}$  from the atmosphere diffuses into the solution and reacts with the Zn acetate to form Zn hydroxide precipitates which settle on the substrate. It has been reported that the ambient humidity is a factor affecting this process and the number of seed layers can need to be varied to account for it.<sup>4</sup> However this is not something which was found to be an issue during this work. The substrates were then annealed at  $350^\circ\text{C}$  in air for 30 minutes to decompose the Zn hydroxide into ZnO. This process produces a thin layer of crystallographically aligned ZnO crystallites on the surface which act as nucleation sites for nanorod growth at later stages.<sup>5,6</sup>

### 2.2.3 Chemical Bath Deposition

The second phase of the three step growth process is the deposition of a buffer layer of aligned ZnO nanorods on the Si substrate by CBD. Three different chemical baths were used during this work, although one was used a large majority of the time. This primary chemical bath used was an aqueous solution of NaOH and Zn nitrate.<sup>1,7</sup> This reaction produces a metastable  $\text{Zn}(\text{OH})_4^{2-}$  solution and the ZnO is

deposited from this. The second bath used was an aqueous solution of Zn nitrate and HMT. The third chemical bath was a simple solution of Zn acetate in deionised water (DI-H<sub>2</sub>O). This results in the direct thermal decomposition of the Zn acetate into Zn hydroxide followed by ZnO. In each case, the solutions were heated for varying period of time during deposition. The laboratory equipment used for this step is similar for all three chemical bath techniques. Figure 2.1 shows a schematic and a photograph of the equipment used. The reactions took place in aqueous solutions in a beaker using a hotplate as the heat source. The seeded substrates were suspended in the reaction solutions as shown. Polytetrafluoroethylene (PTFE)-coated magnetic stirring bars were used to stir the solutions, while the temperature of the solutions was monitored using either an alcohol thermometer or a digital temperature probe. Each of the three chemical baths is described in turn below.

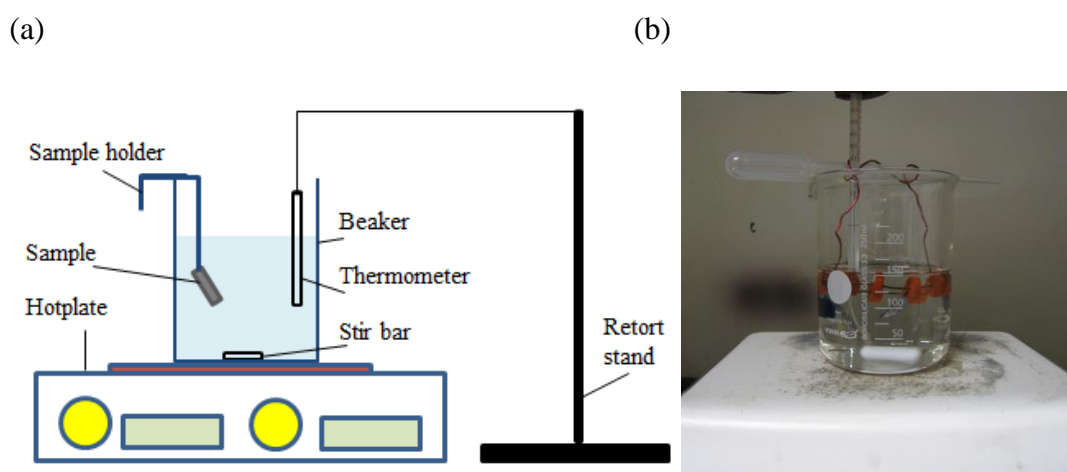


Figure 2.1: (a) Schematic diagram, and (b) photograph, of the experimental setup used for the CBD growth step.

**(i) NaOH-based reaction**

The NaOH-based reaction is the primary chemical bath used during this work and a large majority of samples were produced using this method. Before this step, for the NaOH chemical bath, it is important that the equipment used is clean and free from residual ZnO from any previous growths. Residual ZnO could result in the formation of unwanted precipitates in the solution. The beakers, stirring bars and spatulas to be used were cleaned using a dilute solution of sulphuric acid ( $\text{H}_2\text{SO}_4$ ) and then rinsed with copious amounts of DI- $\text{H}_2\text{O}$  and allowed to dry. The  $\text{H}_2\text{SO}_4$  reacts with any ZnO to form a soluble zinc sulphate solution which can be easily removed by rinsing with copious amounts of DI- $\text{H}_2\text{O}$ , leaving a clean beaker. A solution of 0.02 M Zn nitrate hexahydrate (99.998%, Alfa Aesar) in DI- $\text{H}_2\text{O}$  was prepared and vigorously stirred until the Zn nitrate was fully dissolved. A separate solution of 0.8 M NaOH (99%, VWR) was prepared and was also vigorously stirred until the NaOH was fully dissolved. The Zn nitrate solution was then slowly added to the NaOH solution while stirring vigorously. It was important to stir the mixture vigorously while adding the Zn nitrate to disperse it throughout the mixture and prevent any precipitation of Zn hydroxide from the solution. The solution was clear and does not contain any precipitates when prepared correctly. The mixture was heated to approximately 70 °C and stirred gently. The sample was then submerged in the solution for approximately 25 minutes while the temperature was maintained at 70 °C and the solution stirred gently. The sample was then removed, washed with copious amounts of DI- $\text{H}_2\text{O}$  and dried with a gentle nitrogen stream. Typically a total volume of 160 ml was used for the bath. This was prepared by mixing 80 ml each of Zn nitrate and NaOH solution to give a total reaction volume of 160 ml with concentrations of 0.01 M Zn nitrate and 0.4 M NaOH. This volume of solution allowed for a number of substrates to be submerged at once, usually four or five. However the total volume can be altered (usually to 40 ml or 80 ml) as needed for smaller numbers of samples. The molarities were kept constant when this was done. This bath leaves a layer of densely packed *c*-axis aligned ZnO nanorods which acts as an effective buffer layer for subsequent growth of larger nanorods using VPT.

## **(ii) HMT-based reaction**

To prepare this bath, HMT (99.5%, Fluka) and Zn nitrate hexahydrate (99.998%, Alfa Aesar) were dissolved in DI-H<sub>2</sub>O in concentrations of 25 mM. The Zn nitrate solution was prepared first and dissolved by stirring. HMT was then added to the Zn nitrate solution and dissolved by stirring. The ZnO seeded substrate was then submerged in the bath and the solution was heated to 90 °C for 30 minutes. The sample was then removed, washed with DI-H<sub>2</sub>O and dried in a gentle nitrogen stream. The volume used in this case was typically 80 ml, although this can be varied as needed. An equimolar 25 mM solution equates to 7.4 mg Zn nitrate and 3.5 mg HMT per ml of reaction volume. This reaction produces significant amounts of precipitates in the solution, which can deposit on the substrate surface. This reaction was therefore rarely used in this work.

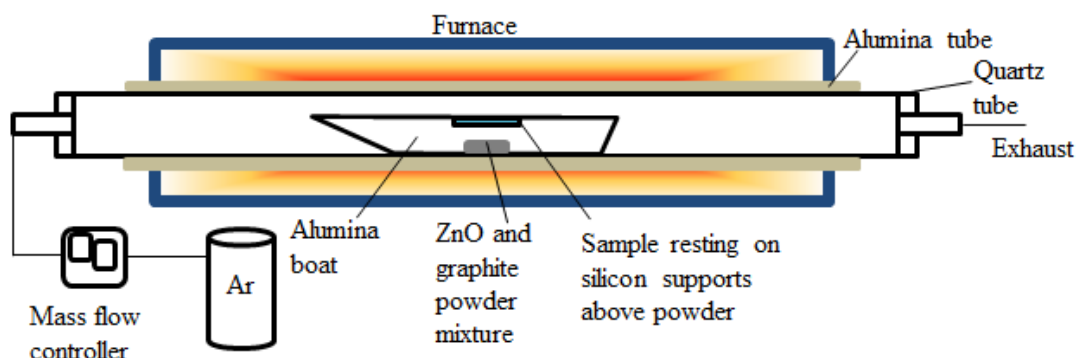
## **(iii) Acetate-based reaction**

Zn acetate dihydrate (Riedel-de Haen) was dissolved by stirring in DI-H<sub>2</sub>O in a concentration of 25 mM. As with the other baths, the volume of solution can be varied with typical volumes of 40 ml or 80 ml being used. The seeded substrates were submerged in the solution and then heated to about 65 °C. This temperature was maintained for up to three hours, but sometimes less, with continuous stirring. Precipitates also form in the bath, so the substrate would be removed, washed with DI-H<sub>2</sub>O, and placed in a freshly prepared bath half way through a three hour growth. Following growth, the sample was washed with DI-H<sub>2</sub>O and dried in a gentle nitrogen stream. The bath was also used rarely during the course of this work.

## 2.2.4 Vapour Phase Transport

The third stage in the growth of ZnO nanorods is CTR-VPT using a VS technique. ZnO will not readily deposit on bare SiO<sub>2</sub>. In addition, ZnO and Si are not lattice matched so any deposition (including by methods other than VPT) will generally result in non-aligned nanorods, especially with the presence of a native oxide layer on the Si. The buffer layer of crystallographically textured ZnO nanorods previously deposited by CBD thus carries out two important roles: it provides energetically favourable sites for the nucleation of ZnO and it allows for the growth vertically aligned *c*-axis nanorods, following the buffer layer alignment. The VPT step was carried out in a fused quartz tube with an internal diameter of 37 mm. The tube was placed inside a large alumina tube, which was itself inside a Lenton Thermal Designs single temperature zone horizontal tube furnace. The tube was connected to a supply of high purity Argon (99.999%) controlled by a mass flow controller (MFC, model Analyt GFC 17). In a typical growth of unenriched <sup>nat</sup>ZnO, 60 mg of high purity ZnO powder (99.9995%, Alfa Aesar) and 60 mg of graphite powder (99.9999%, Alfa Aesar) were carefully weighed out using a mass balance. The two powders were carefully mixed together and placed in a mortar. This mixture was then ground together with a pestle in order to increase the contact area between the two powders and produce a fine homogeneous powder mixture. This powder was then carefully spread over an area of about 2 cm in the middle of a small alumina boat. The sample was suspended above the powder, using thin strips of Si and the edge of the boat as supports, with the ZnO buffer layer facing downwards towards the powder. The alumina boat was then placed into the tube so that the sample was in the centre of the furnace. The quartz tube was sealed and purged with an Ar flow of 90 sccm for about 5-10 minutes. (There was an exhaust at the opposite end of the tube to the Ar MFC.) The temperature was then increased to the desired level of around 850 °C – 950 °C for 1 hour with the Ar flow remaining at 90 sccm. Most of the growths carried out were at a temperature of 925 °C. After one hour, the furnace was allowed to cool. When the temperature reached about 350 °C, the Ar flow was stopped and the alumina boat and sample removed. Figure 2.2 shows a schematic diagram and photograph of the furnace apparatus during the VPT step.

(a)



(b)

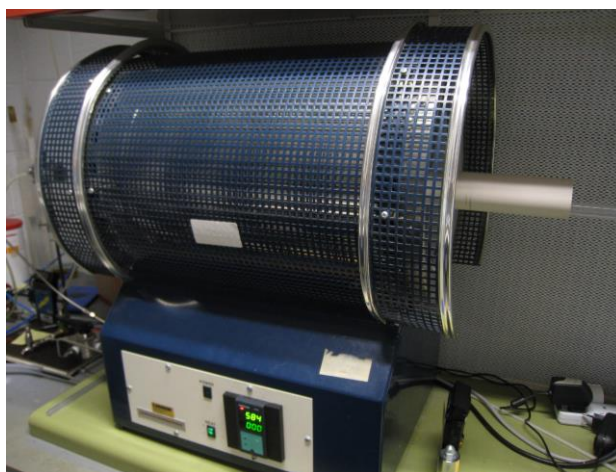


Figure 2.2: (a) Schematic diagram of the furnace setup used for the VPT growth of ZnO nanorods, and (b) photograph of the VPT furnace.

The three step growth procedure above called for 60 mg ZnO and 60 mg graphite powders for the VPT stage. However this proved impracticable for the growth of isotopically enriched ZnO with specific Zn isotope enrichments. This was because the isotopically enriched material is quite expensive and only relatively small amounts of Zn-enriched ZnO powders were available. Therefore the amount of ZnO and graphite powders was reduced to 10 mg of each for the growth of the Zn-enriched nanorods. Nanorods were successfully grown with this lower amount of source powder, in both natural and isotopically pure states, and without any other changes to the procedure. This was expected as only a small amount of the source

powders was generally vapourised during the normal (i.e. 60 mg + 60 mg) VPT growth process, with the rest remaining in the alumina boat.

<sup>nat</sup>ZnO contains Zn isotopes in the proportions shown in table 2.1.<sup>8</sup> In this work, isotopically enriched ZnO samples were grown by substituting the ZnO powder with ZnO powders (Isoflex) enriched with <sup>64</sup>Zn, <sup>66</sup>Zn and <sup>68</sup>Zn. Samples of <sup>64</sup>ZnO, <sup>66</sup>ZnO and <sup>68</sup>ZnO nanorods were therefore grown. The Zn enrichment levels of each source powder is shown table 2.1. Samples were also grown with different proportions of different Zn isotopes present. Samples with equal proportions of two different isotopes were grown using 5 mg of each powder along with 10 mg of graphite powder (<sup>64/66</sup>ZnO, <sup>64/68</sup>ZnO and <sup>66/68</sup>ZnO). Similarly, a sample of three different Zn isotopes was produced using 3 mg of each powder along with 10 mg of graphite (<sup>64/66/68</sup>ZnO). A separate quartz tube, alumina boat, mortar and pestle were used for each sample. The Zn-enriched samples had the usual natural oxygen isotopic distribution of 99.76% <sup>16</sup>O.

<sup>nat</sup> Zn isotopic content		Zn isotopic content in enriched source powders
<sup>64</sup> Zn	48.6%	99.94%
<sup>66</sup> Zn	27.9%	99.29%
<sup>67</sup> Zn	4.1%	
<sup>68</sup> Zn	18.8%	99.34%
<sup>70</sup> Zn	0.6%	

Table 2.1: Natural abundances of Zn isotopes in ZnO and the enrichment levels of the source powders used to produce Zn-isotopically enriched nanorods.

## 2.3 Growth of O Isotope-enriched ZnO Nanorods

Following on from the growth of Zn-enriched ZnO nanorods, this section describes the growth of O-enriched nanorods. This work proved to be more

challenging. However, after extensive trials, which are further outlined in chapter 5, O-enriched ZnO nanorods were successfully grown by two separate methods. The first was a VS method carried out by modifying the CTR-VPT setup used in the growth of Zn-enriched samples. The second was a VLS technique carried out in collaboration with colleagues in the Institute for Solid State Physics in the University of Jena, Germany. These growths were carried out by Mr. Lukas Trefflich and the author in the group of Prof. Carsten Ronning during a research visit by the author in September 2015.

### 2.3.1 Method 1: Modified VS CTR-VPT method in DCU

The CTR-VPT growth described in section 2.2.4 is based on the reduction of ZnO powder by the graphite to produce Zn vapour and carbon monoxide (CO). The Zn vapour is then re-oxidised in a VS process at the energetically favourable sites provided by the aligned CBD buffer layer using residual O<sub>2</sub> present in the tube following the Ar flush. In order to grow ZnO nanorods enriched with <sup>18</sup>O isotopes, it was necessary to remove all the residual O<sub>2</sub> from the tube, and then reintroduce <sup>18</sup>O<sub>2</sub> gas. A schematic of the setup for this experiment is shown in figure 2.3.

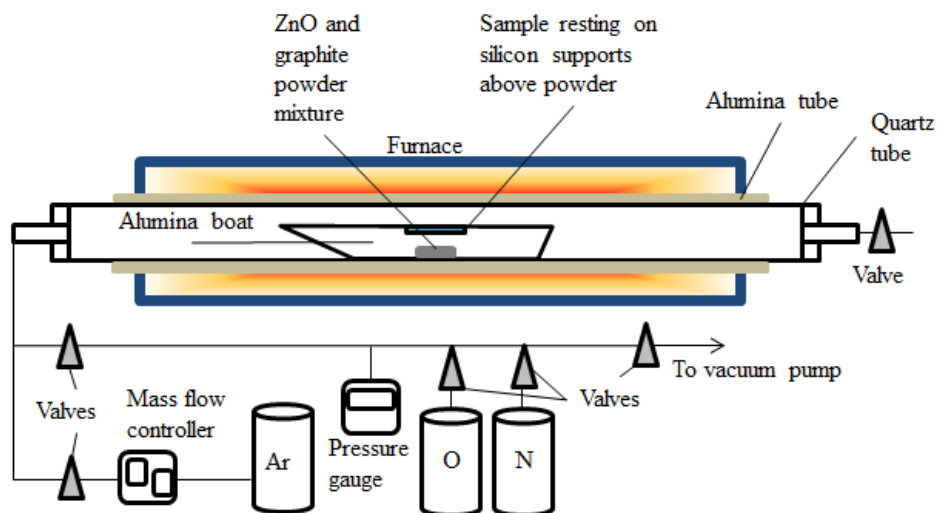


Figure 2.3: Schematic diagram of the experimental setup for the growth of O-enriched ZnO nanorods using a modified VS technique.

The furnace was loaded as before with an alumina boat containing the mixed powder of 60 mg graphite and 60 mg ZnO in its natural isotopic state with a Si substrate previously deposited with a buffer layer of ZnO nanorods by CBD suspended above the powder. The exhaust end of the tube was then sealed using a valve. At the other end, a series of valves connect the tube to a vacuum pump, N and O gases and Ar gas via the MFC as shown. A small regulator was used to control the pressure of the  $^{18}\text{O}_2$  (99%, Sigma Aldrich) lecture bottle. A digital pressure gauge was also present. The tube was slowly evacuated using the vacuum pump to a pressure of <1 mbar. Following this, the tube was refilled to atmospheric pressure with artificial 'air', that is, with ~21%  $^{18}\text{O}_2$  and ~79%  $\text{N}_2$ . This mixture was left for about 15 minutes to allow the gasses to mix and fill the entire tube evenly. The Ar flush at 90 sccm was then started, the exhaust valve opened, and after 5 minutes the temperature was raised to 925°C for 1 hour as before.

Three samples were produced using this method: natural  $\text{Zn}^{16}\text{O}$  by evacuating the tube and re-filling with  $^{16}\text{O}_2$  and  $\text{N}_2$ , isotopically enriched ZnO by re-filling with  $^{18}\text{O}_2$  and  $\text{N}_2$ , and a mixed 50:50  $\text{Zn}^{16/18}\text{O}$  sample by using a mixture of both oxygen isotopes with  $\text{N}_2$ .

### **2.3.2 Method 2: VLS VPT method in Jena**

O-enriched ZnO nanorods were also produced using a VLS method with an Au catalyst in Jena. The method used was based on previous work by that group.<sup>9,10</sup> The setup shows some similarities to that described in section 2.3.1 albeit also with some notable differences. The furnace in Jena contained two alumina tubes, one inside the other. Approximately 120 mg of ZnO powder acted as the source and was spread over about 5-6 cm in an alumina boat and placed at the centre of the furnace. About six to eight pieces of Si substrate had 10 nm of Au deposited on them by plasma sputter coating and were placed in another alumina boat about 16 cm from the ZnO powder, over a range of a few cm. The tube was sealed and evacuated to a pressure of <0.3 mbar. The temperature was raised to 1350°C over a period of 5 hours with a pre-determined ramp controlled by a computer (400°C for 90 mins, 1150°C for 180 mins, 1350°C for 60 mins). When the temperature reached ~600°C

the Ar (99.999%) was introduced at 50 sccm in the reverse direction, i.e. moving any vapour away from the substrates. The pressure was held constant at 100 mbar from this point on. After the temperature was at 1350°C for 60 minutes, the growth then took place as the Ar direction was reversed for a further period of 60 minutes and carried the Zn and O<sub>2</sub> vapours from the source powder to the substrates where they deposited. In this VLS method, the Au coating melts and forms droplets on the substrate which act as energetically favourable nucleation sites. The nanorods in this case are not preferentially aligned. The furnace then cooled overnight before that samples were removed. Figure 2.4 shows the basic setup of this system.

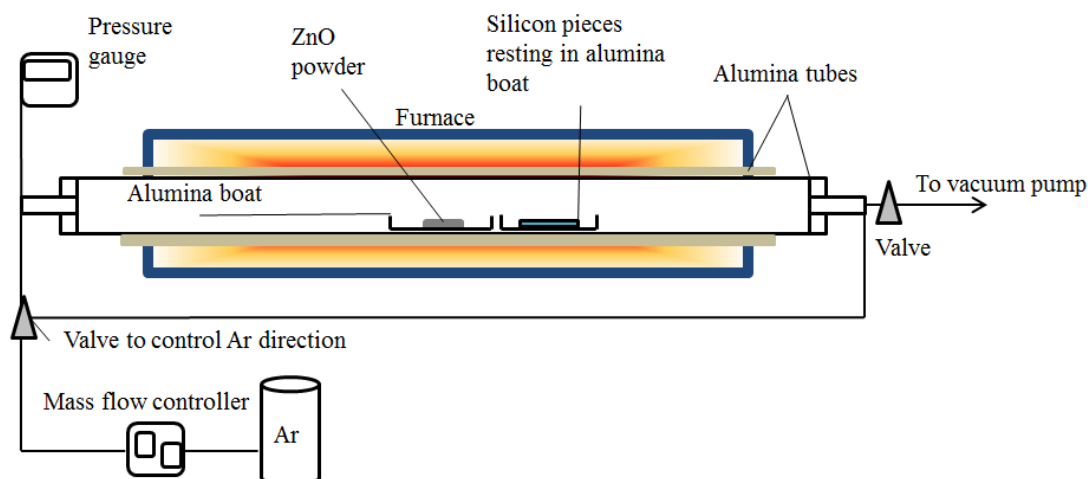


Figure 2.4: Schematic diagram showing the general experimental setup for the growth of O-enriched ZnO nanorods using the VLS technique in Jena.

In this case it is the ZnO source powder which provides both the Zn and O<sub>2</sub> vapours for subsequent growth due to the sublimation of the ZnO powder. In order to produce O-enriched ZnO nanorods therefore, it was necessary to produce enriched ZnO source powder. Zn powder (99.9%, Alfa Aesar) was oxidised in DCU by placing ~160 mg of such powder in an alumina boat in the furnace and evacuating the tube to < 1 mbar. The tube was then filled with ~200 mbar of either <sup>16</sup>O<sub>2</sub> or <sup>18</sup>O<sub>2</sub> and ~550 mbar of N<sub>2</sub> giving a pressure of ~ 750 mbar. This mixture was left to settle for about 15 minutes before the furnace was heated to 800°C for one hour. About 60-90 mg of oxidised powder was recovered from the boat after each run due to

some of the produced ZnO depositing on the tube edges. Separate boats and tubes were used for each isotope and smaller tubes of 18 mm internal diameter were used here to reduce the amount of  $^{18}\text{O}_2$  gas needed as it was in limited supply.

Three growths were then carried out in Jena using these oxidised  $\text{Zn}^{16}\text{O}$  and  $\text{Zn}^{18}\text{O}$  powders:  $\text{Zn}^{16}\text{O}$ ,  $\text{Zn}^{18}\text{O}$  and mixed 50:50  $\text{Zn}^{16/18}\text{O}$  using 60 mg of each powder.

## **2.4 Characterisation Techniques**

This section describes the experimental tools used to characterise the samples produced during this work. The primary method of initial characterisation was the use of SEM to examine the morphology of CBD and VPT grown nanorods. A number of other techniques were then used to study the structural, isotopic, chemical and optical properties. These include XRD, SIMS, EDX, Raman spectroscopy, low temperature PL spectroscopy and reflectance spectroscopy. In some cases external collaborations were leveraged to carry out aspects of these characterisation techniques. Where this occurred details are presented in the relevant sections including who performed the experiments and where they took place.

### **2.4.1 Scanning Electron Microscopy**

SEM was used throughout this work to examine the morphology of the samples. It was necessary to use SEM rather than optical microscopy due to the scale of the features under investigation. Under the Rayleigh criterion, two point sources are considered to be just resolved when the central maximum of the diffraction pattern of one point overlaps with the first minimum of the second point's diffraction pattern, yielding a resolution limit which is linearly proportional to the light wavelength. Since the features under examination here are close to, and in many cases smaller, in size than the wavelength of visible light, an optical microscope was not suitable for examining the morphology of these samples.

Imaging with beams of electrons provides a higher resolution as needed in this work. This is possible since the electrons have a much smaller de Broglie wavelength than visible wavelengths and thus the same diffraction limitations are not present.

SEM works by directing a beam of high energy electrons at the sample. A schematic of a typical SEM system is shown in figure 2.5(a) and (b). The electron beam originates from the electron gun which contains a source such as a tungsten or lanthanum hexaboride cathode. Current is passed through the source and the electrons are emitted by thermionic emission. This is an example of a hot cathode. Cold cathodes can also act as electron sources through field emission. An anode provides an accelerating voltage to the emitted electrons. The beam travels through a column under vacuum, and is shaped, directed and focussed as required by a system of apertures and magnetic lenses by using the Lorentz force. These magnetic lenses can shape and direct the electron beam in a similar way to how optical refracting lenses alter a beam of light. The condenser lens adjusts the spot size and beam current and the objective lens adjusts the beam focus. The beam is raster scanned over the sample surface rather than incident over a large area simultaneously. The sample chamber is also under vacuum ( $\sim 10^{-3}$  mbar). The sample chamber is brought to atmospheric pressure when changing the sample.

The electrons interact with the target material in a number of different ways which produce a number of different signals by which information can be gathered about the sample under investigation. Electrons deflected away from the sample surface in an elastic scattering process are called backscattered electrons. This process depends strongly on the mass of the atoms in the material, with higher atomic masses leading to greater numbers of backscattered electrons. These electrons therefore contain information about the material composition of a sample, with image contrast indicating average elemental atomic weight. Most of these electrons travel back up the optic axis so a circular scintillation or solid state detector surrounding the beam emission point collects these electrons.

When the incident electrons collide with an outer shell electron in the sample they can cause the ejection of these electrons from the sample's atoms. These ejected electrons are called secondary electrons following this inelastic scattering process. Secondary electrons generally have very low energies (the definition is

electrons with energies less than 50 eV) so only ones close to the surface tend to escape the sample. There is a contrast change as the angle between the sample normal and the incident beam increases. This is due to more secondary electrons being emitted as the exposed surface area increases at higher angles. This contributes to the high quality of image formed using these electrons and can be used to determine the orientation of structures on the surface. They are therefore used to collect topographical information about the sample surface. This information is again displayed in the image by changes in contrast. Low energy secondary electrons are attracted by a positive bias to a scintillation detector and multiplied by a photomultiplier tube to produce the signal used to form the image. SEM images have a large depth of field and can display large areas of the sample surface in some detail. Secondary electron imaging was used to produce the images in this work as the focus of this characterisation technique for our purposes was on morphology.

During the inelastic interaction that creates the secondary electrons, another useful signal is also produced. Some ejected electrons can leave behind an empty state in the atom's inner shell. This hole can then combine with another electron from the outer orbitals of that same atom. The energy difference between the orbitals is then released upon recombination in the form of x-rays. This is illustrated in figure 2.5(c). These x-rays can be detected and they are characteristic of the element they came from and therefore can be used to obtain elemental information about a sample or map differences in composite materials. This is the signal used in EDX. This technique has been used occasionally in this work, particularly during early stages of the work on the growth of O-enriched nanorods.

In this work, most SEM characterisation was carried out using a Carl-Zeiss EVO series SEM system with a lanthanum hexaboride source and fitted with secondary electron and EDX detectors. A photograph of this system is shown in figure 2.5(d). The system can also be used in backscatter mode and variable pressure mode, which can be useful for electrically insulating or biological samples. SEM was used to examine the coverage of nanorods on the surface of samples before they were examined using low temperature PL. It was also of interest to observe the orientation and shape of the nanorods as this can vary slightly between growth runs.

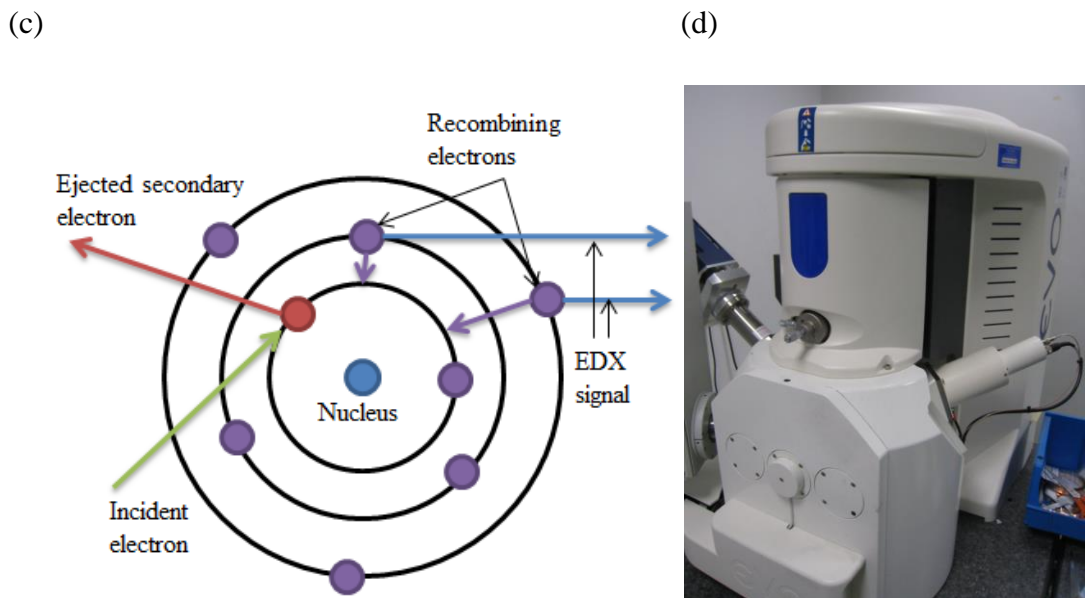
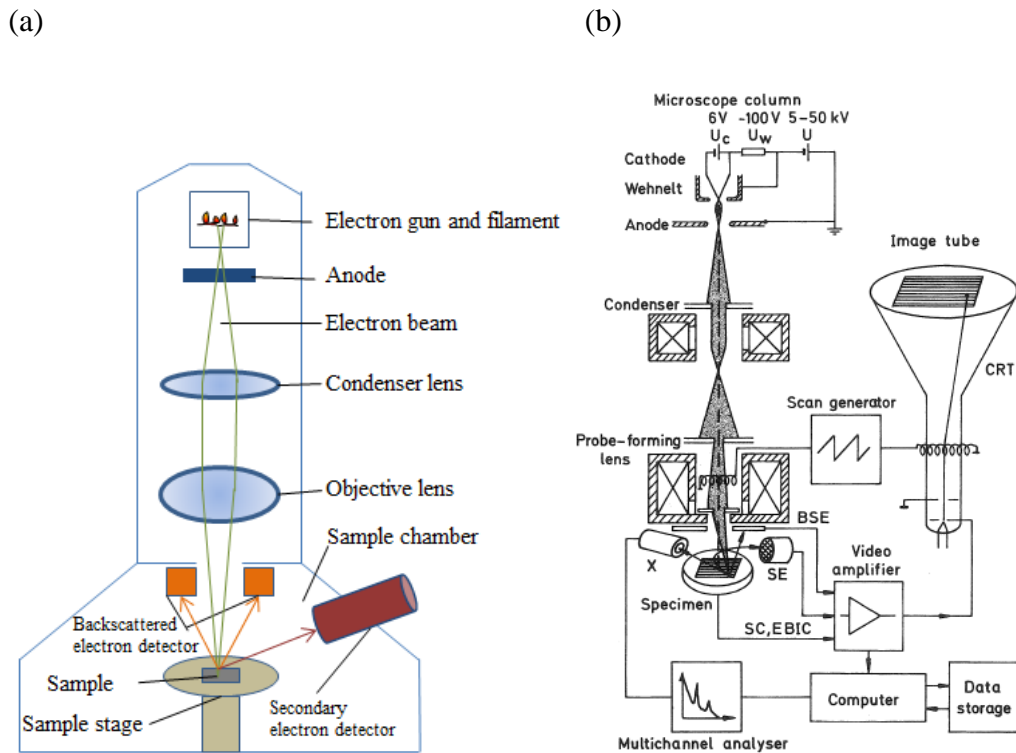


Figure 2.5: (a) Schematic diagram showing the main components of a typical SEM system and (b) a more detailed diagram showing the secondary electron (SE) and backscattered electron (BSE) detectors and the associated electronics (from reference 11). A camera was used instead of the CRT in this work to view the sample. (c) Diagram of the process of generation of EDX signal, (d) Photograph of the Carl-Zeiss SEM system in DCU.

Some SEM images in this work, specifically the images of the O-enriched samples grown in the University of Jena, were obtained there using a FEI Helios NanoLab 600i system by Mr. Lukas Trefflich with the author.

## 2.4.2 X-ray Diffraction

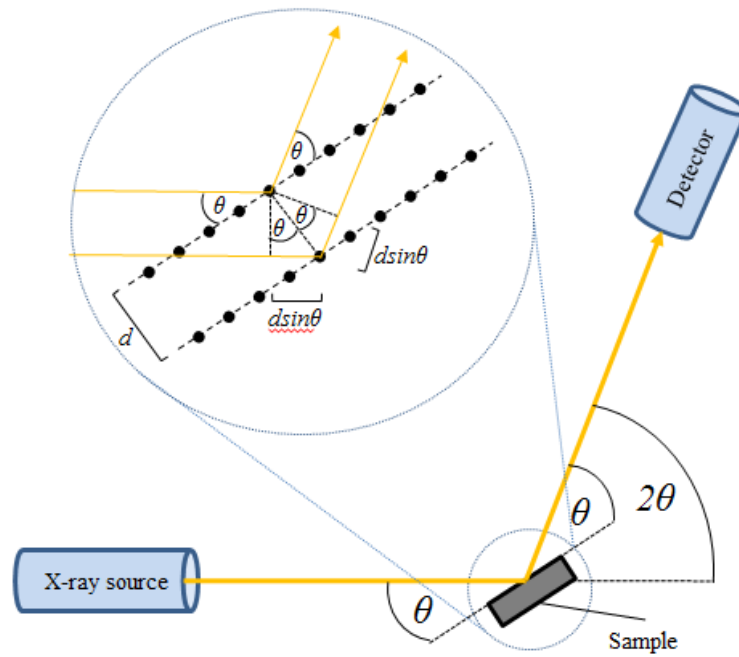
XRD works on the principles of elastic scattering and constructive interference. When a coherent beam of electrons is incident on a sample, some of the x-rays are inelastically scattered resulting in an x-ray of longer wavelength. These waves will not interfere with one another as they will have difference phases and wavelengths to each other. This is known as Compton scattering. They are not relevant here. However, most of the incoming x-rays will be scattered elastically from the sample. This is known as Thompson scattering. The physical structure of a crystalline sample can be viewed as a series of crystal planes of atoms along different directions. The spacing and orientation of these planes is rooted in the crystal structure of the particular material. Elastic scattering and diffraction occurs as x-rays bounce off different layers of atomic planes in the crystal. In some cases, the scattered x-rays from different planes can constructively interfere with each other under certain conditions as they have a definite phase relationship. The condition for constructive interference to occur between all the x-rays scattering from difference planes is described by the Bragg equation (Eqn. 2.1).<sup>12,13</sup>

$$2d\sin\theta = n\lambda \quad \text{Eqn. 2.1}$$

where  $d$  is the distance between atomic planes in the sample,  $\theta$  is the incident angle for the incoming x-rays,  $\lambda$  is the incident x-ray wavelength and  $n$  is an integer indicating the order. The left hand side of the Bragg equation,  $2d\sin\theta$ , is the additional path length travelled by an x-ray scattering off adjacent planes. When this is equal to a whole number of wavelengths constructive interference occurs. Figure 2.6 shows a diagram of the geometry of this situation. Constructive interference of

x-rays coming from different planes occurs at a particular incident angle and results in a sharp peak in the x-ray diffraction spectrum at that angle. Otherwise there is destructive interference between the scattered x-rays and no peak is observed.

(a)



(b)

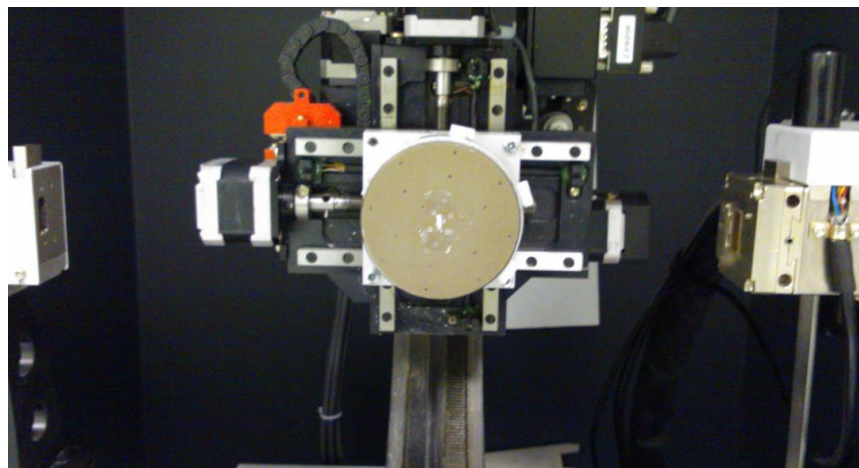


Figure 2.6: (a) Schematic diagram of the layout of an XRD system with zoom showing diffraction from adjacent crystal planes and the geometry of the Bragg equation, and (b) photograph of the Bruker AXS D8 Advance Texture Diffractometer.

The general geometry of an XRD system is shown in figure 2.6(a), along with a photograph of the Bruker AXS D8 Advance Texture Diffractometer used in this work in figure 2.6(b). The incident angle is changed by rotating the sample through the angle  $\theta$ . The diffraction angle is moved through the angle  $\theta$  by moving the detector through the angle  $2\theta$ , so that the situation is that of symmetrical reflection with respect to the sample (i.e. equal incident and reflected angles at all times). The x-ray source does not move. This method is used to collect the  $2\theta$ - $\omega$  spectra, where  $\omega=\theta$ . The detector collects the strong x-ray peaks at the angles when the Bragg equation is satisfied. The other major method of operation that was used in this work is called the rocking curve. In this case, the detector is placed at the correct  $2\theta$  angle of a previously observed peak corresponding to a particular plane or feature. The sample is then rotated about the angle  $\omega$ . The rocking curve generally gives a peak that can be used to compare the crystal quality and degree of nanocrystal alignment between samples.

XRD can be used, with the Bragg equation, to determine the orientation of the crystal planes in a sample and the spacing  $d$  between those planes. The peak positions of many materials are contained in databases (for example JCPDS<sup>14</sup>) which can be consulted in order to identify materials or contaminants in a sample based on the peaks recorded. It is therefore an important technique for material identification and characterisation.

XRD was primarily used throughout this work to confirm the presence of  $c$ -axis aligned ZnO as well as to obtain a quantitative measure of the crystal quality and orientation consistency, i.e. to study the crystalline quality of the deposited material.

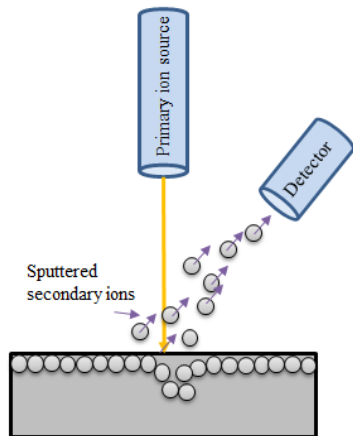
### **2.4.3 Secondary Ion Mass Spectroscopy**

SIMS is a mass spectroscopic technique used to analyse material from samples, including nanostructures and thin films. An ion beam is directed at the sample at a high voltage. This is called the primary ion beam. Upon impact, the ion beam sputters the surface and material is ejected from the sample. Most of the

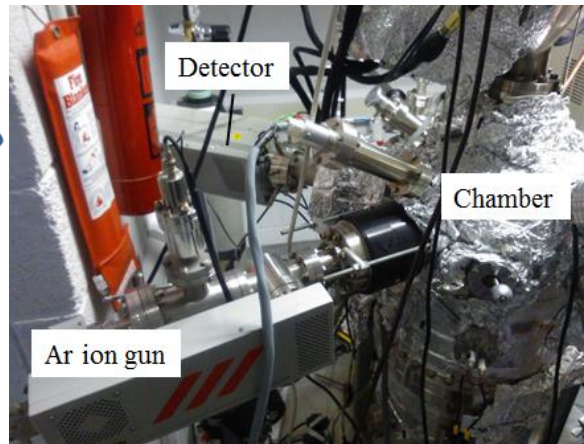
material ejected is not charged, but a small amount is ejected as ions. These secondary ions are then attracted to a detection system by a positive or negative bias, depending on the charge on the ions under investigation. The detection system is designed to differentiate between different materials based on their mass by measuring their charge/mass ratios. In this way different atoms or molecules can be detected. Of specific relevance for this work, isotopic distributions can be examined. SIMS was used in this work to examine isotopic distributions in enriched ZnO samples. The measurements take place under vacuum to ensure the maximum amount of sputtered material reaches the detector and contamination is minimised. Figure 2.7(a) shows a schematic of the main components in a SIMS system. Although SIMS is used to examine surfaces (the primary beam typically sputters to a depth of a few nm), depth profiling is also a very useful SIMS technique. In this case the primary beam continuously sputters the sample and ‘digs’ down past the first few atomic layers. This produces a depth profile of different layers in a composite material. SIMS can scan over a large area, making 3D visualisations possible, as well as examining a single point on a sample surface. When the ion current is set relatively low in order to scan surfaces, it is referred to as static SIMS. By contrast, dynamic SIMS uses a high current density and a focussed beam to maximise sputtering yields and examine bulk material. This is the mode of operation used in depth profiling.

Two different systems were used to carry out SIMS in this work. In the first SIMS system (labelled simply as ‘SIMS’), measurements were performed in an ultra-high vacuum system with a base pressure of  $1 \times 10^{-9}$  mbar. The setup included a Hiden Analytical IG20 ion gun operating with a positive Ar (99.99%) ion beam of 5 keV at a chamber partial pressure of  $5 \times 10^{-5}$  mbar with the analysis chamber not exceeding  $2 \times 10^{-8}$  mbar during analysis. The sample current during analysis ranged from 90 nA to 110 nA. All samples were analysed at an angle of  $\sim 20^\circ$  off normal incidence. This was to try to reduce any effects from the unenriched ZnO buffer layers below the isotopically pure VPT-grown nanorods. Secondary Zn ions were detected using a Hiden Analytical mass spectrometer EQS quadrupole analyser. This is a positive mode SIMS setup i.e. it detects positively charged ions. The actual measurements on this system were carried out by Mr. Conor Byrne in DCU. A photograph of this system is shown in figure 2.7(b)

(a)



(b)



(c)



*Figure 2.7: (a) Schematic diagram showing the sputtering process used in SIMS, (b) photograph of the SIMS system and (c) photograph of the Millbrook miniSIMS alpha system.*

The second system used to carry out SIMS measurements was the benchtop Millbrook miniSIMS alpha system (labelled as ‘miniSIMS’ to distinguish it from the first system). A photograph of this system is shown in figure 2.7(c). This uses a positive Ga ion beam at 6 keV and a quadrupole analyser. The samples were mounted at a 45° angle in this case. The miniSIMS alpha is a complete SIMS system designed for ease of use and quick changing of samples. The sample stage can be ejected, samples mounted and the stage returned to vacuum in about half an hour. The stage also held several samples at once which again speeds up the process of loading and scanning. The system operates at a pressure of about  $1 \times 10^{-7}$  mbar.

All of the systems components, including the Ga source, the sample stage, the detection system and the vacuum systems are contained inside one benchtop apparatus. The PC software allows full control of the entire system. The miniSIMS is capable of switching between positive and negative mode, depending on the ions under investigation, by changing the polarity of the detection system. The instrument is also fitted with charge neutralisation system which allows insulating samples to be examined. Measurements on this system were carried out by the author.

#### **2.4.4 Raman Spectroscopy**

Raman spectroscopy is an optical technique used to examine vibrational, rotational and other low-frequency excitation modes in a material by detecting shifts in energy of scattered light. When a monochromatic light source, usually in the form of a laser, is incident upon a material, it can interact with that material in a number of ways. The simplest form of interaction is for the photons to be scattered elastically. This is known as Rayleigh scattering. Raman scattering occurs when the scattered photon has interacted with phonon modes in the sample and therefore has an energy that is different to that of the incident photon, be it more or less. This is an inelastic process and is much less frequent than Rayleigh scattering with only around one photon in a million undergoing Raman scattering.

Briefly, the incident photon excites the target atom or molecule from some vibrational or rotational state into a higher virtual state. The scattered photon is then emitted but the atom or molecule may end up in a different excitation state to where it began. If the final state has more energy than the original state then it follows that the emitted photon must have less energy than the incident photon. This is called a Stokes shift. Likewise, if the final state has an energy which is less than the original state, then the photon emitted must have a greater energy than the incident photon. This is called an anti-Stokes shift. Figure 2.8 shows a diagram of each of these interactions. Raman scattering ultimately comes about due to the strong electric field associated with the incoming laser beam interacting with the electrons in the target material and inducing a dipole moment in those atoms or molecules, in

combination with the modulation of the dipole polarizability at the excitation frequency of e.g. the vibration or rotation. The combination of these effects leads to the inelastic scattering (essentially sidebands in a classical picture).

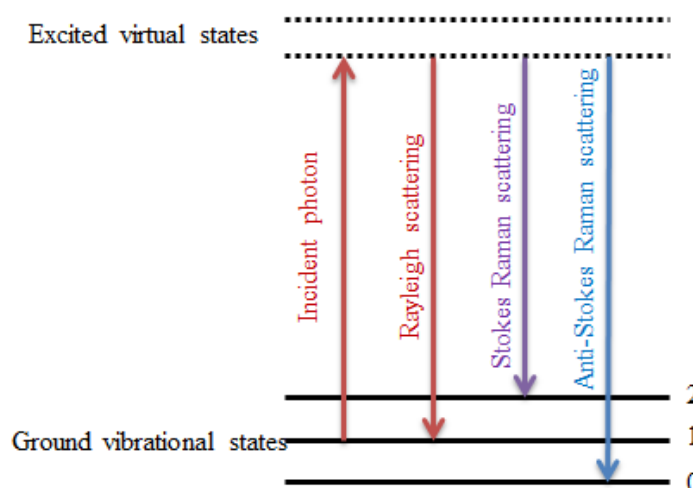


*Figure 2.8: Energy level diagram showing Rayleigh scattering, and Raman Stokes and anti-Stokes scattering processes.*

The vibrational and rotational mode energies of an atom or molecule are unique and Raman can therefore be used to detect and study these properties in specific atoms or molecules and utilise the information as a “fingerprint” for specific materials. Similarly, bulk solids, liquids and gases also have characteristic phonon modes. In this work, shifts in the Raman lines indicate shifts in the characteristic phonon modes in isotopically enriched ZnO material due to the changes in atomic mass.

A typical Raman system will include a laser source, efficient collection and focussing optics, relevant filtering to remove the much stronger elastically scattered signal and a charge-coupled device (CCD) or photomultiplier tube (PMT) detection system. Raman measurements on the  $^{64}\text{ZnO}$ ,  $^{66}\text{ZnO}$  and  $^{68}\text{ZnO}$  samples were performed by Dr. Joseph Cullen at Linköping University, Sweden. They were performed at room temperature using a Horiba LabRAM micro-Raman system. Non-resonant excitation was used to make Raman measurements in the

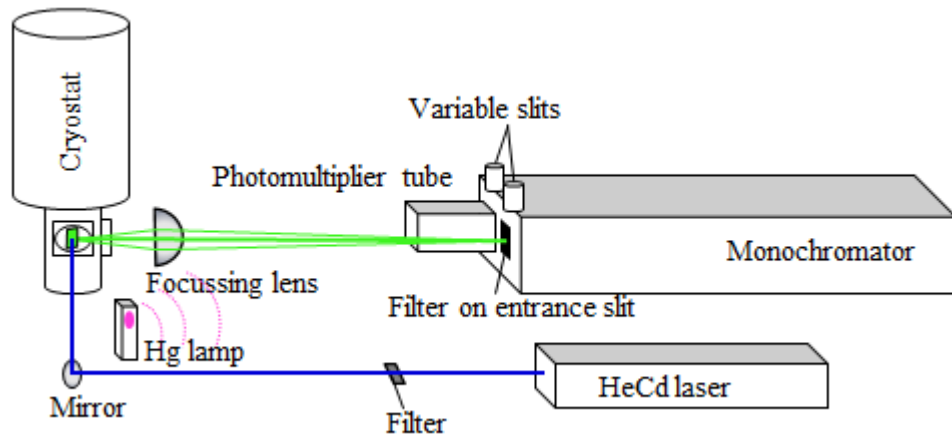
$z(x+y, x+y)\bar{z}$  back-scattering geometry using the 532 nm line of a solid state laser with  $z$ -direction coinciding with the direction of the  $c$ -axis of ZnO. This essentially means that the laser was incident on the sample normally along the  $z$ -direction and  $c$ -axis of the crystal, and that the scattered photons back along this same direction were collected for analysis. Resonant excitation, where the incident photon energy is tuned to an electronic transition in the sample to enhance the associated vibrational modes, is not used here. Raman measurements on the O-enriched samples were obtained in DCU with a similar setup using a Jobin Yvon LabRam HR800 system at room temperature using an Ar laser at 488 nm and an air-cooled CCD detector, with the assistance of Dr. Rajani Vijayaraghavan.

#### **2.4.5 Photoluminescence**

The optical properties of the ZnO nanorod samples were analysed using low temperature PL. The details of the experimental setups and their operation are presented here. More detail on the theory of PL and its application in the study of defects and impurities in semiconductors, and in particular ZnO, is presented in chapter 3. Two separate low temperature PL systems were used in this work. They both have advantages, and they are both described in detail below. In short, samples were placed in a Janis Research closed cycle helium (He) cryostat and cooled to temperatures in the 10-20 K range, depending on the system. The samples were excited by directing a continuous wave helium cadmium (HeCd) laser at a wavelength of 325 nm onto them. The emitted PL light was then collected using a lens and directed to the entrance aperture of the spectrometer. The two systems utilised in the collection of the PL emission from the samples were (i) a diffraction grating spectrometer system and (ii) a Fourier transform (FT) spectrometer system.

(i) **Diffraction grating spectrometer system (SPEX)**

(a)



(b)

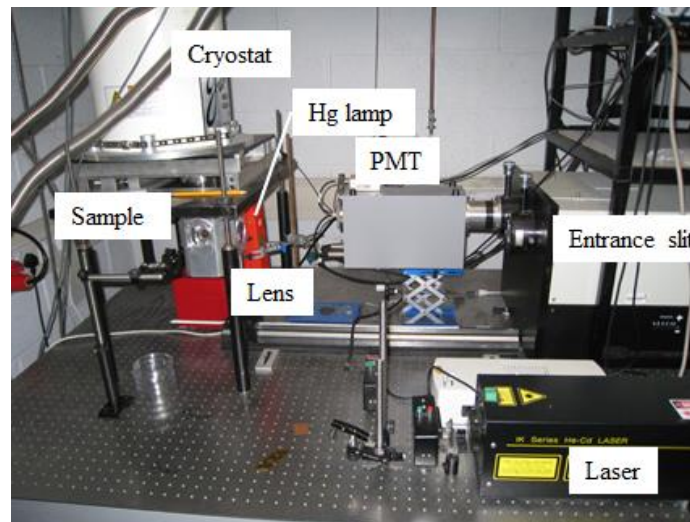


Figure 2.9: (a) Schematic, and (b) photograph, of the optical setup used for PL with the SPEX monochromator.

The dispersion spectroscopic system is based on a 1 m model SPEX 1704 monochromator. The optical setup is shown in figure 2.9. The sample was placed in a Janis Research model SHI-950-5 cryostat and cooled to  $\sim 12$  K. The HeCd laser beam was directed onto the sample by a simple system of mirrors. The sample

surface was at an angle of  $45^\circ$  to the laser beam. The emitted light was carefully collected by a focussing lens (at  $90^\circ$  to the incident laser beam) and focussed onto the entrance slit of the SPEX monochromator. Light entering the monochromator via the variable width entrance slit was directed onto the diffraction grating and then to the detector via the variable width exit slit. A mercury (Hg) spectral lamp was placed in the region of the cryostat so that the light emitted also fell in the entrance slit. The spectral lines from this lamp were used to calibrate the spectra recorded to correct for minor variations from scan to scan due to minor hysteresis in the mechanical drive system which moves the grating. The 365.0158 nm Hg line in each spectrum was aligned to this position. This is the position of this line in air.<sup>15</sup> In addition, the SPEX spectra have been corrected for the refractive index of air by dividing by 1.000285.<sup>16</sup> The spectra were recorded using software on a PC. This dispersion-based system using a diffraction grating essentially scans through the wavelengths by having the grating direct each one in turn onto the exit slit and into the detector. The intensity at each wavelength is then recorded. Schott glass filters were placed at the laser (UG11) to remove longer wavelength lines and at the monochromator entrance slit (WG-345) to remove any shorter wavelength laser and plasma tube light.

The detector was a Hamamatsu model R3310-02 PMT in photon counting mode which was cooled to approximately  $-20^\circ\text{C}$  using a Peltier system EMI FACT50 Cooler. The dark count of the detector at this temperature is very low at around 30 counts per second or about 5 nA.<sup>17</sup> The monochromator grating was blazed at 330 nm with 1200 grooves/mm (ISA model 510-05). The efficiency of this system is limited by two main factors. These are the efficiency of the diffraction grating, and the efficiency of the PMT, both of which vary with wavelength. The grating is very efficient around the band edge region in ZnO of  $\sim 369$  nm, which is a region of strong interest in this work. It is less efficient at the green band energies of around 430-600 nm. The detector is also less efficient at longer wavelengths. Equations and their graphs representing the efficiency curves for the PMT and diffraction grating used in this system can be found in appendix A, as reproduced from reference 18. Because of this some samples needed to be annealed at  $900^\circ\text{C}$  for 10 minutes in order to increase the SGB intensity when we wished to study that relatively weak emission using this system. In addition, some of the O-enriched

samples were annealed in this way to activate the SGB emission as it was not observed in the as-grown samples.<sup>19</sup> This is further elaborated on in chapter 3. The resolving power,  $R$ , of the diffraction grating is related to the resolution,  $\Delta\lambda$ , by the formula

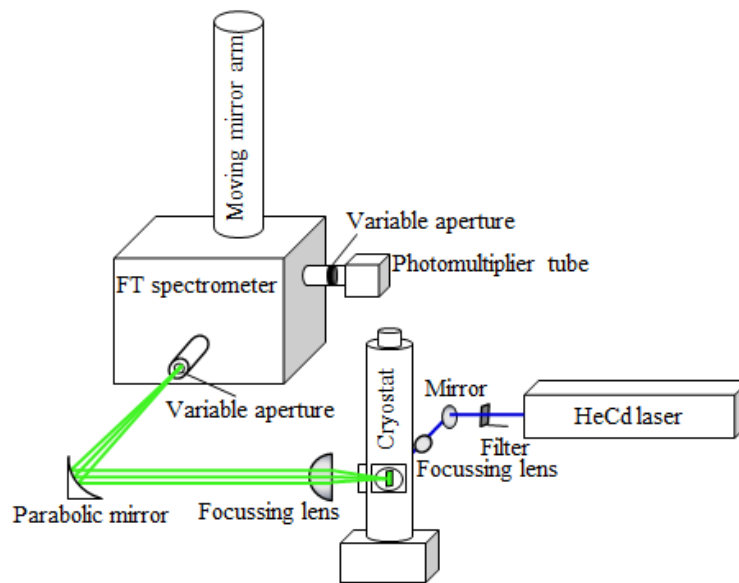
$$R = \frac{\lambda}{\Delta\lambda} = Nm \quad \text{Eqn. 2.2}$$

where  $N$  is number of grooves in the grating,  $m$  is the diffraction order and  $\lambda$  is the wavelength.<sup>18,20</sup> The system's  $f$  number is  $\sim f/9$  and the lenses and optics are chosen to match this. The maximum resolution of this system is 0.008 nm ( $\sim 0.07$  meV). Typically the band edge spectra were recorded using a step size of 0.005 nm (with a resolution of  $\sim 0.07$  meV) and a slit width of 6  $\mu\text{m}$ , and the SGB ZPLs with a step size of 0.01 nm ( $\sim 0.09$  meV) and a slit width of 20  $\mu\text{m}$ . These slit widths are at or below typical pixel sizes in CCD cameras commonly used to record spectra in monochromator systems. Additionally, regarding the calibration, although the Hg lamp was placed slightly off the optical axis of the system and therefore one might expect some broadening of these lines as not all of the light would fall on the diffraction grating, the observed lines remained very sharp and there was sufficient light to use the Hg lines for calibration purposes.

## (ii) Fourier transform spectrometer system (FT)

The second spectroscopic system consisted of a Bomem DA8 FT spectrometer and IPH8200L PMT detector. The optical setup is shown in figure 2.10. The sample was placed in a Janis Research CSS-550 cryostat and cooled to  $\sim 19$  K. The 325 nm HeCd laser beam was directed onto the sample using mirrors and a focussing lens to produce a small, intense spot on the sample. The sample was again at  $45^\circ$  to the incident beam. The emitted light was collected by a lens (at  $90^\circ$  to the incident laser beam) which produced a parallel beam and focussed onto the entrance aperture by a parabolic mirror. In this case the entrance aperture was a variable circular aperture. There was another variable circular aperture at the exit point just before the detector. The spectra were again collected using a PC.

(a)



(b)

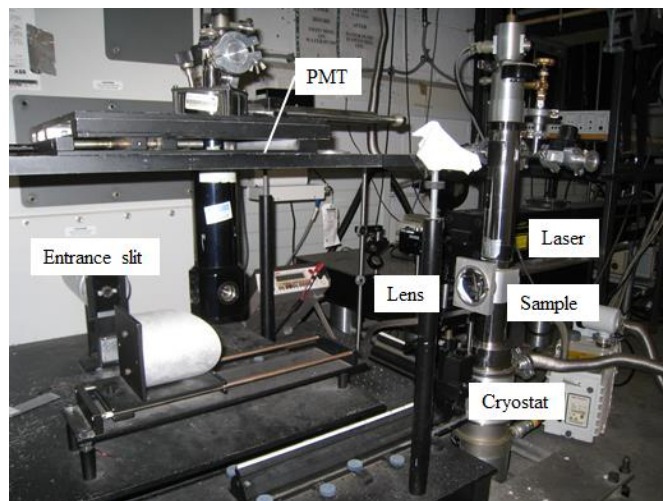


*Figure 2.10: (a) Schematic, and (b) photograph, of the optical setup used for PL with the FT spectrometer.*

The FT spectrometer works on a fundamentally different principle to the diffraction-based dispersion monochromator. Many of the factors that can limit the resolution of a typical dispersion system, such as the slit widths and the grating dispersion, are either not as important or not applicable to an FT system. The FT system is based around the Michelson interferometer. Light entering the system is

split into two beams. Each beam travels along different paths and are then recombined and incident on the detector. One beam travels along a fixed arm and reflects off a stationary mirror. The path length of the second beam is variable by the movement of the mirror from which it reflects. When the two beams recombine they interfere with each other. With light of a single frequency, if the path difference travelled by the two beams equals a whole number of wavelengths, then constructive interference occurs. Otherwise, different interference conditions occur including completely destructive interference when the path difference travelled by the beams corresponds to a difference of half a wavelength. As the moving mirror moves, the detector sees a series of bright and dark fringes in a sinusoidal pattern resulting from the interference of the two beams with changing phase difference. The intensity detected by the PMT is therefore related to the phase difference between the beams and the frequency of the light. However, in examining a spectrum from a sample using PL the signal will contain many difference frequencies of different intensities. The intensity recorded at the detector as the mirror moves will be a complex pattern of interference fringes containing the interference patterns of each individual frequency present in the beam and their intensities. This is called an interferogram. The interferogram is the Fourier transform of the intensity spectrum. Therefore, the spectrometer software performs an inverse Fourier transform on the interferogram, extracts the frequencies and intensities contained therein and produces the optical spectrum.

To briefly describe the relationship between the interferogram and the spectrum we consider the case of a monochromatic source and the interaction in the Michelson interferometer after beam splitting of two standard electromagnetic waves with a phase difference of  $\varphi$ :

$$E_1 = E \cos(kx - \omega t) \quad \text{and} \quad E_2 = E \cos(kx - \omega t + \varphi) \quad \text{Eqn. 2.3}$$

where  $k$  is the wavenumber which is related to the wavelength  $\lambda$  by the relation  $2\pi / \lambda$ , and  $\omega$  is the angular velocity.  $x$  and  $t$  represent position and time respectively. The detector output is the intensity of the wave incident on it, rather than the electric field. The total intensity  $I_T$  is given by the time average of the square of the total electric field  $E_T$  as follows:

$$I_T = \langle E_T^2 \rangle = \langle (E_1 + E_2)^2 \rangle = \langle E_1^2 + E_2^2 + 2E_1E_2 \rangle \quad \text{Eqn. 2.4}$$

This can then be written as

$$I_T = \langle E_T^2 \rangle = \frac{E^2}{2} + \frac{E^2}{2} + E^2 \cos \varphi \quad \text{Eqn. 2.5}$$

$$I_T = \langle E_T^2 \rangle = E^2 + E^2 \cos \varphi \quad \text{Eqn. 2.6}$$

$$I_T = \langle E_T^2 \rangle = E^2(1 + \cos \varphi) \quad \text{Eqn. 2.7}$$

The phase difference between the waves  $\varphi$  can be written as

$$\varphi = \frac{2\pi D}{\lambda} = kD \quad \text{Eqn. 2.8}$$

where  $D$  is the difference in distance travelled by the two waves. Equations 2.7 and 2.8 show that the intensity at the detector varies in a cosinusoidal pattern as a function of the difference in the distance travelled by the two waves (related to the moving mirror) and the wavelength of the light. This relation between the intensity and the mirror position is what produces the interferogram recorded at the detector. However the spectra recorded using an FT spectrometer never contains only one wavelength because even a very close to monochromatic source will not produce light of a single wavelength. There will always be a spread of wavelengths described by the line width. A full spectrum will contain signal at many wavelengths and at different intensities. All these interferograms combined are observed at the detector. In order to capture all of this information, we introduce a function  $I(k)$  which represents the entire spectrum under investigation. Integrating equation 2.7 gives the total intensity detected as

$$I(D) = \int_{-\infty}^{\infty} I(k)(1 + \cos(kD)) dk \quad \text{Eqn. 2.9}$$

This interferogram is the Fourier transform of the emission spectrum under investigation. It contains all the wavelength and intensity information needed to reconstruct the original spectrum. If we perform an inverse Fourier transform we obtain the original spectrum:

$$I(k) = \int_{-\infty}^{\infty} I(D)(1 + \cos(kD)) dD \quad \text{Eqn. 2.10}$$

This is computed by the PC software. The limits on these integrals are infinity, but in practice the system is limited by the range of the moving mirror. The

longer the distance available for it to move, the higher the resolution the system will have. If we consider a single wavelength, the mirror can only move a certain distance,  $P$ . Essentially the integral stops at  $P$ , and the effect is a broadening inversely proportional to  $P$ , with the achievable resolution limited to  $1/P$ . The minimum resolvable  $\Delta k$  for the instrument (representing the line width of an ideal monochromatic source) is given by<sup>21</sup>

$$\Delta k \cong \frac{\pi}{P} \quad \text{Eqn. 2.11}$$

This can also be written in units of  $\text{cm}^{-1}$  as<sup>22</sup>

$$\Delta \nu \approx \frac{0.7}{2P} \quad \text{Eqn. 2.12}$$

For example, if the mirror travelled a distance of 3 cm, then the value of  $\Delta \nu$  would be  $\sim 0.12 \text{ cm}^{-1}$ . The system performance is also limited by a number of factors which complicate the brief description presented here, including aperture size, mirror alignment, detector noise, optical imperfections and the process of converting the signal from analogue to digital. The system contains a HeNe laser which it uses to align the fixed mirror to correct for any misalignment during a scan. The instrument must also determine the zero path difference (ZPD) position. A broad band white light source is used for this. At the ZPD point a large peak occurs as all the wavelengths from this source undergo constructive interference allowing the ZPD point to be determined to high accuracy.

The FT system has a number of distinct advantages in comparison to dispersive grating spectrometer systems. The system records all wavelengths at once as they are all contained in the interferogram recorded. Dispersive monochromators must scan through each wavelength individually. This is known as the multiplex advantage. This can speed up the time it takes to obtain a spectrum. This also produces a signal-to-noise advantage of  $\sqrt{N}$ , for  $N$  spectral channels, excluding photon noise. The circular aperture can allow a much higher throughput which can be important when examining weak signals. This is known as the throughput advantage. It reflects the fact that FT systems do not need their entrance slits to be as narrow as in dispersive systems to produce the same resolution. The resolving power,  $R$ , of a Michelson interferometer due to the aperture is given by<sup>23</sup>

$$R = \frac{2\pi}{\Omega} \quad \text{Eqn. 2.13}$$

with

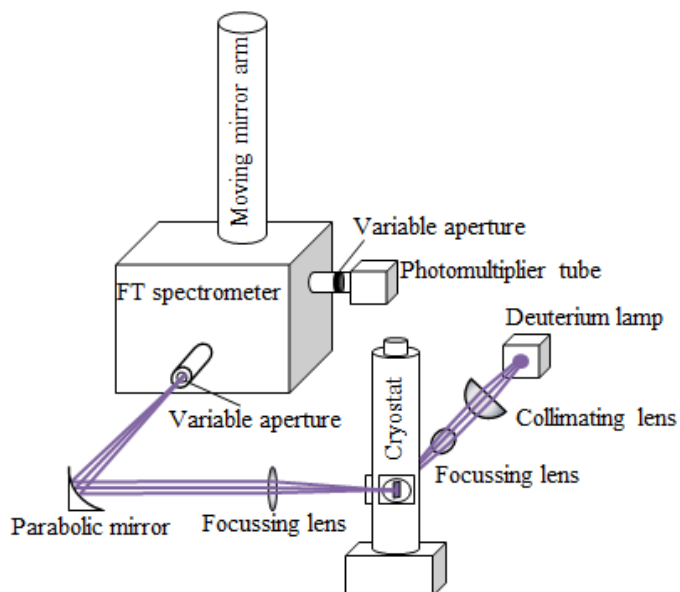
$$\Omega = \pi \left(\frac{\theta}{2}\right)^2 \quad \text{Eqn. 2.14}$$

where  $\theta$  is the solid angle of admittance at the entrance aperture. There is thus a trade-off between higher resolutions and higher signal strength.

However this system still suffers from signal-to-noise problems when measuring very weak signals, as the dark count of the detector was higher than the SPEX system, and therefore a range of filters were used to eliminate spectral regions not of interest when carrying out different scans. Filtering out parts of the spectrum that were not of interest also helps to stop a weak signal from being lost amongst an intense signal. The white light source had all wavelengths below 700 nm filtered out. In addition, a second filter in front of the PMT further reduced interference from wavelengths not of interest during a particular scan. A BG25 Schott glass bandpass filter was used (cut on ~330 nm, cut off ~480 nm) for scans in the UV region, and a 606HSP visible bandpass filter (cut on ~380 nm, cut off ~620 nm) was used for the visible region. A further bandpass filter (3RD, cut on ~430 nm, cut off ~440 nm) was used in conjunction with the 606HSP filter when measuring the ZPL line at 2.68 eV as it very weak. A filter (UG11) was also placed in front of the laser as with SPEX system to remove longer wavelength laser plasma lines. The software also has the option of running many scans and adding them together to reduce the overall signal-to-noise ratio. This was normally done during this work. The FT system is also very accurate and stable, and did not need any external calibration as used with the SPEX system to correct for any minor shifts in wavelength. The system also accounted for the refractive index of air automatically. A detailed description of issues related to Fourier transforms can be found in reference 22. On this system the band edge spectra were recorded with a resolution of a 0.015 meV for the band edge and 0.15 meV for the SGB ZPLs.

## 2.4.6 Reflectance Spectroscopy

(a)



(b)

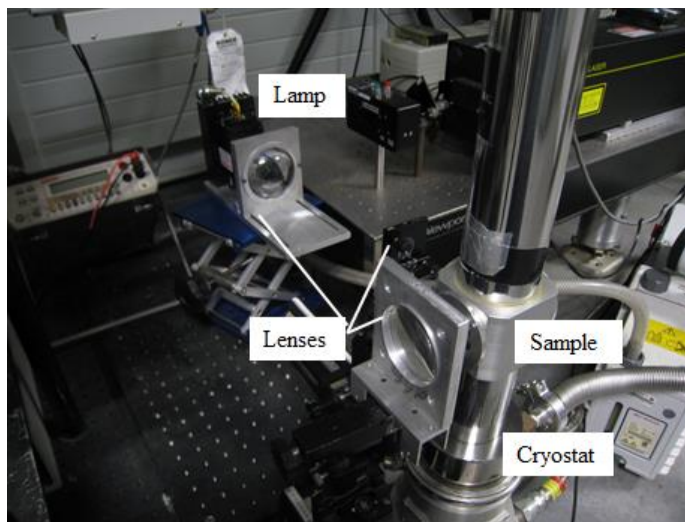


Figure 2.11: (a) Schematic, and (b) photograph, of the optical setup used during reflectance spectroscopy experiments with the FT spectrometer.

Reflectance spectroscopy was performed by using a modified optical set up with the FT spectrometer. This is shown in figure 2.11. A broad band deuterium

lamp was used as the light source. This was collimated using a lens and then focussed to a small spot on the sample. The sample was again at 45° to the incident light. Reflected light was collected by another lens (at 90° to the incident light beam) to form a parallel beam before being directed using parabolic mirror to the entrance slit of the spectrometer. These spectra were collected with a pre-recorded reference spectrum collected using a reflective piece of Al-coated Si automatically subtracted by the software. Reflectance spectroscopy aims to record light reflected from the surface of the samples, rather than light generated by photoluminescence from the samples. It is a useful technique that can be used to record the position of the free excitons and this was the purpose of using this characterisation technique in this work.<sup>24</sup>

## 2.5 References

- <sup>1</sup> D. Byrne, E. McGlynn, K. Kumar, M. Biswas, M.O. Henry, and G. Hughes, *Cryst. Growth Des.* **10**, 2400 (2010).
- <sup>2</sup> L.E. Greene, M. Law, D.H. Tan, M. Montano, J. Goldberger, G. Somorjai, and P. Yang, *Nano Lett.* **5**, 1231 (2005).
- <sup>3</sup> M. Law, L.E. Greene, J.C. Johnson, R. Saykally, and P. Yang, *Nat. Mater.* **4**, 455 (2005).
- <sup>4</sup> Y.-J. Lee, T.L. Sounart, D.A. Scrymgeour, J.A. Voigt, and J.W.P. Hsu, *J. Cryst. Growth* **304**, 80 (2007).
- <sup>5</sup> R.B. Saunders, E. McGlynn, M. Biswas, and M.O. Henry, *Thin Solid Films* **518**, 4578 (2010).
- <sup>6</sup> D. Byrne, R. Fath Allah, T. Ben, D. Gonzalez Robledo, B. Twamley, M.O. Henry, and E. McGlynn, *Cryst. Growth Des.* **11**, 5378 (2011).
- <sup>7</sup> R.B. Peterson, C.L. Fields, and B.A. Gregg, *Langmuir* **20**, 5114 (2004).
- <sup>8</sup> F.J. Manjón, M. Mollar, M.A. Hernández-Fenollosa, B. Marí, R. Lauck, and M. Cardona, *Solid State Commun.* **128**, 35 (2003).

- <sup>9</sup> C. Borchers, S. Mu, D. Stichtenoth, D. Schwen, and C. Ronning, *J. Phys. Chem. B* **110**, 1656 (2006).
- <sup>10</sup> D. Hou, T. Voss, C. Ronning, A. Menzel, and M. Zacharias, *J. Appl. Phys.* **115**, 233516 (2014).
- <sup>11</sup> L. Reimer, *Scanning Electron Microscopy: Physics of Image Formation and Microanalysis*, 2nd ed. (Springer-Verlag, Berlin, Heidelberg, New York, 1998).
- <sup>12</sup> J.J. Rousseau, *Basic Crystallography* (John Wiley & Sons, Sussex, 1998).
- <sup>13</sup> B.D. Cullity and S.R. Stock, *Elements of X-Ray Diffraction*, 3rd ed. (Prentice Hall, New Jersey, 2001).
- <sup>14</sup> International Centre for Diffraction Data. Joint Committee on Powder Diffraction Standards (JCPDS) Database. Available at: <http://www.icdd.com/>
- <sup>15</sup> Kramida, A. Ralchenko, Yu. Reader, J. NIST ASD Team. NIST Atomic Spectra Database (ver. 5.1), [Online]. Accessed 29-10-2013. Available at: <http://physics.nist.gov/asd>
- <sup>16</sup> Stone, J.A. Zimmerman, J.H. Engineering Metrology Toolbox, Refractive Index of Air Calculator, [Online]. Accessed 07-11-2013. Available at <http://emtoolbox.nist.gov/Wavelength/Edlen.asp>
- <sup>17</sup> Hamamatsu R3310-02 Photomultiplier Tube Specif. Sheet (n.d.).
- <sup>18</sup> D. Gorman, *Photoluminescence and Excitation Studies of Semiconductors*, Dublin City University, 2001.
- <sup>19</sup> N.Y. Garces, L. Wang, L. Bai, N.C. Giles, L.E. Halliburton, and G. Cantwell, *Appl. Phys. Lett.* **81**, 622 (2002).
- <sup>20</sup> J. Cullen, *Photoluminescence Studies of ZnO Doped with Stable and Radioactive Impurities*, Dublin City University, 2013.
- <sup>21</sup> M. Biswas, *Growth and Characterisation of ZnO Nanostructures: Excitonic Properties and Morphology*, Dublin City University, 2010.
- <sup>22</sup> J. Chamberlain, *The Principles of Interferometric Spectroscopy* (Wiley, Chichester,

1979).

<sup>23</sup> J. Fryar, *Optical and AFM Studies of ZnO: Excitonic Properties, Surface Morphology and Etching Effects*, Dublin City University, 2005.

<sup>24</sup> C.F. Klingshirn, B.K. Meyer, A. Waag, A. Hoffmann, and J. Geurts, *ZnO: From Fundamental Properties Towards Novel Applications* (Springer-Verlag, Berlin, Heidelberg, 2010).

# **Chapter 3: Background Theory of Elements of Optical Properties of ZnO**

## **3.1 Introduction**

This chapter presents the background information regarding relevant aspects of the optical properties of ZnO under investigation in this work. We begin by introducing the technique of low temperature PL which is a powerful technique in the study of defects and impurities in semiconductor materials. Some general information about defects and impurities in semiconductors is then presented, followed by a general description of the main features of the ZnO PL emission spectrum. One of these features, the Cu-related defect emission at 2.86 eV, is then discussed in detail. This defect is of particular interest in this work. The use of the isotope effect in semiconductor defect studies, and how it pertains to this work, is described. Finally, the main phonon modes investigated using Raman spectroscopy in this work, are described.

## 3.2 Low Temperature Photoluminescence

PL is a powerful and useful technique in the study of semiconductor materials such as ZnO. It can reveal information about the electronic, vibrational and optical characteristics of a material. It is therefore of exceptional use in the study of defects and impurities in materials as these introduce distinctive changes in the electronic and vibrational structure of the material. It is also a non-destructive and non-contact technique which is an obvious advantage in its use.

PL relies on the creation of electrons and holes in the material and the analysis of the photons released during the recombination of same. Electrons are excited from the valence band to the conduction band when a light source with photon energy greater than the band gap is incident on the sample (the ZnO band gap varies from 3.37 eV at 300 K to about 3.44 eV at low temperatures<sup>1,2</sup>). Typically the source of light is a laser. The excited electron leaves a positive hole in the valence band. The electron and hole have a greater energy than the band gap due to the energy imparted to it by the incident photon which was above the band gap energy of the material. These electrons and holes are called hot carriers. They undergo a process called thermalisation where they lose this excess energy to the surrounding crystal, e.g. by collisions with phonons etc. The electron is then localised in energy close to the edge of the conduction band and the hole localised in energy close to the valence band edge (we neglect electron-hole Coulombic interactions for the present and return to this issue later). They can then recombine in a radiative process and emit a photon of energy equal to the band gap of the material. The thermalisation process occurs at a much shorter timescale ( $\sim 5$  ps) than the recombination ( $> 200$  ps) and therefore an excess population of electrons and holes accumulate at the band edges before recombination.

We must also consider whether the material is a direct or indirect band gap semiconductor. ZnO is a direct band gap material. This means that the crystal momentum, or wave vector,  $k$ , is the same for position of the energy at the top of the valence band and the bottom of the conduction band. In this case the electron and hole can recombine in a radiative process involving only a photon since overall momentum can be conserved because the photon has a very small momentum. The

energy, and therefore the wavelength, of the photon emitted during recombination is equal to the band gap of the material and energy is thus conserved. This process involves two particles, the electron and the photon, and therefore the quantum mechanical matrix element, or probability, of this transition is much higher than non-radiative processes. This contributes strongly to direct band gap materials like ZnO being very efficient optical emitters and absorbers.

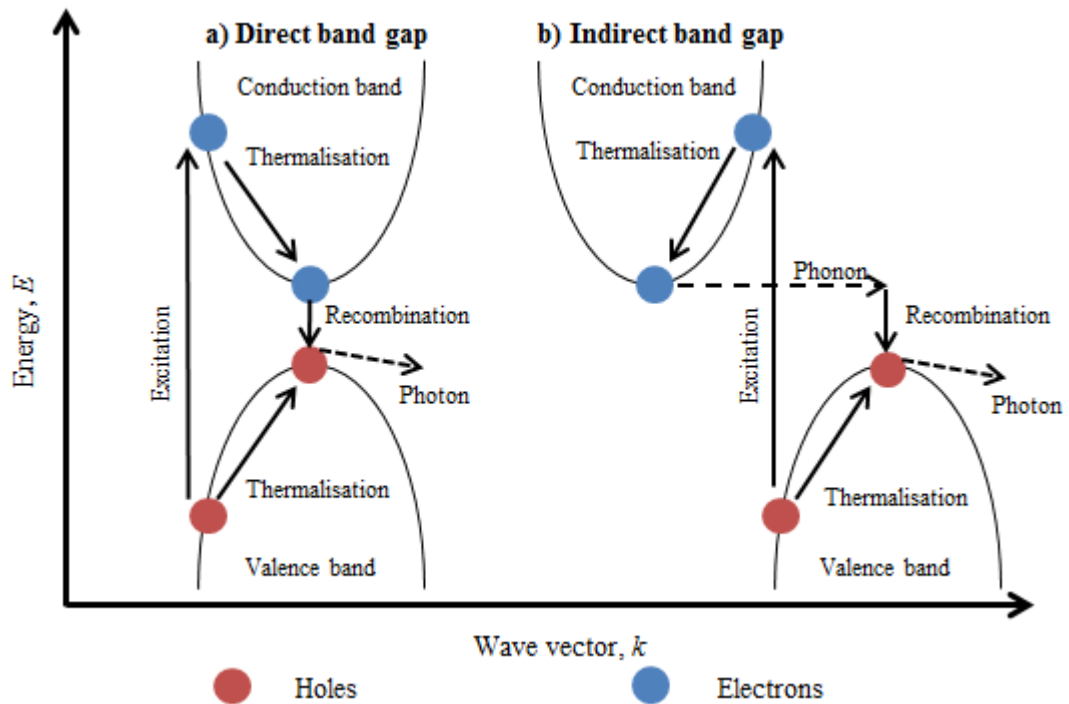


Figure 3.1: Diagram showing the excitation and recombination processes in (a) direct, and (b) indirect, band gap semiconductors.

However, in an indirect band gap material, the edges of the valence and conduction bands do not have the same crystal momentum values. In this case a change in crystal momentum is required for recombination to occur, which cannot be supplied solely by a photon because of the small momentum of the photon. This generally happens by the emission or absorption of phonons to or from the crystal lattice. The emitted photon can therefore be of greater or lesser energy than the band gap of the material, although at room temperatures (and below) the density of phonons is generally so low that the photon and phonon emission process dominates and the photon therefore has a lower energy than the band gap. Due to the

involvement of this additional particle in the process, the quantum mechanical probability of this occurring is much lower than the probability of recombination in a direct band gap material. Competing non-radiative processes therefore can dominate and thus it follows that indirect band gap materials are much less efficient optical emitters and absorbers. The excitation, thermalisation and emission (by direct or indirect band gap) processes described above are shown schematically in figure 3.1.

When an electron-hole pair is created by excitation as previously described, they experience a Coulombic attraction to each other due to the electron's negative charge and the hole's effective positive charge. The electron and hole can become coupled to each other and move through the crystal around their centre of mass as a single 'quasi-particle' which is called an exciton. When excitons travel without restriction through the crystal (in very perfect and pure crystals with no defects or impurities) they are called free excitons (FX).<sup>3,4</sup> They can be thought of in a way similar to the Bohr model of the atom and their binding energy and radius can therefore be calculated using this model taking account of the electron and hole effective masses and the materials dielectric permeability. They have a formation energy slightly smaller than the band gap due to the Coulombic binding energy (60 meV in ZnO).<sup>3</sup>

Two types of excitons are generally identified for different materials.<sup>3</sup> The first are called Frenkel excitons. These are generally present in insulators with very small dielectric constants. In this situation, the material's ability to screen the electric field due to the electron and hole charges is weak and so the Coulombic attraction between the electron and the hole is very strong. These excitons are tightly bound and have small radii of the order of one unit cell in size. Their binding energy is on the order of 1 eV. The second type of excitons are called Mott-Wannier excitons. These occur in materials with larger dielectric constants such as semiconductors and other insulators. In this case the larger dielectric constant leads to increased screening of the Coulombic attraction of the exciton by the material and the exciton has a much larger radius. The electron and hole can be considered to be orbiting their centre of mass with a radius of several unit cells. In addition the binding energy of this type exciton is much smaller, on the order of 0.1 eV, than the Frenkel type. This is the type of exciton formed in ZnO, which has an exciton binding energy of ~ 60 meV and an electron-hole separation of ~ 2 nm.

The importance of excitonic effects is dependent on the size of the exciton binding energy and the temperature at which experiments are performed. At temperatures greater than the exciton binding energy ( $T > E_{\text{binding}}/k$ ) the electron and hole are thermally dissociated and exciton effects are not observed, whereas at lower temperatures ( $T < E_{\text{binding}}/k$ ) excitonic effects are clearly in evidence. For the case of ZnO, where  $E_{\text{binding}} = 60$  meV, excitonic effects persist up to room temperature and above ( $300 \text{ K} \equiv 26 \text{ meV}$ ). Since the electron and hole motions are correlated in the excitonic state and the electron and hole remain close to each other, the quantum mechanical probability of radiative emission is increased for excitons compared to uncorrelated carriers. The fact that ZnO is a direct band gap material with a strongly bound excitonic state means that it is a very efficient light emitter at energies at and below its band gap.

PL essentially relies on the recombinations of excitons in the material under investigation and the corresponding emission of photons. We have discussed in this section the case of a perfect and pure material, where the emitted photons have energies characteristic of the material itself, specifically the material band gap and FX binding energy. However, in less perfect or pure materials some or all of the photons emitted will have energies characteristic of the defect or impurity at an exciton has become bound, as described in the following section.

### **3.3 Defects in Semiconductors**

In ZnO, the FX has an energy 60 meV below the band gap energy. However, this work is more concerned with the case of bound excitons (BX). These are excitons which have bound to defect or impurity sites in the crystal structure and are no longer freely travelling through the crystal. PL is a powerful tool to use in the analysis of defects and impurities as each BX has a unique localisation energy, essentially its binding energy at that impurity, measured relative to the FX position, which is specific to that defect or impurity. They therefore emit photons of a specific energy upon recombination and can be unique fingerprints for identification and study of the impurities/defects involved because the localisation energy depends

on the nature of the defect including its chemical identity, charge state, electronic structure and the details of the nearby lattice. PL can be used to analyse the optical spectrum of a material under optical excitation and can identify many peaks associated with different defects or impurities.

Excitons may be bound at ionised donor sites ( $D^+X$ ) and neutral donor sites ( $D^0X$ ) in ZnO.<sup>3</sup> These appear as peaks in the spectrum at energies just below the FX position, and in that order for ZnO. The ordering for different defect charge states is related to the electron and hole effective masses. These are characterised as shallow defects and this region of the spectrum is called the band edge or near band edge region. Donor-acceptor pair transitions (DAP) can also take place where an electron at a donor site combines with a hole at an acceptor site.<sup>1</sup> Two electron satellites (TES) occur if a  $D^0X$  recombines and leaves the donor atom in an excited 2s or 2p state. Electrons in the conduction band can also combine with holes at acceptor sites, as well as holes in the valence band combining with electrons at donor sites. Figure 3.2 gives an illustration of FX, BX and possible transitions in the band gap. The localisation energies of shallow BX in ZnO are in the range of  $\sim 3$  to  $\sim 20$  meV and thus these excitons become thermally delocalised as temperature rises and are not observed at room temperature, where only features due to FX are seen.

Excitons can also become bound at other defects and lead to emissions at energies far from the band edge energy. This type of emission is referred to as deep level emission (i.e. involving deep levels closer to the centre of the band gap) and the concept of excitons is generally less useful in analysing such emission, which is generally viewed in terms of electron and hole levels localised at the defect, although the initial exciton process is often via the capture of an FX. Once again however the emitted photons have a specific energy upon carrier recombination and are unique fingerprints for identification and study of the impurities/defects involved because the localisation energy depends on the nature of the defect including its chemical identity, charge state, electronic structure and the details of the nearby lattice.

A key parameter of PL is that it allows the energy levels introduced in the forbidden band gap by defects and impurities to be probed. Much more information can be gathered using low temperature PL than making the measurement at room temperature. This is for a number of reasons: (i) thermal effects can degrade PL

emission by delocalisation of excitons or carriers from defects and such effects are reduced or eliminated at low temperatures, (ii) non-radiative processes become much more likely at higher temperatures leading to much lower emission intensity from BX at higher temperatures and (iii) because the spectral line broadening effects of phonons are also reduced at low temperatures, and therefore working at low temperatures leads to strong, narrow emission lines with specific and accurately measurable localisation energies. In addition, low temperatures are therefore vital to study such defects in detail.

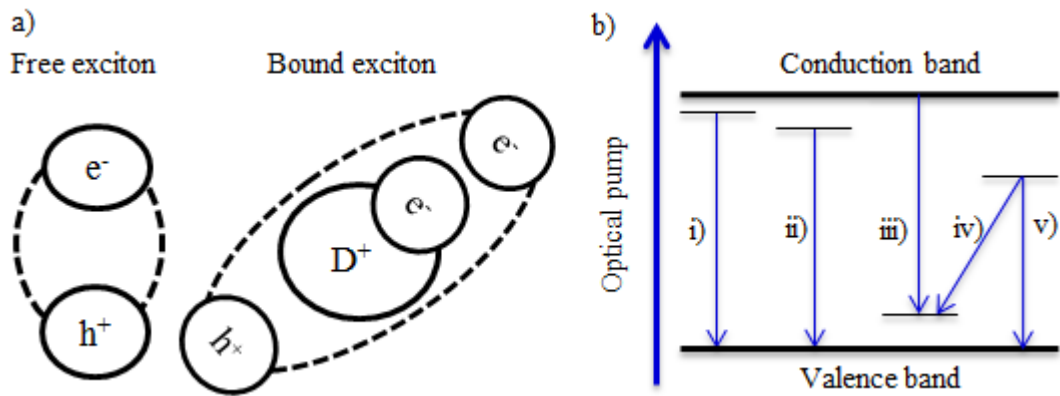


Figure 3.2: (a) Schematic of a FX and  $D^0X$ ; (b) Representation of the main transitions with PL: i) FX, ii) BX, iii) electron to acceptor, iv) donor to acceptor, v) hole to donor.

In addition to radiative transitions such as FX and BX, when the entire energy associated with the excited state energy is released as a photon, situations also occur when exciton recombination takes place whereby some of the energy can be released in non-radiative processes. This occurs when the energy of the exciton is converted into vibrational energy of the lattice called phonons, with the emission coupled to the crystal lattice vibrations, and a lower energy photon is emitted, called a Stokes process (at higher temperatures there is also a possibility for phonon absorption leading to higher energy photon emission – called an anti-Stokes process). This type of coupling is strongest in the case of phonons known as longitudinal optical (LO) phonons. A series of photons are emitted at reduced energies and appear in the spectrum at specific intervals below the main emission which are whole numbers of the phonon energy for the crystal structure. For ZnO, this energy is  $\sim 72$  meV.<sup>5</sup>

These peaks are known as LO phonon replicas. Depending on the level of coupling, described by the Huang-Rhys factor, the LO-phonon replica intensity can be quite large compared to the ZPL intensity, particularly for deep defects near the centre of the band gap.<sup>6</sup> In direct band gap semiconductors, deep centres can produce bright, broad band emissions for this reason. LO replicas are further discussed in section 3.5.

We finally note that levels near the centre of the band gap can be very efficient non-radiative centres and therefore quench the optical emission by means of multiphonon de-excitation.<sup>7</sup> This effect increases at higher temperatures, as noted above, because BX are thermally delocalised to become FX and can diffuse and encounter efficient non-radiative centres near the middle of the band gap.

### 3.4 Structure of the ZnO PL emission spectrum

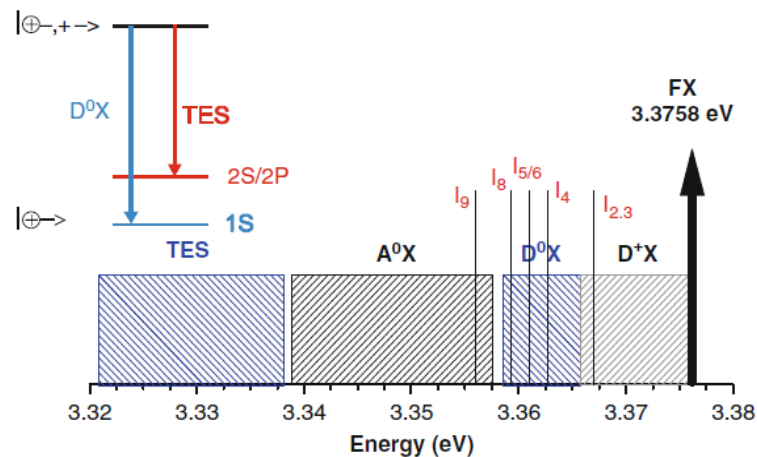


Figure 3.3: Diagram showing the main types of bound exciton in the band edge region of ZnO, reproduced from reference 1 (Note that  $I_9$  is a  $D^0X$ , not an acceptor bound exciton ( $A^0X$ )).

The BX recombinations discussed in the previous paragraph result in photon emission at energies close to the band gap in the so called band edge and near band edge region. Figure 3.3 shows the types of lines observed in this region in ZnO at

low temperatures and discussed in this and the previous sections. These lines appear near the band gap in energy as they originate from shallow defect transitions involving donor levels which are close to the conduction band or acceptor levels close to the valence band. They are clearly visible in the band edge region of the PL spectra of the ZnO samples in this work which are described in subsequent chapters.

The FX line in ZnO appears at  $\sim 3.377$  eV, the band gap minus the exciton binding energy. Two component states of the free A-exciton can be observed, namely  $A_L$  and the lower energy  $A_T$ , corresponding to the longitudinal and transverse polariton A-exciton energies respectively. The BX localisation energies are measured from the  $A_T$  energy. Moving towards lower energies, there is a series of lines arising from  $D^+X$ , and  $D^0X$ . This series of lines, labelled the I-lines, from  $I_1$  to  $I_{11}$ , centred around 3.36 eV. These lines have been extensively studied and are outlined in detail by Meyer et al. in reference 8 and chapter 7 of reference 1.

Briefly,  $I_0$  to  $I_3$  are due to  $D^+X$  and  $I_4$  to  $I_{10}$  are due to  $D^0X$  lines. Not all the lines have been conclusively identified. However of the main lines,  $I_9$  has been shown to be caused by In impurities, as well as its ionised counterpart,  $I_2$ .<sup>9,10</sup> Likewise, Al impurities are the cause of the  $I_6/I_{6a}$  and  $I_0$  lines.<sup>8,11,12</sup>  $I_8$  and  $I_1$  are related to Ga,<sup>13</sup> and  $I_4$  to H.<sup>14</sup> Some of these lines are used to measure shifts in the band edge (and therefore band gap energies) with changing isotopes in this work, particularly the  $I_9$  peak which is the most pronounced in most of the samples used here. The I-lines are very narrow as their full widths at half maximum (FWHM) are reduced due to low thermal broadening at low temperatures and their lack of translational motion at bound sites. Lattice strain can shift line positions<sup>1</sup> and also increase the FWHM (for inhomogeneous strains) so narrow lines indicate high crystal structural quality. No  $A^0X$  lines have been identified in ZnO so the next features of the spectrum as we move to lower energies are TES of the I-lines. Since this occurs when the recombination leaves the donor in an excited 2s or 2p state, the features appear in the spectrum at an energy equal to the difference between this excited state and the ground 1s state below the corresponding BX line. The other main feature of this spectral region as we move to lower energies is the BX LO replica region which shows features at intervals of 72 meV. The LO replicas of the TES peaks can also be visible. Another series of lines appearing at lower energies than the BX I-lines have also been observed in ZnO, labelled the Y-lines.<sup>15</sup> These

are not as well characterised and understood, and they are not of interest in this work.

Aside from the intense UV emission associated with these I-lines, the other main feature of the PL spectrum of ZnO at low temperatures is the green band. This is a broad emission centred in the green region of the visible spectrum around 2.4 eV. There are actually two green bands, known as unstructured and structured (SGB). There is strong evidence that the unstructured green band is related to  $V_O$ <sup>16,17</sup>, while the SGB has been shown to be caused by Cu impurities.<sup>18,19</sup> This emission is discussed in more detail in section 3.5. Spectra of both the band edge and SGB regions are presented in section 4.6.

At room temperatures, the PL spectrum of ZnO has a few key differences. The first is in the band edge region, where the BX I-lines are no longer visible (due to thermal delocalisation of BX) and instead there tends to be a broader band edge emission due to the FX recombinations, and their LO replicas, which are much more numerous in this case. The exact form of this band and its peak position can vary from sample to sample due to the varying exciton-phonon coupling in different sample morphologies.<sup>20</sup> The other main feature is a broad band emission in the visible region. This is usually the unstructured green band, although yellow-orange and red bands are also observed in ZnO at different temperatures, suspected to be due to other metal impurities or native defects.<sup>21</sup> The SGB is only seen at low temperatures.

### **3.5 The Cu-related Defect at 2.86 eV**

PL also provides the opportunity to examine the defects that cause deeper level defects near the middle of the band gap. The Cu-related emission at 2.86 eV at low temperatures in ZnO is one such emission centre and is of major interest in this work. It produces a bright, structured, wide band emission peaking in the green visible region, previously referred to as the SGB. It is made up of a ZPL at 2.86 eV and a series of LO replicas at steps of  $\sim 72$  meV showing strong electron-phonon coupling. Although the emission spectrum of ZnO had been studied for some time,

the origins of this SGB were not certain when Dingle made one of the most fundamental contributions to the discussion in 1969.<sup>18</sup> He presented strong evidence that this SGB resulted from a transition involving a single Cu impurity on a Zn site ( $\text{Cu}_{\text{Zn}}$ ) in a  $\text{Cu}^{2+}$  charge state acting as a neutral deep acceptor. The ground state of this transition is a tightly bound hole in a level slightly below the conduction band. The excited state is at a level  $\sim 450$  meV above the valence band.<sup>18,19</sup> Dingle observed that the ZPL was made up of two distinct lines, both of which behaved identically under uniaxial stress and magnetic fields, and which had an intensity ratio which matched the isotopic distribution of the  $^{63}\text{Cu}$  and  $^{65}\text{Cu}$  isotopes in ZnO. He also noted that one of the states involved had an anisotropic  $g$ -factor closely matched to the  $g$ -factor of one of the states in a  $\text{Cu}^{2+}$  absorption transition reported earlier. This emission also only appears when Cu impurity is present. Dingle concluded that Cu was the cause of the SGB.

Despite Dingle's work, and extensive studies concerning the green band,<sup>22-24</sup> some disagreement persisted regarding its nature,<sup>21,25</sup> and it was not until much more recently that Cu was unambiguously confirmed by direct measurement as being the cause of the SGB emission. This experiment was carried out in our group by Byrne *et al.*<sup>19</sup> ZnO single crystals were specifically doped using  $^{63}\text{Cu}$  and  $^{65}\text{Cu}$  isotopes. The intensities of the respective parts of the ZPL doublet were observed to change directly in proportion with the isotopic distribution of the Cu in a particular sample. These data, in addition to Dingle's data on the  $g$ -factor and stress measurements, were consistent with the assignment of this defect as a single substitutional  $\text{Cu}^{2+}$  atom on a Zn site. However, Byrne *et al.* also noted that a complex of  $\text{Cu}_{\text{Zn}}$  with other defects along the  $c$ -axis would also reproduce this data, for example  $\text{Cu}_{\text{Zn}}\text{-V}_{\text{O}}$  or  $\text{Cu}_{\text{Zn}}\text{-V}_{\text{Zn}}$  complexes, and therefore the exact defect structure was not fully determined. It has been suggested that Cu is present in ZnO as an unintentional dopant in different charge states, lattice locations and in different complexes including with native defects, the last of which is under investigation in this work, involving the use of isotopically enriched ZnO nanorods to investigate whether this defect is a complex involving any of these other native defects.<sup>26-28</sup> It is also reported that annealing at  $900^\circ\text{C}$  may activate the Cu defect responsible for this green emission by changing the charge state from  $\text{Cu}^{1+}$  to  $\text{Cu}^{2+}$ .<sup>29</sup> Byrne *et al.* observed this in ZnO nanorods and suggest this is because much of the Cu in the

nanorods following VPT growth is in the  $\text{Cu}^+$  charge state because of Zn vapour reducing the  $\text{Cu}^{2+}$  to  $\text{Cu}^+$  during growth. Thus annealing at  $900^\circ\text{C}$  for ten minutes has been used in some samples in this work to increase the intensity of SGB in samples where it was very weak relative to the band edge emission, or indeed to ‘activate’ it in cases where it was not observed in the samples as grown.

We note that the unstructured green band was also observed at low temperatures in some samples, but it was clear that the two types of green band emission have different origins. The unstructured band has been attributed to  $\text{Zn}_i$  and  $\text{V}_{\text{Zn}}$  in the past;<sup>30,31</sup> however there is more recent strong evidence that  $\text{V}_\text{O}$  is the cause of this emission.<sup>16,17</sup>

As mentioned in this chapter, the BX and deep defect emission processes can couple to vibrations in the crystal lattice or phonons which results in LO replicas at lower energies than the parent emission. The energy difference depends on the vibration involved with 72 meV being characteristic of the ZnO lattice vibration. This coupling can be described using a configuration coordinate diagram, as in figure 3.4.<sup>6</sup> For simplicity we consider only one mode of vibration and treat the vibrating mode as a harmonic oscillator. Only one coordinate is needed to describe the system in this case, labelled  $Q$ . This configuration coordinate  $Q$  may be thought of in this case as representing the distance between the dopant atom and the nearest adjacent atom, which may vary depending on the electronic and vibrational states the atoms are in, resulting in different levels of overlap in their wavefunctions. Two electronic energy levels are shown, a ground state and excited state, each with a number of vibrational modes. Transitions may occur from the lowest phonon level of the ground state, at  $Q_{og}$  to lowest phonon level of the excited state, at  $Q_{oe}$ , or to the various phonon levels in the excited state. Instantaneous changes in the vibrational modes with electronic transitions are possible because the electronic transition occurs instantaneously compared to the slower motion of the atomic particles (Frank-Condon principle). In the figure for example the highest probability transition is to the third phonon state, with the largest wavefunction overlap. The electron then relaxes to the  $Q_{oe}$  state by thermalisation and recombines back to the ground electronic state. However, because of the difference in  $Q$  value, and therefore wavefunction overlap, the recombination occurs with a higher phonon level in the ground state (shown by solid lines in the figure). The emission is therefore at a

lower energy than the absorption. Indeed, when the oscillation frequencies of the two states are equal, the entire emission spectrum occurs as a mirror image of the absorption spectrum around the ZPL. The difference between the peaks of the absorption and emission spectra is called Stokes shift.

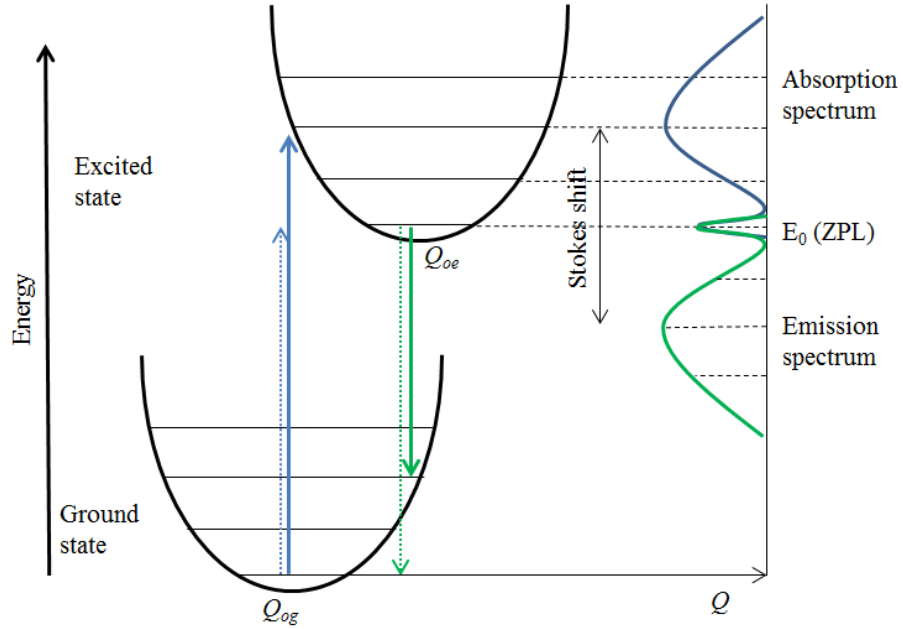


Figure 3.4: Configurational coordinate diagram describing the ground and excited states of an impurity and the absorption and emission spectra due electron-phonon coupling.

There are a number of assumptions made in this model. The two electronic states are assumed to be modelled by a harmonic oscillator, it is assumed that at low temperatures only the lowest phonon mode in the ground state is excited, and it is assumed that both electronic states interact with the lattice in the same way. It is clear therefore that this picture is simply an approximation and the actual behaviour is much more complicated.

The wavefunction overlap between the zero phonon levels in the ground and excited states,  $Q_{og}$  and  $Q_{oe}$ , is quite small and therefore less probable (shown as dotted lines in the figure). However, the ZPL emission is made up of the sum of the ZPLs from all the different vibrational modes which each contribute to the phonon sideband in the PL spectrum. This occurs at the point marked  $E_0$ . The level of

electron-phonon coupling is indicated by the Huang-Rhys parameter,  $S$ , which is related to the oscillation frequency  $\omega$ , the ion effective mass  $M$  and the displacement of the upper and lower state parabola by the formula<sup>6</sup>

$$S = \frac{1}{2} \frac{M\omega^2}{\hbar\omega} (Q_{0e} - Q_{0g})^2 \quad \text{Eqn. 3.1}$$

When  $S$  is zero or small, almost all the emitted energy emerges in the ZPL, with little observed in phonon replica emission. When  $S$  is larger, replica peaks are observed due to the coupling between defect electronic levels and lattice vibrations, as in the band edge region of ZnO. When  $S$  is larger still, this sideband is broadened resulting in a single, broad band, intense, structured emission, as in the Cu-related SGB in ZnO, with characteristic LO replicas. Figure 3.5 gives an illustration of how this band evolves as  $S$  increases.<sup>6</sup> Note that this image refers to the absorption spectrum, but serves as a good illustration of how the emission spectrum behaves, but at energies below the ZPL rather than above in the absorption spectrum. The  $S$  parameter for the Cu-related SGB in ZnO has been reported to be 6.5.<sup>29</sup>

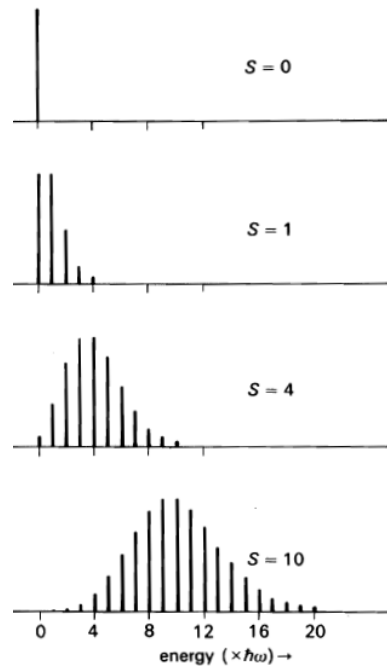


*Figure 3.5: Illustration of how the phonon sideband shape evolves with increasing  $S$  parameter. Note this image refers to the absorption spectrum, but serves as a good illustration of how the emission spectrum behaves but at energies below the ZPL. Image reproduced from reference 6.*

### 3.6 The Isotope Effect

Isotopic enrichment is a well-known and very useful technique in the analysis of defects in semiconductor materials including ZnO, particularly in conjunction with optical methods like PL, and has been studied extensively.<sup>32–34</sup> The growth of isotopically enriched ZnO nanorods in this work presented an opportunity to use these samples in the study of defects and impurities, specifically the Cu-related emission at 2.86 eV and its associated phonon sideband. The high optical quality of the materials produced ultimately made this possible. A general description of the origins of the isotope effect is given here and more discussion is presented alongside the relevant results in later chapters. Briefly, the technique involves enriching the crystal with either specific isotopes of an atom involved in, or suspected of involvement in, a defect or enriching the surrounding native crystal lattice with specific isotopes. The vibrational states in the crystal couple to electronic states, including those at defect sites, to produce so-called vibronic levels via electron-phonon coupling, as discussed above. Transitions between different vibronic levels, either at a defect or the surrounding lattice produce the ZPL and phonon side-bands involving multiple phonon replicas, as seen for the Cu-related SGB in ZnO. Changes in the energies of exciton recombinations may arise due to changes in both the isotopic make up of a defect or a surrounding lattice, both of which affect the vibrational nature of the vibronic levels because of the difference in mass of different isotopes.<sup>6,35</sup>

The isotope effect is fundamentally due to the dependence of the phonon vibrational frequencies on atomic masses. If we consider a situation where a foreign impurity atom vibrates in a particular mode with vibrational frequency  $\omega$ , has a mass  $m$ , and the vibration is characterised by a spring constant of  $k$ , then the frequency is given by

$$\omega = \sqrt{\frac{k}{m}} \quad \text{Eqn. 3.2}$$

It can therefore be clearly seen that, assuming the spring constant (due to the chemical nature of the binding and the interatomic forces produced by this binding) does not change, a change in mass, to  $m+\Delta m$  for example, will result in a change in

the vibrational frequency. For an increase in mass for example, the phonon frequency will reduce. When the upper and lower states have different spring constant values this ultimately leads to a change in the energy of the transitions, shown in the configurational coordinate diagram in figure 3.4, as the energy of the coupled phonon modes changes. This is a simple case with many assumptions, as described previously. A defect will couple to many vibrational modes in a real crystal. The magnitude of the isotope shift is ultimately dependent on both the difference in spring constant between the upper and lower levels and  $\Delta m$ . The influence of the change in mass on the vibrational frequency produces the energy change in the emission spectrum. The variation of phonon frequencies with average mass and fluctuations about the average both contribute to the effect.<sup>22,35,36</sup>

As demonstrated by the work of Byrne *et al.*<sup>19</sup> on the Cu-related 2.86 eV ZPL mentioned above, isotopic substitution is a technique which can provide confirmation of the involvement of a particular atom in a defect complex. In this case the two isotopes of Cu appeared as two distinct lines in the ZPL. In addition to isotopic shifts in this manner (where the impurity atom is present in multiple isotopes, or enriched with a specific isotope) isotopes shifts have been observed in ZnO when the isotopic content of the lattice is enriched. This can occur with enrichment of either or both of the Zn or O atoms in the lattice. Shifts in the band gap have been measured following enrichment of the lattice in this way.<sup>37,38</sup> The corresponding shifts in the FX and BX recombination energies have also been measured using PL and reflectance spectroscopy.<sup>39,40</sup> These reports have focused on enrichment of single crystals of ZnO. In this work, the development of novel methods of growing isotopically enriched ZnO in nanorod morphologies in a quick and efficient manner presents an opportunity to use isotopically enriched nanocrystals to carry out an optical study of defects in isotopically enriched crystals. Specifically, a study of Cu-related defect emission with its ZPL at 2.86 eV was carried out. The objective here was to determine if native defects were involved in this defect, following the unambiguous confirmation of the Cu involvement but with a possible complex with native defects not completely ruled out. By enriching the nanorods as described in chapter 2, we can observe shifts in the energies of the exciton recombinations in both the band edge and SGB ZPL. By changing the masses of the Zn or O atoms in the lattice, the atomic surroundings of defects in both

regions would be altered in same way, and we can expect that the shifts observed would be the same if no native defects complex with the  $\text{Cu}_{\text{Zn}}$ . However, if a native defect is involved in a complex with the  $\text{Cu}_{\text{Zn}}$  defect, for example an additional interstitial or vacancy, then its vibrational surroundings would be changed in an additional way to the change induced by the lattice enrichment. Due to this, a different energy shift may be observed for the defect SGB ZPL compared to that of the band edge emissions.

### 3.7 Phonon modes

Phonon modes can occur in multiple types. The phonon modes which are examined using Raman spectroscopy, and observed as replicas in PL, in this work are described in this section. A more detailed discussion regarding phonon modes in ZnO is presented in the literature<sup>1,41</sup>. As stated above, the LO replicas appearing in the PL spectrum are the longitudinal optical type. Optical phonons are vibrational modes which oscillate in an out-of-phase motion with adjacent atoms moving in different directions. They can occur in either the longitudinal (LO) or transverse (TO) direction relative to the direction of propagation. Optical phonons can interact with incident light via infrared absorption or Raman scattering. The other type of phonons is the acoustic modes labelled LA for the longitudinal mode and TA for the optical mode. Acoustic phonon modes have a coherent oscillation with adjacent atoms moving in the same direction.<sup>3</sup>

The primary optical phonon modes of interest in this work are shown in figure 3.6. They are labelled as the  $E_2^{\text{low}}$  and  $E_2^{\text{high}}$  modes. The  $E_2^{\text{low}}$  mode is dominated by the Zn atom motion, and the  $E_2^{\text{high}}$  mode is dominated by the O atom motion. The ratio of their displacement eigenvector lengths,  $e_{\text{Zn}}/e_{\text{O}}$ , have been reported as -2.4 and 0.417 respectively.<sup>42</sup> In each case, both the Zn and O atoms oscillate in opposite directions perpendicular to the  $c$ -axis. Both modes are non-polar as the compensating displacements of each sub-lattice (Zn or O) leads no overall dipole moment. That is, each Zn or O atom moves in the opposite direction to the neighbouring one at any given time, producing no net electric field, and therefore no

significant coupling to excitons. Since there is no difference between the longitudinal and transverse modes in these cases, they are not referred to as LO or TO. For the backscattered Raman geometry used in this work as described in section 2.4.4, the  $E_2^{\text{low}}$  mode appears in the Raman spectrum at  $\sim 100 \text{ cm}^{-1}$  and the  $E_2^{\text{high}}$  mode appears at  $\sim 439 \text{ cm}^{-1}$ . Raman measurements of phonons in isotopically enriched single crystal ZnO have been carried out previously, particularly on the  $E_2^{\text{high}}$  mode, clearly showing the changes in phonon energies and line widths with changing Zn or O isotopes.<sup>43–45</sup> Similar shifts are also seen in similar materials such as GaN.<sup>46</sup> It is therefore useful to compare Raman measurements made with enriched ZnO nanorods with these previous data, as they can provide a good way confirming the isotopic enrichment of the samples, along with comparisons of the BX line energies using PL.

The LO phonon replicas observed in both the band edge and SGB emission in ZnO are, however, not the  $E_2^{\text{high}}$  or  $E_2^{\text{low}}$  modes. These replicas are due to the  $E_1$  (LO) and  $A_1$  (LO) phonon modes, which have energies of  $590 \text{ cm}^{-1}$  and  $574 \text{ cm}^{-1}$  respectively (they each have TO counterparts at lower energies).<sup>1</sup> These two modes are polar as the Zn and O sub-lattices essentially move in opposite directions at any given time. This leads to significant electric fields which strongly couple to excitons in the crystal and cause the LO replicas in the PL spectrum. Note that the energies of these polar modes are 73.2 meV for  $E_1$  (LO) and 71.2 meV for  $A_1$  (LO) which match the PL LO replica spacing closely. Since these modes are much weaker in intensity and do not appear in the same Raman geometry as the  $E_2$  modes, and since previous studies on the  $E_2^{\text{high}}$  mode in isotopically enriched ZnO are available, the  $E_1$  and  $A_1$  modes are not considered further. Both modes are also shown in figure 3.6.

We also note that the measurement of Raman mode shifts provides a very reliable measurement of sample isotopic enrichment, since the Raman phonon mode energies are much less sensitive to any lattice strain than are PL peaks. For example, Wagner states figures for energy shifts of 3.37 meV/GPa for the  $I_9$  line and just 0.35 meV/GPa ( $< 3 \text{ cm}^{-1}/\text{GPa}$ ) for the  $E_2^{\text{high}}$  phonon energy.<sup>41</sup>

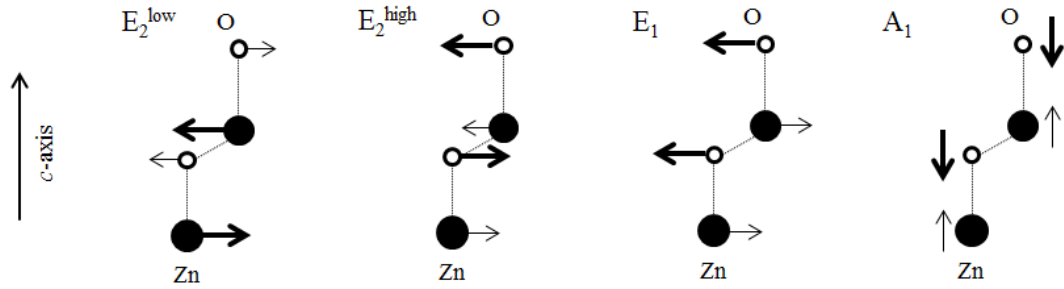


Figure 3.6:  $E_2^{low}$ ,  $E_2^{high}$ ,  $E_1$  and  $A_1$  phonon modes in wurtzite ZnO. Image adapted from reference 1.

### 3.8 Conclusions

The background principles of low temperature PL, emission from semiconductors and defects in semiconductors, the isotope effect and the phonon modes of interest for Raman studies have been introduced in this chapter. The main emissions typically observed in the low temperature PL spectrum of ZnO were described, particularly the band edge region and the Cu-related SGB, in addition to the processes underlying such emissions. This background information will be used in subsequent chapters alongside the presentation of results from studies on Zn- and O- enriched ZnO nanorods, and a detailed optical study of the 2.86 eV Cu-related defects using those materials.

### 3.9 References

- <sup>1</sup> C.F. Klingshirn, B.K. Meyer, A. Waag, A. Hoffmann, and J. Geurts, *ZnO: From Fundamental Properties Towards Novel Applications* (Springer-Verlag, Berlin, Heidelberg, 2010).
- <sup>2</sup> A. Mang, K. Reimann, and S. Rübenacke, *Solid State Commun.* **94**, 251 (1995).
- <sup>3</sup> C. Klingshirn, *Semiconductor Optics*, 2nd ed. (Springer-Verlag, Berlin, Heidelberg, 2005).

- <sup>4</sup> P.Y. Yu and M. Cardona, *Fundamentals of Semiconductors*, 3rd ed. (Springer-Verlag, Berlin, Heidelberg, 2001).
- <sup>5</sup> L. Wang and N.C. Giles, *J. Appl. Phys.* **94**, 973 (2003).
- <sup>6</sup> B. Henderson and G.F. Imbusch, *Optical Spectroscopy of Inorganic Solids* (Clarendon Press, Oxford, 1989).
- <sup>7</sup> E. Rashba and M. Sturge, *Excitons* (North-Holland Publishing Company, Amsterdam, 1982).
- <sup>8</sup> B.K. Meyer, H. Alves, D.M. Hofmann, W. Kriegseis, D. Forster, F. Bertram, J. Christen, A. Hoffmann, M. Straßburg, M. Dworzak, U. Haboek, and A. V. Rodina, *Phys. Status Solidi* **241**, 231 (2004).
- <sup>9</sup> S. Müller, D. Stichtenoth, M. Uhrmacher, H. Hofsäss, C. Ronning, and J. Röder, *Appl. Phys. Lett.* **90**, 012107 (2007).
- <sup>10</sup> J. Cullen, D. Byrne, K. Johnston, E. McGlynn, and M.O. Henry, *Appl. Phys. Lett.* **102**, 192110 (2013).
- <sup>11</sup> M. Schilling, R. Helbig, and G. Pensl, *J. Lumin.* **33**, 201 (1985).
- <sup>12</sup> B.K. Meyer, J. Sann, S. Lautenschläger, M.R. Wagner, and A. Hoffmann, *Phys. Rev. B* **76**, 184120 (2007).
- <sup>13</sup> K. Johnston, M.O. Henry, D. McCabe, E. McGlynn, M. Dietrich, E. Alves, and M. Xia, *Phys. Rev. B* **73**, 165212 (2006).
- <sup>14</sup> E. Lavrov, F. Herklotz, and J. Weber, *Phys. Rev. B* **79**, 165210 (2009).
- <sup>15</sup> M.R. Wagner, G. Callsen, J.S. Reparaz, J.-H. Schulze, R. Kirste, M. Cobet, I. a. Ostapenko, S. Rodt, C. Nenstiel, M. Kaiser, A. Hoffmann, a. V. Rodina, M.R. Phillips, S. Lautenschläger, S. Eisermann, and B.K. Meyer, *Phys. Rev. B* **84**, 035313 (2011).
- <sup>16</sup> F.H. Leiter, H.R. Alves, A. Hofstaetter, D.M. Hofmann, and B.K. Meyer, *Phys. Status Solidi* **226**, R4 (2001).
- <sup>17</sup> F. Leiter, H. Alves, D. Pfisterer, N.G. Romanov, D.M. Hofmann, and B.K. Meyer,

Phys. B Condens. Matter **340-342**, 201 (2003).

<sup>18</sup> R. Dingle, Phys. Rev. Lett. **23**, 579 (1969).

<sup>19</sup> D. Byrne, F. Herklotz, M.O. Henry, and E. McGlynn, J. Physics. Condens. Matter **24**, 215802 (2012).

<sup>20</sup> T. Voss, C. Bekeny, L. Wischmeier, H. Gafsi, S. Börner, W. Schade, a. C. Mofor, A. Bakin, and A. Waag, Appl. Phys. Lett. **89**, 182107 (2006).

<sup>21</sup> H. Morkoç and U. Özgür, *Zinc Oxide Fundamentals, Materials and Device Technology* (Wiley-VCH, Weinheim, 2009).

<sup>22</sup> V. Heine and C. Henry, Phys. Rev. B **11**, 3795 (1975).

<sup>23</sup> J.A. Van Vechten, Phys. Rev. B **13**, 946 (1976).

<sup>24</sup> P. Dahan, V. Fleurov, P. Thurian, R. Heitz, A. Hoffmann, and I. Broser, J. Phys. Condens. Matter **10**, 2007 (1998).

<sup>25</sup> U. Özgür, Y.I. Alivov, C. Liu, a. Teke, M. a. Reshchikov, S. Doğan, V. Avrutin, S.-J. Cho, and H. Morkoç, J. Appl. Phys. **98**, 041301 (2005).

<sup>26</sup> F. Herklotz, E.V. Lavrov, and J. Weber, Phys. B Condens. Matter **404**, 4807 (2009).

<sup>27</sup> H. Qiu, F. Gallino, C. Di Valentin, and Y. Wang, Phys. Rev. Lett. **106**, 066401 (2011).

<sup>28</sup> U. Wahl, E. Rita, J.G. Correia, T. Agne, E. Alves, and J.C. Soares, Superlattices Microstruct. **39**, 229 (2006).

<sup>29</sup> N.Y. Garces, L. Wang, L. Bai, N.C. Giles, L.E. Halliburton, and G. Cantwell, Appl. Phys. Lett. **81**, 622 (2002).

<sup>30</sup> N.O. Korsunskaya, L.V. Borkovskaya, B.M. Bulakh, L.Y. Khomenkova, V.I. Kushnirenko, and I.V. Markevich, J. Lumin. **102-103**, 733 (2003).

<sup>31</sup> X. Yang, G. Du, X. Wang, J. Wang, B. Liu, Y. Zhang, D. Liu, D. Liu, H.C. Ong, and S. Yang, J. Cryst. Growth **252**, 275 (2003).

- <sup>32</sup> M. Cardona, *Phys. Status Solidi* **220**, 5 (2000).
- <sup>33</sup> V.G. Plekhanov, *Applications of the Isotope Effect in Solids* (Springer-Verlag, Berlin, Heidelberg, 2004).
- <sup>34</sup> V. G. Plekhanov, *Isotopes in Condensed Matter* (Springer Berlin Heidelberg, Berlin, Heidelberg, 2013).
- <sup>35</sup> E. McGlynn, *A Photoluminescence Study of Cadmium and Aluminium-Related Defects in Silicon*, Dublin City University, 1996.
- <sup>36</sup> V.G. Plekhanov, *J. Nucl. Sci. Technol.* **43**, 375 (2006).
- <sup>37</sup> F.I. Kreingol'd and B.S. Kulinkin, *Fiz. Tverd. Tela* **28**, 3164 (1986).
- <sup>38</sup> F.I. Kreingol'd, *Fiz. Tverd. Tela* **20**, 3138 (1978).
- <sup>39</sup> F.J. Manjón, M. Mollar, M.A. Hernández-Fenollosa, B. Marí, R. Lauck, and M. Cardona, *Solid State Commun.* **128**, 35 (2003).
- <sup>40</sup> S. Tsoi, X. Lu, A.K. Ramdas, H. Alawadhi, M. Grimsditch, M. Cardona, and R. Lauck, *Phys. Rev. B* **74**, 165203 (2006).
- <sup>41</sup> M.R. Wagner, *Fundamental Properties of Excitons and Phonons in ZnO: A Spectroscopic Study of the Dynamics, Polarity, and Effects of External Fields*, Technical University of Berlin, 2010.
- <sup>42</sup> J. Serrano, a. Romero, F. Manjón, R. Lauck, M. Cardona, and a. Rubio, *Phys. Rev. B* **69**, 094306 (2004).
- <sup>43</sup> J. Serrano, F. Manjón, A. Romero, F. Widulle, R. Lauck, and M. Cardona, *Phys. Rev. Lett.* **90**, 055510 (2003).
- <sup>44</sup> J. Serrano, F. Widulle, A.H. Romero, A. Rubio, R. Lauck, and M. Cardona, *Phys. Status Solidi* **235**, 260 (2003).
- <sup>45</sup> M.A. Gluba, N.H. Nickel, and N. Karpensky, *Phys. Rev. B* **88**, 245201 (2013).
- <sup>46</sup> J.M. Zhang, T. Ruf, M. Cardona, O. Ambacher, M. Stutzmann, J.-M. Wagner, and F. Bechstedt, *Phys. Rev. B* **56**, 14399 (1997).

# Chapter 4: Zn Isotope-enriched ZnO Nanorods

## 4.1 Introduction

This chapter presents the results of the growth and characterisation of ZnO nanorods enriched with Zn isotopes as described in section 2.2. The results of characterisation of the morphology, crystal quality, isotopic enrichment and optical quality of the samples using SEM, XRD, SIMS, Raman spectroscopy and low temperature PL are presented as well as some reflectance data. The eight Zn isotopically enriched samples of ZnO nanorods produced for this study are shown in table 4.1. Figure 4.1 displays a graphical representation of the Zn isotopic content of this set of samples. The mixed samples' labels refer to the nominal ratios of the isotopes by mass as the source powder was weighed during growth.

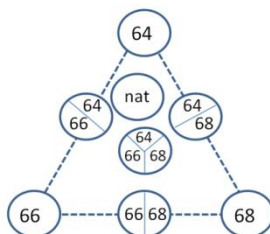


Figure 4.1: Graphical representation of the Zn isotopic content of the eight Zn-enriched samples.

Label	Sample description
$^{64}\text{ZnO}$	$^{64}\text{ZnO}$ sample
$^{66}\text{ZnO}$	$^{66}\text{ZnO}$ sample
$^{68}\text{ZnO}$	$^{68}\text{ZnO}$ sample
$^{64/66}\text{ZnO}$	$1/2$ $^{64}\text{ZnO}$ and $1/2$ $^{66}\text{ZnO}$
$^{66/68}\text{ZnO}$	$1/2$ $^{66}\text{ZnO}$ and $1/2$ $^{68}\text{ZnO}$
$^{64/68}\text{ZnO}$	$1/2$ $^{64}\text{ZnO}$ and $1/2$ $^{68}\text{ZnO}$
$^{64/66/68}\text{ZnO}$	$1/3$ $^{64}\text{ZnO}$ , $1/3$ $^{66}\text{ZnO}$ and $1/3$ $^{68}\text{ZnO}$
$^{\text{nat}}\text{ZnO}$	Natural Zn isotopic distribution, avg. = $^{65.4}\text{ZnO}$

Table 4.1: Set of Zn-enriched ZnO nanorods.

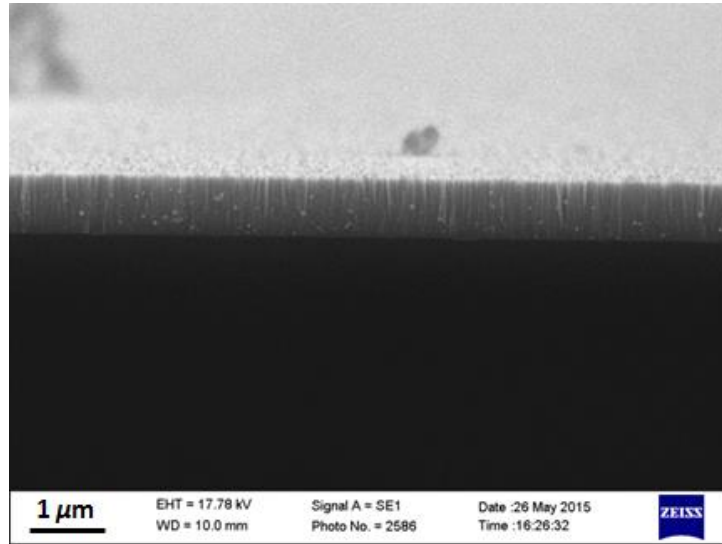


Figure 4.2: Typical buffer layer of CBD deposited nanorods.

As described in section 2.2, these samples were grown using a modified VS CTR-VPT technique on pre-deposited unenriched  $^{\text{nat}}\text{ZnO}$  CBD buffer layers, based on the three-step process previously developed in our group.<sup>1</sup> All of the samples in this set were grown using the NaOH-based chemical bath as proposed by Peterson *et al.*<sup>2</sup> The CBD buffer layer consists of a uniform film of *c*-axis aligned ZnO nanorods of a few hundred nanometres in length on top of the seed layer as proposed by Greene *et al.*<sup>3</sup> Figure 4.2 shows a typical NaOH-method CBD layer. The CBD layer provides energetically favourable sites for subsequent nucleation of the VPT-

grown *c*-axis aligned and isotopically enriched nanorods in the next step as ZnO will not nucleate on unseeded Si substrates. The chemical origins of the seed layer have been described by Byrne *et al.* as well as the three-step growth process in general.<sup>1</sup> This CBD bath was used most often in this work because of the lack of precipitates produced by the process.

The VPT step following CBD deposition involves the use of carbon to reduce the ZnO to metal vapour and carbon monoxide according to equation 4.1.



The reaction then proceeds as a VS process when the Zn vapour condenses and is re-oxidised at the energetically favourable sites provided by the CBD buffer layer. ZnO grown on non-epitaxially matched substrates is typically not aligned, however since the CBD layer is *c*-axis aligned, the VPT grown nanorods are also aligned in such a way. The reaction shown in equation 4.1 dominates at temperatures above ~700°C. Below these temperatures a similar reaction producing mainly CO<sub>2</sub> dominates. The CTR produces Zn vapour at temperatures much lower than those at which significant direct sublimation of ZnO occurs, as discussed in chapter 1. A key aspect to note concerning the CTR reaction in this VPT step is that the oxygen taking part in re-oxidation of the Zn vapour at the CBD nucleation sites is residual O<sub>2</sub> in the furnace quartz tube from atmosphere. Most of this O<sub>2</sub> is removed by the 5-10 minutes Ar flush at the start of the VPT step but a sufficient amount remains for this process. In chapter 5, the growth of O-isotopically enriched ZnO nanorods requires the development of a new growth method involving the removal of this residual O<sub>2</sub>. Note also that, looking at this reaction, replacement of the ZnO source powder with Zn-isotopically enriched source powders should result in correspondingly enriched nanorods.

The first tests required in modifying VPT growth step for such Zn-enriched nanorods was to determine if the VPT process in our system could be carried out using much smaller amounts of source powders, i.e. 10 mg each of ZnO and graphite, as opposed to the usual 60 mg of each used in this process in our group previously. This was a necessity simply because limited amount of the <sup>64</sup>ZnO, <sup>66</sup>ZnO and <sup>68</sup>ZnO powders were available, although it also has the obvious advantage of producing the desired samples at lower cost. Figure 4.3 shows <sup>nat</sup>ZnO nanorods

grown using (a) 60 mg and (b) 10 mg of each powder. Growth was successfully carried out using the smaller amount. This was perhaps not unexpected as significant amounts of the source powders are typically left in the boat with a ‘crust’ present at the end of the process. This is thought to be due to re-deposition of ZnO on the powder mixture forming a layer with no carbon present and limiting the reaction. Following this, a number of tests, using the reduced 10 mg of each powder, were carried out at slightly different growth temperature ranging from 850-950°C. Nanorods were observed in these cases, and a temperature of 925°C was subsequently chosen at which to carry out the isotopically enriched growths. Finally, it is worth noting that there is a temperature overshoot in the furnace of about 100°C above the set point when heating with the temperature then falling to about 50°C above the set point over about 10-15 minutes.

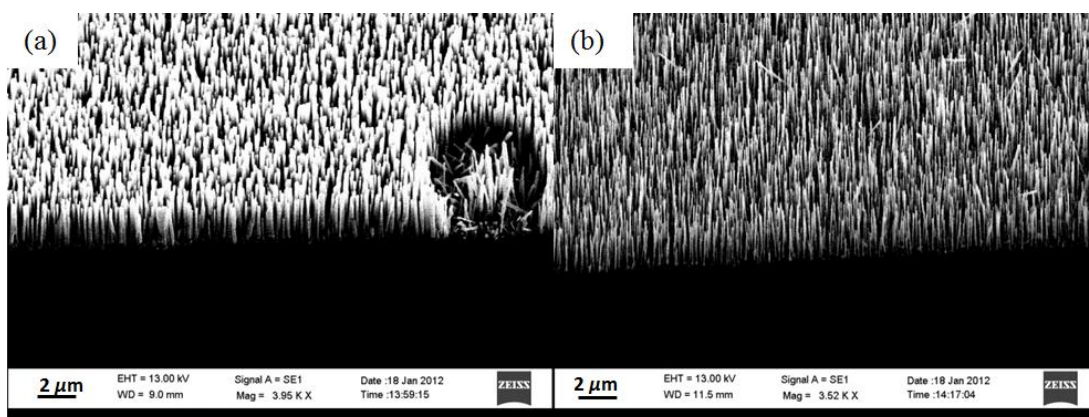


Figure 4.3: VPT-grown ZnO nanorods with (a) 60 mg and (b) 10 mg of each source powder at 900°C.

## 4.2 Morphology - SEM

The growth procedure outlined in chapter 2 and section 4.1 produced ZnO nanorods on the Si substrates. The morphology was examined using SEM. The Si substrates and buffer layers have been covered with a dense array of nanorods in all of the samples in the set. The vertical nanorods are well aligned along the *c*-axis due to the preferential growth in this direction encouraged by the seed and buffer layer textures. Coverage of nanorods on the substrates is generally excellent, with good

growth occurring over the whole substrate, except for the edges in some cases where the sample can be slightly over the edges of the alumina boat and therefore blocked from having nanorods deposited as these areas were not exposed to Zn vapour. The following figures provide examples of the typical morphology seen in the samples. They are imaged from above, at 30° to the vertical and at 90° to the vertical producing cross-sectional images.

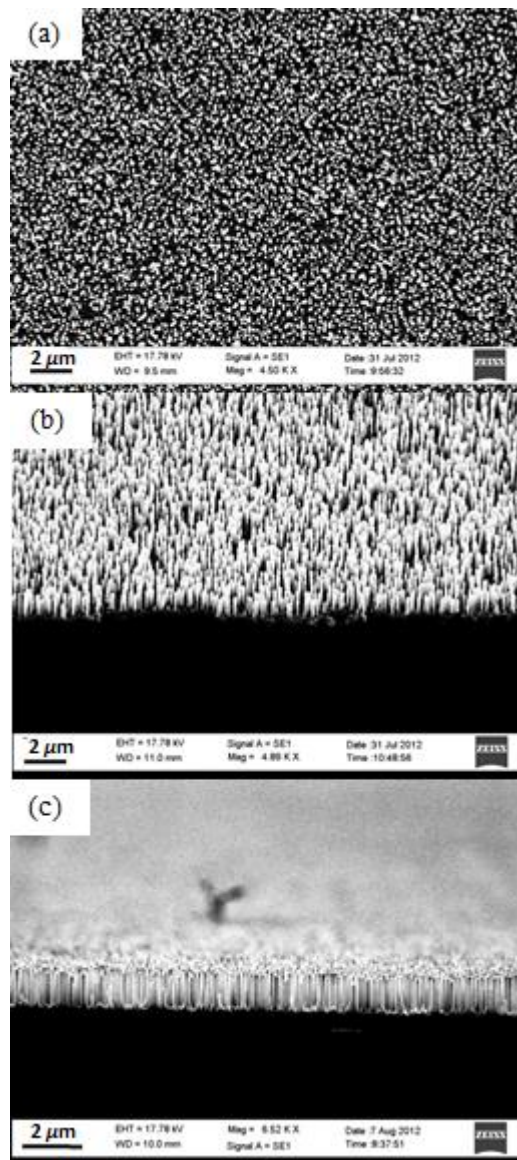


Figure 4.4: SEM images showing typical morphology of the ZnO nanorods: (a) plan view, (b) 30° to the vertical and (c) 90° to the vertical. Images are from the  $^{64}\text{ZnO}$  sample.

As shown in figure 4.4(a), the top of the nanorods are clearly observed. Viewing from an angle of 30° to the vertical, figure 4.4(b) displays the nanorods clearly along a freshly cleaved edge. The nanorods are shown in the most detail in figure 4.4(c). The cross section is shown, again along a freshly cleaved edge through the centre of the sample. The nanorods are approximately 1-2 μm in height, although the variation in a single sample is much smaller than this range. Coverage of the substrate is widespread and dense, and the rods are very well aligned vertically, along the *c*-axis. These images are from the <sup>64</sup>ZnO sample but similar morphology is observed in all other samples. Previous studies carried out in our group investigated the relationship between the nanorod height and diameter.<sup>4</sup> Nanorods of length 1-2 μm typically have diameters of ~100 nm, with shorter nanorods having larger diameters than longer ones. Based on simple observation of the SEM images in this section, the samples in this work appear to fit these typical dimensions.

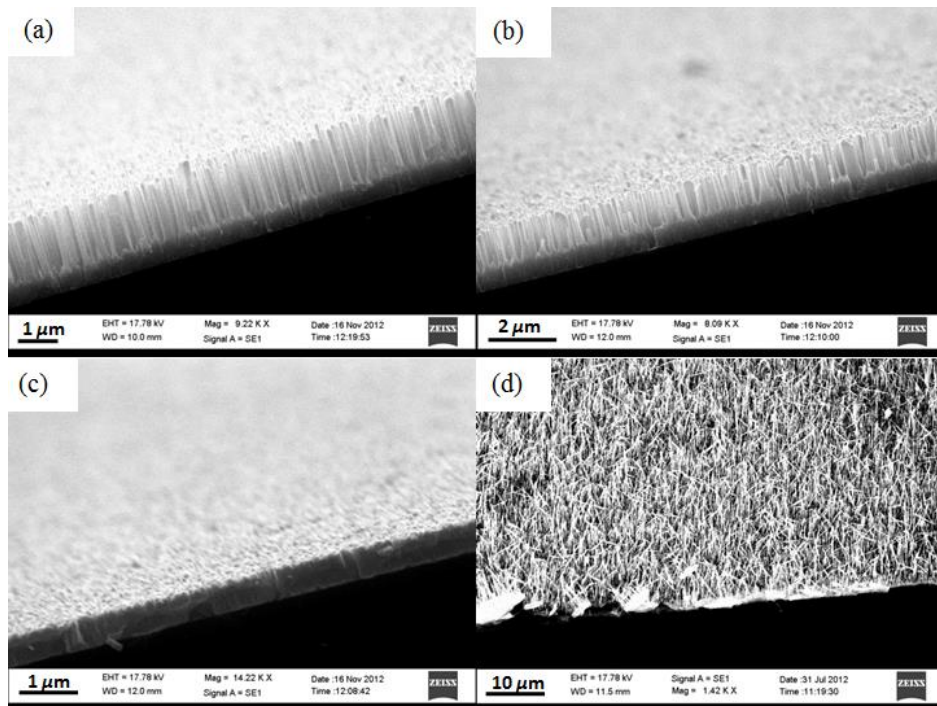


Figure 4.5: (a) 90° angle of <sup>66/68</sup>ZnO nanorods with CBD buffer layer visible; (b) <sup>64/66</sup>ZnO nanorods with CBD buffer layer visible at 90°; (c) CBD buffer layer at 90° in <sup>64/66</sup>ZnO; and (d) 30° view of longer nanorods on part of <sup>66</sup>ZnO which have lost their alignment and become entangled;

Figure 4.5 shows examples of nanorods with isotopic distributions labelled according to table 4.1 as  $^{66}\text{ZnO}$ ,  $^{64/66}\text{ZnO}$  and  $^{66/68}\text{ZnO}$ . The CBD buffer layer is clearly visible in figures 4.5(a) and 4.5(b) with VPT grown nanorods growing from the nucleation sites provided by the buffer layer nanorods. The vertical  $c$ -axis alignment is clearly observed. Figure 4.5(c) shows the CBD buffer layer on its own. This image was taken on a part of sample which was over the side of the alumina boat during growth, thereby preventing VPT phase growth from occurring at this location. Figure 4.5(d) is taken from a part of the  $^{66}\text{ZnO}$  sample. In this case the nanorods are much longer than usual, on the order of a few tens of  $\mu\text{m}$ , and they appear to have lost their alignment in the upper parts of the nanorods after falling over on each other and have become entangled. At stages of this work, it has been noted that sometimes this type of morphology is observed. It is suggested that this could be related to the Ar flush time at the start of the VPT step, as it was noticed that this occurred a number of times when a slightly shorter flush time was used, specifically during the growth of O-enriched nanorods in DCU discussed further in chapter 5. The shorter Ar flush leads to a larger residual  $\text{O}_2$  concentration and therefore a slightly longer nanorod morphology.

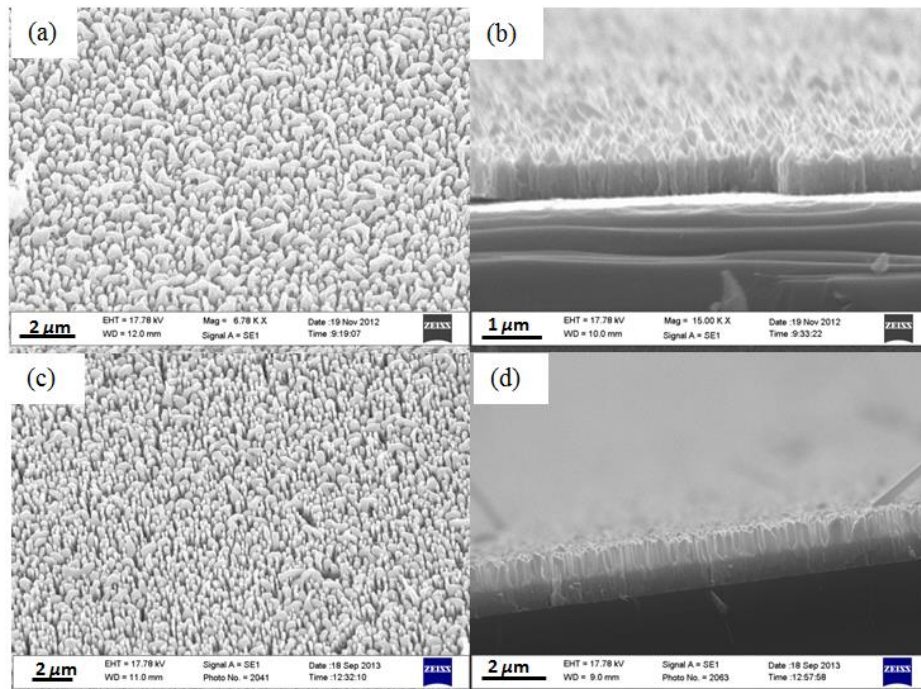


Figure 4.6:  $^{64/66/68}\text{ZnO}$  samples at  $30^\circ$  (a and c),  $90^\circ$  (b and d). The first sample (a and b) shows poor nanorod morphology. The second sample (c and d) has improved nanorod morphology.

The first  $^{64/66/68}\text{ZnO}$  sample displayed poor nanorod morphology as shown in figure 4.6 (a and b). There is very little nanorod growth during the VPT phase and any rods are mostly clumped together in groups, producing a mostly random pattern with no particular structure. It appears that in this case a relatively thin layer of material was deposited on the CBD layer during VPT growth and this has poor nanorod morphology. Visually, the morphology is more similar to the CBD layer itself rather than aligned nanorods usually grown during the VPT step. The growth of this sample was therefore repeated. In the second  $^{64/66/68}\text{ZnO}$  sample, the nanorod morphology is notably improved as shown in figure 4.6 (c and d). In this sample the nanorods are clearly visible although there is still some clumping of rods together. The VPT nanorods are of a slightly shorter length than the other samples also, as seen in figure 4.6(d).

As the SEM data above has illustrated, the growth of isotopically enriched ZnO nanorods utilising the modified three-step process previously used has been very successful. This has been achieved by simply substituting the VPT source powder for isotopically enriched powder and implementing the practical step of reducing the amount of powder used. This easy, reliable and inexpensive method has produced *c*-axis aligned nanorods of a very high quality with dense coverage over a wide substrate area in each sample. This makes them ideal for use in optical studies such as PL as described later. Some variations in morphology in terms of length and width can be seen in the figures above and occur from time to time, and indeed occasionally the morphology does not resemble nanorods as shown in figure 4.6(a). The growth process is sensitive to a number of parameters, including temperature, distance of the sample from the powder and the source powder mixing and particulate size. It is believed that the process of grinding the powders together is vital and that variations in the amount of contact between the powders, as well as temperature, may cause the growth reaction to occur at slightly different rates. This may be responsible for the variations in morphology observed, for example in figure 4.6. Despite this, the batch-to-batch reliability of the growth method is very good, and most of the samples produce nanorods as shown in figure 4.5 over most of their surface area.

### 4.3 Alignment and Crystal Quality - XRD

XRD measurements were carried out on all samples in order to confirm the presence of ZnO following VPT deposition and to study the crystal quality and alignment. The x-ray source was a Cu  $K_{\alpha}$  line with an effective mean wavelength of 0.15418 nm.

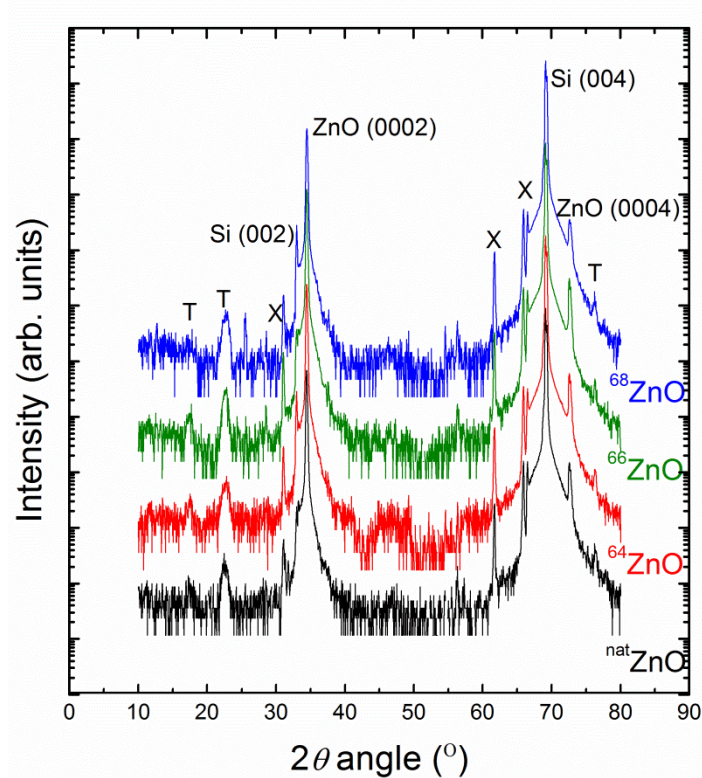


Figure 4.7:  $2\theta$ - $\omega$  spectra of several Zn-enriched ZnO samples dominated by the Si substrate peak at  $69.1^\circ$  and the ZnO peak at  $34.4^\circ$ . A number of other features are observed as described in the text.

Figure 4.7 shows the XRD  $2\theta$ - $\omega$  diffractograms for the  $^{\text{nat}}\text{ZnO}$ ,  $^{64}\text{ZnO}$ ,  $^{66}\text{ZnO}$  and  $^{68}\text{ZnO}$  samples. These curves are typical of those recorded for the other samples in the set. The  $2\theta$ - $\omega$  diffractograms are dominated by the  $69.1^\circ$  Si peak from the (004) Si planes of the substrate and the  $34.4^\circ$  ZnO peak from the (0002) planes in the deposited ZnO nanorods.<sup>5</sup> The second order (0004) ZnO planes are also present.<sup>6</sup> The kinematically forbidden Si (002) is also present in some samples due to double diffraction effects.<sup>7</sup> A number of smaller peaks are observed and are attributed to

the plastic backed adhesive tape used to mount the samples on the stage. These are labelled as T. A number of features are also visible due to  $K_{\beta}$  radiation at  $\sim 62^{\circ}$  from the x-ray tube and tungsten  $L_{\alpha}$  radiation at  $\sim 66^{\circ}$  from contamination of the x-ray tube Cu target by the electron gun tungsten filament.<sup>6</sup> These features are marked as X. The ZnO (0002) is far more intense than the other ZnO reflections, indicating a high degree of alignment of nanostructures with their  $c$ -axes normal to the substrate surface. This is consistent with the SEM images of the samples presented previously. XRD therefore confirms the presence of wurtzite ZnO on the substrate as a result of the growth reactions.

Sample	ZnO (0002) peak $2\theta$ ( $^{\circ}$ )	ZnO (0002) FWHM $2\theta$ ( $^{\circ}$ )	Crystallite size (nm)	ZnO $c$ lattice constant (nm)	Si (004) peak ( $^{\circ}$ )	Si lattice constant (nm)
<sup>64</sup> ZnO	34.43	0.211	44	0.521	69.12	0.544
<sup>66</sup> ZnO	34.43	0.209	45	0.521	69.10	0.544
<sup>68</sup> ZnO	34.45	0.224	41	0.521	69.12	0.544
<sup>64/66</sup> ZnO	34.47	0.219	43	0.520	69.14	0.543
<sup>66/68</sup> ZnO	34.45	0.214	44	0.521	69.13	0.544
<sup>64/68</sup> ZnO	34.47	0.219	43	0.520	69.17	0.543
<sup>64/66/68</sup> ZnO	34.49	0.221	42	0.520	69.13	0.544
<sup>nat</sup> ZnO	34.43	0.203	47	0.521	69.12	0.544

Table 4.2: ZnO (0002) peaks, FWHM and crystallite size and ZnO  $c$  lattice constants, and Si (004) peaks and lattice constants in Zn-enriched nanorods.

Table 4.2 gives the ZnO (0002) and Si (004)  $2\theta$  peak positions, the FWHM of the ZnO (0002) peak and calculated lattice constants for each sample as calculated using equation 2.1. The average value for the  $c$  lattice constant in ZnO was 0.521 nm which agrees with the previously measured value of 0.521 nm stated in chapter 1.<sup>8</sup> Likewise, the average value for the Si lattice constant was found to be 0.544 nm. This is again in good agreement with the reported value of 0.543 nm for the lattice constant in pure Si.<sup>9</sup> An error of  $\pm 0.025^\circ$  in the  $2\theta$  angles leads to an error in these lattice constants of  $\pm 0.004$  nm for the ZnO  $c$  lattice constant and  $\pm 0.002$  nm for the Si lattice constant. The narrow FWHM ( $\sim 0.20$ - $0.22^\circ$  for all eight samples) of the  $34.4^\circ$  ZnO peaks indicates the high crystal quality. This is consistent with the findings from SEM characterisation showing well aligned high quality nanorods described previously. We can calculate the average out-of-plane nanocrystallite size using the Scherrer relation<sup>10</sup>:

$$D = \frac{K\lambda}{\beta_{hkl} \cos \vartheta} \quad \text{Eqn. 4.2}$$

where  $D$  is the crystallite size,  $K$  is a shape factor equal to 0.9,  $\lambda$  is the x-ray wavelength,  $\vartheta$  is half the  $2\theta$  angle and  $\beta_{hkl}$  is the peak width when the instrumental peak broadening of  $\sim 0.10^\circ$  is taken into account by the formula

$$\beta_{hkl} = \sqrt{(\beta_{hkl})_{measured}^2 - (\beta_{hkl})_{instrumental}^2} \quad \text{Eqn. 4.3}$$

These widths measured imply crystallite coherence lengths of  $\sim 41$ - $47$  nm from the Scherrer relation with an error of  $\pm 6$  nm. The figures for each sample are given in table 4.2.

The rocking curves of the  $34.4^\circ$  (0002) ZnO peak from the  $^{nat}\text{ZnO}$ ,  $^{64}\text{ZnO}$ ,  $^{66}\text{ZnO}$  and  $^{68}\text{ZnO}$  samples are shown in figure 4.8. The peak positions and FWHM of the rocking curves of all samples are shown in table 4.3. The high quality of the crystal structure and  $c$ -axis alignment shown in SEM images and  $2\theta$ - $\omega$  scans above is confirmed by the narrow FWHM of the rocking curves. The rocking curves peak at  $\sim 17^\circ$  and have FWHM of  $2.26$ - $3.25^\circ$  for all eight samples. The peak positions vary slightly due to small variations in sample tilt on the stage, due to the mounting process.<sup>5</sup> Again, in this case, the curves shown in figure 4.8 are typical of the other samples in the set. Finally, it is interesting to comment on the  $2\theta$ - $\omega$  diffractograms

of the CBD buffer and seed layers as shown in figure 4.9. The buffer layer displays the ZnO (0002) and (0004) peaks, but only the Si substrate peaks are visible for the seed layer. The inset shows rocking curve of ZnO (0002) peak in the CBD nanorods which had a FWHM of  $5.68^\circ$ , around twice that of the VPT nanorods, indicating that the buffer layer is not as well textured as the VPT nanorods grown subsequently.

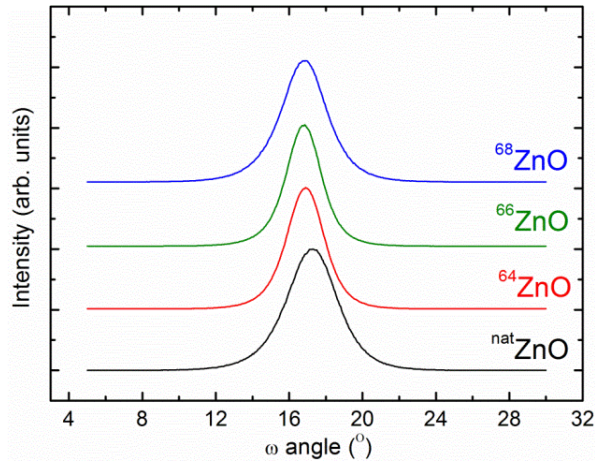


Figure 4.8: XRD rocking curves of the  $34.4^\circ$  (0002) ZnO peak from the  $^{nat}\text{ZnO}$ ,  $^{64}\text{ZnO}$ ,  $^{66}\text{ZnO}$  and  $^{68}\text{ZnO}$  samples.

Sample	Rocking curve peak ( $^\circ$ )	FWHM ( $^\circ$ )
$^{64}\text{ZnO}$	16.91	2.4
$^{66}\text{ZnO}$	16.8	2.26
$^{68}\text{ZnO}$	16.84	2.92
$^{64/66}\text{ZnO}$	17.15	2.67
$^{66/68}\text{ZnO}$	16.95	2.88
$^{64/68}\text{ZnO}$	17.49	2.56
$^{64/66/68}\text{ZnO}$	17.04	2.57
$^{nat}\text{ZnO}$	17.25	3.25

Table 4.3: Peaks and FWHM of the rocking curves of the  $34.4^\circ$  ZnO (0002) peak in all samples.

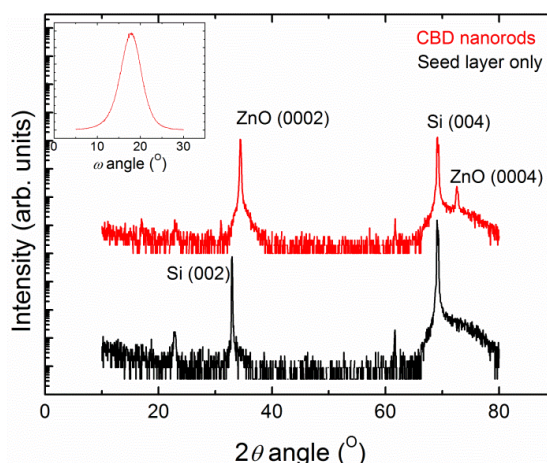


Figure 4.9:  $2\theta$ - $\omega$  diffractograms of CBD buffer layer nanorods and ZnO seed layer only. (Inset shows rocking curve of ZnO (0002) peak in CBD nanorods.)

The SEM and XRD data have illustrated that the growth of ZnO nanorods utilising this modified three-step process is very successful in terms of sample crystallinity and morphology. This has been achieved by substituting the normal, natural isotope content ZnO source powder used in VPT with isotopically enriched powder and implementing the practical step of reducing the amount of powder used. This easy, reliable and inexpensive method has produced well-aligned nanorods of a very high quality with dense coverage over a wide substrate area. This makes them ideal for use in further optical studies such as Raman and PL.

#### 4.4 Isotopic Enrichment - SIMS

SIMS measurements were carried out on the set of eight samples in order to obtain a direct measurement of the isotopic enrichment on two systems as described in section 2.4.3. Figures 4.10 and 4.11 display the spectra from both systems which are referred to as ‘SIMS’ and ‘miniSIMS’ in order to distinguish them. Measurements on the ‘SIMS’ system were carried out by Mr. Conor Byrne in DCU. SIMS in general provides key evidence as to whether isotopic enrichment has been successful during the growth procedure by measuring the masses of the Zn atoms in the samples. The region of interest here is around 64 to 68 amu, as we are measuring

the  $\text{Zn}^+$  ions ejected from the samples under the respective incident ion beams. Each figure shows (a)  $^{\text{nat}}\text{ZnO}$ , (b)  $^{64}\text{ZnO}$ , (c)  $^{66}\text{ZnO}$ , (d)  $^{68}\text{ZnO}$ , (e)  $^{64/66}\text{ZnO}$ , (f)  $^{66/68}\text{ZnO}$ , (g)  $^{64/68}\text{ZnO}$  and (h)  $^{64/66/68}\text{ZnO}$ . Red, green and blue lines show the positions of 64, 66 and 68 amu respectively. The samples have been shifted slightly on the x-axis to correct for a slight calibration error misalignment.

The first thing to note is that, in the  $^{\text{nat}}\text{ZnO}$  samples in both cases, the three main isotopes,  $^{64}\text{Zn}$ ,  $^{66}\text{Zn}$  and  $^{68}\text{Zn}$ , follow the pattern that would be expected due to the isotopic composition of  $^{\text{nat}}\text{ZnO}$  (48.6%  $^{64}\text{Zn}$ , 27.9%  $^{66}\text{Zn}$ , 18.8%  $^{68}\text{Zn}$ ). Looking at the spectra for isotopically pure samples,  $^{64}\text{ZnO}$ ,  $^{66}\text{ZnO}$  and  $^{68}\text{ZnO}$ , it is clear that the expected Zn isotope is dominant in each respective sample, thereby showing that the samples have been enriched to a very high level. For each enriched isotope, there are much smaller peaks at the masses of the other two isotopes. For example, in figure 4.9(b) for  $^{64}\text{ZnO}$ , small peaks are observed at 66 and 68 amu. These small peaks are attributed to some ions of these isotopes arising from the CBD buffer layer, which is not isotopically enriched, and to other ions from any surface contaminants at these masses. The samples were tilted during these measurements, as described in section 2.4.3, in order to reduce effects from the underlying substrate, but even with this precaution the VPT nanorod coverage is not complete and a small fraction of the buffer layer is exposed to the ion beam. Despite this, it is clear from the these data that the nanorod samples have been successfully isotopically enriched to a very high level using this growth method.

In the mixed isotope samples ( $^{64/66}\text{ZnO}$ ,  $^{66/68}\text{ZnO}$ ,  $^{64/68}\text{ZnO}$ ,  $^{64/66/68}\text{ZnO}$ ), the respective isotopes in each mixture are clearly dominant, with the isotope not included in each growth not detected in significant amounts. This confirms the successful enrichment of the mixed isotope samples, although the isotopes present are not always measured to be present in exactly the desired proportions ( $1/2:1/2$  or  $1/3:1/3:1/3$ , particularly in figure 4.10 (h)). This could be a result of some ions from the underlying buffer layer being detected again, although it could also indicate that the mixed samples did not grow in exactly these proportions, as the disproportionality seems to be greater than the signal observed for isotopes not present in the VPT growth for  $^{64}\text{ZnO}$ ,  $^{66}\text{ZnO}$  and  $^{68}\text{ZnO}$ . This is discussed further in chapter 6.

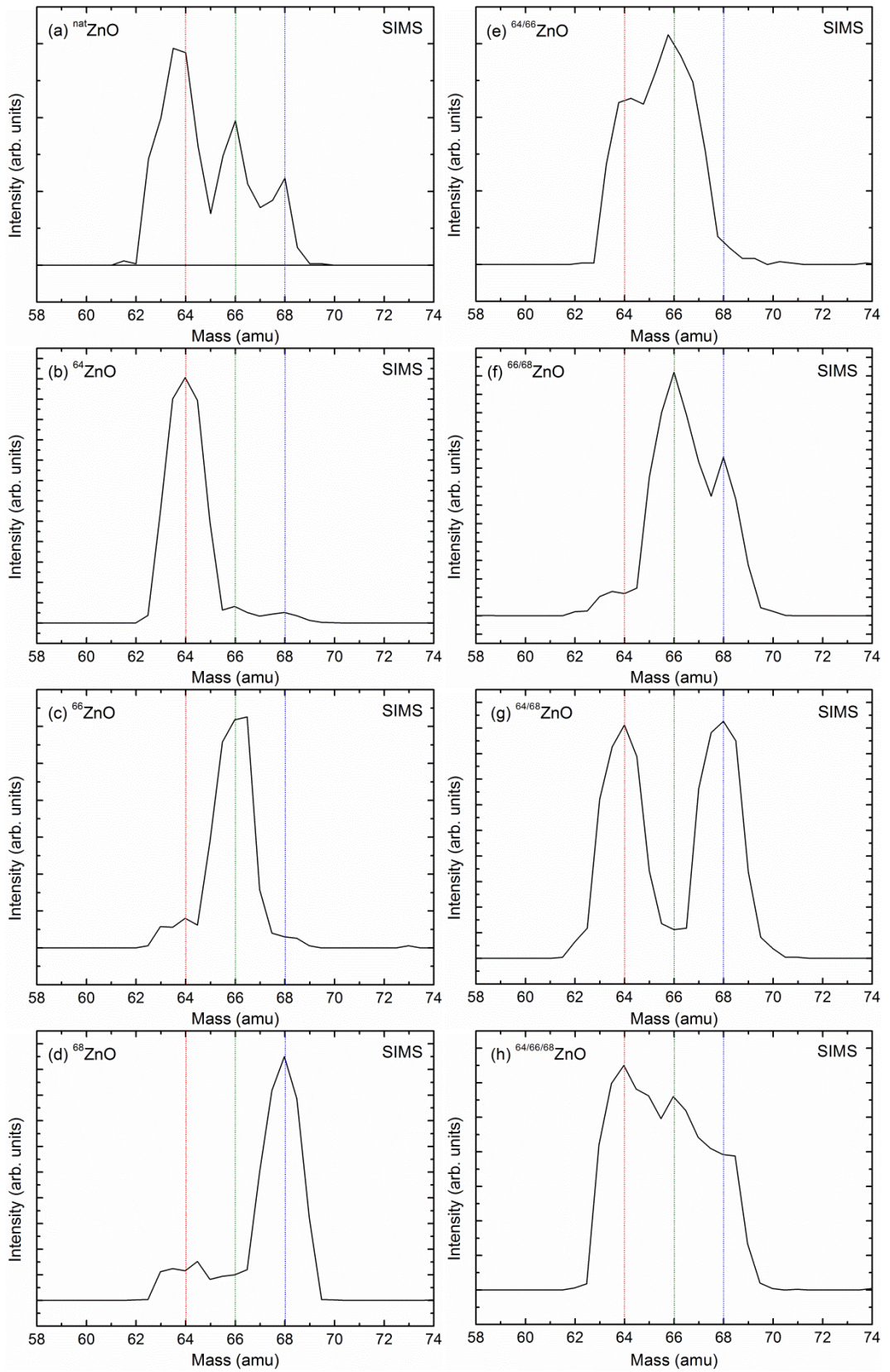


Figure 4.10: SIMS spectra from each sample in the Zn-enriched set.

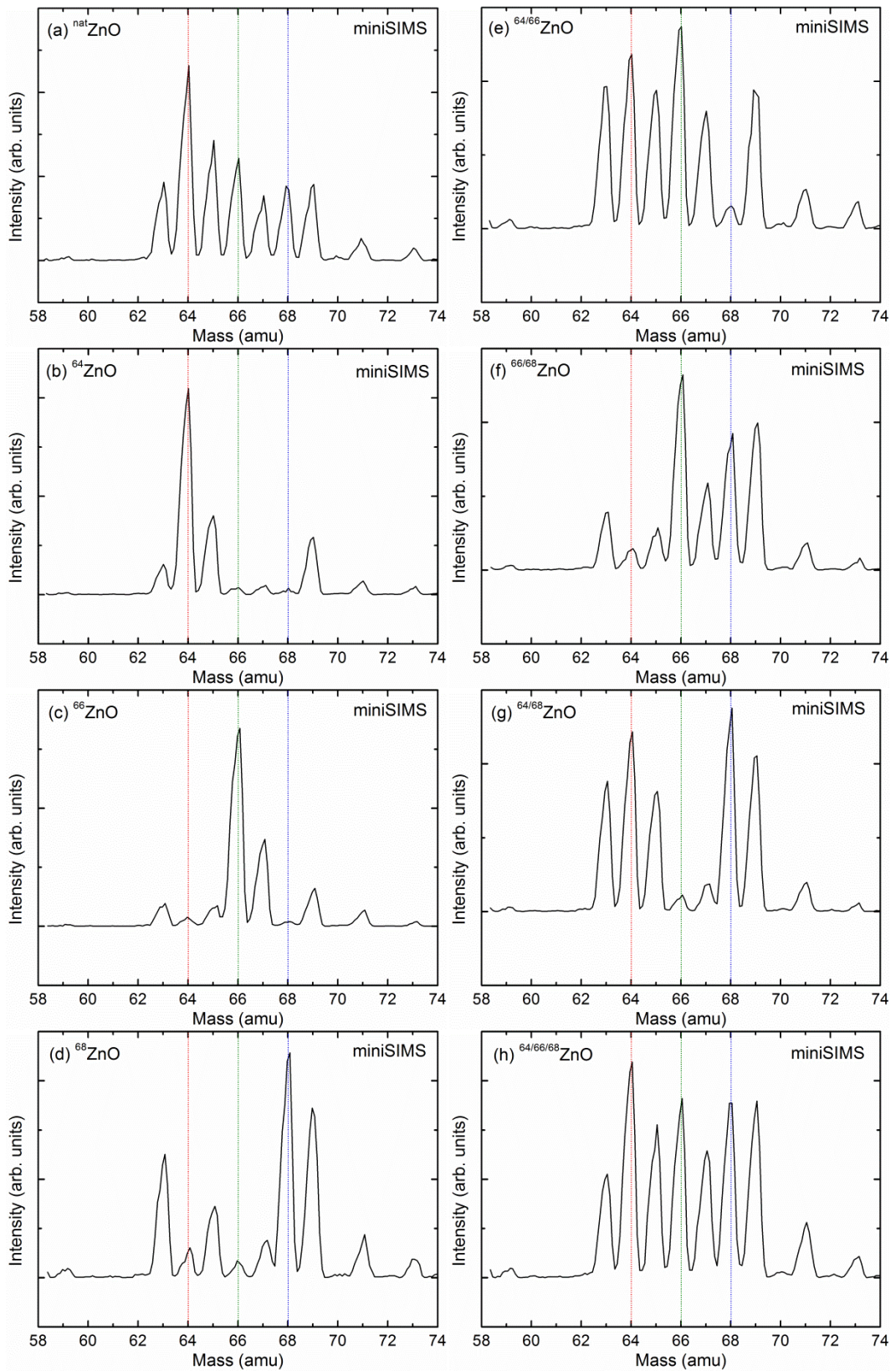


Figure 4.11: miniSIMS spectra from each sample in the Zn-enriched set.

It can be noted that although the samples were tilted as mentioned to try to avoid signal from the buffer layer, tests performed with ion beam normal to the surfaces did not produce notably different results.

Finally it must be noted that, in the miniSIMS spectra in figure 4.11, the other main features are additional peaks observed to the right of each isotope peak, at one amu greater. These are attributed to  $\text{ZnH}^+$  ions<sup>11</sup>, and they appear to mostly follow the behaviour of their ‘parent’  $\text{Zn}^+$  peaks. Some small deviations from this pattern could be the result of the different amounts of these ions generated in the system or to some other species appearing at these masses. Indeed, the miniSIMS systems also displays some other peaks at 63 amu, 71 amu and 73 amu which could be the result of such species either from the sample or remaining in the chamber as the vacuum level here was lower than the SIMS system. We note also that the Ga ion beam in the miniSIMS systems produces isotopes of  $^{69}\text{Ga}$  and  $^{71}\text{Ga}$ , which could also contribute to these peaks. Overall, the SIMS results show conclusively that the novel VPT method developed here has successfully produced a set of isotopically pure ZnO nanorods enriched to a very high level. Data from both the SIMS and miniSIMS systems are consistent and this is consistent with the Raman results and PL spectra below.

## 4.5 Phonon Frequencies - Raman

Data from Raman spectroscopy measurements performed on  $^{64}\text{ZnO}$ ,  $^{66}\text{ZnO}$  and  $^{68}\text{ZnO}$  samples at room temperature are presented in figure 4.12. These measurements were performed by Dr. Joseph Cullen, in Linköping University in Sweden. Raman measurements were carried out in order to measure the Raman frequencies in samples with the different isotopic purities and compare them to previous measurements on enriched single crystals in the literature. In the inset of figure 4.12, the Raman signal from the underlying Si substrate at around  $520\text{ cm}^{-1}$  is shown for reference.

For all three samples, the Raman spectra contain first-order  $E_2^{\text{low}}$  and  $E_2^{\text{high}}$  phonon modes that are typical for crystallite wurtzite ZnO as previously described in

chapter 3. The two Raman modes gradually shift to lower frequencies with increasing Zn isotope mass from  $^{64}\text{ZnO}$  to  $^{68}\text{ZnO}$ , by  $1.81\text{cm}^{-1}$  for  $E_2^{\text{low}}$  and  $2.17\text{cm}^{-1}$  for  $E_2^{\text{high}}$ . These figures are consistent with previous findings of shifts of  $1.59\text{cm}^{-1}$  for  $E_2^{\text{high}}$  at low temperatures ( $\sim 6\text{K}$ ).<sup>12</sup> The frequencies of the  $E_2^{\text{low}}$  and  $E_2^{\text{high}}$  phonon modes for  $^{64}\text{ZnO}$  were  $100.60\text{cm}^{-1}$  and  $439.03\text{cm}^{-1}$  respectively. The frequencies for each sample and their FWHM are summarized in table 4.4.

Shifting phonon frequencies for O and Zn isotopic substitution in ZnO have been observed previously in a number of papers by Serrano *et al.*<sup>12,13</sup> and are observed here for the  $E_2^{\text{high}}$  and  $E_2^{\text{low}}$  phonon modes. Since only the natural abundance of O ( $>99\%$   $^{16}\text{O}$ ) was used during nanorod growth in this work the changing Zn mass is solely responsible for the shifting phonon frequencies. For the  $E_2^{\text{high}}$  phonon mode the observed frequency change for different Zn masses (around  $2\text{cm}^{-1}$ ) is less pronounced than that previously reported for different O masses (around  $20\text{cm}^{-1}$ ) due to the dominating O eigenvector.<sup>13</sup> A similar shift ( $<2\text{cm}^{-1}$ ) is observed for the  $E_2^{\text{low}}$  phonon with changing Zn mass, which is dominated by the Zn eigenvector. Corresponding data for O-enriched ZnO nanorods are presented in chapter 5.

It is also interesting to note the changes in the FWHM of the  $E_2^{\text{high}}$  phonon line with isotopic enrichment. There is significant broadening of the FWHM for this mode, however it is not isotopic in nature. The changing FWHM for different Zn masses results from a change in the overlap of the two-phonon density of states due to changes in phonon frequency. Ab initio calculations performed by Serrano *et al.*<sup>13</sup> show that the  $E_2^{\text{high}}$  phonon mode is near a sharp ‘ridge’ in the two-phonon density of states, the interaction with which results in the variation in FWHM. The overlap is less clearly observed for the  $E_2^{\text{low}}$  mode with no change observed in the FWHM with changing Zn mass. Our data are consistent with the results reported by Serrano *et al.*

The observed shifts in the phonon vibration energies in our samples are consistent with previous findings in the literature and, therefore, demonstrate clearly, and independently of the SIMS and PL experiments, that the desired isotopic enrichment of the samples has been successful.

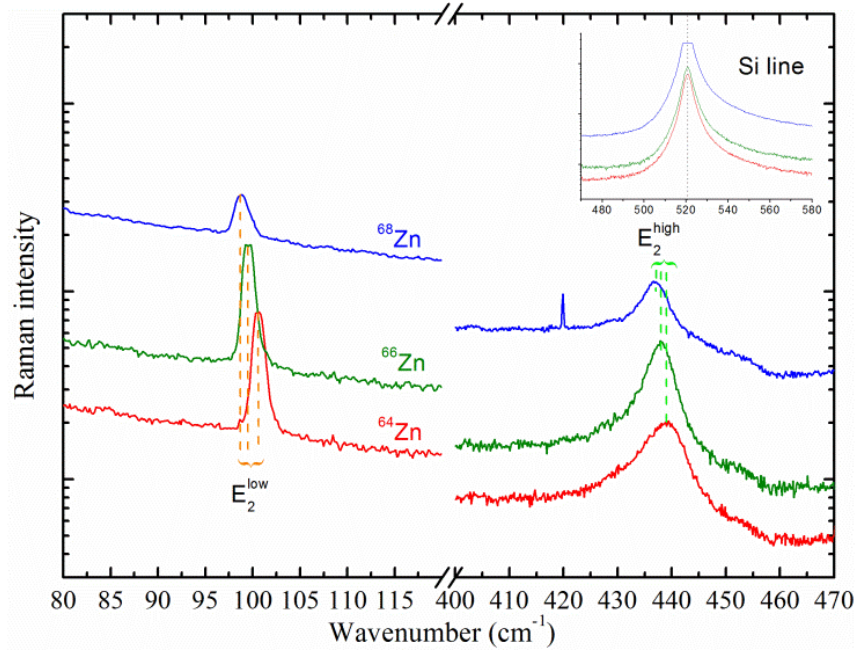


Figure 4.12: Raman spectra of isotopically enriched  $^{64}\text{ZnO}$ ,  $^{66}\text{ZnO}$  and  $^{68}\text{ZnO}$  nanorods. Inset shows the signal from the Si substrate.

Sample	Mode	Wavenumber ( $\text{cm}^{-1}$ )	$\Delta$ Wavenumber ( $\text{cm}^{-1}$ )	FWHM ( $\text{cm}^{-1}$ )	$\Delta$ FWHM ( $\text{cm}^{-1}$ )
$^{64}\text{ZnO}$	$E_2^{\text{high}}$	439.03	-	8.11	-
$^{66}\text{ZnO}$	$E_2^{\text{high}}$	437.73	-1.30	6.94	-1.17
$^{68}\text{ZnO}$	$E_2^{\text{high}}$	436.86	-2.17	5.59	-2.52
$^{64}\text{ZnO}$	$E_2^{\text{low}}$	100.60	-	1.70	-
$^{66}\text{ZnO}$	$E_2^{\text{low}}$	99.57	-1.03	1.70	-0.00
$^{68}\text{ZnO}$	$E_2^{\text{low}}$	98.79	-1.81	1.73	0.03

Table 4.4: Frequencies and FWHM of the  $E_2^{\text{low}}$  and  $E_2^{\text{high}}$  phonons for  $^{64}\text{ZnO}$ ,  $^{66}\text{ZnO}$  and  $^{68}\text{ZnO}$  samples.

## 4.6 Optical Quality and Enrichment - Low temperature PL

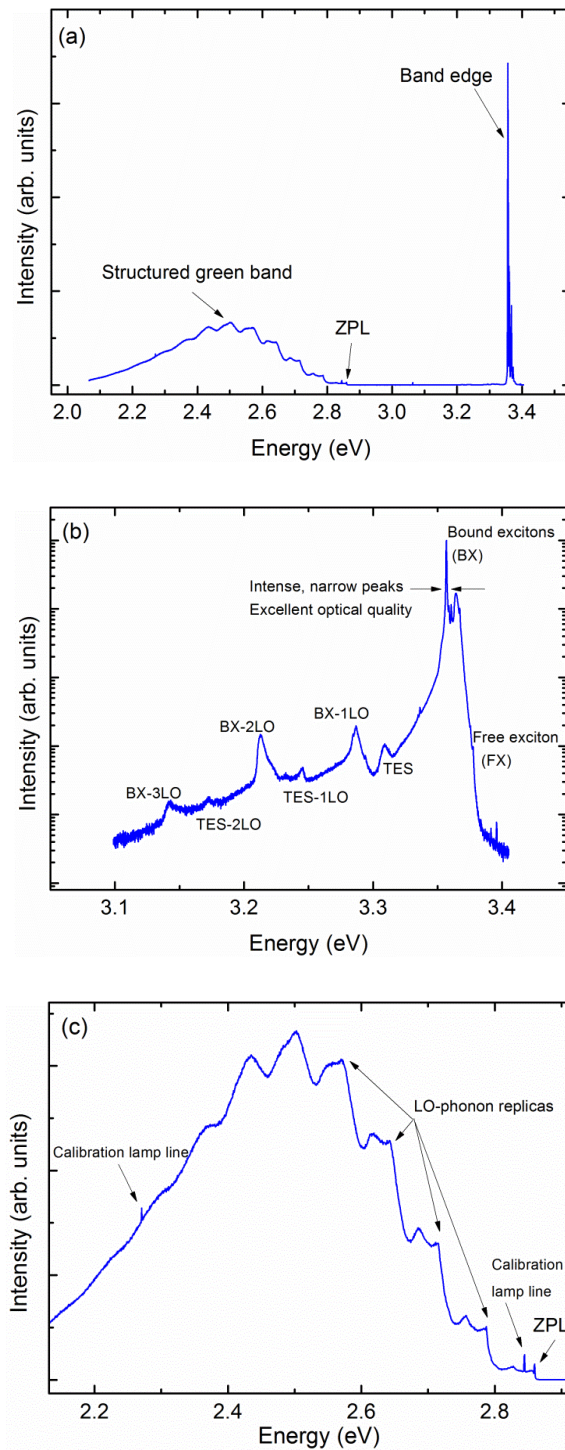


Figure 4.13: PL spectra of the  $^{66}\text{ZnO}$  sample showing (a) a broad range spectrum displaying the typical PL emission from ZnO nanorods, (b) the intense UV band edge emission in detail, and (c) the Cu-related 2.86 eV ZPL and associated SGB (from annealed portion). (Note that (a) is a composite of (b) and (c)).

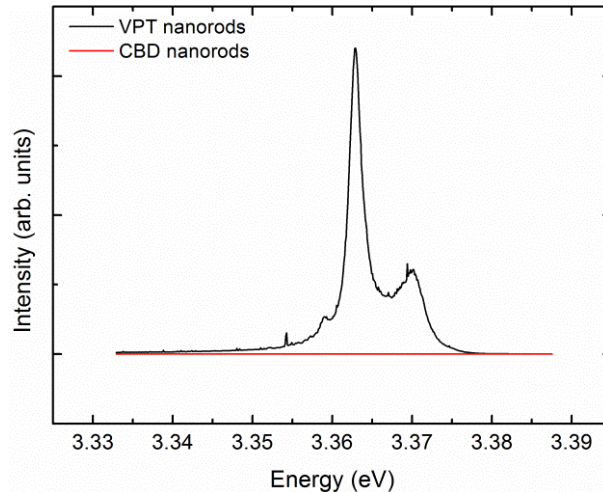
Low temperature PL was carried out on all samples. In this section the general shape of the typical PL spectrum, which was observed in all samples is introduced using spectra recorded with the SPEX spectrometer. The shifts in energy of the BX recombinations in the band edge region are also presented using the  $^{\text{nat}}\text{ZnO}$ ,  $^{64}\text{ZnO}$ ,  $^{66}\text{ZnO}$  and  $^{68}\text{ZnO}$  samples. Further detail and discussion on these, and the other samples in this set, is presented in chapter 6 as part of the discussion on the Cu-related defect at 2.86 eV.

Figure 4.13(a) shows a broad spectrum including the band edge region, as well as the Cu-related ZPL at 2.86 eV and its associated SGB in  $^{66}\text{ZnO}$  (note the linear y-scale here).<sup>14,15</sup>  $^{66}\text{ZnO}$  was chosen to illustrate the general features of these spectra as its spectrum was representative of those obtained from the other samples and typical of the PL spectrum obtained from ZnO nanorods reported in the literature.<sup>16</sup> Note that figure 4.13(a) is a composite of the spectra in figures 4.13(b) and (c) in order to show a broad spectrum.

Figure 4.13(b) shows the band edge region of the  $^{66}\text{ZnO}$  sample in detail (note the logarithmic y-scale). The intense band edge emission due to shallow donor bound excitons is dominant at  $\sim 3.36$  eV. The FX position can also be seen, although this was not clearly observed in all samples. The LO phonon replicas of the BX lines are also present (BX-1LO, BX-2LO and BX-3LO), spaced at intervals of  $\sim 72$  meV, the characteristic LO phonon energy of the ZnO crystal structure.<sup>17</sup> The TES feature is also present, as are its LO replicas (TES-1LO and TES-2LO). The intense peaks and narrow line widths ( $< 1$  meV) of the BX lines indicate the excellent optical quality of the nanorods as grown, as discussed further below. This is consistent with the excellent optical characteristics of ZnO nanorods grown by similar methods reported elsewhere and demonstrates the ability to grow isotopically enriched ZnO materials with excellent optical quality using the straightforward carbothermal reduction VPT method, with mg quantities of source material.<sup>18</sup>

Figure 4.13(c) shows the green band emission region for  $^{66}\text{ZnO}$ . This was recorded using a portion of the  $^{66}\text{ZnO}$  sample which was annealed for ten minutes at 900 °C to increase the ZPL and green band intensity.<sup>18,19</sup> The Cu-related ZPL at 2.86 eV is present and its associated SGB is the dominant feature. Indeed, the SGB is the primary feature of the PL spectrum in addition to the UV band edge emission.

The LO phonon replicas of the ZPL are clearly seen in the SGB at intervals of  $\sim 72$  meV below the ZPL energy. Some weak lines from the Hg lamp used to calibrate the spectra are also observed. Note that the PL emission is associated with the VPT-grown nanorods and there is not a significant emission from the underlying buffer layer. This is illustrated in figure 4.14 which shows that the band edge PL intensity of CBD nanorods is negligible compared to that of the VPT nanorods as recorded under the same conditions (optimised for VPT samples, i.e. very narrow slit widths). In fact, no band edge emission was observed in the CBD nanorods grown by the NaOH method used in these samples. However a slight increase in intensity was observed after the CBD sample underwent a thermal cycle similar to the VPT growth cycle, although this was still barely detectable under these conditions. A more detailed study of the PL emission of CBD-grown nanorods has been reported and shows a greater band edge emission from CBD nanorods grown using the other baths described in section 2.2.3 (HMT-based and acetate-based), although still 2-4 orders of magnitude less intense than the emission from VPT-grown nanorods.<sup>20,21</sup>



*Figure 4.14: Comparison of PL intensities of VPT and CBD nanorods.*

Figure 4.15 shows representative band edge spectra from selected samples. The dominant feature in the band edge spectra is the  $I_9$  line attributed to  $\text{In}^{22}$  donor bound impurities. The  $I_8$  and  $I_6$  lines attributed to Ga and Al impurities are also

clearly observed.<sup>23–25</sup> The  $I_2$  line attributed to ionised In impurities<sup>26</sup> and the surface exciton<sup>27</sup> (SX) emission are also visible and labelled in the figure.

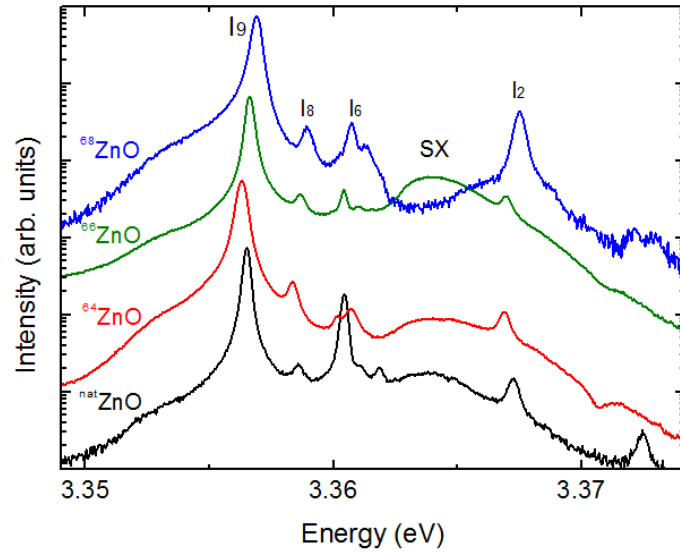


Figure 4.15: Typical PL spectra of selected enriched ZnO nanorod samples showing the band edge region including the  $I_9$  line (spectra shifted vertically for clarity).

Sample	Average Zn isotopic content (amu)	$I_9$ energy (eV)	$I_9$ FWHM (meV)
$^{64}\text{ZnO}$	64	3.35629	0.44
$^{66}\text{ZnO}$	66	3.35662	0.36
$^{68}\text{ZnO}$	68	3.35689	0.41
$^{64/66}\text{ZnO}$	65	3.35641	0.33
$^{66/68}\text{ZnO}$	67	3.35682	0.33
$^{64/68}\text{ZnO}$	66	3.35643	0.35
$^{64/66/68}\text{ZnO}$	66	3.35603	0.35
$^{\text{nat}}\text{ZnO}$	65.4	3.35650	0.31

Table 4.5: Energies and FWHM of the  $I_9$  exciton recombination in samples with different Zn isotopic enrichments.

The position of the I<sub>9</sub> In bound exciton recombination in unenriched material at ~3.356 eV was used to measure changes in the band edge positions with changing Zn isotope enrichment, and the other lines followed its trend. The peak positions of the I<sub>9</sub> line were extracted by fitting Gaussian curves to the data. The position of the I<sub>9</sub> line in each sample is given in table 4.5, along with its FWHM. The I<sub>9</sub> BX energy increases with increasing Zn isotopic mass from <sup>64</sup>ZnO to <sup>68</sup>ZnO by 0.6 meV. The blue shift in energy recorded in the band edge region when the Zn isotope mass is changed (0.6 meV) is comparable to that previously reported in the literature. Tsoi *et al.* report an increase of ~1.0 meV in the A-exciton band gap over this range.<sup>28</sup> This is further verification of the successful isotopic enrichment of our samples. We note that Manjón *et al.* report blue shifts in the band edge region of ~1.7 meV from <sup>64</sup>ZnO to <sup>68</sup>ZnO for single crystals.<sup>29</sup> However since Manjón *et al.*'s results come from measurements of the I<sub>4</sub> bound exciton recombination and since this emission has been attributed to H at an O site<sup>30</sup> (i.e. a H atom surrounded by Zn atoms), this recombination may be more strongly affected by Zn isotopic changes (due to both local and extended vibronic modes) and undergo a different shift than other shallow donor bound excitons on Zn sites surrounded by O atoms (such as the In-related I<sub>9</sub>).

The very narrow FWHM of the exciton recombinations in these nanorod samples demonstrates their excellent optical quality and therefore their suitability for use in defect and impurity studies using PL. The I<sub>9</sub> FWHMs here are in the range of 0.31-0.44 meV as shown in table 4.5 (comparable to very high optical quality commercial single crystal ZnO<sup>26</sup>). This is much narrower than the line widths observed by others in single crystal isotopically enriched ZnO. Manjón *et al.* have reported line widths of < 5 meV<sup>29</sup> and Tsoi *et al.* observed BX PL features of widths of ~2-8 meV<sup>28</sup> in single crystal isotopically enriched ZnO samples. Given this excellent optical quality, these samples were used to carry out a number of detailed optical studies of defects in ZnO, including the Cu-related emission ZPL at 2.86 eV, as well as the manifold of closely spaced near band edge I-lines due to donor bound exciton emission.

## 4.7 FX Energies - Reflectance Spectroscopy

Reflectance spectroscopy was carried out as outlined in chapter 2. The purpose of this was to obtain the FX energies (specifically the A-exciton) of the isotopically enriched samples. This would complement the PL results outlined in section 4.6. It was hoped that the same trend as seen with the BX lines of increasing exciton recombination energy with the Zn isotopes moving from  $^{64}\text{Zn}$  to  $^{68}\text{Zn}$  would be observed. The valence band of ZnO is split into three bands called the A, B and C bands, each of which has a specific FX energy which can be observed using reflectance spectroscopy, depending on the electric field polarisation.<sup>28,31</sup> Further detail on the valence band splitting and the structure of the ZnO reflectance spectrum can be found in reference 16.

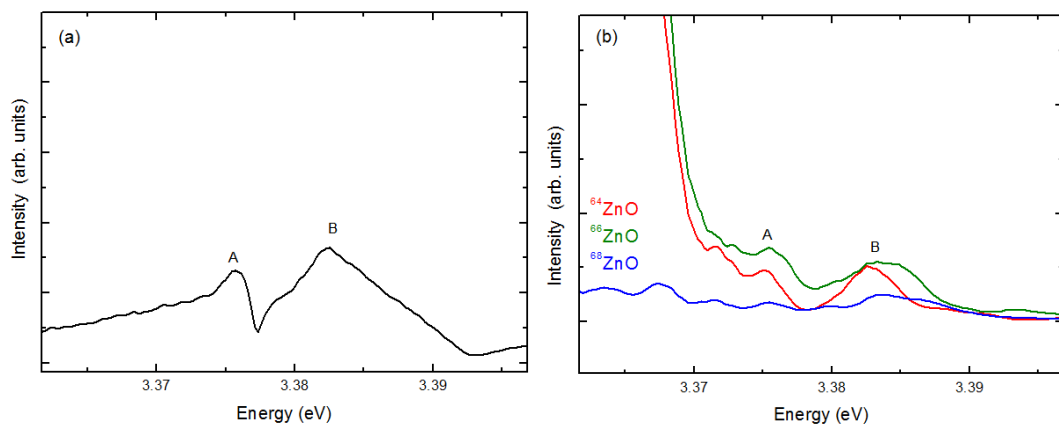


Figure 4.16: Reflectance spectrum of a (a) single crystal ZnO sample showing the A-exciton and B-exciton clearly, and (b) reflectance spectrum of the  $^{64}\text{ZnO}$ ,  $^{66}\text{ZnO}$  and  $^{68}\text{ZnO}$  samples. A and B label the A- and B-excitons.

Figure 4.16 shows the reflectance of a sample of (a) a ZnO single crystal and (b) representative spectra of the Zn-enriched nanorods recorded using the FT spectrometer. The A- and B-excitons are clearly shown in (a) and are observed in (b) also. The spectra displayed strong band edge PL emission arising from the above band gap light emanating from the deuterium lamp which dominated the reflected light. However it proved difficult to observe the FX energies clearly in the nanorod

samples and it was not possible to detect any trend in the change in energy with different isotopic content. The spectra are noisy because the nanorod sample morphology leads to strong scattering and absorption (with subsequent PL emission) and little specular reflection due to the dull and diffusely reflecting surfaces in these samples. Extensive efforts were made to limit noise by using lenses to focus the light to a bright spot on the sample, using filtering to ensure only light from the region of interest reached the FT spectrometer, running and averaging many scans, careful optical alignment and other measures. These measures were ultimately unsuccessful, however this does not undermine the evidence of successful isotopic enrichment obtained using other methods as presented in this chapter.

## 4.8 Conclusions

The three-step growth process, previously developed in our group, has been successfully adapted in order to grow nanorods of ZnO isotopically enriched with different Zn isotopes. Samples of  $^{\text{nat}}\text{ZnO}$ ,  $^{64}\text{ZnO}$ ,  $^{66}\text{ZnO}$ ,  $^{68}\text{ZnO}$ ,  $^{64/66}\text{ZnO}$ ,  $^{66/68}\text{ZnO}$ ,  $^{64/68}\text{ZnO}$  and  $^{64/66/68}\text{ZnO}$  were grown using this VS CTR-VPT techniques on CBD buffer layers using this novel method. SEM revealed a dense coverage of vertical,  $c$ -axis aligned nanorods over a large sample area for nearly all samples, with slight variations seen in one sample. XRD confirmed the presence of wurtzite ZnO and excellent nanorod alignment and crystal quality. SIMS data confirm the successful isotopic enrichment consistently using two independent SIMS systems. Raman data show a shift of  $>1\text{ cm}^{-1}$  in the peak position of the Raman scattered peaks due to the  $E_2^{\text{low}}$  and  $E_2^{\text{high}}$  phonon modes when the Zn isotope is changed from  $^{64}\text{Zn}$  to  $^{68}\text{Zn}$ , consistent with previous work on samples with different isotopic enrichments, again confirming successful isotopic substitution. Low temperature PL measurements revealed the excellent optical quality of the samples with band edge emission emissions displaying strong and spectrally narrow BX lines in all samples. An increase in the  $I_9$  exciton recombination energy of  $\sim 0.6\text{ meV}$  when the Zn isotopic content was changed from  $^{64}\text{ZnO}$  to  $^{68}\text{ZnO}$ , and narrow line widths of  $<1\text{ meV}$ , were observed. This is consistent with previous results reported for single crystals, further confirming successful isotopic substitution of these high structural and optical

quality nanorods using this simple and reliable growth method. The excellent optical quality also confirms the potential for the use of these samples in defect and impurity studies using PL.

## 4.9 References

- <sup>1</sup> D. Byrne, E. McGlynn, K. Kumar, M. Biswas, M.O. Henry, and G. Hughes, *Cryst. Growth Des.* **10**, 2400 (2010).
- <sup>2</sup> R.B. Peterson, C.L. Fields, and B.A. Gregg, *Langmuir* **20**, 5114 (2004).
- <sup>3</sup> L.E. Greene, M. Law, D.H. Tan, M. Montano, J. Goldberger, G. Somorjai, and P. Yang, *Nano Lett.* **5**, 1231 (2005).
- <sup>4</sup> R.B. Saunders, S. Garry, D. Byrne, M.O. Henry, and E. McGlynn, *Cryst. Growth Des.* **12**, 5972 (2012).
- <sup>5</sup> E. McCarthy, R.T. Rajendra Kumar, B. Doggett, S. Chakrabarti, R.J. O’Haire, S.B. Newcomb, J.-P. Mosnier, M.O. Henry, and E. McGlynn, *J. Phys. D. Appl. Phys.* **44**, 375401 (2011).
- <sup>6</sup> R.T.R. Kumar, E. McGlynn, M. Biswas, R. Saunders, G. Trolliard, B. Soulestin, J.-R. Duclere, J.P. Mosnier, and M.O. Henry, *J. Appl. Phys.* **104**, 084309 (2008).
- <sup>7</sup> B.-H. Hwang, *J. Phys. D. Appl. Phys.* **34**, 2469 (2001).
- <sup>8</sup> S. Desgreniers, *Phys. Rev. B* **58**, 14102 (1998).
- <sup>9</sup> W.C. O’Mara, R.B. Herring, and L.P. Hunt, editors, *Handbook of Semiconductor Silicon Technology* (Noyes Publications, Park Ridge, New Jersey, USA, 1990).
- <sup>10</sup> V. Mote, Y. Purushotham, and B. Dole, *J. Theor. Appl. Phys.* **6**, 6 (2012).
- <sup>11</sup> K. Ghule, A.V. Ghule, B.-J. Chen, and Y.-C. Ling, *Green Chem.* **8**, 1034 (2006).
- <sup>12</sup> J. Serrano, F. Widulle, A.H. Romero, A. Rubio, R. Lauck, and M. Cardona, *Phys. Status Solidi* **235**, 260 (2003).
- <sup>13</sup> J. Serrano, F. Manjón, A. Romero, F. Widulle, R. Lauck, and M. Cardona, *Phys. Rev. Lett.* **90**, 055510 (2003).
- <sup>14</sup> R. Dingle, *Phys. Rev. Lett.* **23**, 579 (1969).

- <sup>15</sup> D. Byrne, F. Herklotz, M.O. Henry, and E. McGlynn, *J. Physics. Condens. Matter* **24**, 215802 (2012).
- <sup>16</sup> C.F. Klingshirn, B.K. Meyer, A. Waag, A. Hoffmann, and J. Geurts, *ZnO: From Fundamental Properties Towards Novel Applications* (Springer-Verlag, Berlin, Heidelberg, 2010).
- <sup>17</sup> L. Wang and N.C. Giles, *J. Appl. Phys.* **94**, 973 (2003).
- <sup>18</sup> G. Xing, G. Xing, M. Li, E.J. Sie, D. Wang, A. Sulistio, Q. Ye, C.H.A. Huan, T. Wu, and T.C. Sum, *Appl. Phys. Lett.* **98**, 102105 (2011).
- <sup>19</sup> N.Y. Garces, L. Wang, L. Bai, N.C. Giles, L.E. Halliburton, and G. Cantwell, *Appl. Phys. Lett.* **81**, 622 (2002).
- <sup>20</sup> D. Byrne, *The Growth and Characterisation of Ordered Arrays of Zinc Oxide Nanostructures and Optical Studies of Defects in Zinc Oxide*, Dublin City University, 2012.
- <sup>21</sup> D. Byrne, E. McGlynn, J. Cullen, and M.O. Henry, *Nanoscale* **3**, 1675 (2011).
- <sup>22</sup> S. Müller, D. Stichtenoth, M. Uhrmacher, H. Hofsäss, C. Ronning, and J. Röder, *Appl. Phys. Lett.* **90**, 012107 (2007).
- <sup>23</sup> K. Johnston, M.O. Henry, D. McCabe, E. McGlynn, M. Dietrich, E. Alves, and M. Xia, *Phys. Rev. B* **73**, 165212 (2006).
- <sup>24</sup> M. Schilling, R. Helbig, and G. Pensl, *J. Lumin.* **33**, 201 (1985).
- <sup>25</sup> B.K. Meyer, H. Alves, D.M. Hofmann, W. Kriegseis, D. Forster, F. Bertram, J. Christen, A. Hoffmann, M. Straßburg, M. Dworzak, U. Haboek, and A. V. Rodina, *Phys. Status Solidi* **241**, 231 (2004).
- <sup>26</sup> J. Cullen, D. Byrne, K. Johnston, E. McGlynn, and M.O. Henry, *Appl. Phys. Lett.* **102**, 192110 (2013).
- <sup>27</sup> M. Biswas, Y.S. Jung, H.K. Kim, K. Kumar, G.J. Hughes, S. Newcomb, M.O. Henry, and E. McGlynn, *Phys. Rev. B* **83**, 235320 (2011).
- <sup>28</sup> S. Tsoi, X. Lu, A.K. Ramdas, H. Alawadhi, M. Grimsditch, M. Cardona, and R. Lauck, *Phys. Rev. B* **74**, 165203 (2006).
- <sup>29</sup> F.J. Manjón, M. Mollar, M.A. Hernández-Fenollosa, B. Marí, R. Lauck, and M. Cardona, *Solid State Commun.* **128**, 35 (2003).

<sup>30</sup> E. Lavrov, F. Herklotz, and J. Weber, Phys. Rev. B **79**, 165210 (2009).

<sup>31</sup> H. Alawadhi, S. Tsoi, X. Lu, A.K. Ramdas, M. Grimsditch, M. Cardona, and R. Lauck, Phys. Rev. B **75**, 205207 (2007).

# Chapter 5: O Isotope-enriched ZnO Nanorods

## 5.1 Introduction

This chapter presents the results of the growth of ZnO nanorods enriched with the  $^{18}\text{O}$  isotope. These samples were produced using two separate methods as described in section 2.3. The first was a VS method carried out by modifying the CTR-VPT setup used in the growth of the Zn-enriched samples. The second was a VLS technique carried out in collaboration with colleagues in the Institute for Solid State Physics in the University of Jena, Germany. Specifically, this second set of growths was carried out by Mr. Lukas Trefflich and assisted by the author in the group of Prof. Carsten Ronning during a research visit by the author in September 2015, using isotopically enriched source powders produced beforehand in DCU by the author. The SEM images of these samples presented in section 5.2 were obtained during this visit by Mr. Trefflich and assisted by the author. Both sets of samples were characterised using SEM, XRD, SIMS, Raman spectroscopy and low temperature PL. In this chapter, some initial, unsuccessful, attempts to produce O-enriched nanostructures are described, followed by the results of the two successful methods. Table 5.1 presents a summary of the O-enriched ZnO nanorods successfully produced by the two methods, including those with natural  $\text{Zn}^{16}\text{O}$ , and

nominal  $\text{Zn}^{18}\text{O}$  and  $\text{Zn}^{16/18}\text{O}$ , compositions. They are distinguished by VS or VLS labels to indicate the growth method.

Label	Sample composition	Description
$\text{Zn}^{16}\text{O-VS}$	$\text{Zn}^{16}\text{O}$	Method 1: Modified VS CTR-VPT (in DCU)
$\text{Zn}^{16/18}\text{O-VS}$	$\text{Zn}^{16/18}\text{O}$	
$\text{Zn}^{18}\text{O-VS}$	$\text{Zn}^{18}\text{O}$	
$\text{Zn}^{16}\text{O-VLS}$	$\text{Zn}^{16}\text{O}$	Method 2: VLS VPT (in Jena)
$\text{Zn}^{16/18}\text{O-VLS}$	$\text{Zn}^{16/18}\text{O}$	
$\text{Zn}^{18}\text{O-VLS}$	$\text{Zn}^{18}\text{O}$	

*Table 5.1: Sets of O-enriched ZnO nanorods successfully produced using both methods.*

### 5.1.1 Initial Experiments regarding O-enriched Material

The process of devising a method to grow O-enriched ZnO nanorods proved significantly more difficult than for the Zn-enriched material. A number of attempts were made using the VPT furnace, however ultimately these attempts did not produce deposits of the nanorod morphology desired. More importantly, these deposits did not display the very high optical quality required for detailed PL studies of defects. These unsuccessful efforts are described briefly in this section in order to give some sense of the challenges involved. However, the rest of this chapter is devoted to the characterisation of samples produced using the two ultimately successful methods.

The central challenge confronting all these experiments is that we wished to be able to control the amount of  $^{18}\text{O}_2$  gas used (since this is an expensive material) and also to be able to remove as much as possible the ubiquitous  $^{16}\text{O}$  when we wished to grow fully  $^{18}\text{O}$  enriched material.

For this reason we looked firstly at a few methods centred on direct oxidation of Zn material, for which approach some recipes are available in the literature. The

tests of these growth recipes were all actually conducted with natural O in the first instance, to determine if nanostructured material of suitable morphology and optical quality would be obtained. We would naturally only have proceeded to the use of  $^{18}\text{O}_2$  in the event of successful growths with natural O. The first tests involved attempting to deposit some ZnO by heating Zn powder at temperatures around  $\sim 500$ - $600^\circ\text{C}$ , using CBD buffers or Au-coated Si, both in Ar flows and in oxygen atmospheres at low pressures. In some cases a slow temperature ramp was also used. Some of these experiments resulted in ZnO deposits on the inside of the quartz tube, but none resulted in nanostructure deposits on the substrates. This was followed by an attempt at growing nanowires from the Zn powder simply deposited on bare Si substrates by direct oxidation similar to reports in the literature.<sup>1,2</sup> However, the nanorods obtained by this method were of very poor optical quality. Another series of experiments using CBD buffer layers or Au-coated Si, a temperature of  $\sim 600$ - $900^\circ\text{C}$  and an oxygen atmosphere of  $\sim 10$  mbar was carried out. These resulted in ZnO deposits on the tube and placing the samples at different locations in the tube resulted in ZnO deposits, but again these were not nanostructured and were of poor optical quality.

We then decided that direct oxidation methods seemed rather unpromising, so experiments based on carrying out the normal VPT procedure, but with extra steps involving evacuation and backfilling the tube with an 21:79  $\text{O}_2:\text{N}_2$  mix, to simulate an air atmosphere, but using a smaller diameter tube were also unsuccessful. This approach was intended to allow us to control the O isotope in the artificial air atmosphere, but also to use a smaller amount of  $^{18}\text{O}_2$  in the smaller tube. In this case, although the Ar flow rate was adjusted proportionately to the tube cross sectional area, no deposits were obtained. This demonstrates just how sensitive the VPT process is to any change in parameters. A series of experiments were then carried out based on previous work in our group involving controlling the amount of oxygen in the tube with another MFC along with the Ar flow.<sup>3</sup> However these also did not lead to the desired nanorod growth, perhaps again due to changing parameters such as the tube size and oxygen flow, in order to minimise future enriched  $\text{O}_2$  gas usage. Finally, direct sublimation based on the work of Prof. Carsten Ronning's group<sup>4</sup> was attempted but was not successful due to our VPT furnace being limited in temperature to  $1100^\circ\text{C}$ .

While these experiments were not successful in achieving the desired ZnO nanorods of high structural and optical quality, they were important as they formed part of the process of guiding our thinking in terms of developing the growth methods which ultimately were successful. The rest of this chapter is devoted to those methods.

### 5.1.2 Method 1: Modified VS CTR-VPT method

As described in sections 2.3.1 and 4.1, the CTR-VPT growth used for the Zn-enriched growths is based on the reduction of ZnO powder by the graphite to produce Zn vapour and carbon monoxide (CO) by equation 4.1. The Zn vapour is then re-oxidised using the residual oxygen in the tube (rather than the O initially in the ZnO powder, which is captured by C to form CO) in a VS process at the energetically favourable sites provided by the CBD layer produced using the NaOH-based reaction. The work described in section 5.1.1 above in terms of evacuating and backfilling a smaller tube with a 21:79 O<sub>2</sub>:N<sub>2</sub> mix, to simulate an air atmosphere, but now using the normal CTR-VPT tube size was the natural next step. When this method was tried O-enriched ZnO nanorods were successfully produced by removing all the residual atmospheric O<sub>2</sub> from the tube by evacuation to 1 mbar, and then reintroducing O<sub>2</sub> gas with the desired isotopic content, and in the same amounts as typical atmosphere (~21%), along with N<sub>2</sub> gas (79%), to a total starting pressure of 1 atmosphere and carrying out the VPT growth as before. This method had the disadvantage of requiring significant quantities of isotopically enriched <sup>18</sup>O<sub>2</sub> gas, but was otherwise very successful. The samples produced with this procedure are labelled 'VS' as in table 5.1. In order to try and confirm that only the residual O<sub>2</sub>, which can be evacuated and replaced with <sup>18</sup>O<sub>2</sub>, contributes to the O in the ZnO nanorods, growth of a sample was attempted by this method in a nitrogen atmosphere only. This would confirm that there is no contribution of O from the ZnO source material, or from older deposited ZnO material on the tube from previous growths. Figure 5.1 shows an SEM image of this sample. The CBD buffer layer appears slightly cracked, perhaps due to thermal expansion at the VPT temperatures, and shows some grain alteration, but there is no evidence of VPT

nanowire growth and thus it was confirmed that no VPT nanorod growth occurred under these conditions. This is consistent with previous work in our group that found that the growth process is quenched when the residual  $O_2$  in the tube is sufficiently depleted by a longer Ar flow during the initial steps of the CTR-VPT process, e.g. after about 15-30 minutes Ar flow.<sup>3,5</sup>

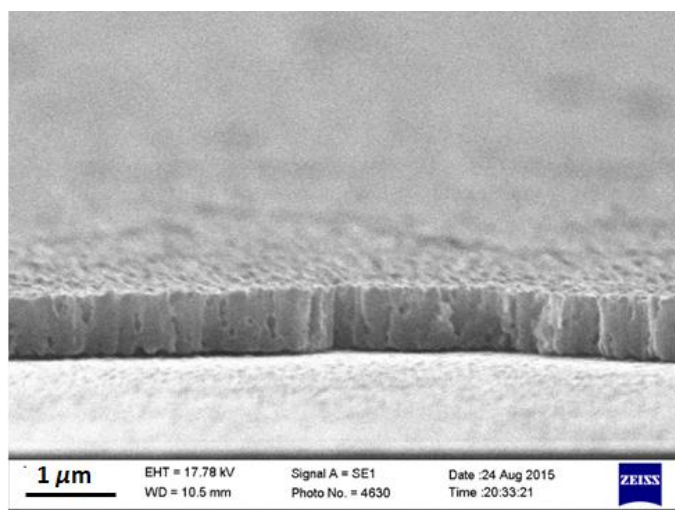


*Figure 5.1: Image of CBD buffer following VPT step in oxygen-depleted atmosphere. No nanorod growth is observed.*

### **5.1.3 Method 2: VLS VPT method**

We were aware that certain groups (including our collaborators in Jena) use a direct sublimation of ZnO powders to grow ZnO nanostructures (and that the O in the nanostructures comes from the initial powder). Given that we had developed some knowledge in how to directly oxidise Zn to create ZnO material (as described in section 5.1.1 above for the unsuccessful attempts) we decided that we could use a direct oxidation of Zn metal to “trap” the  $^{18}O$  to form a  $Zn^{18}O$  powder, which could then be used in the VLS VPT method. Having produced such powders we decided to go to our Jena collaborators to actually perform the VLS VPT growths, since our own furnace does not reach the required temperatures, but more importantly since they have the necessary experience in producing samples with such a method, and

establishment of a new growth method in a new location is quite a time-consuming task, even if one has the recipe, because of the sensitivity of such high temperature methods to a range of parameters, as commented on previously. Because we had effectively “trapped” the  $^{18}\text{O}$  to form a  $\text{Zn}^{18}\text{O}$  powder, we could transport the source material quite easily.

For this VLS method, as described in section 2.3.2, source powders of  $\text{ZnO}$  and isotopically enriched  $\text{Zn}^{18}\text{O}$  were produced in DCU by oxidising  $\text{Zn}$  metal powder. The samples were grown on substrates coated with  $\text{Au}$ . The  $\text{Au}$  coating melts during growth and forms droplets on the substrate which act as the energetically favourable nucleation sites. The nanorods in this case are not preferentially aligned as the  $\text{ZnO}$  is not epitaxially matched to  $\text{Si}/\text{SiO}_2$  and there is no textured CBD buffer layer in this case. The samples produced with this procedure are labelled ‘VLS’ as in table 5.1.

## 5.2 Morphology – SEM

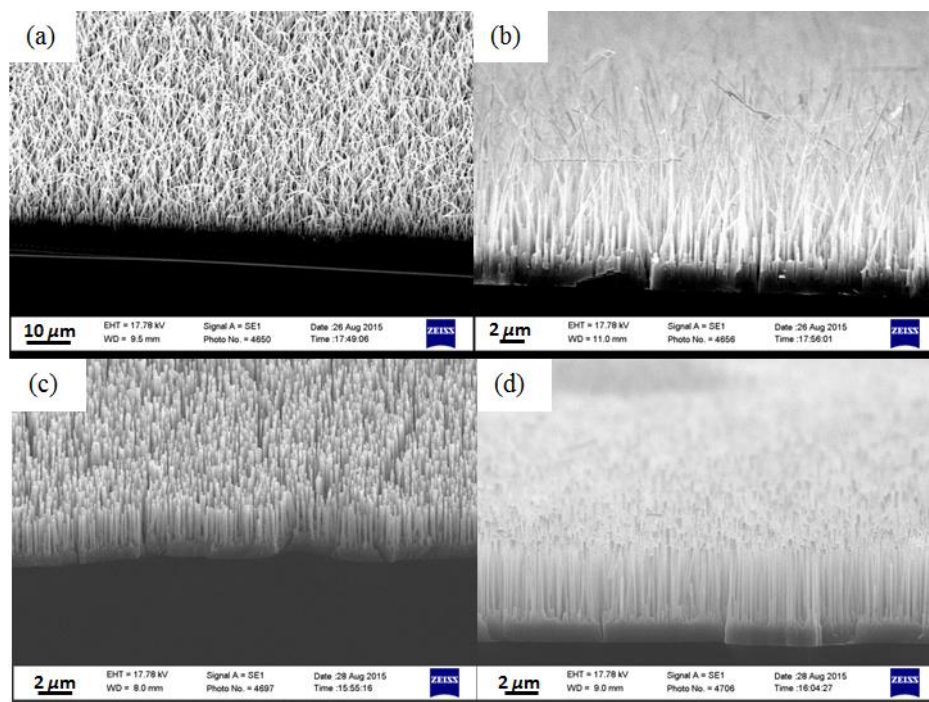


Figure 5.2: SEM images of sample  $\text{Zn}^{16}\text{O-VS}$  at (a)  $\sim 40^\circ$  and (b)  $\sim 90^\circ$ , and the middle of sample  $\text{Zn}^{16/18}\text{O-VS}$  at (c)  $\sim 40^\circ$  and (d)  $\sim 90^\circ$ .

Typical images of the morphology of the VS samples grown by method 1 are shown in figure 5.2. Figures 5.2(a) and (b) shows the morphology observed in the Zn<sup>16</sup>O-VS sample. This is also typical of the morphology observed in the Zn<sup>18</sup>O-VS sample, as well as near the edges of the Zn<sup>16/18</sup>O-VS sample. The morphology is similar to that shown in previously in figure 4.5(d), where the nanorods are on the order of 10 μm in length. They have become entangled as described previously in chapter 4. Figures 5.2(c) and (d) are from the middle part of the Zn<sup>16/18</sup>O-VS sample. In this case, the nanorods are the more typical 2-3 μm in length and are more clearly vertically aligned. In this case, the length of the nanorods increased, moving from the middle of the sample to the edge. It is interesting to note that for this sample a slightly longer Ar flush time was used than the other VS samples of about 6-7 minutes instead of 5 minutes. This is closer to the usual flush time as used in the Zn-enriched set. This would result in a smaller amount of residual O<sub>2</sub> in the tube as the temperature was increased and therefore shorter nanorods due to the growth ceasing when the residual oxygen levels are depleted. This provides a demonstration of just how extremely sensitive the VPT process is to the various parameters, in this case the residual oxygen content during the growth phase. Overall, the dimensions of these nanorods are in line with those previously described for the Zn-enriched samples in chapter 4. Coverage on these samples was excellent, with the entire sample coated with well aligned ZnO nanorods with high density and structural quality.

Figure 5.3 displays examples of the typical morphology observed using the SEM system in Jena of the VLS samples grown there using method 2. Of the 7-8 pieces of Au-coated Si placed in the furnace for these growths, ZnO nanorods were deposited typically on the middle three or four pieces, which were ~15 cm from the middle of the ZnO source powder. The temperature of the tube here was lower than at the centre of the furnace where the source powder was located, around ~950-1150°C<sup>4</sup>, and this appears to be a key parameter in whether deposits were observed on a particular piece, as the pieces were spread over a few cm.

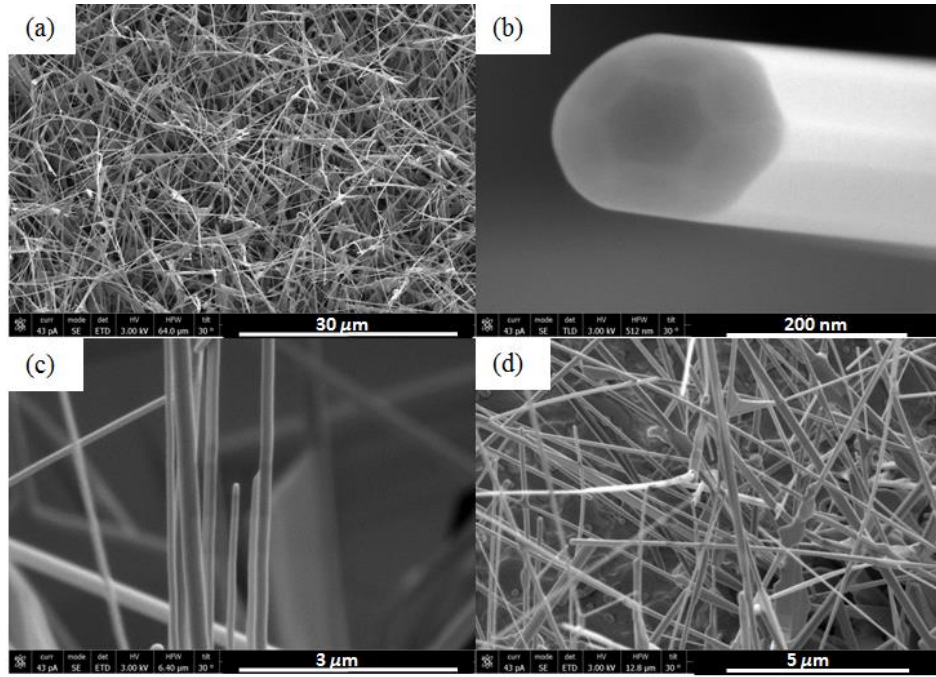


Figure 5.3: SEM images of the morphology of the VLS samples with  $30^\circ$  tilt; (a)  $\text{Zn}^{16}\text{O}$ -VLS, (b)  $\text{Zn}^{16}\text{O}$ -VLS showing hexagonal structure, (c)  $\text{Zn}^{18}\text{O}$ -VLS and (d)  $\text{Zn}^{16/18}\text{O}$ -VLS.

Figure 5.3(a) shows an example from the  $\text{Zn}^{16}\text{O}$ -VLS sample of the typical morphology observed on all the substrates with deposits across all three isotopic compositions as listed in table 5.1. The nanorods are generally longer than seen in the VS O- or Zn-enriched samples, with lengths of several tens of  $\mu\text{m}$  observed in all samples. The diameters of several individual nanorods were measured and were in the range of  $\sim 100\text{-}220$  nm, with most being between 120-150 nm. These dimensions agree with the ranges previously reported using this growth technique.<sup>4,6</sup> Figure 5.3(b) shows a close up of the end of a nanorod of  $\text{Zn}^{16}\text{O}$ -VLS clearly showing the hexagonal crystal structure associate with wurtzite material. Figures 5.3(c) and (d) are from the  $\text{Zn}^{18}\text{O}$ -VLS and  $\text{Zn}^{16/18}\text{O}$ -VLS samples respectively, and display similar morphology. The greatest difference in morphology between these samples and those grown with method 1 is that there is no preferential alignment of the nanorods along the  $c$ -axis. This is because of the lack of an epitaxially matched  $c$ -axis matched buffer layer in this case. Coverage on the substrates with deposits was excellent, with the entire surface containing these high density nanorods of high structural quality.

### 5.3 Alignment and Crystal Quality – XRD

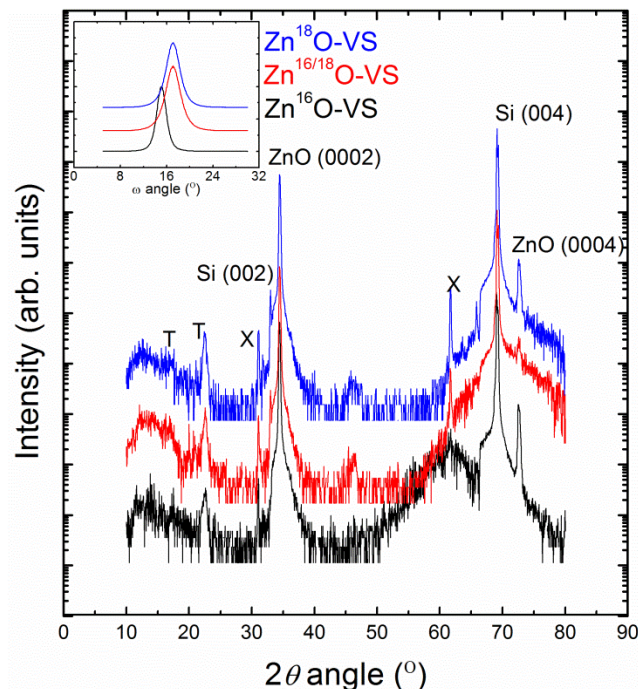


Figure 5.4:  $2\theta$ - $\omega$  diffractograms of the VS O-enriched samples dominated by the Si substrate peak at  $69.1^\circ$  and the ZnO peak at  $34.4^\circ$ . Inset shows rocking curves of the ZnO (0002) peak.

Figure 5.4 shows the  $2\theta$ - $\omega$  XRD scans of the VS samples grown with method 1. In this case, the diffractograms are similar to those of the Zn-enriched samples presented in section 4.3. The diffractograms are again dominated by the ZnO (0002) reflection at  $\sim 34.4^\circ$  and the Si (004) substrate reflection at  $\sim 69.1^\circ$ . The second order ZnO (0004) reflection and the forbidden Si (002) reflection<sup>7</sup> are present similar to the Zn-enriched samples, as also are some features assigned to the backing tape used to mount the samples and contamination from the x-ray tube<sup>8</sup>, marked T and X respectively. Table 5.2 lists the peaks position of the ZnO (0002) reflection and their FWHM. This strong reflection indicates successful deposition of wurtzite ZnO on the substrate. The narrow values of FWHM ( $<0.2^\circ$ ) indicate high crystal quality in terms of out-of-plane coherence length. The inset shows the rocking curves of the

ZnO (0002) reflection. Their peak positions and FWHM are listed in table 5.3. The high quality of the ZnO crystal structure, and the high degree of preferential alignment along the  $c$ -axis, is demonstrated by the narrow line widths of the rocking curves (1.96-3.08°). These data are again consistent with the SEM images of these samples presented in section 5.2. The peak position of the Zn<sup>16</sup>O-VS rocking curve is slightly shifted due to a variation in the tilt of the samples as mounted on the instrument stage.<sup>9</sup>

Sample	ZnO (0002) peak $2\theta$ (°)	ZnO (0002) FWHM $2\theta$ (°)	Crystalline size (nm)	ZnO $c$ lattice constant (nm)
Zn <sup>16</sup> O-VS	34.41	0.199	48	0.521
Zn <sup>16/18</sup> O-VS	34.45	0.189	52	0.521
Zn <sup>18</sup> O-VS	34.45	0.197	49	0.521
Zn <sup>16</sup> O-VLS	34.44	0.203	47	0.521
Zn <sup>16/18</sup> O-VLS	34.41	0.212	44	0.521
Zn <sup>18</sup> O-VLS	34.42	0.192	51	0.521

Table 5.2: ZnO (0002)  $2\theta$  peak and FWHM, and calculated crystallite size and  $c$  lattice constant for the VS and VLS O-enriched samples.

Sample	Rocking curve peak (°)	FWHM (°)
Zn <sup>16</sup> O-VS	16.00	1.96
Zn <sup>16/18</sup> O-VS	17.13	3.08
Zn <sup>18</sup> O-VS	17.13	2.86

Table 5.3: Peaks and FWHM of the rocking curves of the 34.4° ZnO (0002) reflection the VS O-enriched samples.

Figure 5.5 shows the corresponding  $2\theta$ - $\omega$  diffractograms for the VLS samples grown using method 2. The diffractograms have a distinctly different appearance to those previously observed in the VS samples and the Zn-enriched ones. The diffractograms are dominated by the Si (004) reflection of the substrate,

and the Si (002) reflection is again present. However, instead of being dominated by the ZnO (0002) reflection at  $34.4^\circ$  indicating *c*-axis aligned wurtzite ZnO, there are a number of peaks associated with different planes in wurtzite ZnO present. These include the *c*-plane (0002), the *m*-plane (10-10), the *s*-plane (10-11), the *r*-plane (10-12), the *a*-plane (11-20) and the (10-13) reflection. (These assignments are made using JCPDS card number 65-3411.<sup>10</sup>) The presence of such a number of different ZnO planes in the  $2\theta$ - $\omega$  spectrum indicates that the material is not preferentially aligned. Each nanorod is in a different orientation to their neighbours, and so there are some nanorods in the appropriate orientation for each of these planes to appear as their reflections satisfy the Bragg equation, i.e. an approximation to the powder pattern is seen. These measurements are consistent with the SEM images in section 5.2 for these samples which show nanorods have grown all directions without any preferential alignment. They are also consistent with the VLS growth method used which made use of Au catalyst and not a buffer layer of *c*-axis aligned nanorods. The peak positions of the ZnO (0002) reflection, and their FWHM, are shown in table 5.2. Again the FWHM ( $\sim 0.2$ ) indicated a high quality crystal structure has been deposited using this growth method. The inset of figure 5.5 shows the rocking curves of these reflections. However, in this case, the rocking curves have very large FWHM and are weaker due to the unaligned nature of the growth, as expected and in agreement with the  $2\theta$ - $\omega$  diffractograms generally and the SEM images of these samples.

The out-of-plane nanocrystallite sizes and the *c* lattice constants were calculated using the Scherrer relation (eqn. 4.2)<sup>11</sup> and the Bragg formula (eqn. 2.1) respectively for both the VS and VLS samples and are also shown in table 5.2. The crystalline sizes (44-52 nm) are similar to those calculated for the Zn-enriched samples, and the *c* lattice constant is at the expected value of 0.521 nm in all samples.<sup>12</sup> The error is  $\pm 7$  nm in the nanocrystallite size and  $\pm 0.004$  nm in the lattice constant.

Overall, these data indicate that ZnO nanorods of high quality crystal structure have been successfully produced using both the VS and VLS methods. Preferential alignment along the *c*-axis is displayed in the VS samples, but not in the VLS ones, in agreement with the SEM data and expectations arising from the growth methods used.

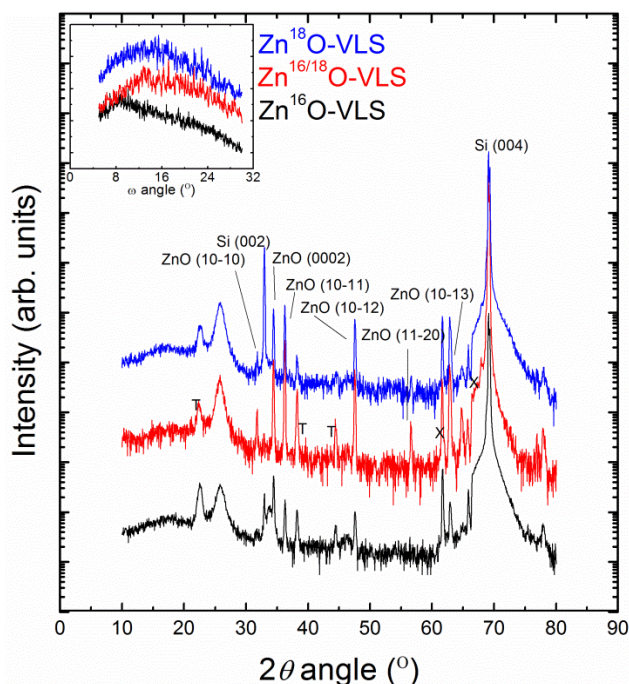


Figure 5.5:  $2\theta$ - $\omega$  diffractograms of the VLS O-enriched samples dominated by the Si substrate peak at  $69.1^\circ$  and containing multiple ZnO peaks. Inset shows rocking curves of the ZnO (0002) peak.

### 5.3.1 Note on Strain

The state of strain in a crystal can affect both the PL emission line energies as well as (though to a lesser extent) Raman line positions and this has relevance to some of our further characterisation measurements. The  $2\theta$ - $\omega$  diffractograms above provide information concerning the crystal state and strain in a direction perpendicular to the substrate, i.e. out-of-plane (due to the symmetric nature of the reflections), because this method essentially maps along a line in reciprocal space normal to the substrate. XRD also allows us to examine the sample crystallinity and strain along directions which are not perpendicular to the substrate (i.e. with an in-plane component) by mapping along a line in reciprocal space which is not normal to the substrate. Since the nanorods produced here are essentially ‘free standing’ structures (i.e. with nanorod sidewalls unconstrained by neighbouring material) on ZnO buffer layers, we expect that strain in these samples would be minimal, as each individual nanorod is essentially a small isolated single crystal in terms of structure.

The  $2\theta$ - $\omega$  diffractograms above confirm that we see no evidence of out-of-plane strain at the resolution of our XRD instrument. Using our scan step size of for these out-of-plane scans of  $0.05^\circ$ , this leads to a minimum detectable strain of 0.00145, and stress of 0.3045 GPa. In order to check for in-plane strain, the  $2\theta$  positions of a number of other planes in the  $c$ -axis aligned VS samples were measured by tilting the sample to suitable angles and then measuring the  $2\theta$ - $\omega$  diffractograms but with asymmetric reflections, which enables the mapping along a line in reciprocal space which is not normal to the substrate. Specifically, the  $s$ -plane and  $r$ -plane were selected for this measurement as they are among the stronger reflections. To access these reflections in the  $c$ -axis aligned nanorods, the samples were tilted in the XRD apparatus by the angle between these planes and the  $c$ -axis. This essentially aligned these planes with the x-ray source and detector as if they were vertical like the  $c$ -plane was previously. Figure 5.6 illustrates the general physics of this in a diagram, although the actual experimental setup was slightly different. Case (a) is the normal XRD set up with the  $c$ -planes parallel to the substrate satisfying Bragg's Law with symmetric reflections around the  $c$ -axis normal to the substrate. In case (b) the sample is tilted so that a different plane experiences the symmetric reflections to satisfy Bragg's Law, however now the reflections around the normal to the substrate are asymmetric, illustrated by angles  $\alpha$  and  $\beta$ . Finally, (c) shows the effect of this in reciprocal space, showing the mapping along a line which is not normal to the substrate.

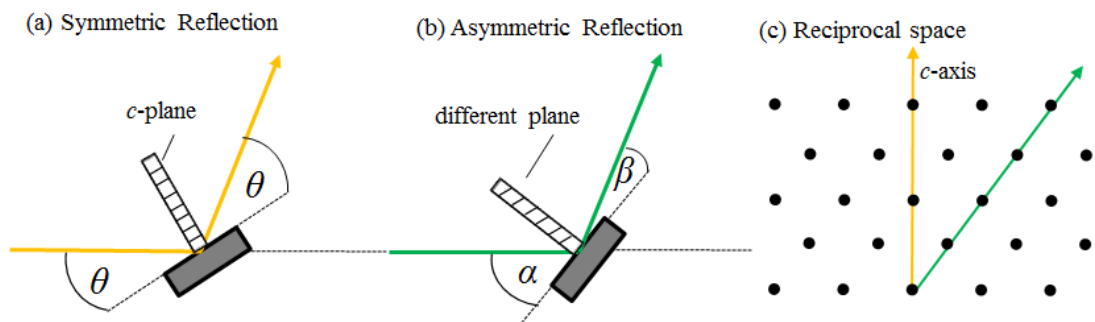


Figure 5.6: (a) Symmetric and (b) asymmetric XRD reflections, which enables (c) the mapping along a line in reciprocal space which is not normal to the substrate.

The angles of tilt needed were calculated using the formula for the angle between planes  $(hkl)_1$  and  $(hkl)_2$  in a hexagonal structure:

$$\cos \rho = \frac{h_1 h_2 + k_1 k_2 + \frac{1}{2}(h_1 k_2 + h_2 k_1) + \left(\frac{3a^2}{4c^2}\right) l_1 l_2}{\sqrt{\left\{ \left[ h_1^2 + k_1^2 + h_1 k_1 + \left(\frac{3a^2}{4c^2}\right) l_1^2 \right] \left[ h_2^2 + k_2^2 + h_2 k_2 + \left(\frac{3a^2}{4c^2}\right) l_2^2 \right] \right\}}}$$

Eqn. 5.1

where  $h$ ,  $k$  and  $l$  correspond to each plane using Miller notation,  $a$  and  $c$  are the ZnO lattice constants and  $\rho$  is the angle between planes. The angles of tilt calculated were  $61.6103^\circ$  for the  $s$ -plane and  $42.7728^\circ$  for the  $r$ -plane. A  $2\theta$ - $\omega$  scan was then performed in each case. Strain in the nanorods can be expected to appear in the spectra as a shift in the  $2\theta$  peak position as the peak angle and inter-planar distance are linked through the Bragg equation.<sup>13</sup>

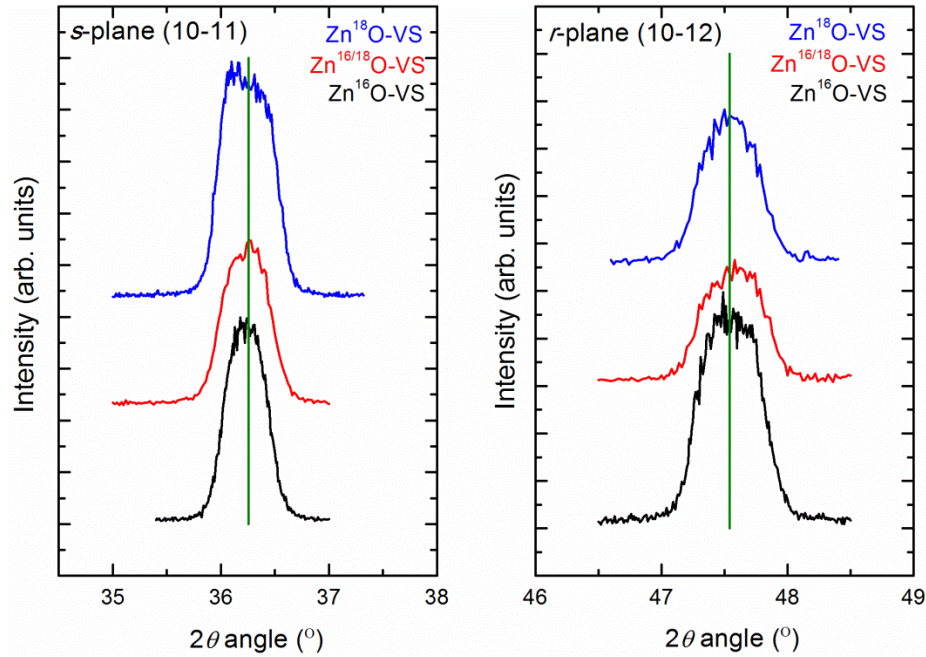


Figure 5.7:  $s$ -plane and  $r$ -plane  $2\theta$  peaks (with in-plane component) in the tilted VS O-enriched samples. The green vertical lines represent the calculated reference values from the JCPDS card number 65-3411<sup>10</sup>.

<b>Sample</b>	<b>ZnO <i>s</i>-plane (10-10) peak <math>2\theta</math> (°)</b>	<b>ZnO <i>r</i>-plane (10-12) peak <math>2\theta</math> (°)</b>
<b>Zn<sup>16</sup>O-VS</b>	36.253	36.544
<b>Zn<sup>16/18</sup>O-VS</b>	36.253	36.574
<b>Zn<sup>18</sup>O-VS</b>	36.248	36.543
<b>Zn<sup>16</sup>O-VLS</b>	36.258	47.543
<b>Zn<sup>16/18</sup>O-VLS</b>	36.230	47.530
<b>Zn<sup>18</sup>O-VLS</b>	36.244	41.549

*Table 5.4: *s*-plane and *r*-plane  $2\theta$  peaks in the VS (with in-plane component) and VLS O-enriched samples (from standard out-of-plane diffractograms for comparison).*

Figure 5.7 displays the *s*-plane and *r*-plane reflections with in-plane components in the *c*-axis aligned VS samples. The green lines represent the calculated reference values of  $36.256^\circ$  and  $47.541^\circ$  respectively (JCPDS card number 65-3411<sup>10</sup>) and the values observed are shown in table 5.4. Table 5.4 also includes the out-of-plane peak positions of these reflections in the non-aligned VLS samples for comparison. The peaks recorded for the VS samples in these out-of-plane scans were quite weak and noisier than the normal  $2\theta$ - $\omega$  scans due to the lack of epitaxial in-plane alignment of the nanowires meaning that only a fraction matched the diffraction condition for any azimuthal angular setting, and were also broader since the coherence length is geometrically shortened compared to the out-of-plane value. The peaks have very good agreement with the expected values, to within  $0.01^\circ$  in all but one case. The Zn<sup>16/18</sup>O-VS sample had the largest change, although this was still limited to  $\sim 0.03^\circ$  which is within the resolution limit of our XRD system. These data show that there is no detectable strain in these samples using our XRD system, which may cause shifts in the Raman phonon energies and PL band edge peaks, and that supports the other measurements indicating very high structural quality.

Note that between the submission of this thesis for examination and the *viva-voce* examination, the XRD strain measurements with an in-plane component described here for the VS O-enriched samples were carried out on the Zn-enriched samples and the VLS O-enriched samples, in order to complete this study on the full set of samples presented in this work. These data are presented in appendix C and ultimately indicate no discernible strain in agreement with this section.

## 5.4 Isotopic Enrichment – miniSIMS

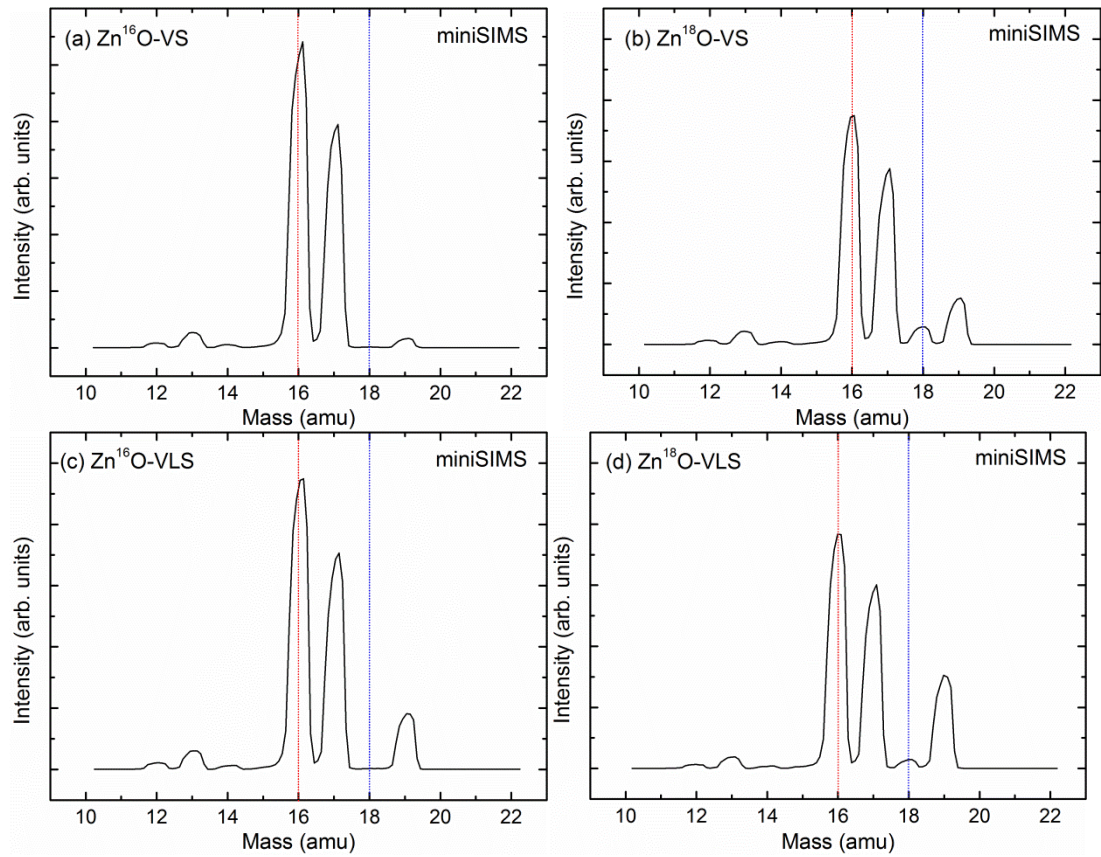


Figure 5.8: Typical miniSIMS spectra of the Zn<sup>16</sup>O and Zn<sup>18</sup>O samples in the VS set (a and b) and the VLS set (c and d).

While SIMS and miniSIMS measurements carried out on the Zn-enriched samples (section 4.4) were successful in confirming the high purity of isotopic enrichment in those samples, such measurements of the O-enriched samples proved

to be less successful. These were carried out using the miniSIMS system only as the SIMS system did not operate with the negative mode needed to measure negative ions such as  $O^-$ . Figure 5.8 shows typical miniSIMS spectra recorded for the (a)  $Zn^{16}O$ -VS, (b)  $Zn^{18}O$ -VS, (c)  $Zn^{16}O$ -VLS, and (d)  $Zn^{18}O$ -VLS samples. For the  $Zn^{16}O$  samples, (a and c), there is a large peak at 16 amu which is attributed to  $O^-$  ions, and nothing is observed at 18 amu. This indicated the presence of  $^{16}O$  as was expected for these samples. The peak at 17 amu is attributed to  $OH^-$  ions.

When testing the  $Zn^{18}O$  samples, it expected that these two peaks would shift to 18 amu and 19 amu respectively, and therefore indicate the presence of  $^{18}O^-$  and  $^{18}OH^-$  ions. This would be a nice confirmation of successful oxygen enrichment, analogous to the confirmation of Zn enrichment in those samples. However, as seen in figure 5.8(b and d), the  $Zn^{18}O$  only display a very small peak at 18 amu and the large peaks at 16 amu and 17 amu remain. While this shows the presence of  $^{18}O$  as expected, it does not give direct confirmation of enrichment because of the continued presence of  $^{16}O$ . It is strongly suspected that, since the samples are exposed to air, that adsorbed oxygen compounds on the samples lead to this result. The unenriched buffer layer in the VS samples, and the vacuum of only  $\sim 10^{-6}$  mbar in this system, could lead to the continued presence of natural oxygen and its compounds thus preventing a direct measurement of O-enrichment. It is also notable that one might expect to see a peak at 18 amu in any case due to  $H_2O$  molecules adsorbed in the sample or in the chamber, however this was not observed in these measurements as it is a positive ion.

A number of attempts were made to isolate the  $Zn^{18}O$  nanorods from such contamination. This included (i) using the depth profile mode to ‘dig’ into the sample and bypass surface contamination, (ii) imprinting the nanorods on a clean piece of Au wire which had been baked in vacuum by lightly pressing the sample face down in the Au surface, (iii) imprinting some nanorods on a fresh piece of Si which had its native oxide layer removed by etching with hydrofluoric acid. Despite these and other extensive attempts, we were unable to isolate the  $Zn^{18}O$  nanorods from such  $^{16}O$  contamination and all other spectra recorded resembled those in figure 5.8. However, even without such direct confirmation in this case, the Raman and PL data presented later in this chapter provide compelling evidence that O-enrichment has been successful in both the VS and VLS samples.

## 5.5 Phonon Frequencies and Enrichment – Raman

Raman spectroscopy was performed on both VS and VLS O-enriched samples, focussing on the  $E_2^{\text{high}}$  and  $E_2^{\text{low}}$  phonon modes as was done with the Zn-enriched samples in section 4.5, in DCU with the assistance of Dr. Rajani Vijayaraghavan.

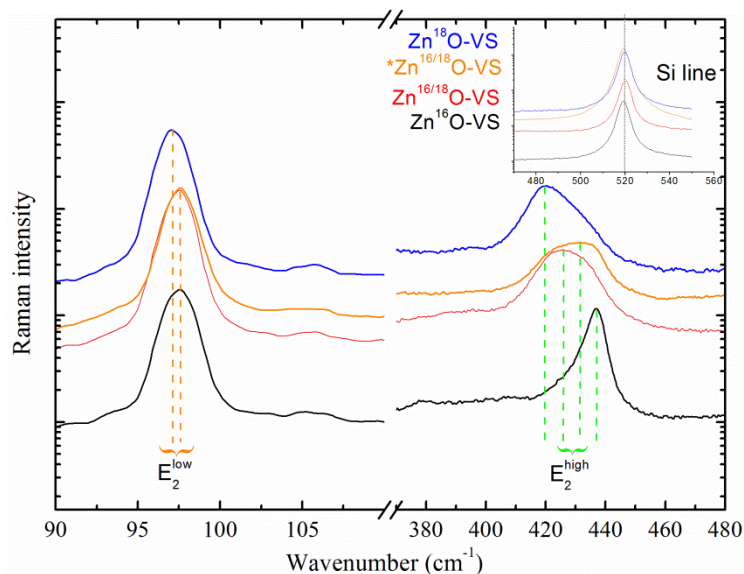


Figure 5.9: Raman spectra of the VS method O-enriched ZnO nanorods. Inset shows the signal from the Si substrate. \*Orange line is the second scan of the Zn<sup>16/18</sup>O-VS sample in middle of sample in region with shorter nanorods.

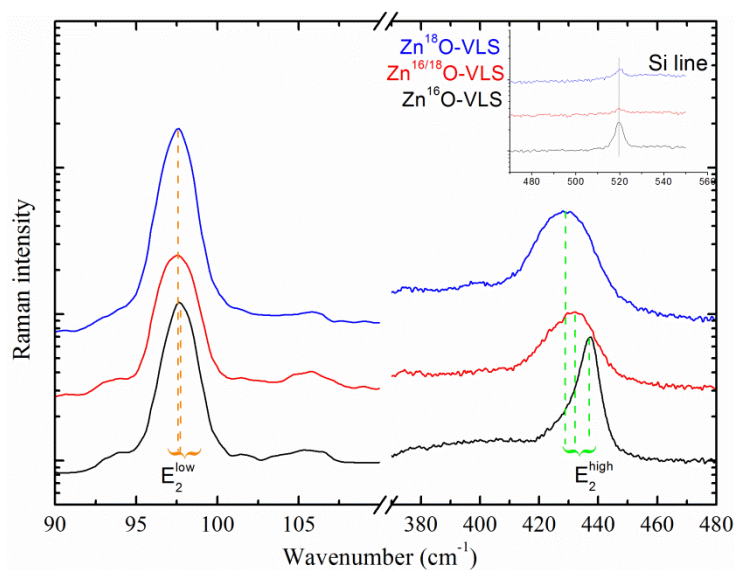


Figure 5.10: Raman spectra of the VLS method O-enriched ZnO nanorods. Inset shows the signal from the Si substrate.

Figures 5.9 and 5.10 show these spectra for the VS and VLS sets respectively. Table 5.5 gives the line phonon frequencies, their FWHM, and the differences in these from the Zn<sup>16</sup>O sample in each case. Note that in the case of the Zn<sup>16/18</sup>O-VS sample, Raman was performed both at the edge (where the morphology) matched the other samples in this set, and in the middle (where the nanorods were shorter as shown figure 5.2). This extra scan is shown in orange in figure 5.9 and marked with \* in table 5.5.

Changing the isotope from <sup>16</sup>O to <sup>18</sup>O, the E<sub>2</sub><sup>high</sup> mode induces a shift of 16.51 cm<sup>-1</sup> in the VS set and 8.42 cm<sup>-1</sup> in the VLS set. These figures are much larger than the 2.17 cm<sup>-1</sup> shift observed when changing the Zn isotope from <sup>64</sup>Zn to <sup>68</sup>Zn. This is not surprising as this mode is dominated by the O atom vibration and therefore we would expect a larger change when changing the O isotope than the Zn. Shifts of ~21 cm<sup>-1</sup> have been reported by Serrano *et al.* at low temperatures<sup>14</sup> and ~23 cm<sup>-1</sup> at room temperatures.<sup>15</sup> The widths of these lines, in the samples with <sup>18</sup>O included, are much larger than those observed for Zn enrichment, in some cases three times greater. Serrano *et al.* also observed the increase in line widths, and attributes the change in line widths in the isotopically pure samples to the ‘ridge’ in the two-phonon density of states in this region as discussed in section 4.5. The changing O masses shift the phonon frequencies along this ridge, which itself only depends on the Zn mass in the region of E<sub>2</sub><sup>high</sup> which they studied. There is an additional broadening effect for the mixed Zn<sup>16/18</sup>O samples, which they attribute to additional elastic scattering of phonons due to the O isotopic variations and a reduction in phonon lifetime as a result, and they observed this sample to have the widest line. It is noted that although the broad trends are in agreement with these reports, the widths recorded here are larger than those reported by Serrano *et al.*, who observed an increase in the widths of these lines from 6 cm<sup>-1</sup> to 11 cm<sup>-1</sup> moving from Zn<sup>16</sup>O to Zn<sup>18</sup>O at room temperature.<sup>15</sup> We observe such changes from 6 cm<sup>-1</sup> to 16 cm<sup>-1</sup>, and 6 cm<sup>-1</sup> to 18 cm<sup>-1</sup>, in the VS and VLS samples respectively. In addition, for the VLS samples, the Zn<sup>18</sup>O-VLS sample is the widest, not the Zn<sup>16/18</sup>O-VLS sample. It is also of note that the peak position of the middle and edge parts of Zn<sup>16/18</sup>O-VS don’t match, although we do not think morphology changes should have this effect.

The  $E_2^{\text{low}}$  mode however experiences very little change as this mode is Zn-dominated. The shifts of  $0.37 \text{ cm}^{-1}$  and  $0.14 \text{ cm}^{-1}$  are much smaller than the  $1.81 \text{ cm}^{-1}$  shift observed for this mode in the Zn-enriched samples. This mode also remains quite narrow in width and has only small changes in width, although larger than the changes in width seen with Zn isotope changes.

Sample	Mode	Wavenumber ( $\text{cm}^{-1}$ )	$\Delta$ Wavenumber ( $\text{cm}^{-1}$ )	FWHM ( $\text{cm}^{-1}$ )	$\Delta$ FWHM ( $\text{cm}^{-1}$ )
<b>VS samples</b>					
<b>Zn<sup>16</sup>O-VS</b>	$E_2^{\text{high}}$	436.85	-	6.73	-
<b>Zn<sup>16/18</sup>O-VS</b>	$E_2^{\text{high}}$	426.25	-10.6	20	13.27
<b>Zn<sup>16/18</sup>O-VS (*)</b>	$E_2^{\text{high}}$	430.43	-6.42	21.9	15.17
<b>Zn<sup>18</sup>O-VS</b>	$E_2^{\text{high}}$	420.34	-16.51	16.37	9.64
<b>Zn<sup>16</sup>O-VS</b>	$E_2^{\text{low}}$	97.51	-	2.1	-
<b>Zn<sup>16/18</sup>O-VS</b>	$E_2^{\text{low}}$	97.52	0.01	1.93	-0.17
<b>Zn<sup>16/18</sup>O-VS (*)</b>	$E_2^{\text{low}}$	97.59	0.08	1.92	-0.18
<b>Zn<sup>18</sup>O-VS</b>	$E_2^{\text{low}}$	97.14	-0.37	1.96	-0.14
<b>VLS samples</b>					
<b>Zn<sup>16</sup>O-VLS</b>	$E_2^{\text{high}}$	437.32	-	6.35	-
<b>Zn<sup>16/18</sup>O-VLS</b>	$E_2^{\text{high}}$	432.07	-5.25	16.27	9.92
<b>Zn<sup>18</sup>O-VLS</b>	$E_2^{\text{high}}$	428.9	-8.42	18.54	12.19
<b>Zn<sup>16</sup>O-VLS</b>	$E_2^{\text{low}}$	97.71	-	1.76	-
<b>Zn<sup>16/18</sup>O-VLS</b>	$E_2^{\text{low}}$	97.54	-0.17	2.32	0.56
<b>Zn<sup>18</sup>O-VLS</b>	$E_2^{\text{low}}$	97.57	-0.14	1.81	0.05

Table 5.5: Frequencies and FWHM of the  $E_2^{\text{low}}$  and  $E_2^{\text{high}}$  phonons for the VS and VLS O-enriched samples. \*Second scan of the Zn<sup>16/18</sup>O-VS sample in middle of sample in region with shorter nanorods.

While the Raman spectra indicate that O-isotopic enrichment has been successful in both sets, it appears to indicate a lower level of enrichment than expected, and additionally that the VLS samples have been enriched to a lesser

extent than the VS samples, resulting in smaller  $E_2^{\text{high}}$  mode Raman shifts. This is consistent with the PL data presented in the next section. The wider line widths in our samples, and in particular our  $\text{Zn}^{18}\text{O}$ -VLS sample which had a wider line than the  $\text{Zn}^{16/18}\text{O}$ -VLS samples, also indicate that O-enrichment may be lower than expected. Further discussion on the Raman and PL data regarding the enrichment levels is presented in chapter 6.

## 5.6 Optical Quality and Enrichment - Low temperature PL

Low temperature PL was carried out on all samples in both the VS and VLS set. The PL data is briefly introduced here using spectra recorded on the SPEX system and a more complete treatment, including all the PL data and the study of the Cu-related defect at 2.86 eV is presented in chapter 6.

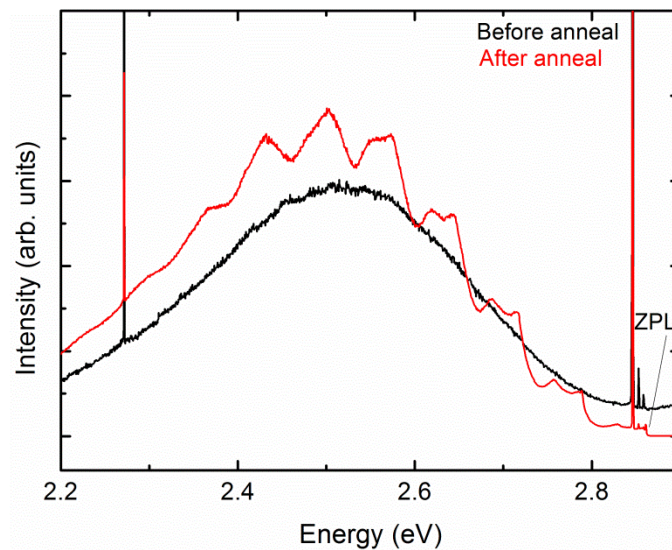


*Figure 5.11: Effect of the 900°C 10 minute anneal on the green band region. (Note the unstructured spectrum has been multiplied x10 for clarity. The intense, sharp lines are from the Hg lamp used for calibration.)*

The Cu-related SGB was not present in the spectra of the as prepared VS samples. All three of these samples were annealed at 900°C for ten minutes to

activate the SGB.<sup>16,17</sup> The only other difference in this case to the Zn-enriched samples which were annealed in this way is that the O-enriched samples were annealed in the atmosphere in which they were grown, i.e. ~79% N<sub>2</sub>, and ~21% <sup>16</sup>O<sub>2</sub>, <sup>18</sup>O<sub>2</sub> or mixed <sup>16/18</sup>O<sub>2</sub>. The effect of this anneal on the green band is shown in figure 5.11 using Zn<sup>16</sup>O-VS as an example. The SGB is present afterwards, displaying the 2.86 eV ZPL and LO replicas, with only a weak unstructured green band present in the as grown samples.

The features observed in both the VS and VLS samples were similar to those described in section 4.6 for the Zn-enriched samples. The spectra contain a strong band edge emission and a wide SGB (after anneal in the VS samples). The LO replicas are also present. Figure 5.12 shows the band edge spectra in detail for both (a) the VS samples and (b) the VLS samples. The main features are once again the In I<sub>9</sub> line and the Al I<sub>6</sub> line<sup>18,19</sup>. Other prominent features which appear include the SX feature<sup>20</sup> which is present in some of the VS samples and the ionised In I<sub>2</sub> line<sup>21</sup> and ionised Al I<sub>0</sub> line<sup>22</sup> which are present in the VLS samples. The position of the I<sub>9</sub> In BX recombination in unenriched material at ~3.356 eV was once again used to measure changes in the band edge positions, in this case with changing O isotope enrichment, and the other lines followed its trend. The positions of the I<sub>9</sub> line in each sample is given in table 5.6, along with their FWHM. There is an increase in energy as the O isotopic mass changes from natural <sup>16</sup>O to <sup>18</sup>O. This blue shift is ~3.24 meV in the VS sample set, and ~2.11 meV for the VLS samples. The changing positions of the band edge BX lines are strong evidence of successful isotopic enrichment of the samples. Manjón *et al.* have reported shifts of the BX recombinations of ~6 meV over this range.<sup>23</sup> In addition, Tsoi *et al.* have reported a similar shift of ~6 meV in the A-exciton band gap over this range.<sup>24</sup> Both of these measurements used single crystal samples.

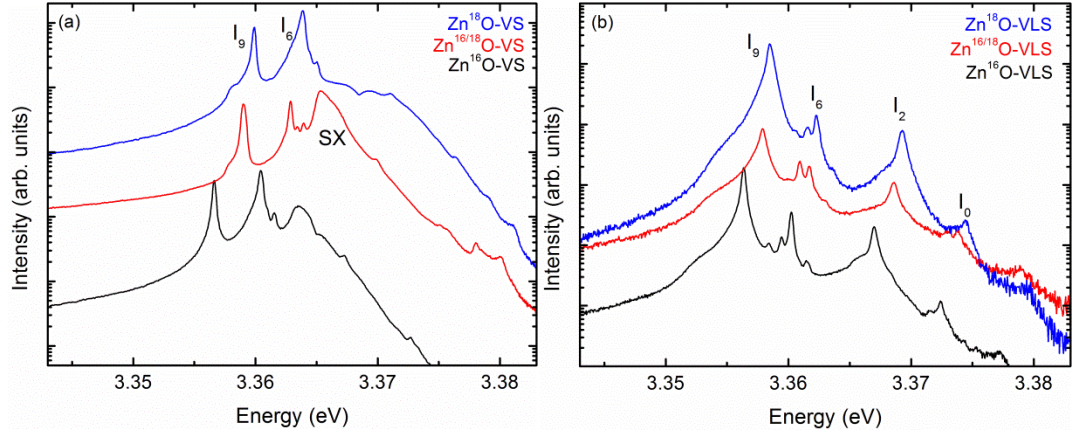


Figure 5.12: Band edge region of the PL spectrum in the (a) VS and (b) VLS O-enriched samples. (Spectra offset vertically for clarity.)

Sample	I <sub>9</sub> energy (eV)	I <sub>9</sub> FWHM (meV)
Zn <sup>16</sup> O-VS	3.35662	0.35
Zn <sup>16/18</sup> O-VS	3.35903	0.48
Zn <sup>18</sup> O-VS	3.35986	0.34
Zn <sup>16</sup> O-VLS	3.35635	0.41
Zn <sup>16/18</sup> O-VLS	3.35783	0.67
Zn <sup>18</sup> O-VLS	3.35846	0.80

Table 5.6: Peak positions and FWHM of the I<sub>9</sub> exciton recombination in the VS and VLS O-enriched samples.

The first thing to note about these figures is that these previously reported shifts are larger than those in our samples. This appears to indicate a lower level of enrichment than expected, and additionally that the VLS samples have been enriched to a lesser extent than the VS samples, compared to the enriched samples used in previous reports. This is consistent with the reduced phonon frequency changes observed in these samples in section 5.5, and is discussed further in chapter 6 regarding the levels of enrichment. The line widths of the BX lines in our VS and

VLS samples are, similarly to the Zn-enriched samples, very narrow ( $<1$  meV) and specifically much narrower than those reported by Manjón *et al.* ( $<5$  meV) or Tsoi *et al.* (2-8meV) in their single crystal samples. The very narrow line widths in our VS and VLS samples once again demonstrate their excellent optical quality and their potential for use in detailed optical studies of defects and impurities using low temperature PL.

## 5.7 Conclusions

Two methods have been developed to ZnO nanorod samples isotopically enriched with  $^{18}\text{O}$ . Firstly the modified three-step process used to grow Zn-enriched ZnO nanorods as discussed in chapter 4 has been further modified, by replacing the atmospheric  $\text{O}_2$  with enriched  $^{18}\text{O}_2$ , in order to grow O-enriched ZnO nanorods using this VS method on CBD buffer layers. In addition, O-enriched ZnO nanorods were successfully grown in collaboration with our colleagues in Jena, using isotopically enriched source powders, produced in DCU, in their VLS growth system. SEM studies confirmed the success of both growth methods in terms of nanostructure morphology, although in the case of the VLS samples, the nanorods were not *c*-axis aligned due to the nature of the substrate used. A variety of XRD scans of the VS samples indicated that these samples are not strained at the limit of detection of our XRD system. miniSIMS spectra clearly showed the presence of  $^{16}\text{O}$  in the natural samples, and although it showed the presence of  $^{18}\text{O}$  as expected in enriched samples, it did not give direct confirmation of enrichment because of the continued presence of  $^{16}\text{O}$  contamination from a number of sources. However, Raman and PL studies indicated clearly that O-enrichment was successful in both cases, although the figures indicate the enrichment may be at a lower level in our samples compared to previous reports with the same nominal enrichment levels. This is discussed further in the next chapter. The very narrow line widths in our VS and VLS demonstrate their excellent optical quality and their potential for use in detailed optical studies of defects and impurities using low temperature PL.

## 5.8 References

- <sup>1</sup> T.-W. Koo and D. Whang, *Nano* **03**, 477 (2008).
- <sup>2</sup> A. Umar, S.H. Kim, and Y.B. Hahn, *Superlattices Microstruct.* **39**, 145 (2006).
- <sup>3</sup> R.B. Saunders, S. Garry, D. Byrne, M.O. Henry, and E. McGlynn, *Cryst. Growth Des.* **12**, 5972 (2012).
- <sup>4</sup> C. Borchers, S. Mu, D. Stichtenoth, D. Schwen, and C. Ronning, *J. Phys. Chem. B* **110**, 1656 (2006).
- <sup>5</sup> R.B. Saunders, *Theoretical and Experimental Studies of ZnO Nanowires Grown by Vapour Phase Transport*, Dublin City University, 2012.
- <sup>6</sup> M.A. Zimmler, T. Voss, C. Ronning, and F. Capasso, *Appl. Phys. Lett.* **94**, 241120 (2009).
- <sup>7</sup> B.-H. Hwang, *J. Phys. D. Appl. Phys.* **34**, 2469 (2001).
- <sup>8</sup> R.T.R. Kumar, E. McGlynn, M. Biswas, R. Saunders, G. Trolliard, B. Soulestin, J.-R. Duclere, J.P. Mosnier, and M.O. Henry, *J. Appl. Phys.* **104**, 084309 (2008).
- <sup>9</sup> E. McCarthy, R.T. Rajendra Kumar, B. Doggett, S. Chakrabarti, R.J. O’Haire, S.B. Newcomb, J.-P. Mosnier, M.O. Henry, and E. McGlynn, *J. Phys. D. Appl. Phys.* **44**, 375401 (2011).
- <sup>10</sup> International Centre for Diffraction Data. Joint Committee on Powder Diffraction Standards (JCPDS) Database. Available at: <http://www.icdd.com/>
- <sup>11</sup> V. Mote, Y. Purushotham, and B. Dole, *J. Theor. Appl. Phys.* **6**, 6 (2012).
- <sup>12</sup> S. Desgreniers, *Phys. Rev. B* **58**, 14102 (1998).
- <sup>13</sup> B.D. Cullity and S.R. Stock, *Elements of X-Ray Diffraction*, 3rd ed. (Prentice Hall, New Jersey, 2001).
- <sup>14</sup> J. Serrano, F. Widulle, A.H. Romero, A. Rubio, R. Lauck, and M. Cardona, *Phys. Status Solidi* **235**, 260 (2003).
- <sup>15</sup> J. Serrano, F. Manjón, A. Romero, F. Widulle, R. Lauck, and M. Cardona, *Phys. Rev. Lett.* **90**, 055510 (2003).
- <sup>16</sup> G. Xing, G. Xing, M. Li, E.J. Sie, D. Wang, A. Sulistio, Q. Ye, C.H.A. Huan, T.

Wu, and T.C. Sum, *Appl. Phys. Lett.* **98**, 102105 (2011).

<sup>17</sup> N.Y. Garces, L. Wang, L. Bai, N.C. Giles, L.E. Halliburton, and G. Cantwell, *Appl. Phys. Lett.* **81**, 622 (2002).

<sup>18</sup> S. Müller, D. Stichtenoth, M. Uhrmacher, H. Hofsäss, C. Ronning, and J. Röder, *Appl. Phys. Lett.* **90**, 012107 (2007).

<sup>19</sup> M. Schilling, R. Helbig, and G. Pensl, *J. Lumin.* **33**, 201 (1985).

<sup>20</sup> M. Biswas, Y.S. Jung, H.K. Kim, K. Kumar, G.J. Hughes, S. Newcomb, M.O. Henry, and E. McGlynn, *Phys. Rev. B* **83**, 235320 (2011).

<sup>21</sup> J. Cullen, D. Byrne, K. Johnston, E. McGlynn, and M.O. Henry, *Appl. Phys. Lett.* **102**, 192110 (2013).

<sup>22</sup> B.K. Meyer, J. Sann, S. Lautenschläger, M.R. Wagner, and A. Hoffmann, *Phys. Rev. B* **76**, 184120 (2007).

<sup>23</sup> F.J. Manjón, M. Mollar, M.A. Hernández-Fenollosa, B. Marí, R. Lauck, and M. Cardona, *Solid State Commun.* **128**, 35 (2003).

<sup>24</sup> S. Tsoi, X. Lu, A.K. Ramdas, H. Alawadhi, M. Grimsditch, M. Cardona, and R. Lauck, *Phys. Rev. B* **74**, 165203 (2006).

# **Chapter 6: Optical Properties and the Cu-related Defect in Isotopically Enriched ZnO**

## **6.1 Introduction**

The optical properties of isotopically enriched ZnO nanorods are a central focus of this work, as the high optical quality of the material produced allows detailed study of such properties at low temperatures. This chapter presents the full set of low temperature PL data, from both the SPEX and FT spectroscopic systems, and from the Zn- and O- enriched samples grown by the three novel methods as presented in chapter 4 and 5. Specifically, the near band edge data is first presented, followed by the SGB ZPL, data for each set. These results are used in subsequent study of the Cu-related defect at 2.86 eV regarding any involvement of native defects. Not every spectrum for every sample is presented, but a sub-set representative of those observed in all samples is shown. Both the SPEX and FT systems were used to record spectra of the band edge regions and the green band ZPLs of each sample and the spectra are treated as described in chapter 2.

There has been a reasonable degree of prior study of FX and Raman feature behaviour in isotopically enriched ZnO, but much less work done on BX emissions.

Based on previous work in the field<sup>1-3</sup>, we have worked on the assumption that the FX binding energy is unaffected by isotopic mass and thus that the FX and shallow BX features follow the band gap variation with isotopic mass. Such an assumption is not generally valid for all materials<sup>4-6</sup> but has been shown to be valid for ZnO and allows us to compare our BX and deep emission data with the FX behaviour reported previously.

## 6.2 Zn-enriched Nanorods

### 6.2.1 PL Spectra

Figure 6.1 shows the band edge and Cu-related 2.86 eV ZPLs as recorded on the SPEX and FT systems for the Zn-enriched samples. (Figure 6.1(a) is the same as previously presented in figure 4.15.) Figure 6.1(a) and 6.1(b) show representative spectra from the SPEX and FT systems from the band edge region using the ‘pure’ isotope samples. The samples with mixed isotopic distributions produced similar spectra. The SPEX system produces much less noisy spectra than the FT. The dominant feature in the spectra is the I<sub>9</sub> line attributed to In impurities which is of particular interest, as shown below.<sup>7</sup> The I<sub>8</sub> and I<sub>6</sub> lines attributed to Ga and Al impurities are also clearly observed.<sup>7-9</sup> The I<sub>2</sub> line attributed to ionised In impurities<sup>10</sup> and the surface exciton<sup>11</sup> (SX) emission are also visible and labelled in the figure. These impurities most probably come from the laboratory environment where the growth takes place, for example from the alumina boat, or the source powders. Overall the SPEX spectra are very detailed and have good signal to noise ratios, while the FT spectra suffer from slightly more noise, probably due to the smaller dynamic range of the instrument and the very high intensity of the band edge emissions from these samples, which is particularly apparent when shown on a log scale as in this figure. However, the position of the I<sub>9</sub> line can still be determined with high accuracy. The I<sub>6</sub> line is the only other readily identifiable line in the FT spectra.

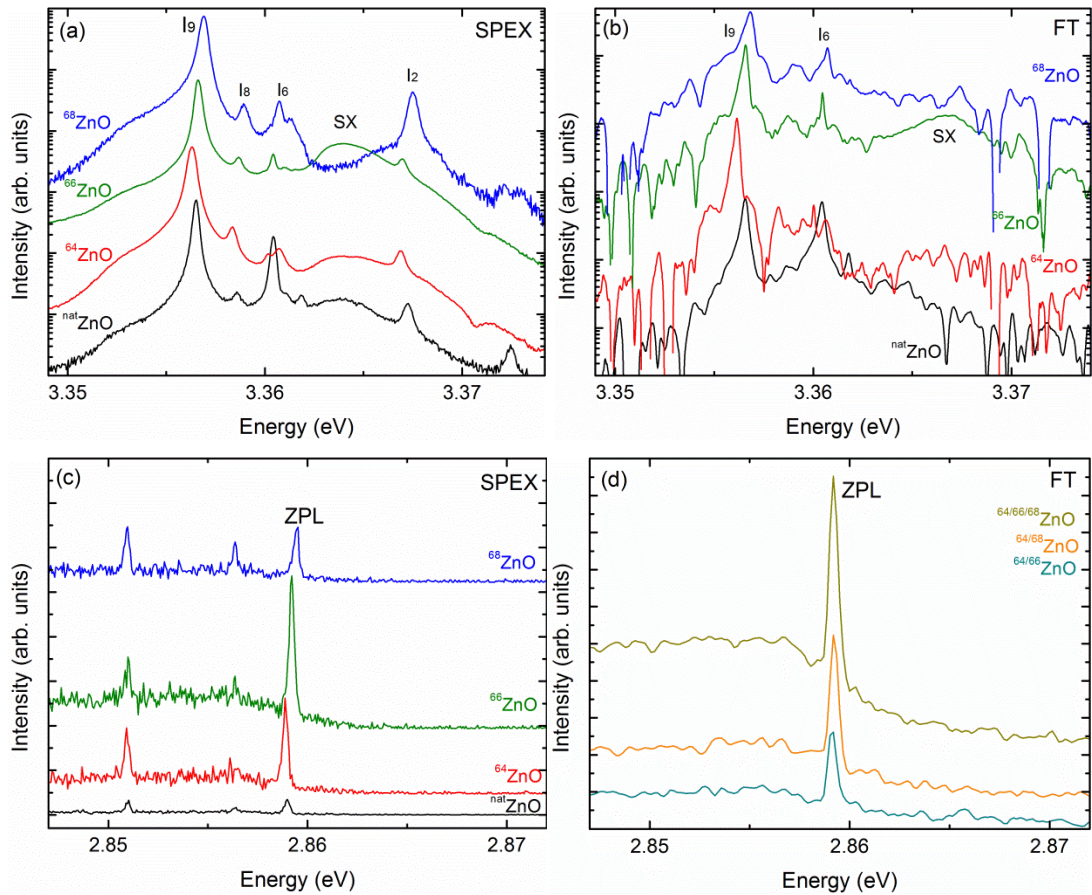


Figure 6.1: Band edge (a and b) and Cu-related 2.86 eV ZPL (c and d) spectra from the Zn-enriched samples from the SPEX system (a and c) and the FT system (b and d), (spectra shifted vertically for clarity).

In contrast to the band edge spectra, the FT system is more suited to recording the deep level ZPL spectra, as shown in figure 6.1(c) and (d). This stems mainly from the diffraction grating in the SPEX monochromator, which is blazed so to be most effective in the band edge region. It is much less efficient around the ZPL and green band region. It was therefore difficult to obtain spectra of the ZPL on the SPEX system. A portion of each sample was annealed for ten minutes at 900°C to try and increase the green band intensity for the SPEX scans.<sup>12</sup> This was successful in the cases of  $^{64}\text{ZnO}$ ,  $^{66}\text{ZnO}$  and  $^{68}\text{ZnO}$ . The ZPLs shown for these samples have been taken from annealed samples. The ZPLs for the other samples are not from annealed samples. This is because, in those cases, the samples gave more intense, less noisy spectra before annealing than after. This could be due to the self-limiting nature of the SGB intensity in ZnO.<sup>13</sup> As the concentration of Cu grows, the

luminescence intensity increases but then begins to decrease. The concentration of Cu was not controlled in this experiment. Nevertheless, the intensities of the ZPLs in the mixed samples are notably weaker than the others, and their spectra are therefore noisier. Variation in intensity between samples is also observed in the FT spectra, where none of the samples were annealed. However the FT spectra of the ZPLs were much less noisy than the SPEX ones for most samples, such as the mixed isotope samples shown here for example. Overall the variations in intensity could be attributed to differences in Cu content and slight differences in optical alignment between samples.

### **6.2.2 Discussion on Energy Shifts and Involvement of $Zn_i$ or $V_O$ in the Cu-related Emission at 2.86 eV**

In order to determine if there is any involvement of  $Zn_i$  or  $V_O$  in the Cu-related 2.86 eV ZPL and associated SGB in ZnO, we compare the shifts and line widths in exciton recombination energies in the band edge region with those of the 2.86 eV ZPL. Band edge energy shifts were observed in these samples (both Zn-enriched and O-enriched) when the isotopic content of the crystal was changed, as presented in chapters 4 and 5, due to the change in mass and corresponding change in the energy of the vibrational states involving the defect and the surrounding lattice due to the isotope effect as discussed in chapter 3. This isotope effects both the BX positions in the band edge, as well as the Cu-related ZPL. However if a native defect, such as an interstitial or vacancy, was also involved in the 2.86 eV ZPL, in addition to the Cu substitutional atom, then we could expect a different shift and also possibly a different line width to occur here. This is because the additional native defect would result in a change in the local configuration and/or vibrational properties at this defect site that would not be present for the shallow donor bound defects. We can therefore look for any evidence of native defect involvement in the 2.86 eV ZPL by examining the positions and line widths of the BX at the band edge and the 2.86 eV ZPL and looking for any relative energy shift between them or change in line width when the isotopic content of the surrounding crystal is changed.

Any relative shifts could indicate the presence of  $Zn_i$  or  $V_O$  native defects complexing with the Cu atom in this defect. A substitutional Cu atom on a Zn site is surrounded by O atoms in the lattice. An additional Zn atom complexing with the Cu atom, or indeed a missing O atom (and the corresponding effects on the Zn atoms surrounding the O vacancy), could affect the local vibrational environment in such a way as to produce an anomalous shift relative to the vibrational changes induced in the background lattice by changes in the Zn isotopic masses in the lattice. Only changes in the background lattice would affect the  $I_9$  BX, which is known with confidence to be due to an isolated In atom substituting on a Zn site ( $In_{Zn}$ )<sup>14</sup>, with no complexing with native defects, and in any case this bound exciton is loosely localised and thus samples a large crystal area and is less sensitive to the local environment of the  $In_{Zn}$ . Thus the shift in the  $I_9$  line serves as a natural reference reflecting the changes in the background lattice only. However, an additional native defect in the Cu defect would produce a distinct change in vibrational environment since the carriers in this defect are much more strongly localised and thus will be strongly affected by both the local defect environment as well as the changes in the background lattice, and hence the relative energy shift between the defect ZPL and the  $I_9$  emission provides a method whereby the presence of such local complexing phenomena can be studied.

The position of the  $I_9$  In BX recombination was selected as a reference energy to measure changes in the band edge positions with changing isotope enrichment. The positions and line widths of the  $I_9$  line and the Cu-related 2.86 eV ZPL were measured in each sample by fitting Gaussian curves to these peaks. This was done for both the SPEX spectra and the FT spectra separately.

Sample	Average Zn		$I_9$ energy (eV)	$I_9$ FWHM (meV)	ZPL energy (eV)	ZPL FWHM (meV)
	isotopic content (amu)					
$^{64}\text{ZnO}$	64		3.35629	0.44	2.85888	0.30
$^{66}\text{ZnO}$	66		3.35662	0.36	2.8592	0.30
$^{68}\text{ZnO}$	68		3.35689	0.41	2.85942	0.30
$^{64/66}\text{ZnO}$	65		3.35641	0.33	2.85917	0.20
$^{66/68}\text{ZnO}$	67		3.35682	0.33	2.85929	0.43
$^{64/68}\text{ZnO}$	66		3.35643	0.35	2.85914	0.10
$^{64/66/68}\text{ZnO}$	66		3.35603	0.35	2.85909	0.34
$^{\text{nat}}\text{ZnO}$	65.4		3.35650	0.31	2.85897	0.31

Table 6.1: Energies and widths of the  $I_9$  and ZPL lines in Zn-enriched ZnO, from the SPEX system.

Sample	Average Zn		$I_9$ energy (eV)	$I_9$ FWHM (meV)	ZPL energy (eV)	ZPL FWHM (meV)
	isotopic content (amu)					
$^{64}\text{ZnO}$	64		3.35616	0.25	2.85897	0.60
$^{66}\text{ZnO}$	66		3.35660	0.25	2.85925	0.47
$^{68}\text{ZnO}$	68		3.35683	0.38	2.85951	0.53
$^{64/66}\text{ZnO}$	65		3.35635	0.30	2.85913	0.51
$^{66/68}\text{ZnO}$	67		3.35666	0.22	2.85940	0.47
$^{64/68}\text{ZnO}$	66		3.35647	0.30	2.85922	0.50
$^{64/66/68}\text{ZnO}$	66		3.35655	0.34	2.8592	0.55
$^{\text{nat}}\text{ZnO}$	65.4		3.35657	0.33	2.85918	0.53

Table 6.2: Energies and widths of the  $I_9$  and ZPL lines in Zn-enriched ZnO, from the FT system.

For the Zn-enriched samples, the positions and line widths of each of the  $I_9$  lines and ZPL lines, for both the SPEX and FT systems, are shown in tables 6.1 (SPEX) and 6.2 (FT). The positions of the lines from the SPEX and FT systems are quite consistent. The average difference between the readings with the two systems for the  $I_9$  line peaks is 0.13 meV, with the largest difference being 0.52 meV. Similarly, for the ZPLs, the average is 0.1 meV with the largest difference being 0.21 meV. There is therefore very good agreement on the line positions between the two systems and the line widths are also consistent across all samples for both BX and ZPL emissions. We note that the optical quality of the material is excellent, with BX line widths from the SPEX system given in section 4.6 are far smaller ( $< 1$  meV) than those reported by previous authors of  $< 5$  meV, and 2-8 meV.<sup>15,16</sup> No particular trend is evident regarding  $I_9$  or ZPL line width changes with isotopic mass.

The following figures present the data from tables 6.1 and 6.2 in visual format. Figure 6.2(a) contains data from the SPEX system and figure 6.2(b) contains data from the FT system. In each graph, the left hand y-axis (black) shows the  $I_9$  energies, and the right hand y-axis (blue) shows the ZPL energies. The  $I_9$  axes both cover the same range (3.3559 - 3.357 eV), and the ZPL axes also cover this range of 1.1 meV but with these axes shifted to align the ZPL energy and the  $I_9$  energy in the  $^{64}\text{ZnO}$  sample at the same point on each graph. In this way, it is easy to observe the shifts of both the  $I_9$  and ZPL energies in each sample with changing isotopic composition, and to compare any changes between them. The error bars of the graphs represent the resolution for each scan to give an indication of the accuracy of the positions. These are again  $\pm 0.035$  meV for the  $I_9$  lines and  $\pm 0.045$  meV for the ZPLs on the SPEX and  $\pm 0.007$  meV for the  $I_9$  lines and  $\pm 0.07$  meV for the ZPLs on the FT.

We first consider the results for the SPEX system in figure 6.2(a). The  $I_9$  energy increases with increasing Zn isotopic mass from  $^{64}\text{ZnO}$  to  $^{68}\text{ZnO}$  by 0.6 meV (as described in section 4.6). Similarly, the ZPL energy increases by 0.54 meV. The difference energy change here is 0.06 meV. Now turning to the FT system, in figure 6.2(b) the  $I_9$  energy increases when moving from  $^{64}\text{ZnO}$  to  $^{68}\text{ZnO}$  by 0.67 meV and the ZPLs increase by 0.54 meV. The difference in energy change here is 0.13 meV.

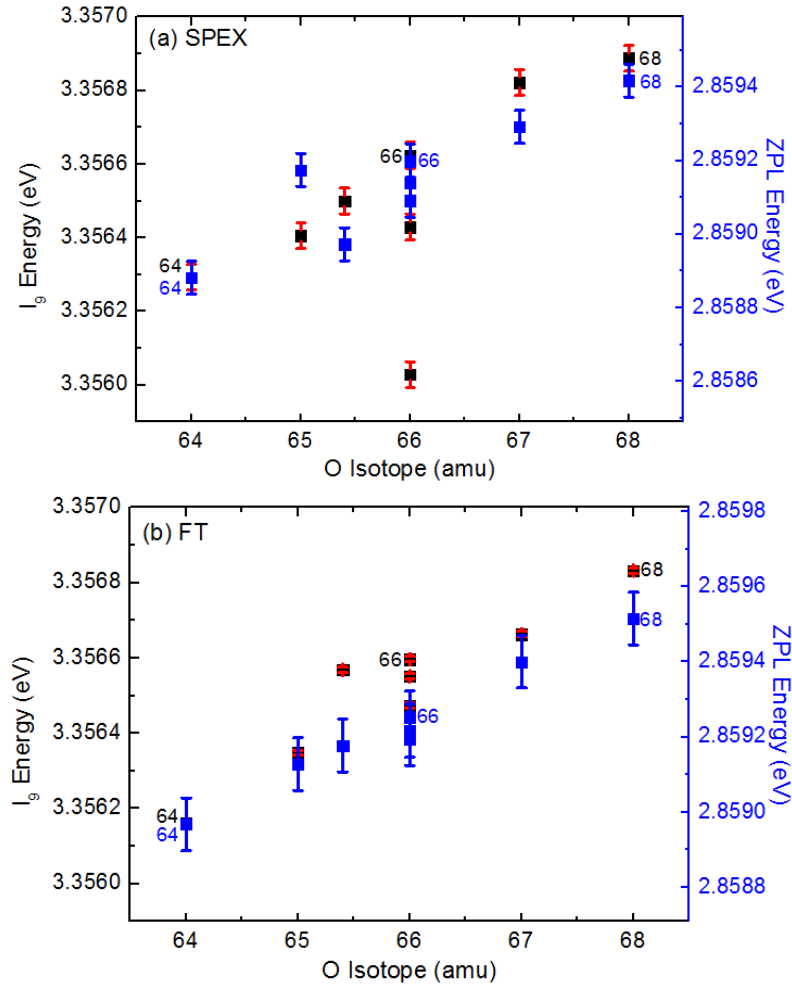


Figure 6.2: Energies of the  $I_9$  lines (black) and Cu-related ZPL lines (blue) in the Zn-enriched ZnO samples, from the (a) SPEX and (b) FT systems.

The trends shown in figure 6.2 clearly indicate that there is a consistent increase in  $I_9$  and ZPL line positions from  $^{64}\text{ZnO}$  to  $^{68}\text{ZnO}$  of  $\sim 0.6$  meV and that the relative energy shifts are as small as  $\sim 0.1$  meV. This latter figure is in the region of the difference in line position between scans with the SPEX and FT systems. It is also close to the step sizes of the ZPL scans on each system, indicating that it is close to the experimental error considering the scan resolutions. These trends are clearly shown when considering the  $^{64}\text{ZnO}$ ,  $^{66}\text{ZnO}$  and  $^{68}\text{ZnO}$  samples as marked. There are some outliers, particularly with the 1/3 mixed isotope sample in figure 6.2(a). This could be attributed to the very weak ZPLs recorded by the SPEX for these samples making it difficult to determine the peaks clearly due to noise. It is also the case in the mixed samples that, despite careful mixing of the powders, the amount of each

powder consumed during growth and therefore deposited on the sample may not have been exactly equal. This may result in the average isotopic mass being slightly different than desired, and hence the positions on the graphs.

The figures from both SPEX and FT data are consistent with each other. The increases in band edge and ZPL positions are of the same order as those reported previously for ZnO single crystals.<sup>15,16</sup> There appears to be neither a significant shift in ZPL position relative to the band edge position nor any change in line width of this feature. Furthermore, there is no significant change in line width of the I<sub>9</sub> line across the set of samples. Taken together, the absence of a discernible relative spectral shift, in addition to the constant line width of the I<sub>9</sub> and ZPL features for all samples, along with previous work showing that the Cu atom in this defect is on a Zn site and therefore surrounded by O atoms, this result provides very strong evidence that there is no involvement of Zn<sub>i</sub> or V<sub>O</sub> native defect complexing in the Cu-related 2.86 eV ZPL and SGB emission in ZnO.

## 6.3 O-enriched Nanorods

### 6.3.1 PL Spectra

Figure 6.3 displays typical band edge and ZPL spectra as recorded on the SPEX and FT systems for the O-enriched samples. Specifically, figures 6.3(a) and 6.3(b) show the band edge regions in the VS and VLS samples from the FT system (the corresponding spectra from the SPEX data were presented in figure 5.12). As previously, the BX region is dominated by the I<sub>9</sub> In line and the I<sub>6</sub> Al line.<sup>9,14</sup> Some other BX lines also appear in some samples, similarly to the spectra presented in section 5.6. Figure 6.3(c) shows the ZPL line in the VS samples on the SPEX system and figure 6.3(d) shows those in the VLS samples on the FT system. These are typical of the ZPL lines seen in all the O-enriched samples on both systems. Note that the other lines in the FT spectra in this region are from the Hg calibration lamp. The FT band edge spectra from these samples are less noisy than those from the Zn-enriched samples and the BX lines are more clearly determined, perhaps due

to stronger band edge emission in these samples. The VS samples were all annealed to activate the SGB as described in section 5.6, while the VLS samples required no such anneal as the SGB was present as grown. Similarly to the Zn-enriched samples, these BX and Cu impurities are common in ZnO and most probably are due to the growth environment, i.e. source powders and the boats and tubes used.

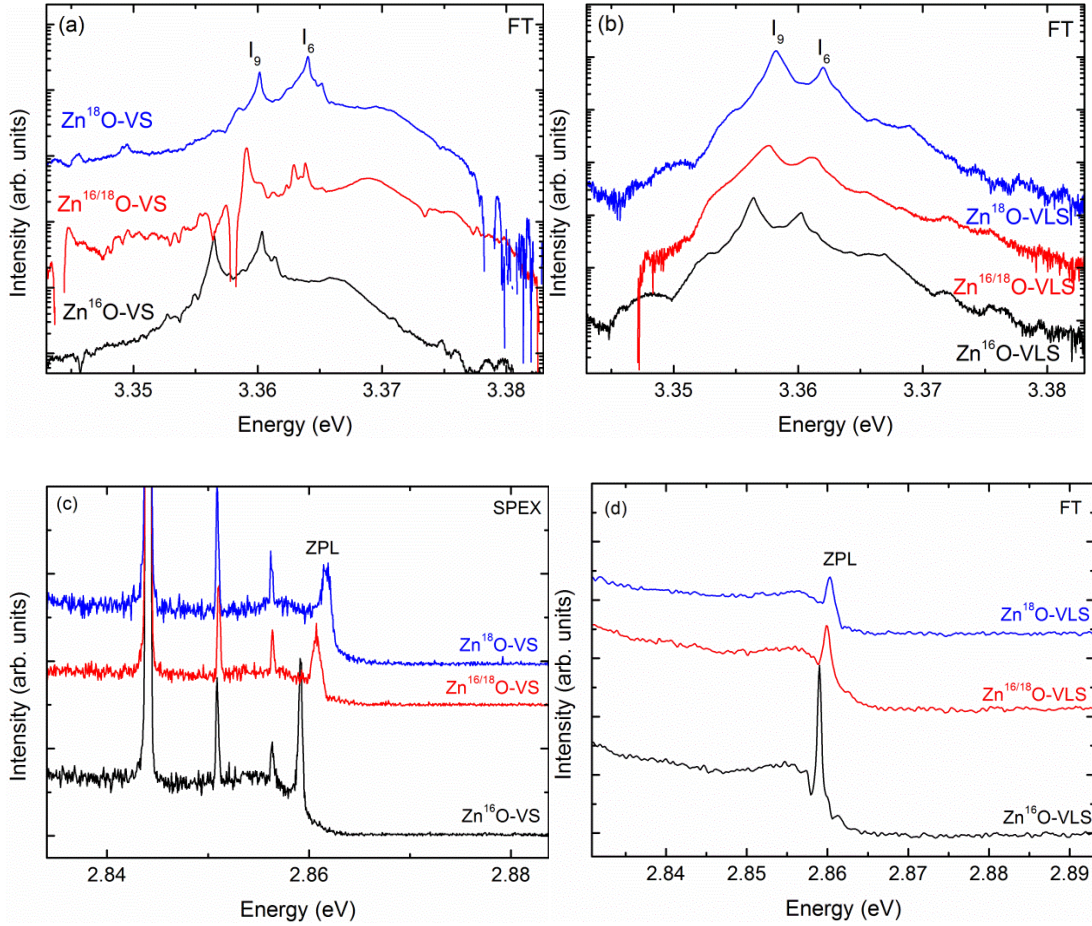


*Figure 6.3: Band edge (a and b) and Cu-related 2.86 eV ZPL (c and d) spectra from the VS and VLS O-enriched samples from the FT system (a, b and d) and the SPEX system (c). (Spectra shifted vertically for clarity. Artefact in mixed sample in (a) is due to FT apodisation. Vertical lines in (c) are from Hg calibration lamp.)*

Overall, in figure 6.3, the high optical quality of the samples is clearly apparent, and the shifts to higher energies with increasing O isotopic mass, for both the BX and Cu ZPL regions, are readily apparent. We note that the optical quality of the material is excellent, with BX line widths from the SPEX system given in section 5.6 are far smaller ( $< 1$  meV) than those reported by previous authors of  $< 5$  meV,

and 2-8 meV.<sup>15,16</sup> Also of note is the clear increase in the line width of the ZPL lines moving from the Zn<sup>16</sup>O samples to the Zn<sup>18</sup>O samples, which is not seen for the BX emissions. This is discussed further below.

### 6.3.2 Energy Shifts

The peak positions and line widths of the I<sub>9</sub> and Cu ZPL lines in both the VS and VLS samples are shown in tables 6.3 and 6.4, for the SPEX and FT systems, respectively. Once again, the peaks were fitted with Gaussians to determine the peak positions and line widths as for the Zn-enriched samples. Similarly to the Zn-enriched samples, there is good agreement between the SPEX and FT systems regarding the peak energies for these lines. The average difference across each sample between the two systems for the I<sub>9</sub> lines was 0.2 meV, with the largest difference being 0.31 meV. For the ZPLs, the average difference between the two systems is 0.17 meV, with the largest being 0.36 meV. These figures are very similar to those observed in the Zn-enriched samples and this demonstrates the good and consistent agreement between the systems.

Sample	Average O isotopic content (amu)	I <sub>9</sub> energy (eV)	I <sub>9</sub> FWHM (meV)	ZPL energy (eV)	ZPL FWHM (meV)
Zn <sup>16</sup> O-VS	16	3.35662	0.35	2.85915	0.44
Zn <sup>16/18</sup> O-VS	17	3.35903	0.48	2.86070	0.79
Zn <sup>18</sup> O-VS	18	3.35986	0.34	2.86162	1.18
Zn <sup>16</sup> O-VLS	16	3.35635	0.41	2.85895	0.36
Zn <sup>16/18</sup> O-VLS	17	3.35783	0.67	2.85993	0.76
Zn <sup>18</sup> O-VLS	18	3.35846	0.80	2.86032	0.93

Table 6.3: Energies and widths of the I<sub>9</sub> and ZPL lines in O-enriched ZnO, from the SPEX system.

Sample	Average O isotopic content (amu)	I <sub>9</sub> energy (eV)	I <sub>9</sub> FWHM (meV)	ZPL energy (eV)	ZPL FWHM (meV)
Zn <sup>16</sup> O-VS	16	3.35648	0.41	2.85879	0.68
Zn <sup>16/18</sup> O-VS	17	3.35913	0.41	2.86057	1.08
Zn <sup>18</sup> O-VS	18	3.36013	0.37	2.86140	1.14
Zn <sup>16</sup> O-VLS	16	3.35649	0.95	2.85897	0.58
Zn <sup>16/18</sup> O-VLS	17	3.35752	1.53	2.85979	1.03
Zn <sup>18</sup> O-VLS	18	3.35820	1.31	2.86020	1.09

Table 6.4: Energies and widths of the I<sub>9</sub> and ZPL lines in O-enriched ZnO, from the FT system.

The set of graphs below show the energies of the I<sub>9</sub> and Cu-related ZPL lines in each O-enriched sample from tables 6.3 and 6.4. Figure 6.4 shows the data from the (a) VS, and (b) VLS samples recorded on the SPEX system and figure 6.5 shows the same data from the FT system. In each graph, the left hand y-axis (black) shows the I<sub>9</sub> energies, and the right hand y-axis (blue) shows the ZPL energies. The I<sub>9</sub> axes all cover the same range (3.356 - 3.3605 eV), and the ZPL axes also cover this range of 4.5 meV but with these axes shifted to align the ZPL energy and the I<sub>9</sub> energy in the Zn<sup>16</sup>O sample at the same point on each graph. Once again, it is easy to observe the shifts of both the I<sub>9</sub> and ZPL energies in each sample with changing isotopic composition, and to compare any changes between them. As with the Zn-enriched samples, the error bars of the graphs represent the step size for each scan to give an indication of the accuracy of the positions. These are again  $\pm 0.035$  meV for the I<sub>9</sub> lines and  $\pm 0.045$  meV for the ZPLs on the SPEX and  $\pm 0.007$  meV for the I<sub>9</sub> lines and  $\pm 0.07$  meV for the ZPLs on the FT.

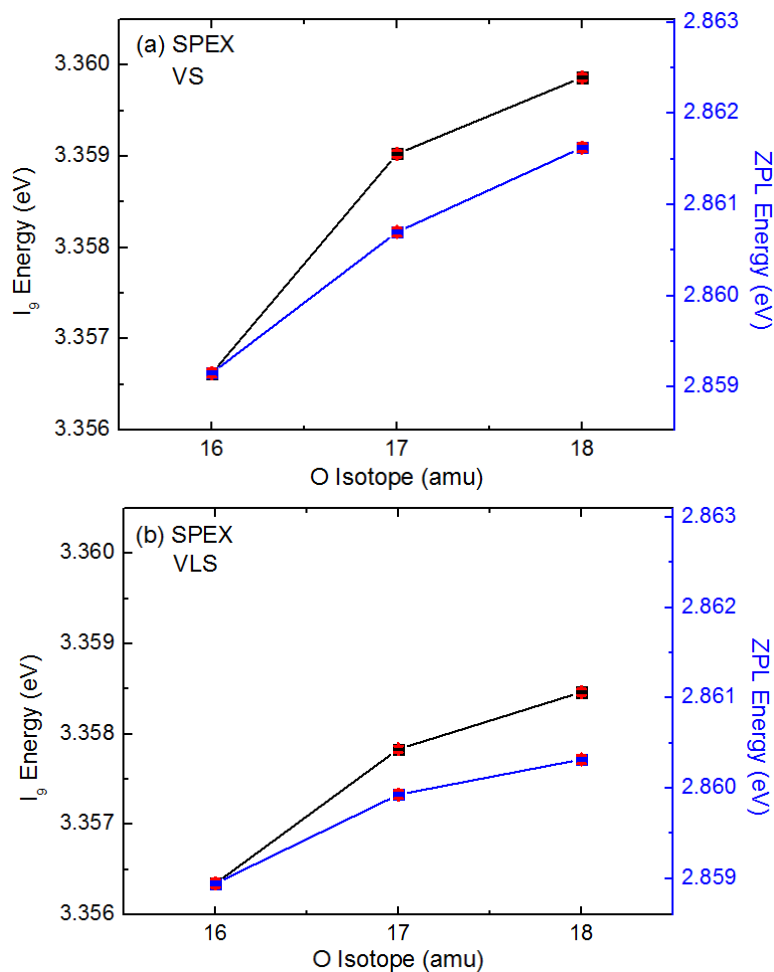


Figure 6.4: Energies of the  $I_9$  lines (black) and Cu-related ZPL lines (blue) in the (a) VS, and (b) VLS, O-enriched ZnO samples, from the SPEX system.

The increases in the energies of both the  $I_9$  and Cu-related ZPL lines are clearly shown in figures 6.4 and 6.5. This indicates that isotopic enrichment with different compositions of O isotopes has been successful. However, there are a number of things to note while examining these energy shifts as described in the next section. Table 6.5 summarises the shifts observed between the  $Zn^{16}O$  and  $Zn^{18}O$  samples, for the  $I_9$  and ZPL lines, in both the VS and VLS samples, and with both the SPEX and FT systems. The ratio of the  $I_9$  shifts to the ZPL shifts in each case is also shown in the table.

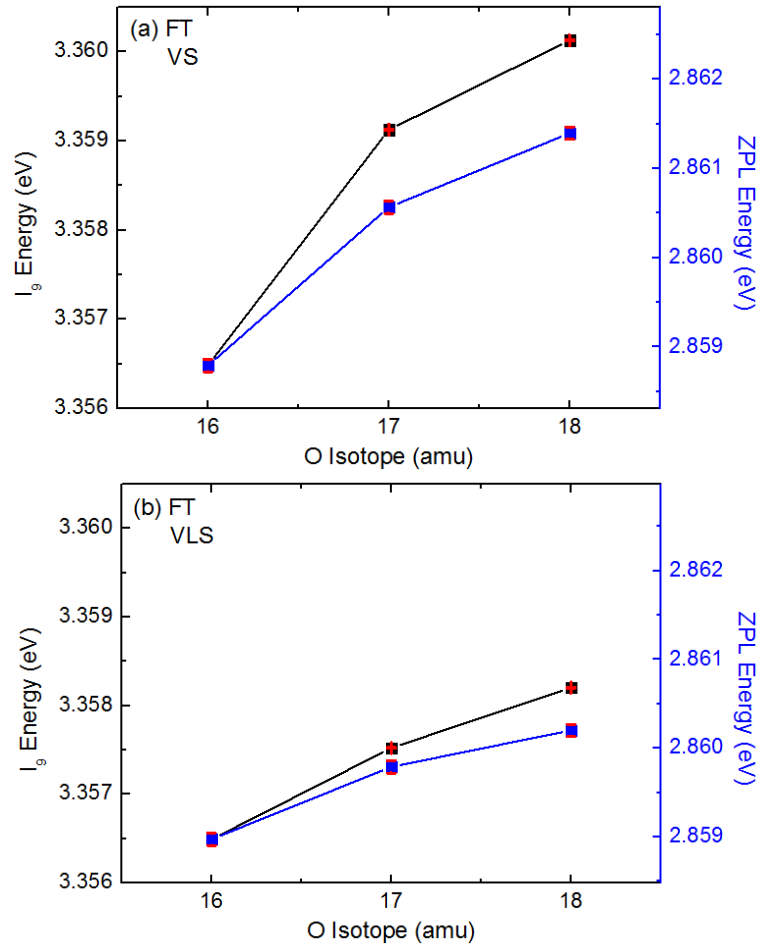


Figure 6.5: Energies of the  $I_9$  lines (black) and Cu-related ZPL lines (blue) in the (a) VS, and (b) VLS, O-enriched ZnO samples, from the FT system.

	$I_9$ energy shift from $Zn^{16}O$ to $Zn^{18}O$ (meV)	ZPL energy shift from $Zn^{16}O$ to $Zn^{18}O$ (meV)	Ratio $I_9/ZPL$
<b><u>SPEX</u></b>			
<b>VS samples</b>	3.24	2.47	1.31
<b>VLS samples</b>	2.11	1.37	1.54
<b><u>FT</u></b>			
<b>VS samples</b>	3.65	2.61	1.40
<b>VLS samples</b>	1.71	1.23	1.39

Table 6.5: Summary of the band edge and ZPL energy shifts in the O-enriched samples.

Finally, we note again that the ZPLs for the O-enriched samples, presented in figure 6.3(c) and (d), display a broadening effect moving from Zn<sup>16</sup>O to Zn<sup>18</sup>O, which is not seen for the BX emissions. This suggests possibly poorer enrichment in the samples than expected, as the presence of both isotopes would produce this line broadening effect, as discussed below (essentially because the ZPL lines are highly susceptible to their local environment.), whereas no such broadening would be expected if the <sup>18</sup>O sample were close to an actual 100% enrichment. For example, in figure 6.3(c) (SPEX, VS samples) the ZPLs broaden from 0.24 meV to 1.25 meV moving from Zn<sup>16</sup>O to Zn<sup>18</sup>O, and in figure 6.3(d) (FT, VLS samples) the ZPLs broaden from 0.58 meV to 1.09 meV moving from Zn<sup>16</sup>O to Zn<sup>18</sup>O. These figures are typical of those for these samples with both spectrometers as shown in tables 6.3 and 6.4. No particular trend is evident from the I<sub>9</sub> line widths.

### 6.3.3 Discussion on Energy Shifts, Line Widths and Involvement of O<sub>i</sub> or V<sub>Zn</sub> in the Cu-related Emission at 2.86 eV

The first thing to note here is that the I<sub>9</sub> energy shifts between the Zn<sup>16</sup>O and Zn<sup>18</sup>O samples are less than those previously reported in the literature for the same nominal degree of <sup>18</sup>O enrichment. For example, Manjón *et al.* reported BX shifts over this range of ~6.4 meV using the I<sub>4</sub> recombination, and Tsoi *et al.* reported a figure of ~6.5 meV for shifts in the A-exciton energy.<sup>15,16</sup> However, in our VS samples, the I<sub>9</sub> energy shifts are recorded as 3.24 meV in the VS samples, and just 2.11 meV in the VLS samples using the SPEX data moving from <sup>16</sup>O to <sup>18</sup>O. The corresponding figures from the FT system are listed in table 6.5 and follow this general trend. This would appear to indicate that our samples are not as fully enriched as expected from the growth processes as designed and carried out. This is consistent with the E<sub>2</sub><sup>high</sup> frequencies presented in chapter 5 which were also less than reported previously. The Zn<sup>16/18</sup>O energies also appear closer to Zn<sup>18</sup>O than Zn<sup>16</sup>O, i.e. the shift with isotopic mass is nonlinear. This is also observed by Manjón *et al.*

Secondly, the VLS samples grown in Jena consistently display a smaller shift than the corresponding one in the VS samples grown in DCU. This is observed in

both the SPEX and FT spectroscopic systems, and both for the  $I_9$  and SGB ZPL recombinations. This suggests that not only are both the VS and VLS samples enriched to a lesser degree than thought, but that within this work, the VLS samples are themselves enriched to a lesser degree than the VS samples. The phonon energies measured by Raman spectroscopy for these samples presented in chapter 5 are also consistent with this.

Thirdly, it is clear that the shifts in the ZPL energies in all the O-enriched samples are less than the corresponding shifts in the band edge region. This is observed across the VS and VLS samples, and on both spectroscopic systems. For example, using the SPEX data, the  $I_9$  shift in the VS samples is 3.24 meV, but the ZPL shift is just 2.47 meV. Likewise, the  $I_9$  shift in the VLS samples is 2.11 meV, but the ZPL shift is just 1.37 meV. The ratio of the  $I_9$  shifts to the ZPL shifts in table 6.5 shows a consistent relative shift of between the two in each case, with a slightly larger relative shift recorded on the SPEX for the VLS samples. There are also clear increases in the ZPL line widths, which are not seen in the BX emissions. There are various ways to interpret these data. The first is that this indicates the presence of  $O_i$  or  $V_{Zn}$  native defects in complex with the Cu atom at this defect. Since the  $Cu_{Zn}$  defect is a substitutional Cu atom on a Zn site, it is surrounded by O atoms in the lattice. An additional O atom, or a missing Zn atom (and the corresponding effects on the O atoms surrounding the Zn vacancy), could affect the local vibrational environment in such a way as to produce an anomalous shift and line broadening. In principle each possible configuration of the surrounding O atoms would lead to a distinct line<sup>17</sup>, allowing a study of the possible numbers of O atoms involved, but the small shifts associated with different configurations mean that these overlap and simply broaden the ZPL emission. A second possibility is that there exists a number of different configurations of the 4 O atoms surrounding the Cu due to the varying possible combinations of  $^{16}O$  and  $^{18}O$  atoms that the Cu atom could be adjacent to (e.g. 4 x  $^{16}O$ , 1 x  $^{18}O$  + 3 x  $^{16}O$  etc.). The effect of the varying O-isotopic masses in the 4 closest O atoms in the vicinity of the Cu defect could be the cause of the anomalous shifts and the line broadening. Once again in principle each possible configuration of the surrounding atoms would lead to a distinct line,<sup>17</sup> allowing a study of the possible numbers of O atoms involved, but the small shifts associated with different configurations mean that these overlap and simply broaden the ZPL

emission. Line broadening of this type is expected for a deep defect with localised carriers strongly affected by the local defect configuration, whereas it is not expected for the shallow BX emissions where the small exciton confinement energy means that the local defect configuration is less important, and the BX samples a larger volume of the crystal and the line energy is affected by the average isotopic mass in this volume, but the line width is unaffected.

Ultimately, because of the small line shifts and the inability to resolve lines associated with individual O atomic configurations we do not have enough information to determine which of these possibilities is the case, although we consider it more likely that it is the latter as it would agree with the previous work of Dingle<sup>18</sup> and Byrne *et al.*<sup>19</sup>, in terms of the defect symmetry ( $C_{3v}$ )<sup>20</sup> and other known aspects of the defect. The likelihood of a complex of a Cu atom with 3 native defects ( $O_i$  or  $V_{Zn}$ ) producing a defect with overall  $C_{3v}$  symmetry seems very small. By contrast, the starting configuration of the 4 O atoms surrounding the Zn site on which the Cu atom substitutes has this symmetry naturally, and it seems a far more likely explanation that any relaxation of the surrounding O after Cu substitution will maintain this symmetry.

Finally, as discussed above, because the ZPL for the nominally 100% enriched <sup>18</sup>O sample shows a considerable broadening (whereas no such broadening would be expected if the <sup>18</sup>O sample were close to an actual 100% enrichment) we believe that the samples are not as highly enriched as the nominal enrichment values, and we estimate the actual <sup>18</sup>O enrichments below.

### 6.3.4 Estimate of Level of Enrichment in O-enriched ZnO

Several aspects of our data appear to point towards the nominally 100% <sup>18</sup>O-enriched ZnO nanorods not being 100% enriched with the desired isotopic composition. These data include Raman and band edge PL shifts being smaller than those reported previously in the literature, and the broadening of the Raman and ZPL lines with increased <sup>18</sup>O enrichment. It is useful to make an estimate of the level of enrichment achieved in our samples by comparing our band edge region BX energy

shifts to those reported by Manjón *et al.* and Tsoi *et al.*, assuming these data reported previously are from samples actually enriched to nominally 100%.<sup>15,16</sup> Moving from Zn<sup>16</sup>O to Zn<sup>18</sup>O, the average shift in those two reports is ~ 6.45 meV. Using this as a reference, table 6.6 then gives the shifts observed in the band edge region in our VS and VLS samples as a percentage of this, for both the Zn<sup>18</sup>O and the Zn<sup>16/18</sup>O mixed isotope samples, from both spectroscopic systems. The same calculation can also be carried out using the E<sub>2</sub><sup>high</sup> phonon energy shifts in section 5.5 compared to the room temperature value of ~23 cm<sup>-1</sup> reported by Serrano *et al.*<sup>21</sup> Across the two PL spectroscopic systems, and the Raman data, this gives an average estimated enrichment of 60% for Zn<sup>18</sup>O-VS, 32% for Zn<sup>18</sup>O-VLS, 41% for Zn<sup>16/18</sup>O-VS and 21% for Zn<sup>16/18</sup>O-VLS. The ratios of the <sup>18</sup>O enrichment in the VS samples to the VLS samples in each case is also shown in table 6.6, and range from 1.5-2.1 in the <sup>18</sup>O samples and 1.6-2.6 in the <sup>16/18</sup>O samples. The average ratios are 1.9 in the <sup>18</sup>O samples and 2.1 in the <sup>16/18</sup>O samples.

	<sup>18</sup> O-enrichment as % of literature reference for Zn <sup>18</sup> O nanorods	<sup>18</sup> O-enrichment as % of literature reference for Zn <sup>16/18</sup> O nanorods
<b><u>SPEX PL</u></b>		
VS samples	50	37
VLS samples	33	23
<i>Ratio VS/VLS</i>	1.5	1.6
<b><u>FT PL</u></b>		
VS samples	57	41
VLS samples	27	16
<i>Ratio VS/VLS</i>	2.1	2.6
<b><u>Raman</u></b>		
VS samples	72	46
VLS samples	37	23
<i>Ratio VS/VLS</i>	2.0	2.0

Table 6.6: <sup>18</sup>O enrichment as % of literature PL and Raman references for Zn<sup>18</sup>O and Zn<sup>16/18</sup>O nanorods.

## 6.4 Discussion on Possible Causes of Reduced Oxygen Enrichment

As discussed above, a number of pieces of evidence presented in this chapter, and in chapter 5, regarding O-enriched ZnO nanorods, point to the likelihood that these samples are not enriched to the nominal levels stated, and expected from the growth processes as performed. It is therefore worthwhile to discuss the possible sources of this reduced  $^{18}\text{O}$  enrichment. During both the growth of the VS samples by method 1, and the oxidation of the Zn metal powders to produce the ZnO powders for the VLS growths by method 2, as described in chapter 2, every effort was made to ensure that only the appropriate O isotope was present.

Considering firstly method 1, the growth of  $^{18}\text{O}$ -enriched ZnO nanorods by the modified VS method, involving evacuating the furnace tube and refilling with  $^{18}\text{O}_2$ , we must consider any possible sources of natural  $^{16}\text{O}_2$  as a contaminant which could lead to reduced  $^{18}\text{O}$  enrichment as observed in these samples. One obvious source of this is the natural  $^{16}\text{O}_2$  in the tube at the start of the experiment. The tube was evacuated to a pressure of  $<1$  mbar and then filled 21% atmosphere with  $^{18}\text{O}_2$  and to atmosphere with  $\text{N}_2$ . This would indicate a possible contamination level of  $\sim 0.1\%$   $^{16}\text{O}_2$ , or  $\sim 0.5\%$  of the oxygen being this isotope. This certainly would not explain the enrichment being reduced by about half as indicated by the PL data. The  $\text{N}_2$  used in the experiment only has  $\text{O}_2$  impurities of  $<5$  ppm, or around  $0.0005\%$ . Clearly this would not be the source of such reduced enrichment in the atmosphere inside the tube during growth. The system was extensively checked for leaks several times during the set up and testing of the system. All line connections and seals were thoroughly checked, and the lines and were purged of natural  $^{16}\text{O}_2$  before growth. This also included the regulator used on the  $^{18}\text{O}_2$  cylinder. The natural  $^{16}\text{O}$  in the ZnO source powder (or adsorbed on the graphite powder) is also not likely to be the cause of this effect, as the CTR reaction leads to the formation of CO molecules, thereby trapping the O in the ZnO source powder and not allowing it to react on the substrate, as the residual atmospheric  $\text{O}_2$  does. Attempts at growth with just  $\text{N}_2$  gas in the tube, described in chapter 5, and the lack of observed growth from such attempts, support this conclusion. We also considered whether residue on the inside of the furnace tube (or some remaining in the alumina boat) from previous

growths could contribute some O<sub>2</sub> to the growth by a small amount of it being disassociated when heated, as the <sup>18</sup>O-enriched VS growths were carried out in the same tube as the normal natural growths. However, the temperatures of 925°C were not sufficient for this to occur. The final source of unwanted <sup>16</sup>O<sub>2</sub> in the system could simply be a leak. However, as mentioned above, the system was extensively leak tested, and even if we consider, for example, 10 mbar of <sup>16</sup>O<sub>2</sub> entering the system during pump-down and refill, this would not come close to causing the reduced PL and Raman shifts observed with these samples. Ultimately, we emphasise once again that the fact that, when the system was tested using a pure N<sub>2</sub> atmosphere with no O<sub>2</sub> gas of any kind introduced, no VPT growth occurred, strongly indicates that leaks or another unwanted sources of <sup>16</sup>O<sub>2</sub> in the system were not the cause of the poorer enrichment.

We now consider the VLS sample growths in Jena with our collaborators. The system used to oxidise the Zn metal powder, using <sup>16</sup>O<sub>2</sub> or <sup>18</sup>O<sub>2</sub>, to produce Zn<sup>16</sup>O and Zn<sup>18</sup>O powders to be used in these growths was similar to the VS system and there much of the previous paragraph also applies regarding leaks and the N<sub>2</sub> gas. In this case, a smaller tube was used to reduce the amount of gas needed. Additionally, a separate clean tube and boat was used for the <sup>18</sup>O isotope oxidation, to eliminate possible contamination. This, coupled with the lower temperatures of ~800°C, means we can be quite confident of having no contamination here. Initial experiments on oxidising Zn powder were carried out using old powder which had oxidised in air over time, however completely fresh Zn metal powder was used for the <sup>18</sup>O oxidation runs. It is considered likely that the cause of the even further reduced enrichment in the VLS samples compared to the VS samples is that the growth system in Jena led to increased <sup>16</sup>O contamination. These growths were carried out using an alumina boat and tube that had deposits from previous growths present. This is considered the most likely source of additional <sup>16</sup>O<sub>2</sub> in the tube due to the higher temperatures (~1350°C) needed for the sublimation of the ZnO sources powders also producing some <sup>16</sup>O<sub>2</sub> from the previous deposits.

Based on the discussion above, we are confident that our experimental methods are sound and that we have effectively reduced or eliminated the obvious sources of contamination, in terms of all the possible sources of <sup>16</sup>O<sub>2</sub> while planning the experiment, while the testing carried out before the growth proceeding indicated

that there was not a problem with  $^{16}\text{O}_2$  contamination. If we consider the explanation in the previous paragraph for the difference between the VS and VLS samples, we must then consider the possibility that the cause of the reduced enrichment in both the VS samples in DCU and the oxidised source powders produced in DCU for the VLS growths in Jena originate from a common source. Ultimately, it was considered that a possible source of  $^{16}\text{O}_2$  was the lecture bottle of  $^{18}\text{O}_2$ , and that perhaps this was not enriched properly to its rated value of >99%. However we note that a point against this hypothesis is that the estimated enrichment levels are not consistent with a fixed  $^{16}\text{O}_2$  contamination of the  $^{18}\text{O}_2$  gas used. This would be a both a surprising and disappointing result, given that the gas bottle was purchased from a reputable supplier and was clearly rated for a high enrichment level and was properly handled at all stages.

Finally, between the submission of this thesis and the *viva-voce* examination, a number of further tests were carried out in an attempt to clarify the source of the  $^{16}\text{O}$  contamination of these samples. Firstly, a further sample of  $\text{Zn}^{18}\text{O}$ -VS was grown using the same CTR-VPT method except with a fresh bottle of  $^{18}\text{O}_2$  gas sourced from a different supplier (CK Isotopes, 98%). PL using the SPEX system showed a band edge shift of 3.12 meV for the  $I_9$  line and 1.97 meV for the ZPL. These figures are similar to those reported in this chapter and this test indicates that the original bottle of  $^{18}\text{O}_2$  gas was not contaminated with  $^{16}\text{O}_2$ . Secondly, the same growth was repeated using a fresh tube and alumina boat which has no deposits from previous unenriched growths. The results here were a band edge shift of 3.45 meV for the  $I_9$  line and 1.79 meV for the ZPL which indicates that there is no contamination from old deposits on the equipment. Finally a further VPT test was carried out using a long 1 hour Ar flush at the start (versus the usual ~ 5 mins). This removes all the residual oxygen from the tube and should result in no VPT nanorod growth, and this is what was observed. This implies no other source of  $^{16}\text{O}_2$  in the system and is consistent with the nitrogen only test described in chapter 5 and previous tests by others using this system.<sup>22</sup> Ultimately, we must conclude that the final source of the  $^{16}\text{O}_2$  contamination was not conclusively identified during these tests. We tentatively suggest that there could be some diffusion of  $^{16}\text{O}$  from the unenriched CBD buffer layer, or the Si native oxide layer in the VLS samples, which could be contributing to this effect, especially since enhanced diffusion along the

nanorod sidewalls may be possible, compared to diffusion in single crystals.<sup>23</sup> Alternatively some  $^{16}\text{O}_2$  could be being released from these layers during the growth, creating a concentration of  $^{16}\text{O}_2$  in the immediate vicinity of the nanorods during growth, although this possibility seems unlikely since it is not consistent with our tests with either just  $\text{N}_2$  in the tube, or after a long Ar flush. Effects such as these would be consistent with the thermal effects observed in the CBD layer when they underwent a growth cycle which resulted in no VPT growth (i.e. with only  $\text{N}_2$  in the tube or after a long Ar flush), where observable changes in morphology are seen, and would also be consistent with the differing departures from the nominal enrichment levels seen for the VS and VLS samples, since the efficiency of the processes might well be different for the CBD buffer layer and the Si native oxide layer, used in these two methods, respectively.

## 6.5 Conclusions

The low temperature PL data for the Zn-enriched, and both the VS and VLS O-enriched ZnO nanorods were presented. The optical quality of all samples was excellent, in that they each displayed intense band edge emissions with narrow BX emission lines, far narrower than those reported previously in the literature. The SGB was also present in all samples, although some samples required annealing to increase its intensity to allow spectroscopy study. The Zn-enriched samples displayed a shift of  $\sim 0.6$  meV as the isotopic composition changes  $^{64}\text{ZnO}$  to  $^{68}\text{ZnO}$ , in line with previously published work, for both the  $\text{I}_9$  BX recombination and the SGB ZPL and no changes in line width of either emission with changes in isotopic composition. This indicated no involvement of  $\text{Zn}_i$  or  $\text{V}_\text{O}$  native defects in the Cu-related defect at 2.86 eV. The O-enriched samples displayed band edge shifts of around 3.5 meV as the isotopic content changed from  $\text{Zn}^{16}\text{O}$  to  $\text{Zn}^{18}\text{O}$  for the VS samples, and smaller shifts of around  $\sim 2$  meV for the VLS samples. These were smaller than the shifts of  $>6$  meV reported previously. This, coupled with the phonon frequency data presented in chapter 5, and line width broadening in the ZPL lines, indicated that the  $^{18}\text{O}$  enrichment of these samples was not as expected. The levels of such enrichment were estimated at of 60% for  $\text{Zn}^{18}\text{O}$ -VS, 32% for  $\text{Zn}^{18}\text{O}$ -

VLS, 41% for Zn<sup>16/18</sup>-VS and 21% for Zn<sup>16/18</sup>O-VLS. The reasons for this reduced enrichment were discussed and it is concluded that the <sup>18</sup>O<sub>2</sub> gas source used was the most likely source, in addition to residue on the tube and boat used for the VLS samples causing a further reduction in the enrichment of those samples. Smaller relative shifts and line width broadening for the ZPL versus the band edge in the O-enriched samples are attributed to changes in the local defect environment due to different occupancy of O sites by <sup>16</sup>O and <sup>18</sup>O atoms in the mixed composition samples, which seems a much more likely cause of the effects seen than complexing with O<sub>i</sub> or V<sub>Zn</sub> defects, taking account of the known C<sub>3v</sub> defect symmetry.

## 6.6 References

- <sup>1</sup> F.I. Kreingol'd, *Fiz. Tsvend. Tela* **20**, 3138 (1978).
- <sup>2</sup> F.I. Kreingol'd and B.S. Kulinkin, *Fiz. Tsvend. Tela* **28**, 3164 (1986).
- <sup>3</sup> F.I. Kreingol'd, *Fiz. Tsvend. Tela* **27**, 2839 (1985).
- <sup>4</sup> F.I. Kreingol'd, K.F. Lider, and M.B. Shabaeva, in *Fiz. Tsvend. Tela* (Cambridge, 1984), pp. 3490–3491.
- <sup>5</sup> A. Klochikhin and V.G. Plekhanov, *Fiz. Tsvend. Tela* **22**, 585 (1980).
- <sup>6</sup> V.G. Plekhanov, V.A. Pustovarov, A.A. O'Connell-Bronin, T.A. Betenekova, and S.O. Cholakh, *Fiz. Tsvend. Tela* **18**, 2438 (1976).
- <sup>7</sup> B.K. Meyer, H. Alves, D.M. Hofmann, W. Kriegseis, D. Forster, F. Bertram, J. Christen, A. Hoffmann, M. Straßburg, M. Dworzak, U. Haboek, and A. V. Rodina, *Phys. Status Solidi* **241**, 231 (2004).
- <sup>8</sup> K. Johnston, M.O. Henry, D. McCabe, E. McGlynn, M. Dietrich, E. Alves, and M. Xia, *Phys. Rev. B* **73**, 165212 (2006).
- <sup>9</sup> M. Schilling, R. Helbig, and G. Pensl, *J. Lumin.* **33**, 201 (1985).
- <sup>10</sup> J. Cullen, D. Byrne, K. Johnston, E. McGlynn, and M.O. Henry, *Appl. Phys. Lett.* **102**, 192110 (2013).

- <sup>11</sup> M. Biswas, Y.S. Jung, H.K. Kim, K. Kumar, G.J. Hughes, S. Newcomb, M.O. Henry, and E. McGlynn, *Phys. Rev. B* **83**, 235320 (2011).
- <sup>12</sup> N.Y. Garces, L. Wang, L. Bai, N.C. Giles, L.E. Halliburton, and G. Cantwell, *Appl. Phys. Lett.* **81**, 622 (2002).
- <sup>13</sup> G. Xing, G. Xing, M. Li, E.J. Sie, D. Wang, A. Sulistio, Q. Ye, C.H.A. Huan, T. Wu, and T.C. Sum, *Appl. Phys. Lett.* **98**, 102105 (2011).
- <sup>14</sup> S. Müller, D. Stichtenoth, M. Uhrmacher, H. Hofsäss, C. Ronning, and J. Röder, *Appl. Phys. Lett.* **90**, 012107 (2007).
- <sup>15</sup> F.J. Manjón, M. Mollar, M.A. Hernández-Fenollosa, B. Marí, R. Lauck, and M. Cardona, *Solid State Commun.* **128**, 35 (2003).
- <sup>16</sup> S. Tsoi, X. Lu, A.K. Ramdas, H. Alawadhi, M. Grimsditch, M. Cardona, and R. Lauck, *Phys. Rev. B* **74**, 165203 (2006).
- <sup>17</sup> S. Feofilov, A. Kulinkin, K. Ovanesyan, A. Petrosyan, and C. Dujardin, *Phys. Chem. Chem. Phys.* **16**, 22583 (2014).
- <sup>18</sup> R. Dingle, *Phys. Rev. Lett.* **23**, 579 (1969).
- <sup>19</sup> D. Byrne, F. Herklotz, M.O. Henry, and E. McGlynn, *J. Physics. Condens. Matter* **24**, 215802 (2012).
- <sup>20</sup> C. Solbrig, *Z. Phys. A.* **211**, 429 (1968).
- <sup>21</sup> J. Serrano, F. Manjón, A. Romero, F. Widulle, R. Lauck, and M. Cardona, *Phys. Rev. Lett.* **90**, 055510 (2003).
- <sup>22</sup> R.B. Saunders, *Theoretical and Experimental Studies of ZnO Nanowires Grown by Vapour Phase Transport*, Dublin City University, 2012.
- <sup>23</sup> A.C.S. Sabioni, M.J.F. Ramos, and W.B. Ferraz, *Mater. Res.* **6**, 173 (2003).

# Chapter 7: Conclusions and Future Work

## 7.1 Conclusions

In this work, the three-step growth process previously developed in our group<sup>1</sup>, itself based upon previous developments in the literature, has been successfully adapted in order to grow ZnO nanorods containing different isotopes of Zn and O by several novel methods. In doing so we have demonstrated the possibility of using ZnO nanorods for studies of the effects of isotopic enrichment, using relatively simple growth techniques, and have shown that the nanorods possess excellent crystalline and optical quality, enabling detailed optical studies of both band edge and deeper level emissions. A key original and novel feature of this present work is that this is the first time isotopically enriched ZnO has been produced in nanostructured form and we further note that the optical quality of these nanorods, in terms of their band edge emission intensities, and more specifically their line widths, is significantly better than that reported previously for ZnO bulk single crystals.<sup>2,3</sup>

For the Zn-enriched nanorods, the growth process consisted of depositing a ZnO seed layer by drop coating, followed by growth of a ZnO nanorod buffer layer

using CBD and the growth of ZnO nanorods by CTR-VPT. The previous growth process was altered by reducing the amount of ZnO source powders used. Samples of  $^{nat}\text{ZnO}$ ,  $^{64}\text{ZnO}$ ,  $^{66}\text{ZnO}$ ,  $^{68}\text{ZnO}$ ,  $^{64/66}\text{ZnO}$ ,  $^{66/68}\text{ZnO}$ ,  $^{64/68}\text{ZnO}$  and  $^{64/66/68}\text{ZnO}$  were grown, by altering the Zn isotopic composition of the ZnO sources powder, using this VS method. The samples were characterised using SEM, XRD, SIMS, Raman, low temperature PL and reflectance spectroscopy. SEM confirmed the dense coverage of vertical, *c*-axis aligned nanorods over a large sample area. The morphology was typical of that observed in previous work. Some variations in morphology were observed such as differing heights of nanorods, nanorods becoming ‘entangled’ and such loss of vertical alignment, reduced density and poor nanorod morphology in one sample. However, these differences were mainly confined to small areas of the samples and some sample to sample variation of this nature is expected with our CTR-VPT growth process. The growth process is easy, quick and very reliably produces high quality ZnO nanorods. XRD confirmed the presence of wurtzite ZnO with an intense ZnO peak at  $34.4^\circ$ . The Si peak at  $69.1^\circ$  was also clearly visible. The FWHM of the  $34.4^\circ$  ZnO peak rocking curves were very narrow at  $\sim 2\text{-}3^\circ$  and this confirmed the high levels of alignment and crystal quality in the samples. SIMS data confirmed the successful Zn isotopic enrichment consistently using two independent SIMS systems.

Raman data show a shift of  $>1\text{ cm}^{-1}$  in the peak position of the Raman scattered peaks due to the  $E_2^{\text{low}}$  and  $E_2^{\text{high}}$  phonon modes when the Zn isotope is changed from  $^{64}\text{Zn}$  to  $^{68}\text{Zn}$ , consistent with previous work on samples with different isotopic enrichments, again confirming successful isotopic substitution.<sup>4,5</sup> Low temperature PL measurements, using both the SPEX monochromator and FT spectrometer revealed the excellent optical quality of the samples, with line widths of  $<1\text{ meV}$ . The results from the two systems were consistent and revealed increases in the  $I_9$  and ZPL energies of  $\sim 0.6\text{ meV}$  with Zn isotopic content changing from  $^{64}\text{ZnO}$  to  $^{68}\text{ZnO}$ . This is similar to previous results for single crystals, although we note previously reported figures of  $>1\text{ meV}$ .<sup>2,3</sup> Despite this, we are confident of good enrichment in these samples as supported by the SIMS and Raman data. Relative to the band edge, the ZPL line shift reduces to  $\sim 0.1\text{ meV}$  in both systems. We conclude that there is no detectable relative shift between the band edge and Cu-related  $2.86\text{ eV}$  ZPL when the Zn isotopic content of the lattice is changed. This

result allows us to conclude that we detect no involvement of the native defects  $Zn_i$  or  $V_O$  in this Cu-related defect.

Two novel methods were developed to produce O-isotopically enriched ZnO nanorods. Following extensive development and testing, a further modified VS VPT method was successful in growing ZnO nanorods enriched with  $^{18}O$ . Samples of  $Zn^{16}O$ ,  $Zn^{16/18}O$  and  $Zn^{18}O$  were grown by evacuating the tube in the growth furnace and refilling it with a mixture of ‘artificial’ atmosphere containing  $\sim 21\%$   $^{18}O_2$  and  $\sim 79\%$   $N_2$  (or a 50:50 mix with natural  $O_2$ ). This made use of the fact that it is the residual atmospheric  $O_2$  in the tube which contributes to the ZnO nanorods. A second method of producing O-enriched ZnO nanorods was also developed in collaboration with our colleagues in Jena, Germany. This was a VLS VPT method based on the direct sublimation of ZnO source powder at higher temperatures. For this, O-enriched ZnO powders were produced by oxidising Zn metal powder in DCU prior to these growths taking place in Jena.

These O-enriched samples were again characterised using SEM, XRD, miniSIMS, Raman spectroscopy and low temperature PL. SEM studies confirmed the success of both growth methods in terms of nanostructure morphology, although in the case of the VLS samples, the nanorods were not *c*-axis aligned due to the nature of the substrate used. XRD again confirmed the growth of high quality wurtzite ZnO nanorods. XRD scans of the VS samples indicated that these samples are not strained at the limit of detection of our XRD system. miniSIMS spectra clearly showed the presence of  $^{16}O$  in the natural samples, and although it showed the presence of  $^{18}O$  as expected in enriched samples, it did not give direct confirmation of enrichment because of the continued presence of  $^{16}O$  contamination from a number of sources. However, Raman and PL studies indicated clearly that O-enrichment was successful in both cases, although the figures indicate the enrichment may be at a lower level in the VLS samples compared to the VS samples, as these displayed smaller shifts, for example 3.24 meV vs 2.11 meV in the PL band edge region, from the SPEX monochromator, moving from  $Zn^{16}O$  to  $Zn^{18}O$ . The very narrow  $I_9$  and other BX line widths in our VS and VLS again demonstrate their excellent optical quality.

A number of factors suggest that the O-enrichment of the VS and VLS ZnO nanorods may not be as great as expected. The band edge shifts above are notably less than those previously reported of  $>6$  meV for bulk single crystals.<sup>2,3</sup> The phonon energies in the Raman data are also less than those reported previously for single crystals, and the line widths wider for samples containing  $^{18}\text{O}$ .<sup>4,5</sup> In addition, the Cu-related ZPL at 2.86 eV displayed a line broadening effect in samples nominally containing only  $^{18}\text{O}$ . This also indicates the continuing presence of  $^{16}\text{O}$  in larger amounts than expected. Using the band edge shifts and Raman phonon energy shifts in comparison to the literature, the level of  $^{18}\text{O}$  enrichment in each sample was estimated at 60% for  $\text{Zn}^{18}\text{O}$ -VS, 32% for  $\text{Zn}^{18}\text{O}$ -VLS, 41% for  $\text{Zn}^{16/18}$ -VS and 21% for  $\text{Zn}^{16/18}\text{O}$ -VLS. The Cu-related ZPL shifts are also smaller than those at the band edge in these O-enriched samples in addition to the line broadening in the mixed isotope samples mentioned above. While these data could possibly indicate  $\text{O}_i$  or  $\text{V}_{\text{Zn}}$  defects at the defect site, we consider it more likely, based on considerations related to the defect symmetry, that the effect of the varying occupancy of the 4 closest O atoms in the vicinity of the Cu defect by different O-isotopic masses is the cause of the anomalous shifts and the line broadening.

Finally, a number of other experiments were carried out using samples produced during this work and are presented in appendix A as examples of the potential uses of ZnO nanorods grown using these methods in other studies. These experiments were often carried out by collaborators using the samples produced during this work. This included TRPL measurements carried out on the  $^{64}\text{ZnO}$ ,  $^{66}\text{ZnO}$  and  $^{68}\text{ZnO}$  samples, CBD-grown ZnO nanorods produced used in experiments on third harmonic UV generation, and some experiments carried out on particle acceleration and the generation of x-rays from nanostructured targets using ZnO nanorods grown using CBD on Ti targets.

## 7.2 Future Work

There are a number of further experiments proposed in this section in order to provide a fuller understanding of the outcomes of the work contained in this thesis. From our perspective the reduced O-enrichment in both the VS and VLS samples is

the most confusing result from this work and thus is one aspect that we would consider a high priority to investigate further. We feel we have carefully considered all the possible sources of natural  $^{16}\text{O}$  enrichment in the VS growth apparatus, and have tentatively suggested that there could be some diffusion of  $^{16}\text{O}$  from the unenriched CBD buffer layer, or the Si native oxide layer in the VLS samples, which could be contributing to this. Alternatively (although less likely we feel) some  $^{16}\text{O}_2$  could be being released from these layers during the growth, creating a concentration of  $^{16}\text{O}_2$  in the immediate vicinity of the nanorods during growth. This could have affected both the VS samples grown in DCU and the VLS samples grown in Jena, albeit to different extents, consistent with our data. A more detailed study of these possible effects is suggested.

In addition to this, and given that our miniSIMS measurements did not provide a conclusive measurement of the O-enrichment in those samples, a direct measurement of such enrichment is still desirable, and specifically to check if such a measurement concurred with our estimates of the enrichment levels based on the PL and Raman shifts. This would also be of relevance to efforts to conclusively identify the source of  $^{16}\text{O}_2$  contamination during growth. Efforts to obtain such data by measuring the enrichment in single nanorods in collaboration with a group with access to an atom probe system are currently underway.

While we are confident that our Zn-enriched nanorods are enriched to high levels because of our SIMS and Raman data, the band edge PL shifts are slightly lower than those previously reported, and this could be a sign of lower enrichment than thought. It would be an interesting experiment to get a further, independent and direct measurement of the Zn-enrichment in these samples to investigate this irregularity, although the SIMS and Raman data appear to be strongly supportive of good enrichment in these samples. Once again, efforts to obtain such data by measuring the enrichment in single nanorods in collaboration with a group with access to an atom probe system are currently underway.

Finally, while we have produced Zn-enriched and O-enriched ZnO nanorods in this work, the full set could be completed by producing Zn-enriched nanorods with enriched  $^{18}\text{O}$ . Assuming that if any problem with  $^{16}\text{O}_2$  contamination during growth was remedied, this would allow a complete study of the Raman and PL shifts in

isotopically enriched ZnO nanorods to be carried out, using all the possible isotopic combinations. A more detailed study of the Cu-related centre at 2.86 eV could also be done. If, in the future, we were certain of proper O-enrichment, then the band edge vs. Cu SGB ZPL energy shifts could be studied without the possible effects of the presence of multiple O isotopes.

### 7.3 References

- <sup>1</sup> D. Byrne, E. McGlynn, K. Kumar, M. Biswas, M.O. Henry, and G. Hughes, *Cryst. Growth Des.* **10**, 2400 (2010).
- <sup>2</sup> F.J. Manjón, M. Mollar, M.A. Hernández-Fenollosa, B. Marí, R. Lauck, and M. Cardona, *Solid State Commun.* **128**, 35 (2003).
- <sup>3</sup> S. Tsoi, X. Lu, A.K. Ramdas, H. Alawadhi, M. Grimsditch, M. Cardona, and R. Lauck, *Phys. Rev. B* **74**, 165203 (2006).
- <sup>4</sup> J. Serrano, F. Manjón, A. Romero, F. Widulle, R. Lauck, and M. Cardona, *Phys. Rev. Lett.* **90**, 055510 (2003).
- <sup>5</sup> J. Serrano, F. Widulle, A.H. Romero, A. Rubio, R. Lauck, and M. Cardona, *Phys. Status Solidi* **235**, 260 (2003).

# Appendix A: Some Applications of these Growth Methods and Materials in other Experiments

## A.1 Introduction

Nanostructures such as ZnO nanorods lend themselves to many types of experiments and measurements which can reveal useful and interesting data. This chapter briefly presents the results of a number of other experiments carried out using samples produced by the author during this work and supplied to other groups. These illustrate just a few examples of the potential uses of ZnO nanorods grown using these methods in other studies, often in very diverse fields. These examples include measurements on the Zn-enriched ZnO nanorods, and other studies carried out using CBD-grown ZnO nanorods on a number of substrates. The actual experiments were generally carried out by collaborators using the samples produced during this work, rather than by the author, but they are included here since some time and effort went into sample production and in some cases published outputs have resulted (see for example references 1–3).

Specifically, time-resolved photoluminescence (TRPL) was carried out on the  $^{64}\text{ZnO}$ ,  $^{66}\text{ZnO}$  and  $^{68}\text{ZnO}$  samples grown during this work by our colleague Dr. Joseph Cullen in Linköping University in Sweden. CBD grown ZnO nanorods produced during this work were used in experiments on third harmonic UV generation by Prof. Enda McGlynn and colleagues at the Max Born Institute for Nonlinear Optics and Short-Pulse Spectroscopy in Berlin, Germany, including Dr. Ruediger Grunwald. Finally, some experiments were carried out on the generation of x-rays from nanostructured targets using ZnO nanorods grown using CBD on titanium (Ti) targets. These experiments were carried out by collaborators Dr.

Matthias Schnürer and Julia Braenzel, also in the Max Born Institute in Berlin, during a research visit there by the author in 2013.

## A.2 TRPL of Zn-enriched ZnO nanorods

TRPL was carried out on the pure Zn-enriched samples in order to study the BX decay lifetimes. Data from various samples is presented in figure A.1. Figure A.1(a) shows the TRPL decay of the I<sub>9</sub> BX recombination in <sup>64</sup>ZnO, <sup>66</sup>ZnO and <sup>68</sup>ZnO nanorods. Figure A.1(b) shows the same data for the first LO replica of the I<sub>9</sub> line. The decay in all cases can be described by two exponentials, a fast component  $\tau_f$ , and a slow component  $\tau_s$ .<sup>4</sup> These time constants and their relative amplitudes ( $A_{\tau_f}$  and  $A_{\tau_s}$ ) for the I<sub>9</sub> BX recombination in each sample are shown in table A.1. The fast component can be attributed to surface effects and the slow component to the intrinsic BX radiative recombination rate. The figures in table A.1 are consistent with those previously reported for ZnO nanorods, and we note this report also contains a study on the changes in lifetimes with nanorods size.<sup>4</sup> The I<sub>9</sub> exciton displays an almost single exponential decay as shown by the (close to) straight lines in figure A.1(a), which indicates that the decay is dominated by the slow component indicating very high quality samples. The <sup>68</sup>ZnO sample I<sub>9</sub> exciton decay departs from linearity slightly more than that of <sup>64</sup>ZnO or <sup>66</sup>ZnO samples. This indicates that for this sample the fast component had a greater relative impact, which implies a greater influence of surface defects in this sample. This is seen in the  $A_{\tau_f}/A_{\tau_s}$  ratio in table A.1. The biexponential nature of the decay in the <sup>68</sup>ZnO is more pronounced in the I<sub>9</sub>-1LO data shown in figure A.1(b). Figure A.1(c) shows a comparison of the TRPL data for the I<sub>9</sub> and SX recombinations. The almost single exponential decay of the I<sub>9</sub> exciton is contrasted with the much more pronounced biexponential decay of the SX, with a very fast initial decay. This is to be expected as the fast component associated with surface effects is naturally more important for this emission. The fast component is again fitted with a greater amplitude for the <sup>68</sup>ZnO sample than in the <sup>66</sup>ZnO and <sup>64</sup>ZnO samples, confirming a greater influence of surface defects in this sample.

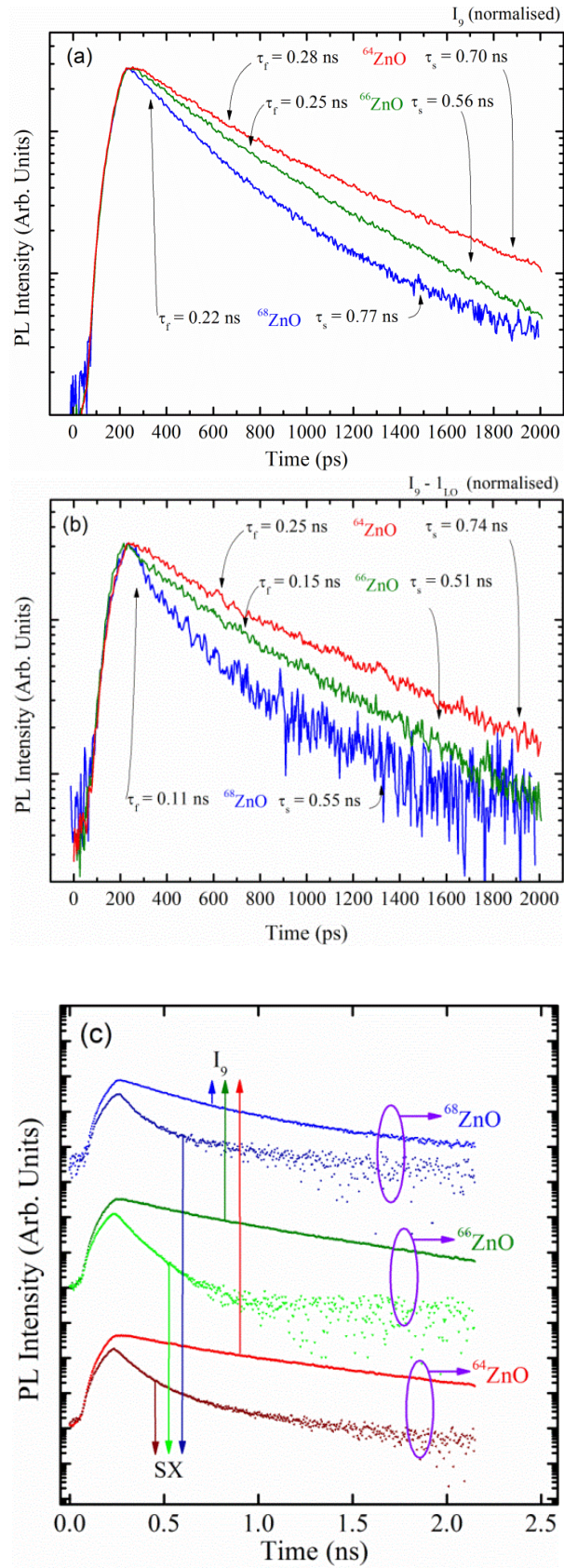


Figure A.1: TRPL decay curves of (a) the  $I_9$  recombination, (b) the  $I_9$ - $I_{LO}$  line, and (c) the  $I_9$  and SX features, in Zn-enriched ZnO nanorods

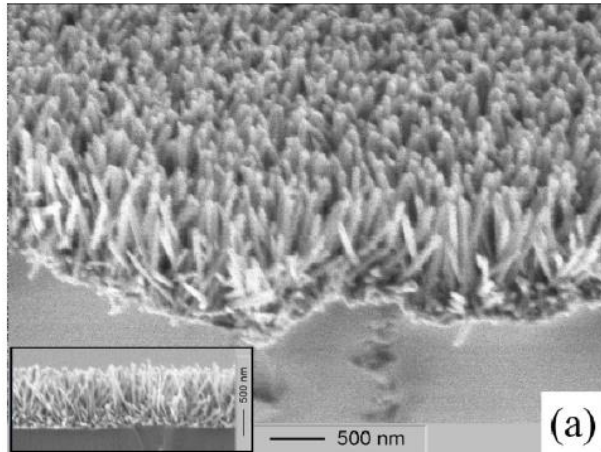
Sample	<sup>64</sup> ZnO	<sup>66</sup> ZnO	<sup>68</sup> ZnO
$\tau_f$ (ps)	277.9±8.6	250.3±8.5	223.8±2.1
$\tau_s$ (ps)	698.5±20.3	557.4±19.7	774.2±35.1
$A_{\tau_f}/A_{\tau_s}$	1.21:1.00	1.40:1.00	6.88:1.00

Table A.1: Fast ( $\tau_f$ ) and slow ( $\tau_s$ ) component time constants of the  $I_9$  decay lifetime and their relative amplitudes in Zn-enriched ZnO nanorods.

The TRPL data supports the previous SEM and XRD data in chapter 4 that the ZnO nanorod samples are of very high quality, although the <sup>68</sup>ZnO sample appears have a poorer surface quality, as evidenced by the larger fast component amplitude in TRPL measurements of the biexponential decay, which adversely affects its TRPL properties. We see no other clear correlation with changes in isotopic mass in these TRPL measurements.

### A.3 Third harmonic UV generation with ZnO nanorods

Non-enriched ZnO nanorods were grown on fused silica substrates using the NaOH-based chemical bath. The procedure for growing such nanorods was the same as for Si substrates, as described in section 2.2.3, and resulted in a dense film of textured,  $c$ -axis aligned ZnO nanorods of  $\sim 1 \mu\text{m}$  in thickness. This sample was then used by our colleagues in Berlin in experiments regarding UV third harmonic generation (THG).<sup>1,2</sup> Figure A.2 shows an image of the CBD-grown nanorods on these substrates.



*Figure A.2: CBD grown ZnO nanorods on a fused silica substrate. Reproduced from reference 1.*

THG generation has potential application in, to give some examples, characterisation of ultrashort femtosecond laser pulses and local photodynamic therapy in the human body.<sup>5,6</sup> ZnO nanorods grown by CBD have been used to study this to the level of single cells.<sup>7</sup> These CBD samples were studied in addition to VPT samples produced by VLS growth by others, as regards their THG efficiency. The incident laser had a central wavelength of 810 nm and the THG signal was observed in both samples at  $\sim 272$  nm. Ultimately, both the CBD sample produced by the author and the other VPT sample were shown to be efficient sources for UV THG compared to a bare quartz substrate. This was in contrast to the typical linear optical characteristics of samples produced by these methods where VPT samples typically display much higher optical quality than CBD samples (as shown in chapter 4) and elsewhere.<sup>8,9</sup> This study showed the suitability of ZnO nanorods as an efficient generator of UV emission by up-conversion of red/near infrared laser pulses. The samples were also shown to be effective in the characterisation of femtosecond laser pulses.

## A.4 Particle and X-ray generation using ZnO nanorods

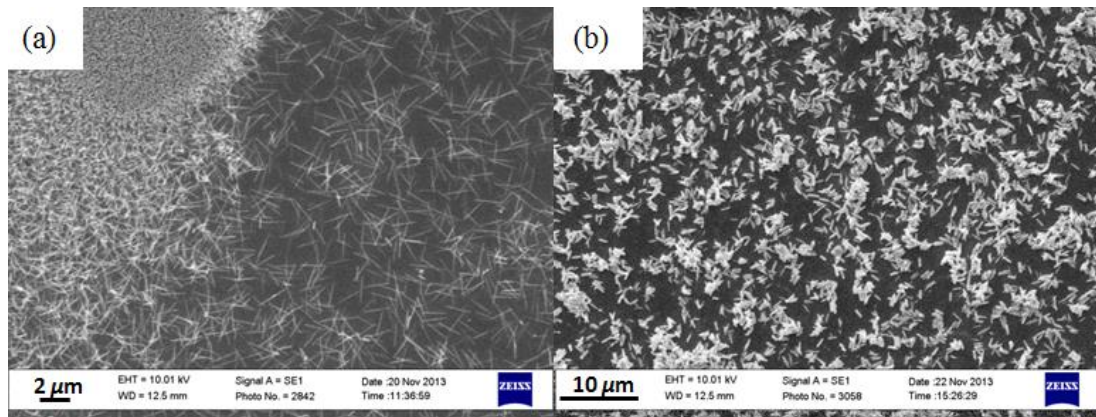


Figure A.3: ZnO nanorods on Ti foil grown by the (a) NaOH and (b) HMT chemical baths.

Some ZnO nanorods were also produced during this work for a research visit undertaken to the Max Born Institute in Berlin in November 2013. For this, ZnO nanorods were produced using the NaOH chemical bath but using Ti foil as a substrate. The deposition process was also the same as used with Si substrates. Some samples of ZnO nanorods were also grown using the HMT method on these substrates. Coverage on these samples was however less uniform than was typical for this growth method in our laboratory. The seed layer is most likely the cause of this as it was more difficult to achieve a smooth and uniform drop-coat of seed solution on the Ti as it did not wet as easily as the Si. Figure A.3 gives an example of ZnO nanorods grown by the (a) NaOH and (b) HMT chemical baths on the Ti foil substrates.

Our colleagues in Berlin used these samples in their study of particle acceleration with a number of nanostructured targets using high intensity, ultra short, laser pulses (Ti:Sapphire, 1.3 J,  $\sim 30$  fs).<sup>3</sup> Whether the nanorods, or other nanostructured morphologies, improve the laser to target coupling, and thus the particle and x-ray emission efficiency, was investigated.<sup>10</sup> The basic principle here is that lasers at very high relativistic intensities interact with the electrons in the sample and cause an acceleration of the electron distribution with ions accelerated to

high kinetic energies subsequently. These laser-induced nano-plasmons can significantly improve the particle acceleration mechanism. Such interaction of high energy light with matter has attractive opportunities in research and potential applications. A theoretical model was compared to experimental results and our CBD samples were among others included in this study. The energy spectral distributions of protons and carbon ions following an incident laser shot showed that the ion numbers were significantly enhanced in our CBD nanorods samples, and others, in comparison to the plain Ti foil.

## A.5 References

- <sup>1</sup> S.K. Das, F. Güell, C. Gray, P.K. Das, R. Grunwald, and E. McGlynn, *Opt. Mater. Express* **4**, 701 (2014).
- <sup>2</sup> S. Kumar Das, F. Güell, C. Gray, D. Byrne, P. Kumar Das, R. Grunwald, G. Steinmeyer, and E. McGlynn, in *Prog. Nonlinear Nano-Optics*, edited by S. Sakabe, C. Lienau, and R. Grunwald (Springer International Publishing, Cham, 2015), pp. 193–206.
- <sup>3</sup> A. Andreev, K. Platonov, J. Braenzel, A. Lübcke, S. Das, H. Messaoudi, R. Grunwald, C. Gray, E. McGlynn, and M. Schnürer, *Plasma Phys. Control. Fusion* **58**, 014038 (2016).
- <sup>4</sup> S. Hong, T. Joo, W. Il Park, Y.H. Jun, and G.-C. Yi, *Appl. Phys. Lett.* **83**, 4157 (2003).
- <sup>5</sup> Y. Kobayashi, D. Yoshitomi, K. Iwata, H. Takada, and K. Torizuka, *Opt. Express* **15**, 9748 (2007).
- <sup>6</sup> J. Li, D. Guo, X. Wang, H. Wang, H. Jiang, and B. Chen, *Nanoscale Res. Lett.* **5**, 1063 (2010).
- <sup>7</sup> S.M. Al-Hilli, M. Willander, A. Öst, and P. Strålfors, *J. Appl. Phys.* **102**, 084304 (2007).
- <sup>8</sup> D. Byrne, *The Growth and Characterisation of Ordered Arrays of Zinc Oxide Nanostructures and Optical Studies of Defects in Zinc Oxide*, Dublin City

University, 2012.

<sup>9</sup> D. Byrne, E. McGlynn, J. Cullen, and M.O. Henry, *Nanoscale* **3**, 1675 (2011).

<sup>10</sup> M.A. Purvis, V.N. Shlyaptsev, R. Hollinger, C. Bargsten, A. Pukhov, A. Prieto, Y. Wang, B.M. Luther, L. Yin, S. Wang, and J.J. Rocca, *Nat. Photonics* **7**, 796 (2013).

# Appendix B: Efficiency of the SPEX grating and PMT

As discussed in section 2.4.5, the efficiency curves for the diffraction grating and PMT used with the SPEX spectrometer, along with their equations, are shown in figure B.1 and below (reproduced from reference 1).

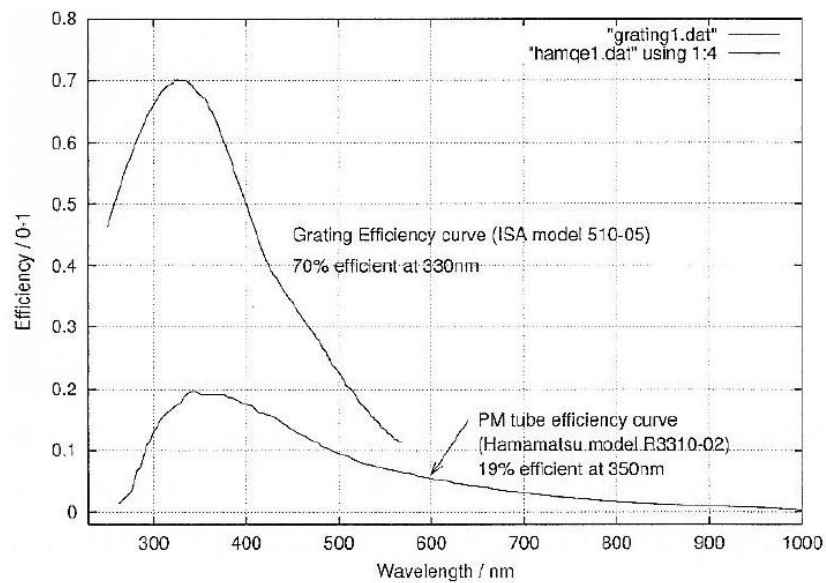


Figure B.1: SPEX grating and PMT efficiency curves.

Grating efficiency curve:

$$y = -59.649 + 0.5479x - 0.00181x^2 + 2.5857 \times 10^{-6}x^3 - 1.3598 \times 10^{-9}x^4$$

PMT efficiency curve:

$$y = -1056.763 + 10.6889x - 0.0424x^2 + 8.6543 \times 10^{-5}x^3 - 9.6602 \times 10^{-8}x^4 + 5.621 \times 10^{-11}x^5 - 1.336 \times 10^{-14}x^6$$

## B.1 References

<sup>1</sup> D. Gorman, Photoluminescence and Excitation Studies of Semiconductors, Dublin City University, 2001.

# Appendix C: XRD Strain measurements for the Zn-enriched and VLS O-enriched samples.

As stated in section 5.3.1, between the submission of this thesis for examination and the *viva-voce* examination, the XRD strain measurements described in that section for the VS O-enriched samples were carried out on the Zn-enriched samples and the VLS O-enriched samples, in order to complete this study on the full set of samples presented in this work. The peaks positions of the *s*- and *r*-planes with an in-plane component as recorded in these samples and described in section 5.3.1 are contained table C.1. For the Zn-enriched samples, the *s*-plane peaks vary by  $\sim 0.13^\circ$  and the *r*-planes by  $\sim 0.1^\circ$ , although there is no particular trend by mass. For the VLS O-enriched samples, the *s*-plane peaks vary by  $\sim 0.03^\circ$  and the *r*-planes by  $\sim 0.06^\circ$ , and again there is no particular trend by mass. The actual peak positions vary slightly from the expected values of  $36.256^\circ$  and  $47.541^\circ$  respectively. This could be attributed to an instrument calibration which took place in the meantime. The small shifts in peak positions, and the lack of trend by either average mass or pure versus mixed samples, indicates there is no discernible strain in our samples. This is consistent with the result of this experiment for the VS O-enriched samples discussed in detail in section 5.3.1.

<b>Sample</b>	<b>ZnO <i>s</i>-plane (10-10) peak <math>2\theta</math> (°)</b>	<b>ZnO <i>r</i>-plane (10-12) peak <math>2\theta</math> (°)</b>
<sup>nat</sup> ZnO	36.431	47.739
<sup>64</sup> ZnO	36.347	47.695
<sup>66</sup> ZnO	36.453	47.764
<sup>68</sup> ZnO	36.323	47.679
<sup>64/66</sup> ZnO	36.427	47.765
<sup>66/68</sup> ZnO	36.342	47.664
<sup>64/68</sup> ZnO	36.418	47.751
<sup>64/66/68</sup> ZnO	36.338	47.695
Zn <sup>16</sup> O-VLS	36.386	47.701
Zn <sup>16/18</sup> O-VLS	36.365	47.769
Zn <sup>18</sup> O-VLS	36.396	47.701

*Table C.1: *s*-plane and *r*-plane  $2\theta$  peaks (with in-plane component) in the Zn-enriched and VLS O-enriched samples.*